UNIVERSITAT DE BARCELONA

OPA1 deficiency drives muscle inflammation

La deficiència d'OPA1 resulta en inflamació muscular

Aida Rodríguez Nuevo

UNIVERSITAT DE BARCELONA

FACULTAT DE BIOLOGIA

DEPARTAMENT DE BIOQUÍMICA I BIOMEDICINA MOLECULAR

OPA1 deficiency drives muscle inflammation

La deficiència d'OPA1 resulta en inflamació muscular

Aida Rodríguez Nuevo

Barcelona, 2018

UNIVERSITAT DE BARCELONA

FACULTAT DE BIOLOGIA

DEPARTAMENT DE BIOQUÍMICA I BIOMEDICINA MOLECULAR

INSTITUTE FOR RESEARCH IN BIOMEDICINE (IRB BARCELONA)

PROGRAMA DE DOCTORAT EN BIOMEDICINA

OPA1 deficiency drives muscle inflammation

La deficiència d'OPA1 resulta en inflamació muscular

Memòria presentada per Aida Rodríguez Nuevo per optar al grau de doctora per la Universitat de Barcelona.

Aida Rodríguez Nuevo — *Doctoranda*

Antonio Zorzano Olarte — *Director i tutor*

Barcelona, 2018

CONTENTS

FIGURE CONTENTS

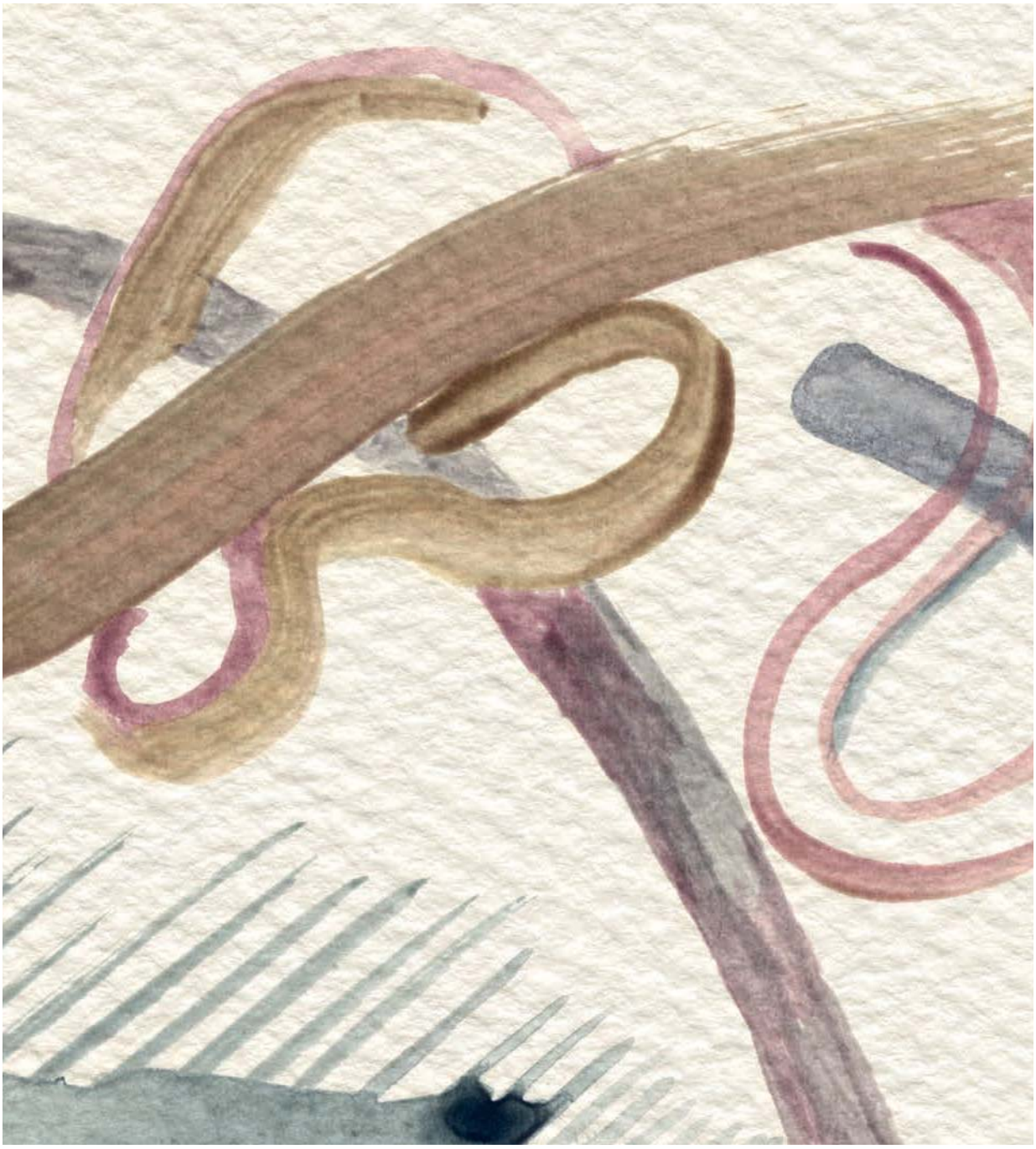

ABBREVIATIONS

A
Ab: Antibody
ADOA: Autosomal dominant optic atrophy
ADP: Adenosine diphosphate
Adv: Adenovirus
AIM2: Absten in melanoma 2
ARP: Actin related protein
ASC: Apoptosis-associated speck-like protein containing a CARD
ATCC: American Type Culture Collection
ATF4: Activating transcription factor 4
ATP: Adenosine triphosphate
ATP5a1: ATP synthase (complex V) subunit alpha 1

B
BCA: Bicinchoninic acid
bp: Base pairs
BSA: Bovine Serum Albumin

C
CI - CV: mitochondrial OXPHOS complex I to V
CCCP: Carbonyl cyanide m-chlorophenyl hydrazone
cDNA: Complementary DNA
cGMAP: cyclic GMP-AMP
cGAS: Cyclic GMP-AMP synthase
CJs: Cristae junctions
CK: Creatine kinase
CMT2A: Charcot- Marie Tooth type 2A
CMA: Chaperone-mediated autophagy
CQ: Chloroquine
CS: Citrate synthase
CSA: Cross-sectional area
CTX: Cardiotoxin
CYTB: Cytochrome b

D
DAMP: Damage-associated molecular pattern
DKD: Double KD
DKO: Double KO
DMEM: Dulbecco's modified Eagle's medium
DMSO: Dimethyl sulfoxide
DNA: Deoxyribonucleic acid
DRP1: Dynamin-related protein 1
dsDNA: double stranded DNA
DTT: Dithiothreitol

E
ECAR: Extracellular acidification rate
EDTA: Ethylenediaminetetraacetic acid
EEA1: Early endosome antigen 1
EGTA: Ethylene glycol tetraacetic acid
ELISA: Enzyme-linked immune-sorbent assay
ER: Endoplasmic reticulum
ESCRT: Endosomal sorting complexes required for transport

EtBr: Ethidium Bromide

F
FBS: Fetal Bovine Serum
FCCP: Carbonyl cyanide-4-(trifluoromethoxy)phenylhydrazone
FGF21: Fibroblast growth factor 21
FIS1: Fission homologue 1

G
G6P: Glucose-6-Phosphatase
GAPDH: Glyceraldehyde-3-phosphate dehydrogenase
GFP: Green fluorescent protein
GHR: Growth hormone receptor
GTP: guanosine triphosphate
GTPasa: guanosine triphosphatase

H
HE: High exposure
HEPES: Hydroxyethyl piperazineethanesulfonic acid
Hmgb1: High mobility group box 1
HSP60: Heat shock protein 60
Hygro: Hygromycin

I
IBM: Inner boundary membrane
IFIT1: Interferon induced protein with tetratricopeptide repeats 1
IFN: Interferon
IGF-1: Insulin-like growth factor 1
IL-1β: Interleukine 1 beta
IL-6: Interleukin 6
IMM: Inner mitochondrial membrane
IMS: Intermembrane space
IRF3: Interferon regulatory factor 3
IRF7: Interferon regulatory factor 7
ISG: Interferon stimulated genes
ISG15: Interferon-stimulated gene 15

K
KD: Knock-down
KO: Knock-out

L
LAMP1: Lysosomal-associated membrane protein 1
LBPA: Lysobisphosphatidic acid
LDH: Lactate deshidrogenase
LE: Low exposure
Loxp: Locus of X(cross)-over in P1

M
MAVS: Mitochondrial antiviral-signaling protein
MCAD: Medium-chain acyl-coenzyme A dehydrogenase
MEF: Mouse embryonic fibroblasts
MEF2c: Myocyte-specific enhancer factor 2C

MFF: mitochondrial fission factor
MFN1: Mitofusin 1
MFN2: Mitofusin 2
MHC: Major histocompatibility complex
miRNA: microRNA
MPP: Mitochondrial processing peptidase
mtDNA: mitochondrial DNA
MTS: mitochondrial targeting sequence
Myd88: Myeloid differentiation primary response 88

N
ND4: Mitochondrially Encoded NADH Dehydrogenase 4
nDNA: nuclear DNA
NDUFA9: NADH Dehydrogenase (Ubiquinone) 1 Alpha Subcomplex, 9
NF-κB: Nuclear factor kappa B
Nlrp3: NLR Family Pyrin Domain Containing 3
NSE: Non-specific esterase

O
OCR: Oxygen consumption rate
OMA1: Overlapping Activity With M-AAA Protease
OMM: Outer mitochondrial membrane
OPA1: Optic Atrophy 1
OXPHOS: Oxidative phosphorylation
O/N: Overnight

P
P-: phosphorylated
PAMP: Pathogen-associated molecular pattern
PARK-2: Parkinson disease (autosomal recessive, juvenile) 2, parkin
PARP: poli ADP ribosa polimerasa
PBS: Phosphate buffered saline
PCR: Polymerase Chain Reaction
PEI: Polyethylenimine
PEPCK: Phosphoenolpyruvate carboxykinase
PGC-1a: Peroxisome proliferator-activated receptor γ coactivator 1 alpha
PINK1: PTEN-induced putative kinase 1
PMSF: Phenylmethylsulfonyl fluoride
Puro: Puromycin

R
Rage: AGER (Advanced Glycosylation End-Product Specific Receptor)
RNA: Ribonucleic acid
ROS: Reactive oxygen species
rpm: revolutions per minute
rRNA: ribosomal RNA
RT: Room temperature

S
Scr: Scramble
SDHA: Succinate dehydrogenase [ubiquinone] flavoprotein subunit
SDS: Sodium dodecyl sulfate

SOCS3: Suppressor of cytokine signaling 3
SR: Sarcoplasmic reticulum
STAT5: Signal transducer and activator of transcription 5
STING: Stimulator of interferon genes protein

T
TCA: tricarboxylic acid
TERT: Telomerase Reverse Transcriptase
TFAM: Transcription Factor A, Mitochondrial
TIM44: Translocase of inner mitochondrial membrane 44
TLR: Toll-like receptor
TMRM: Tetramethylrhodamine
TNF-a: Tumor necrosis factor alpha
TOM20: Translocase of outer mitochondrial membrane 20
tRNA: transference RNA

U
UQCRC2: Ubiquinone cytochrome c reductase subunit core 2 (complex III)
USP18: Ubiquitin Specific Peptidase 18

V
VLCAD: Very long chain acyl-CoA dehydrogenase
VPS4: Vacuolar Protein Sorting 4

ΔΨ: Membrane potential difference

INTRODUCTION

2.1. Mitochondria: origin and features

Mitochondria arose around two thousand million years ago, which makes them one of the most ancient endomembrane system in eukaryotic cells. In 1967 Lynn Margulis rescued the long-term forgotten endosymbiont theory of organelle origin (Sagan, 1967). This theory describes the origin of eukaryotic cells as derived from the engulfment of an α-proteobacterium by the eukaryotic progenitor. The resemblance of modern mitochondria to their bacterial ancestor supports this theory: Among other features, mitochondria are comprised of two functionally different and separated membranes that surround a matrix compartment which contain the unmethylated mitochondrial circular genome organized as nucleoids throughout the matrix (Nunnari and Suomalainen, 2012). In 50 years, there have been significant advances in the subject. Nowadays, it is well recognized that, although the mitochondrial genomes originate entirely from that α-proteobacterium, the major part was rapidly lost or transferred to the nuclear genome. Differently, the mitochondrial proteome composition is plastic in nature and origin, for instance, mitochondrial DNA (mtDNA) replication and transcription machines have evolved from bacteriophages, while translational machinery has its origin in bacteria. The evolutionary plasticity of the mitochondrial proteome also entails it to adapt to the cellular and tissue-specific requirements.

Mitochondria are pivotal organelles for many cellular functions. Mitochondria are the primary energy-generating system in most eukaryotic cells. As the site of oxidative phosphorylation, these double-membrane organelles provide a highly efficient route for eukaryotic cells to generate ATP from energy-rich molecules. Additionally, they participate in intermediary metabolism, regulation of programmed cell death, calcium homeostasis, and the generation and control of reactive oxygen species (ROS) (Hockenbery *et al.*, 1990; Gunter *et al.*, 1998; Nunnari and Suomalainen, 2012)

The architecture of mitochondria is essential for the proper function of the organelle. At the ultrastructural level mitochondria are comprised by two membranes: the outer mitochondrial membrane (OMM) and the inner mitochondrial membrane (IMM), and the space between them defines

the intermembrane space (IMS). The mitochondrial matrix is the space enclosed by the IMM. The OMM is structurally simple and highly permeable to small molecules and ions, while at the same time, it is able to protect the cell from noxious mitochondrial products including ROS, immunogenic mtDNA (Zhang *et al.*, 2010) and death signals. The IMM is morphologically more complex, and it creates an impermeable barrier between the matrix and the IMS. It includes both the inner boundary membrane (IBM), which lies parallel to the OMM, and the cristae formed by tubular IMM invaginations. Cristae junctions (CJs) separate the IBM and cristae, with an opening of only 20-50nm in diameter, thus permitting these two subcompartments to perform distinct functions (Vogel *et al.*, 2006). The permeability of the IMM is very restricted and it is indeed the major barrier between the cytosol and the mitochondrial matrix, which in physiological conditions allows for the establishment of a proton gradient. This restrictive permeability together with proper cristae morphology are the two major physical features that enable mitochondria to perform oxidative phosphorylation (Jayashankar, Mueller and Rafelski, 2016). Electrons from oxidative substrates are transferred to oxygen, via a series of redox reactions, to generate water. In the process, protons are pumped from the matrix across the IMM through respiratory complexes I, III, and IV. When protons return to the mitochondrial matrix down their electrochemical gradient, ATP is synthesized.

The IMS contains several proteins involved in protein transport, cellular homeostasis, mitochondrial bioenergetics and cell death, for example: cytochrome C, apoptosis inducing factor and mitochondrial creatine kinase. Lastly, the mitochondrial matrix accommodates essential mitochondrial processes like the tricarboxylic acid (TCA) cycle, fatty acids β-oxidation, transamination, and Fe-S and Heme-group biosynthesis. Also, this matrix contains the mitochondrial genome or mtDNA, distributed in mtDNA nucleoids throughout the matrix, and the machines involved in its replication, transcription, translation and quality control; the biology of which will be explained in chapter 2.6.

Mitochondrial content and morphology varies dramatically not only between different cell types, but also under divers energetic or cellular demands. Thus, the regulatory elements that control both content and morphology need to be perfectly tuned. Mitochondrial biogenesis is defined as the process by which

a cell induces the production of more mitochondria, either in response to mitochondrial damage or increased energetic demands. This process occurs by the division and growth of existing mitochondria, because mitochondria are not synthetized *de novo.* Given that only 13 of the 1000 mitochondrial proteins are encoded in the mtDNA, there is a need of a two-ways communication between nuclear and mitochondrial transcription machineries. In this case, this regulation lays on the transcription factors: NRF-1, NRF-2, PPARα, ERRα, and transcription coactivators: PGC-1α, PGC-1β y PRC (Scarpulla, Vega and Kelly, 2012; Palikaras and Tavernarakis, 2014). The contrary process is also essential, mitochondrial degradation is under the regulation of mitochondrial quality control system, which will be revised in chapter 2.5.

2.2. Mitochondrial dynamics

The study of mitochondrial dynamics is the subject that examines how mitochondria undergo fusion and fission events by which they are shaped to response and adapt to the cell environment and metabolic requirements (Bereiter-Hahn and Voth, 1994; Mariathasan *et al.*, 2006; Liesa, Palacin and Zorzano, 2009; Westermann, 2010; Chan, 2012). Genetic studies in yeast were instrumental in identifying the molecular players in mitochondrial dynamics (Hermann and Shaw, 1998; Bleazard *et al.*, 1999; Tieu *et al.*, 2002; Okamoto and Shaw, 2005; Klionsky *et al.*, 2016). The key factors in both fusion and fission are large GTP-hydrolyzing enzymes of the dynamin superfamily (Mishra and Chan, 2014).

Mitochondrial fusion consists of two sequential steps: first the fusion of the OMM and then the fusion of the IMM (Malka *et al.*, 2005). Mitofusins are GTPases localized to the OMM. Mammals have two mitofusin genes, MFN1 and MFN2 (Chen *et al.*, 2003). These are the only mammalian outer membrane proteins known to be essential for mitochondrial fusion (Koshiba *et al.*, 2004). Optic Atrophy 1 (OPA1) is the dynamin-related protein responsible for the IMM fusion (Cipolat *et al.*, 2004; Chen, Chomyn and Chan, 2005)

The opposing process is mitochondrial fission. Dynamin-related protein 1 (DRP1) is the master regulator of mitochondrial fission in most eukaryotic organisms. In this process DRP1 is recruited from the cytosol

onto mitochondria at sites marked by endoplasmic reticulum (ER) tubules (Friedman *et al.*, 2011). Four DRP1 receptors exist in mammals: mitochondrial fission 1 (FIS1), mitochondrial fission factor (MFF), Mitochondrial dynamics protein of 49 kDa (MID49) and MID51; and these are located on the mitochondrial OM (Liesa, Palacin and Zorzano, 2009; Otera *et al.*, 2010; Loson *et al.*, 2013). Assembly of DRP1 in a polymeric helical structures wrapping around mitochondrial surface causes constriction of the organelle and eventual division of the mitochondrion into two separate entities (Labrousse *et al.*, 1999; Yoon and McNiven, 2001; Ingerman *et al.*, 2005).

Mitochondrial fusion and fission need to be in perfect balance (Wai and Langer, 2016). Reduced fusion or increased fission causes mitochondrial fragmentation. Symmetrically, reduced fission or increased fusion results in elongation of the mitochondrial network (Liesa, Palacin and Zorzano, 2009). The control of mitochondrial morphology is crucial for mitochondria to adapt to the cellular needs. Elongated morphology is related to situation of higher cellular energetic demands such as in amino acid starvation conditions. Also, during viral infection, mitochondrial tubular morphology potentiates mitochondria as innate immune hubs, and in turn cell survival. In contrast, fragmented mitochondria are easier to transport. Hence, they present this individualized shape in chemotaxing lymphocytes and during asymmetrical cell division to preserve cellular pluripotency (Pernas and Scorrano, 2016).

Despite the substantial importance of mitochondrial dynamics in the control of mitochondrial morphology, it is not the only endpoint of undergoing constant fission and fusion. On the contrary, mitochondrial metabolism, quality control, and response to apoptotic stimuli are partly controlled through the balance between mitochondrial fusion and fission (Zorzano *et al.*, 2010). Also, mitochondrial fusion clearly preserves mitochondrial function itself, by acting as a buffer of mitochondrial damage (Chen, McCaffery and Chan, 2007; Detmer and Chan, 2007). This function is specifically important in the case of mtDNA mutations accumulation, and can serve as an example for other mitochondrial components. In a cellular context of heteroplasmy, mitochondrial dynamism results in a highly intermixed composition of the different genomes, resulting in mitochondrion with a combination of healthy and mutated genomes, thus preventing the genetic drift of mtDNA (Chan, 2006).

2.3. Optic Atrophy 1: OPA1

This work is centered on the dynamin-related GTPase, Optic Atrophy 1 (OPA1) (Alexander *et al.*, 2000; Delettre *et al.*, 2000). The gene was found years after describing the association of mutations in the locus containing it with autosomal dominant optic atrophy (ADOA; MIM165500) (Eiberg *et al.*, 1994). Although it is expressed in all the tissues tested, OPA1 shows highest expression in retina, brain, testis, liver, heart, skeletal muscle, and pancreas (Akepati *et al.*, 2008; Liesa, Palacin and Zorzano, 2009).

OPA1 is composed by a N-terminal mitochondrial targeting sequence, which is cleaved by matrix-processing peptidase (MPP) after OPA1 mitochondrial import (Alexander *et al.*, 2000; Delettre *et al.*, 2000; Akepati *et al.*, 2008). Continuing towards C-terminal, OPA1 contains a transmembrane (TM) domain, and then the region that suffers mRNA alternative splicing, conferring different structures to the adjacent C-terminal coiled-coil domain, thus modulating its interactions. Contiguous, there are the GTPase domain, middle domain and C-terminal GTPase effector domain (Delettre *et al.*, 2000).

OPA1 is localized in the IMM and the IMS, these plural localization results from the complex posttranscriptional regulation of OPA1, both at mRNA and at protein levels. There are eight *OPA1* isoforms in humans, derived from the alternative splicing of exons 4, 4b and 5b (Delettre *et al.*, 2001; A. Olichon *et al.*, 2007). In mice, there are four, which are formed by the splicing of exons 4b and 5b (Akepati *et al.*, 2008) (Figure 1).

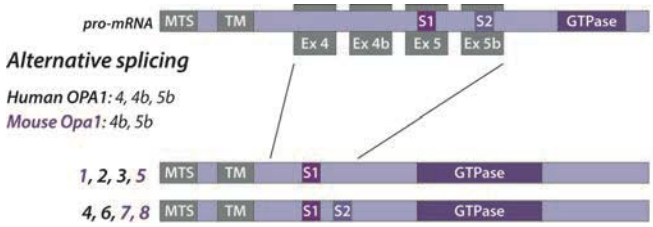

Splicing Variant	Exons 4, 4b, 5b	Cleavage sites	Found in mouse
1	4	S1	Yes
2	-	S1	
3	4b	S1	
4	5b	S1, S2	
5	4, 4b	S1	Yes
6	4b, 5b	S1, S2	
7	4, 5b	S1, S2	Yes
8	4, 4b, 5b	S1, S2	Yes

Figure 1. Optic Atrophy 1 (OPA1) alternative splicing. In humans eight splicing variants are generated from alternative splicing of exons 4, 4b, and 5b. In mice, exon 4 is not spliced, thus there is only 4 splicing variants, named after the human numeration. In both species, two types of variants are formed, one type containing cleavage site S1 and another type containing cleavage sites S1 and S2.

Isoforms 1 and 7 are predominantly expressed both in humans and in mice (Delettre *et al.*, 2001; Ishihara *et al.*, 2006; A. Olichon *et al.*, 2007; Akepati *et al.*, 2008).

After the OPA1 import to mitochondria and MPP processing of the mitochondrial targeting sequence, membrane-bound long (L)-OPA1 forms can be processed at two protease cleavage sites, S1 and S2, to generate short (S)-OPA1 forms (Ishihara *et al.*, 2006) (Figure 2). In humans, every L-OPA1 polypeptide contains an S1 site and half of them also contain an S2 site (Song *et al.*, 2007). The presence of two cleavage sites permits both the constitutive and the inducible proteolytic processing of OPA1 by two IMM proteases, which have their catalytic sites exposed to the IMS (Anand *et al.*, 2014). On one hand, the i-AAA protease (i, intermembrane space oriented) or YME1L acts constitutively at S2, thus only a half of OPA1 isoforms are converted. On the other hand, m-AAA (m, matrix oriented) zinc metalloprotease OMA1 is able to cleave all L-OPA1 at S1 (Käser *et al.*, 2003). The activity of these two IMM proteases establishes a near equimolar equilibrium of long and short OPA1 forms under basal conditions (Ishihara, 2004; Griparic, Kanazawa and Van Der Bliek, 2007; Song *et al.*, 2007; Wai and Langer, 2016) (Figure 2).

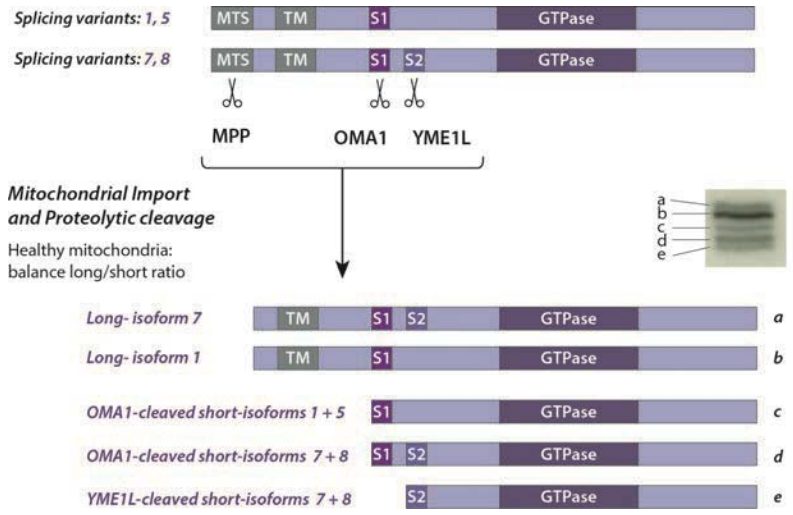

Figure 2. OPA1 proteolytic processing in healthy conditions. Mitochondrial processing peptidase (MPP) cleavage site (mitochondrial targeting sequence, MTS) and products. OMA1 cleavage site (S1) and products of all isoforms. YME1L cleavage site (S2) and products of isoforms 7 and 8. Products of MTS scission and S1 or S2 cleavage are represented as they appear when analyzed by 7,5 % acrylamide SDS-PAGE and immunoblot, tagged from (a) to (e).

Several studies report that OPA1 processing is regulated in response to different kinds of mitochondrial stress: mitochondrial dysfunction, oxidative stress, heat stress, or mitochondrial membrane potential dissipation (Ishihara *et al.*, 2006; Quirós *et al.*, 2012). Stress-induced OPA1 processing inhibits fusion by complete conversion of L-OPA1 to S-OPA1 forms (Figure 3) (Duvezin-Caubet *et al.*, 2006; Ishihara *et al.*, 2006; Song *et al.*, 2007; Guillery *et al.*, 2008), which causes cristae morphology disruption, mitochondrial fragmentation, and the segregation of damaged mitochondria (Twig *et al.*, 2008). If the stress persists, irreversibly damaged mitochondria are selectively degraded by mitophagy (Narendra *et al.*, 2008; Twig *et al.*, 2008) or eventually it induces apoptosis (Jiang *et al.*, 2014).

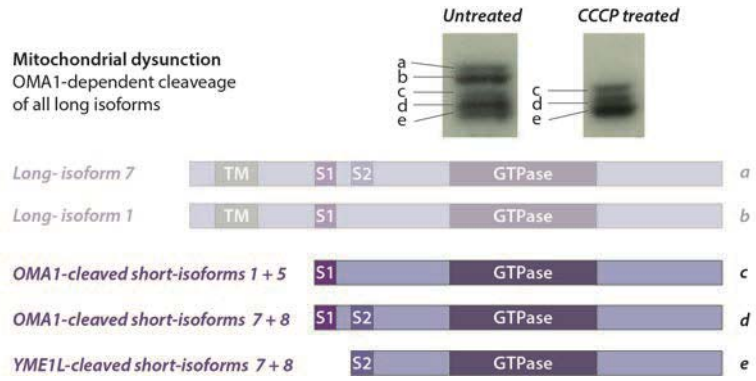

Figure 3. OPA1 proteolytic processing upon membrane depolarization. All long OPA1 isoforms (a-b) are converted to short forms (c-e). After 3h of CCCP treatment there is a complete loss of long OPA1 isoforms (a-b).

Various stress stimuli affecting the IMM membrane potential or intra-mitochondrial ATP levels were found to trigger OMA1 protease (Baricault *et al.*, 2007). The reversibility of the effect when the stimuli disappears is ensured by the autocatalytic turnover of OMA1 upon activation (Baker *et al.*, 2014).

OPA1 has been describe to be responsible for the fusion of the IMM and essential to maintain cristae morphology (Olichon *et al.*, 2003; Cipolat *et al.*, 2004; Frezza *et al.*, 2006; Griparic, Kanazawa and Van Der Bliek, 2007; Merkwirth *et al.*, 2008; Song *et al.*, 2009). OPA1 loss-of-function causes fragmentation of the tubular mitochondrial network. Conversely, over-production of OPA1 protein promotes mitochondrial elongation in cells where mitochondria are punctuated (Olichon *et al.*, 2003; Griparic, Kanazawa and Van Der Bliek, 2007; Song *et al.*, 2009). The profusion activity of OPA1 is further confirmed

by experiments showing that mitochondrial fusion is impaired in OPA1-depleted or *Opa1*$^{-/-}$ cells (Cipolat *et al.*, 2004; Chen, Chomyn and Chan, 2005; Song *et al.*, 2007, 2009). Both long and short OPA1 forms are essential for basal IMM fusion. Recently, it has been shown that L-OPA1 can mediate IMM fusion together with cardiolipin in a heterotypic manner. However, membrane tethering needs homotypic *trans*-OPA1 interaction (Ban *et al.*, 2017)

Independent on the function related to fusion, OPA1 controls cristae morphology. It has been shown that OPA1 oligomers formed in the cristae junction control its width as well as the width of the cristae lumen. On one hand, OPA1 control of cristae morphology has been observed to be crucial for the induction of pro-apoptotic-dependent cytochrome C release upon OPA1 cleavage. (Frezza *et al.*, 2006). Moreover, by maintaining mitochondrial cristae morphology, OPA1 has a direct metabolic effect stabilizing respiratory chain supercomplexes (Olichon *et al.*, 2003; Aurelien Olichon *et al.*, 2007; Cogliati *et al.*, 2013; Mishra *et al.*, 2014; Civiletto *et al.*, 2015; Varanita *et al.*, 2015; Cogliati, Enriquez and Scorrano, 2016).

Mounting evidence support the idea that OPA1 is involved in mtDNA stability. First, global loss of OPA1 causes depletion of mtDNA (Chen *et al.*, 2010). Second, missense mutations in OPA1 in humans cause accumulation of multiple deletions in skeletal muscle associated with other pathological manifestations framed in the ADOA-1 plus syndrome (OMIM #125250) which will be discussed in chapter 2.4. The study of ADOA patients-derived fibroblasts corroborate OPA1 involvement in mitochondrial function, through cristae morphology maintenance, OXPHOS activity, mitochondrial dynamics and also mtDNA stability (Belenguer and Pellegrini, 2013).

Different hypothesis to explain how OPA1 can influence on mtDNA stability have been formulated, here we revise three. First, OPA1 could influence mtDNA stability through the maintenance of the IMM structure, where mtDNA is anchored (Griparic *et al.*, 2004). Second, OPA1 as part of the mitochondrial dynamics proteome, could prevent mtDNA instability by facilitating exchange of mitochondrial contents (Hudson *et al.*, 2008). Third, OPA1 N-terminal region, facing the mitochondrial matrix could interact with

mtDNA nucleoids. In this regard, very interesting results were reported from studies in which each of the 8 human *Opa1* isoforms were expressed in mouse embryonic fibroblast depleted for *Opa1* (Del Dotto *et al.*, 2017). Any of the 8 isoforms were able to restore mtDNA copy number, the only prerequisite is a minimal reconstitution of cristae organization. Del Dotto and colleagues suggest that this could be indicative of an important role for the N-terminal domain of OPA1 in mtDNA stability (Del Dotto *et al.*, 2017). Which further supports the study of Elachouri and colleagues, which described an small peptide resulting from the proteolytic processing of exon 4b-containing OPA1 isoform (Elachouri *et al.*, 2011). The authors suggest that this peptide contributes to the IMM attachment of mtDNA nucleoids and promotes its replication. In this work, it is described a correlation between exon 4b-containing isoforms and mtDNA copy number (Elachouri *et al.*, 2011).

2.4. Mitochondrial fusion and disease

Appropriate mitochondria dynamics is essential in the maintenance of cellular health. Alteration in both MFN2 and OPA1 are associated with neurodegenerative diseases (Alexander *et al.*, 2000; Delettre *et al.*, 2000; Zuchner *et al.*, 2004). Mutations in *MFN2* cause Charcot-Marie-Tooth (CMT) type 2A (OMIM #605588) (Zuchner *et al.*, 2004). CMT is a group of diseases characterized by pathology in the longest motor and sensory nerves, which innervate the hands and feet (Zuchner *et al.*, 2005). Most of the over 20 *MFN2* mutations found in CMT2A patients are missense with mutations autosomal dominant inheritance; consequently, they may show haploinsufficiency or a dominant gain-of-function (Zuchner *et al.*, 2004; Kijima *et al.*, 2005; Lawson, Graham and Flanigan, 2005; Engelfried *et al.*, 2006; Verhoeven *et al.*, 2006).

OPA1 missense mutations have been reported in patients affected by autosomal dominant optic atrophy or ADOA (OMIM #165500) (Alexander *et al.*, 2000; Delettre *et al.*, 2000; Lenaers *et al.*, 2012). The fundamental pathology of ADOA is a primary degeneration of retinal ganglion cells, followed by increasing atrophy of the optic nerve and ultimately leading to blindness (Johnston *et al.*, 1979; Hoyt, 1980; Kjer, Jensen and Klinken, 1983; Votruba, Moore and Bhattacharya, 1998; Ichinohe, Pang and

Iwasaki, 2010). More than three hundred *OPA1* gene mutations have been identified as the cause of the 60-80% of the cases, frequently family-specific (Ferre *et al.*, 2005, 2015). Near 50% of the mutations cause truncation of the OPA1 protein, and most of the mutations are detected in the GTPase domain and are thus likely to eliminate mitochondrial fusion. The pathogenesis of ADOA occurs, in most cases, as a result of haploinsufficiency (loss-of-function) (Delettre *et al.*, 2000; Pesch *et al.*, 2001; Baris *et al.*, 2003; Kim *et al.*, 2005), but not always, ADOA can also develop as a result of a dominant negative mechanism. Human skin fibroblasts carrying *OPA1* mutations show impaired oxidative phosphorylation and mitochondrial fusion (Zanna *et al.*, 2008) . Some of these *OPA1* missense mutations are associated with altered mitophagy and parkinsonism (Carelli *et al.*, 2015). In addition to dominant optic atrophy, *OPA1* mutations also cause a multi-systemic disorder called ADOA plus syndrome (OMIM #125250), which account for 20% of ADOA cases and results in severe myopathy and progressive external ophtalmoplegia. Interestingly, these patients show multiple mtDNA deletions in muscles, which suggests a role of OPA1 on mtDNA stability (Hudson *et al.*, 2008; Zeviani, 2008; Dick *et al.*, 2016; Amati-Bonneau *et al.*, 2018).

2.5. Mitochondrial autophagy or mitophagy

In order to review mitochondrial autophagy or mitophagy is essential to describe the general process named autophagy. Two main features that characterize *bona fide*, functional autophagic responses, irrespective of type are: (i) they involve cytoplasmic material; and (ii) they culminate with (and strictly depend on) lysosomal degradation (Galluzzi *et al.*, 2017).

There are three major types of autophagy: (i) microautophagy/endosomal microautophagy, (ii) chaperone mediated autophagy, and (iii) macroautophagy (Figure 4) (Galluzzi *et al.*, 2017). After the terminological unification published in Galluzzi 2017, autophagy types are described as follows: (i) Microautophagy is a LAMP2A-independent autophagic response that proceeds upon direct membrane invagination at the surface of the lysosome/vacuole. Endosomal microautophagy is an ESCRT-dependent, LAMP2A-independent autophagic response that relies on direct membrane invagination at

the surface of late endosomes. (ii) Chaperone-mediated autophagy (CMA) is an HSPA8- and LAMP2A-dependent autophagic response that involves the translocation of substrates across the lysosomal membrane. (iii) Macroautophagy is a type of autophagic response that relies on the formation of autophagosomes (Figure 4).

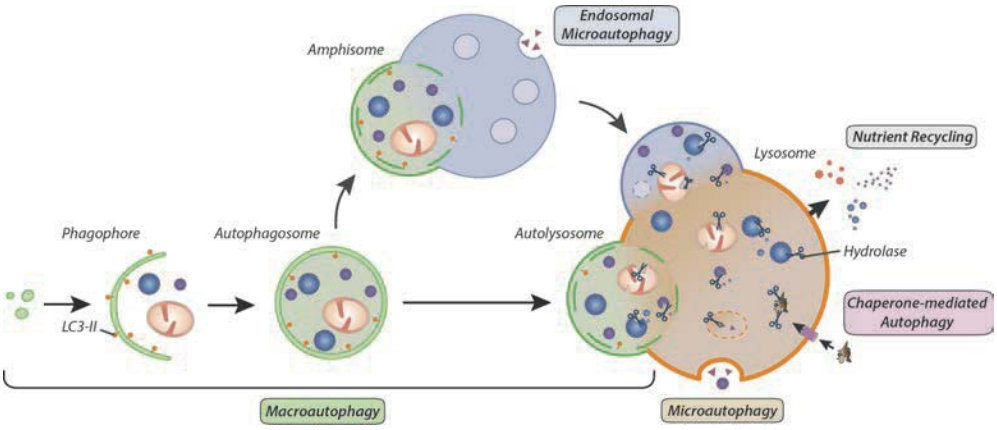

Figure 4. Autophagy types. Three major types of autophagy are represented: microautophagy (to the lysosome) or endosomal microautophagy (to the late endosome), chaperone-mediated autophagy, and macroautophagy.

This third type is the best studied and described autophagic process. Four relevant structures can be distinguished in macroautophagy: Phagophores (isolation membranes), autophagosome, amphisome and autolysosome. Phagophores are the precursors of autophagosomes. Forming mammalian phagophores membranes recruit the ULK1 complex and ATG14 (Karanasios *et al.*, 2008), which facilitates the assembly of the autophagy-specific Class III PI3K complex (Matsunaga *et al.*, 2010). This enables the association of the PI3P-binding proteins DFCP1 and WIPI2 (Polson *et al.*, 2010), the formation of ATG12-ATG5:ATG16L1 complexes, and consequent local LC3 lipidation (Dooley *et al.*, 2014). Autophagosomes are transient, double-membraned organelles (mean diameter in mammals 0.5-1.5 μm) that mediate cargo sequestration and delivery to lysosomes in the course of macroautophagic responses (Shibutani and Yoshimori, 2014). Amphisomes are single- or double-membraned organelles that originate from the fusion of autophagosomes and late endosomes (Gordon and Seglen, 1988). Given their origin, amphisomes contain both autophagosome and endosomal markers. Moreover, amphisomes have been proposed to contain small amounts of the lysosomal V-type ATPase, which

would be responsible for progressive acidification of their lumen (Fader and Colombo, 2009; Fader *et al.*, 2009; Bader *et al.*, 2015; Chandra *et al.*, 2015). Lastly, autolysosomes are single-membraned organelles that form in the course of macroautophagy upon fusion of autophagosomes and lysosomes (Klionsky, Eskelinen and Deretic, 2014). Autolysosomes are positive for lysosomal enzymes and classical endo/lysosomal markers, including LAMP1, LAMP2, and the V-type ATPase, but may display low levels of autophagosomal markers such as lipidated LC3, especially if autophagic flux is high (unless lysosomal hydrolases are pharmacologically or genetically inhibited) (Klionsky, Eskelinen and Deretic, 2014).

Micro and macro-autophagy can operate in a non-selective manner with the objective to obtain new substrates for bioenergetics metabolism or repair processes upon lysosomal degradation and recycling (E. Y. Liu *et al.*, 2015; Sica *et al.*, 2015). All three types of autophagy can operate in a specific manner, through a mechanism that involves the recognition of autophagy substrates by dedicated receptors, and are induced in response to specific cellular requirements or specific organelle damage (Youle and Narendra, 2011; Farré and Subramani, 2016). Given that this work is centered in mitochondria, mitochondrial macroautophagy is further revised below.

Mitochondrial macroautophagy (mitophagy, hereafter) has been described in a wide panel of model organisms, including yeast, nematodes, flies, and mammals. This process contributes to the removal of superfluous mitochondria that have no functional defects *a priori,* as well as to the degradation of mitochondria that are damaged beyond repair, hence dysfunctional and potentially cytotoxic (which is critical for the maintenance of cellular homeostasis, especially in highly metabolic tissues such as the brain) (Palikaras and Tavernarakis, 2014).

Mitophagy is described to play a physiological role only in two situations leading to complete mitochondrial removal: erythrocytes maturation aided by BCL2 interacting protein 3-like (BNIP3L; best known as NIX); and (ii) paternal mitochondrial degradation in early embryonic development, with the participation of PINK/PARK-2 (PTEN-induced putative kinase 1/Parkinson disease (autosomal

recessive,juvenile) 2, parkin) system in mammals (Al Rawi *et al.*, 2011; Sato and Sato, 2011; Politi *et al.*, 2014; Rojansky, Cha and Chan, 2016).

Mitophagy receptors can be classified into two types, ubiquitin-dependent and -independent (Hamacher-Brady *et al.*, 2016; Khaminets, Behl and Dikic, 2018). On one hand, the former uses the Pink1/Park2 system to ubiquitinate OMM proteins (Clark *et al.*, 2006; Park *et al.*, 2006), which in turn recruits receptor with ubiquitin binding domains: Optineurin, NDP52, p62 and NBR1 (Wei *et al.*, no date; Wong and Holzbaur, 2014; Heo *et al.*, 2015; Lazarou *et al.*, 2015; Moore and Holzbaur, 2016; Yamano, Matsuda and Tanaka, 2016; Fakruddin *et al.*, 2018). On the other hand, ubiquitin independent mitophagy uses specific receptors localized constitutively in the OMM: BNIP3, NIX, BCL2L13 and FUNDC1 (Liu *et al.*, 2012; Hamacher-Brady *et al.*, 2016). The activity of both types of mitophagy receptors is regulated transcriptionally and by its binding to Atg8 family proteins (mostly, LC3 and GABARAP), which in turn can be modulated by the phosphorylation of interacting adjacent residues (Zhang *et al.*, 2013; Hamacher-Brady *et al.*, 2016).

2.6. Mitochondrial DNA

The mitochondrial genome is a double stranded circular DNA molecule of around 16 kilobase, present in hundreds to thousands copies per cell. It is packed in structures denominated nucleoids, which are slightly elongated, irregularly shaped structure of approximately 80–100 nm associate with the IMM and distributed throughout the mitochondria (Gustafsson, Falkenberg and Larsson, 2016). These structures contain relatively high levels of mitochondrial transcription factor A (TFAM) (1 subunit every 16–17 bp of mtDNA), which is essential for mtDNA maintenance because is responsible for mtDNA packaging (Clayton, 1982; Larsson *et al.*, 1998; Kaufman *et al.*, 2000; Bogenhagen, 2012; Ngo *et al.*, 2014; Kukat *et al.*, 2015). There is some debate on the number of mtDNA copies per nucleoid, while some describe several copies per nucleoid (Brown *et al.*, 2011), others published a study suggesting that there is usually only one copy of mtDNA per nucleoid (Kukat *et al.*, 2011, 2015). The organization of mtDNA into nucleoids is essential for their correct distribution and segregation. In this regard, ER-

mitochondria contacts has been shown to determine mtDNA replication together with fission events (Lewis, Uchiyama and Nunnari, 2016). In this regard, mitochondrial dynamics are crucial, as well, to ensure proper mixing of nucleoids upon mitochondrial fusion, thus preventing mtDNA genetic drift (Legros, 2004; Chen, McCaffery and Chan, 2007; Vidoni *et al.*, 2013).

The mitochondrial genome encodes for 22 tRNA, 2 rRNA and 13 essential subunits of the mitochondrial oxidative phosphorylation system: complex I (ND1—ND6), complex III (Cyt b), complex IV (COX I—COX III) and complex V (A8 and A6). Also, it contains a few non-coding sequences, the largest being the D-loop or displacement loop, which contains promoters and origins of replication (Anderson *et al.*, 1981).

The replication of mtDNA starts with the formation of an RNA priming sequence generated by mitochondrial RNA polymerase (POLRMT) through the transcription of the light strand promoter (LSP). Then, endoribonuclease mitochondria RNA processing (MRP) generates a 3' end primer to initiate DNA replication of the heavy chain. Replication is performed by DNA polymerase γ assisted by the helicase TWINKLE that unwinds the DNA duplex, and by single strand binding proteins (mtSSB) that keep the DNA in a single stranded form. The mtDNA transcription starts from the promoters present in each strand producing polycistronic RNAs carried out by a mitochondrial RNA polymerase (POLRMT) assisted by a TFAM, and by mitochondrial transcription factor B1 or B2 (TFB1M and TFB2M) (Gustafsson, Falkenberg and Larsson, 2016). Mitochondria possess the majority of known nuclear DNA repair machineries: base excision repair, mismatch repair, homologous recombination, non-homologous end joining and trans-lesion synthesis. However, the proximity of the mitochondrial genome to ROS production sites results in increased mtDNA damage (Stein and Sia, 2017). Although mtDNA only encodes for 13 proteins (the mitochondrial proteome, comprising a thousand proteins), it has been proven to be essential. Because mutations in mtDNA are the cause of different alterations depending on the region affected: (i) mutations in rRNA or tRNA inhibit translation, (ii) mutations in protein coding regions affect protein structure and OXPHOS functionality, and interestingly, (iii) mutation in non-coding regions induce mtDNA instability (Vidoni *et al.*, 2013).

2.7. Mitochondrial DNA as a DAMP

The appropriate homeostasis of mitochondria is essential in the maintenance of cellular health. The immune system is educated to recognize pathogen-associated molecular patters (PAMPs), coming from infection, through a variety of different receptors. However, misplaced self-molecules or damage-associated molecular patters (DAMPs) can also trigger similar types of response. Mitochondria are describe to be source of several DAMPs, N-Formyl peptides, TFAM, cytochrome c, ATP, cardiolipin, ROS, and mtDNA, which serve as danger flags for immunological signaling (Figure 5) (Zhang *et al.*, 2010; Arnoult *et al.*, 2011; Krysko *et al.*, 2011; Yu and Bennett, 2014; Nakahira, Hisata and Choi, 2015).

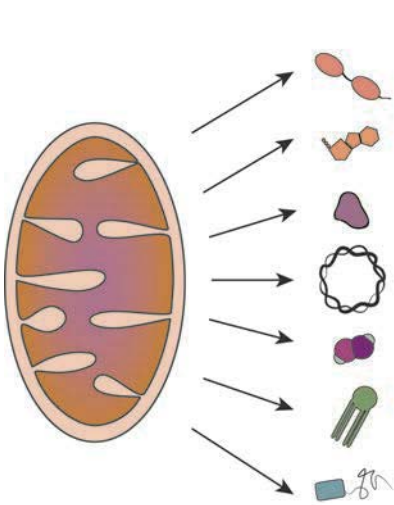

DAMP	Mechanism
TFAM	Recognised by RAGE, which guides TFAM-mtDNA complexes to the endosomal pathway.
ATP	Extracellular ATP signals through P2XR to induce inflammasome activation, apoptosis and ROS.
Cytochrome C	Pro-apoptotic factor.
Mitochondrial DNA	Extra-mitochondrial mtDNA is detected by different PRR.
ROS	Responisble for the oxidation of other molecules which increases their immunogenicity.
Cardiolipin	Immunogenic when found in the OMM.
N-formyl peptides	Extracellular N-formyl peptides act as chemoat-tractants of neutrophil via FP receptors.

Figure 5. Mitochondrial-derived damage-associated molecular patterns (DAMPs).

Besides being the source of DAMPs, mitochondria are also related to immunity through their role as innate immune platforms harboring the mitochondrial antiviral-signaling protein (MAVS) as a viral RNA sensor, and the Nod-like receptor 3 (NLRP3) inflammasome as a plural immunogenic receptor (Koshiba *et al.*, 2011; West, Shadel and Ghosh, 2011; Zhou *et al.*, 2011; Sutterwala, Haasken and Cassel, 2014; Mills, Kelly and O'Neill, 2017).

Relevant for this work, owing to the α-proteobacterial origin of mitochondria, mtDNA has unique features that are important for its role in innate immune responses and inflammation. Misplaced mtDNA is widely shown to induce a pro-inflammatory state (Zhang *et al.*, 2010; Nakahira *et al.*, 2011; Oka *et al.*, 2012; McCarthy *et al.*, 2015; West *et al.*, 2015; Picca *et al.*, 2017). Methylation of the CpG regions in the mtDNA is different than the nuclear DNA, which confers it immunogenic potential due to its resemblance to pathogenic DNA. Some authors describe that there is null methylation in the mtDNA, while others report that the nuclear DNA methyltransferase (DNMT1) is found in mitochondria which suggest some degree of methylation in mammalian cells (Shock *et al.*, 2011; Hong *et al.*, 2013). Besides hypomethylation, the mtDNA can suffer oxidative damage which is immunogenic and can be recognized by pattern recognition receptors (PRRs), independently of the methylation degree (Collins *et al.*, 2004; Shimada *et al.*, 2012). Furthermore, it has been reported that mtDNA stress elicited by TFAM deficiency triggers cytosolic antiviral signaling, promoted by cytosolic mtDNA leakage (West *et al.*, 2015). Thus, the degree of packaging, the stability, the localization and the presence of oxidative damage modifications or mutations are the properties implicated in mtDNA-innate immune signaling (West, Shadel and Ghosh, 2011).

2.8. Mitochondrial DNA immunogenic recognition

Since nucleic acids are central for the replication and propagation of most pathogens, their detection is covered by different kinds of PRRs localized in diverse cellular compartments. Particularly, mtDNA is described to be recognized by 5 innate immune receptors: cytosolic cyclic GMP-AMP synthase (cGAS), endosomal toll-like receptor 9 (TLR9), and 3 inflammasome types: absent in melanoma 2 (AIM2), NLR family CARD domain-containing protein 4 (NLRC4), and NOD, LRR and Pyrin domain-containing protein 3 (NLRP3) (Takeuchi and Akira, 2010; West and Shadel, 2017). This work has been centered in simple signals, thus the involvement of the different inflammasomes has not been characterized. Therefore, below there is a revision of cGAS and TLR9 as mtDNA sensors.

2.8.1. Mitochondrial DNA and cGAS signaling

cGAS is the DNA sensor most recently described, it was identified only in 2013 (Sun *et al.*, 2012; Wu *et al.*, 2013). Cytosolic dsDNA activates cGAS to form a dimeric cGAS-DNA complex which synthetizes cyclic GMP-AMP or cGAMP from ATP and GTP. This cGAMP functions as a second messenger because it is a

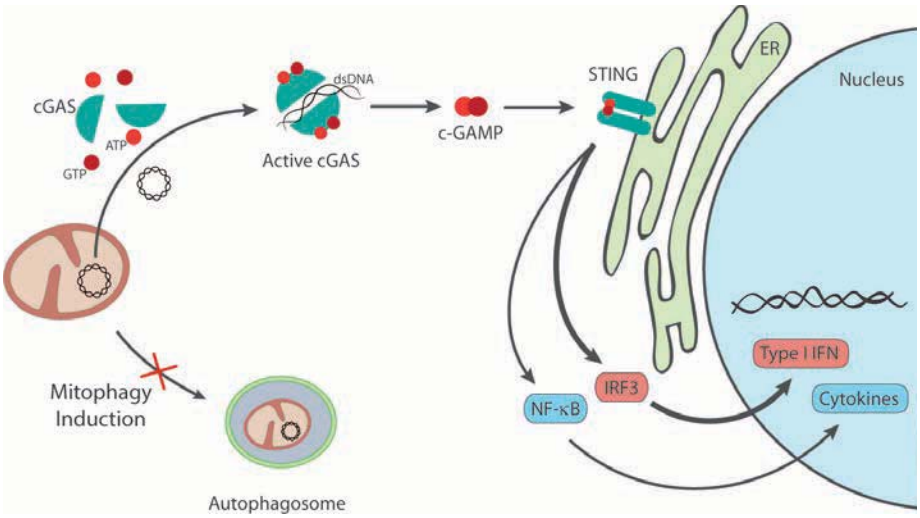

Figure 6. cGAS activation by mtDNA leakage to the cytosol. Homodimers of cGAS with dsDNA produce c-GAMP that interacts with STING triggering IRF3 or NF-κB, and in turn the expression of type I IFNs or cytokines, respectively.

high-affinity ligand for the endoplasmic-reticulum membrane adaptor protein stimulator of interferon genes (STING) (Cai, 2009). cGAMP induces conformation changes in STING which results in the subsequent activation of the transcription factors NF-κB and IRF3 through the kinases IKK and TBK1, respectively (Figure 6) (Ishii *et al.*, 2006; Stetson and Medzhitov, 2006; Ishikawa and Barber, 2008; Zhong *et al.*, 2008; Ishikawa, Ma and Barber, 2009).

Furthermore, when DNA is bound to HMGB1 or TFAM and forms a protein-DNA ladders, cGAS signaling is promoted (Andreeva *et al.*, 2017). Specifically, mtDNA has been reported to trigger a type I IFN response and expression of interferon stimulated genes (ISG) in a *Tfam* heterozygous context (West *et al.*, 2015). West and colleagues found mtDNA stress, characterized by reduced nucleoid number and increase nucleoid size. In these conditions, mtDNA was found in the cytosolic fraction in a context of

mitochondrial hyperfusion. Interestingly depletion of mitochondrial fusion protein Mfn1 normalized ISG expression.

2.8.2. Mitochondrial DNA as a TLR9 agonist

TLR9 was the first protein from the toll-like receptor family to be described as a nucleic acid sensor. It binds specifically unmethylated CpG DNA, like the mtDNA, in the endolysosomal compartment (Latz *et al.*, 2004; Lamphier *et al.*, 2006; Barbalat *et al.*, 2011; West, Shadel and Ghosh, 2011). TLR9 signals through the myeloid differentiation primary response protein 88 (MyD88), which activates different kinases and transcriptional factors: mitogen-activated protein kinases (MAPK), nuclear factor-κB (NF-κB) and the transcription factor IRF7 to enhance pro-inflammatory and type I interferon responses, respectively. Nucleic-acid sensing TLRs are not detectable at the cell surface but instead they reside within internal compartments. In particular, full-length TLR9 localizes in the ER under unstimulated conditions (Leifer *et al.*, 2004). More recent studies have identified that, upon stimulation, a TLR9 full-length traffics through the Golgi apparatus to the endolysosomal compartment, guided by UNC93B1, where it is cleaved to become DNA sensing-competent (Figure 7) (Tabeta *et al.*, 2006; Ewald *et al.*, 2008; Chockalingam *et al.*, 2009; Fukui *et al.*, 2009; Pelka *et al.*, 2014).

Furthermore, the specific endolysosomal compartment in which the interaction between DNA and TLR9 takes place is determinant for the type of immune response that is being generated (Honda *et al.*, 2005; Hayashi, Sasai and Iwasaki, 2015). Lee and Barton, review the topic and in their model, TLR9 signaling from late endosomes leads to activation of NF-κB (Figure 7). TLR9 signaling from a distinct population of endosomes leads to the recruitment of IRF and induction of type I IFN (IFN-a, IFN-b). This alternative compartment is hypothesized to be either early endosomes or different types of lysosomes related compartments (Lee and Barton, 2014; Duhamel *et al.*, 2016). Interestingly, triggering TLR9 in ER of cardiomyocytes is describe to have a protective role reducing energy metabolism (Shintani *et al.*, 2013).

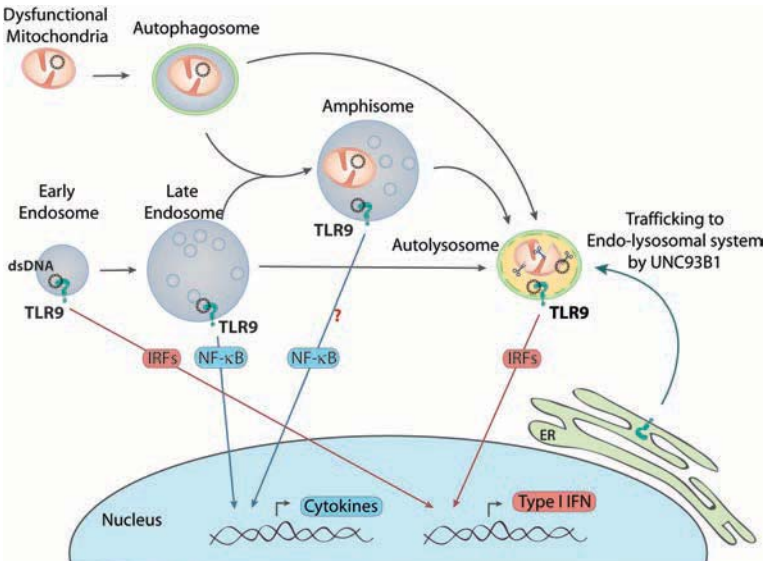

Figure 7. TLR9 activation by dsDNA from different compartment. TLR9 is recruited from the ER to the endo-lysosomal system guided by UNC93B1. Engagement of TLR9 in early endosomes or lysosomes results in type I IFN expression through different IRFs. Interaction of dsDNA with TLR9 in late endosomes results in NF-κB activation. Given the resemblance of amphisomes to late endosomes TLR9 engagement in amphisomes could result in cytokine production.

Regarding the mtDNA, it has been reported that unmethylated CpG motifs from mtDNA trigger TLR9 signaling. On one hand, several studies have reported the relevance of circulating or extracellular mtDNA in TLR9-dependent inflammation in diverse diseases (Li, Berke and Modis, 2012; Yu and Bennett, 2014; Zhang *et al.*, 2014, 2016; McCarthy *et al.*, 2015; Bao *et al.*, 2016; Garcia-Martinez *et al.*, 2016). Moreover, secreted high mobility group protein B1 (HMGB1) can bind extracellular CpG ODN and associate receptor for advanced glycation end-products (RAGE) to mediate self-nucleic acid uptake and delivery to TLR9 (Tian et al., 2007). Similarly, extracellular TFAM-bound mtDNA can induce a further stronger NF-κB activation because, plasma membrane receptor RAGE interacts with TFAM and delivers mtDNA to TLR9 (Julian *et al.*, 2012).

On the other hand, mtDNA is reported to engage with TLR9 cell-autonomously in the lysosomes in DNase II-deficient hearts, suggesting that undegraded mtDNA in the lysosomal compartment can induce TLR9 signaling inflammatory response in cardiomyocytes (Oka *et al.*, 2012). In parallel, De Leo *et al* reported a non-inflammatory role of the TLR9-DNA interaction in the lysosome cargo response, which

is required to sustain the autophagic flux (De Leo *et al.*, 2016). Other less characterized response is the TLR9 involvement in tumor growth by hypoxia induced interaction of mtDNA and HMGB1 in the cytosol (Y. Liu *et al.*, 2015). Divers mechanisms have been implicated in TLR9 associated pathologies but, as many immune receptors its regulation is important to ensure a balanced response in front of an infection or injury (Santiago-Raber, Baudino and Izui, 2009; Green and Marshak-Rothstein, 2011; Lamphier *et al.*, 2014).

2.9. Previous studies on the effects of OPA1 deficiency in skeletal muscle

Previous studies performed by Dr Àngels Díaz Ramos and Dr Eduard Noguera in our group assessed the impact of OPA1 deficiency in challenged muscle situations. Skeletal muscle regeneration was assessed in a cardiotoxin (CTX)-induced injury model in gastrocnemius muscles in wild type animals at a range of times. This type of assay is used to study how the muscle recovers from and injury, thus is a model for the study of muscle differentiation. The experimental setup is explained in Figure 8.

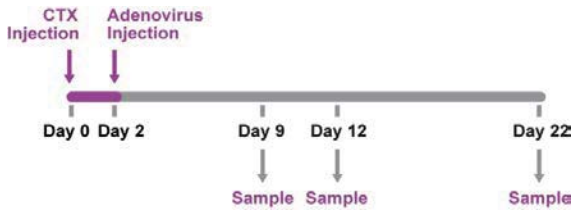

Figure 8. Schematic representation of the cardiotoxin (CTX)-induced injury model.

Two days post-injury (dpi), when satellite cells become active, muscles were treated with adenoviruses encoding for engineered miRNAs against *Opa1* or with control miRNA with no homology in the mouse genome. OPA1 deficiency not only caused impaired muscle regeneration but also increased the presence of immune cells and reduced muscle fiber size in regenerating myofibers (Figure 9).

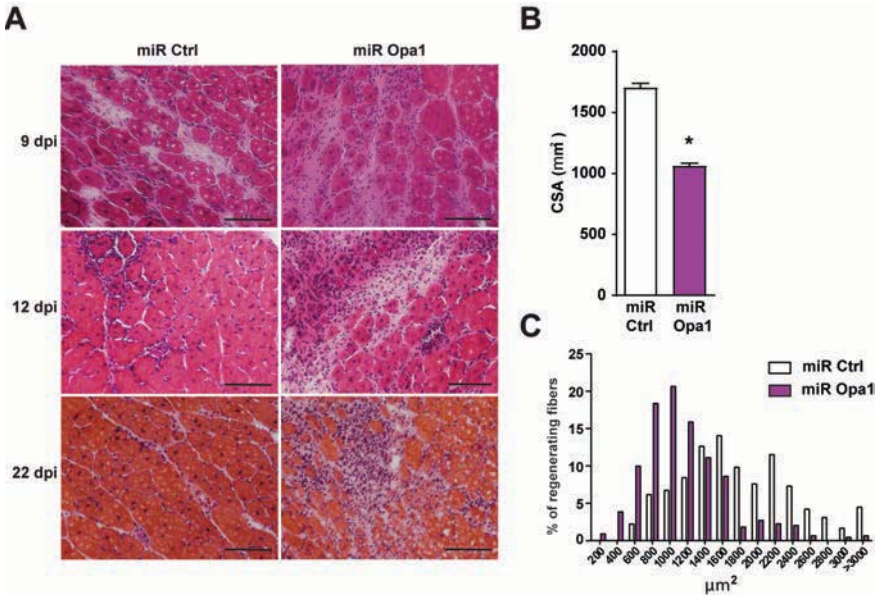

Figure 9. Histological examination of CTX-induced injury regeneration experiment. (A) Hematoxilin and eosin staining of muscles at 9, 12 and 22 days post injury (dpi), transduced with control miRNA (miR ctrl) or with miRNA against *Opa1* (miR Opa1). Scale bar, 100µm. (B) Mean cros-sectional area (CSA) of 150 myofibers per gastrocnemius muscles at 12dpi. (C) Distribution of myofiber size. Data represent mean ± SEM. * p<0.01 vs. control loxP mice.

Immunostaining of the developmental form of MHC (dMHC) revealed a reduction in controls between 9 and 12 days post-CTX treatment, whereas OPA1-deficient muscles showed sustained high expression of dMHC, indicating impaired muscle fiber maturation (Figure 10).

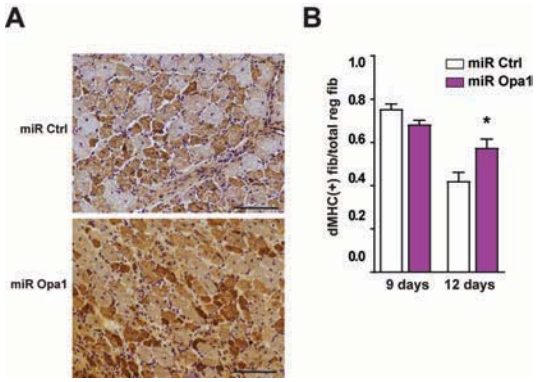

Figure 10. Study of developmental myosin heavy chain (dMHC) expression. (A) Representative image of dMHC immune-histochemistry from gastrocnemius muscle treated with miR Ctrl or miR Opa1 adenoviruses (12 dpi). Scale bar, 100 µm. (B) Quantification of positive dMHC myofibers vs. total regenerating myofibers of gastrocnemius muscle treated with miR Ctrl or miR Opa1 adenoviruses at dpi 9 and 12. Data represent mean ± SEM. * p<0.01 vs. control loxP mice.

Based on these data, the impact of OPA1 depletion was analyzed on muscle homeostasis by the generation of skeletal muscle-specific knockout mice. This was performed by crossing homozygous Opa1$^{loxP/loxP}$ mice with a mouse strain expressing Cre recombinase under the control of the myogenin promoter an the MEF2C enhancer (Figure 11) (Li *et al*, 2005; Wang *et al*, 2001; Liu *et al*, 2014).

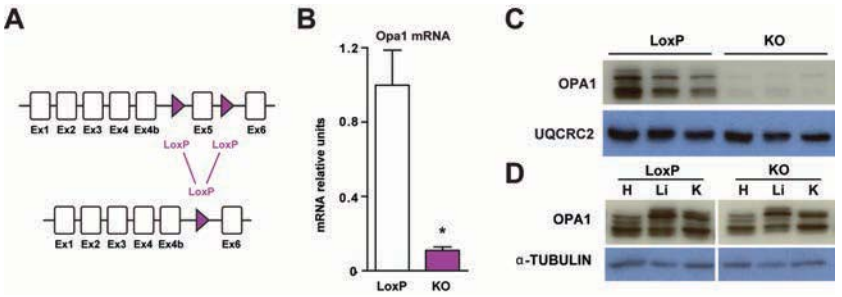

Figure 11. Skeletal muscle-specific OPA1 KO mouse model generation. (A) Partial genomic structure of the *Opa1* gene showing the scission of exon 5, thus deleting all OPA1 protein isoforms. (B) *Opa1* mRNA levels in the gastrocnemius muscle of loxP (non-expressing Cre *Opa1* loxP/loxP mice) and skeletal muscle-specific KO mice (KO) (n=10). (C-D) OPA1 protein levels in tissue homogenates of gastrocnemius muscle (panel C), and tissues: heart (H), liver (Li), and kidney (K) (panel D), from control (loxP) and skeletal muscle-specific KO mice (KO). Data represent mean ± SEM. * p<0.001 vs. control loxP mice.

OPA1 ablation in this specific tissue induced a dramatic reduction in lifespan, more than 50% of OPA1 KO mice did not survive more than 8 weeks. Moreover, skeletal muscle ablation of OPA1 caused impaired growth (Figure 12).

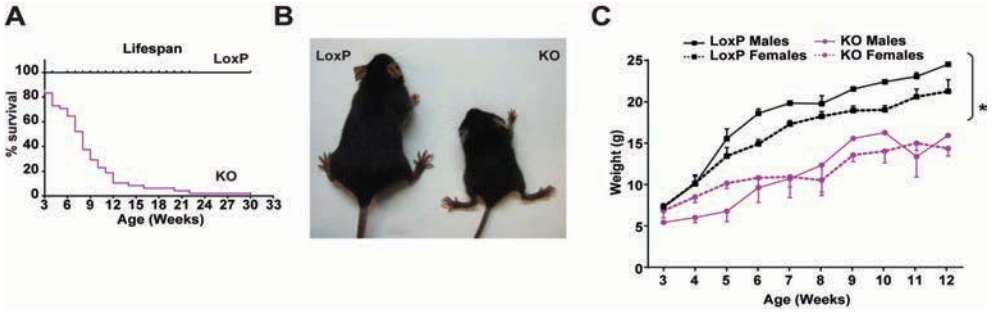

Figure 12. OPA1 KO mice present reduced lifespan and growth. (A) Survival curves for loxP and OPA1 KO (KO) mice (n=25). (B) Picture of loxP and KO mice at 9 weeks of age. (C) Body weight of loxP and KO male and female mice (n=25). Data represent mean ± SEM. * p<0.001 vs. control loxP mice.

At 9 weeks of age, OPA1 KO mice showed a reduction in relative weight of skeletal muscle and no change in various organs and tissues (Figure 13). Muscle force was also lower in OPA1 KO mice. In keeping with this, histological analyses of KO mice indicated a marked decrease in fiber size and cross-sectional area in quadriceps (Figure 13).

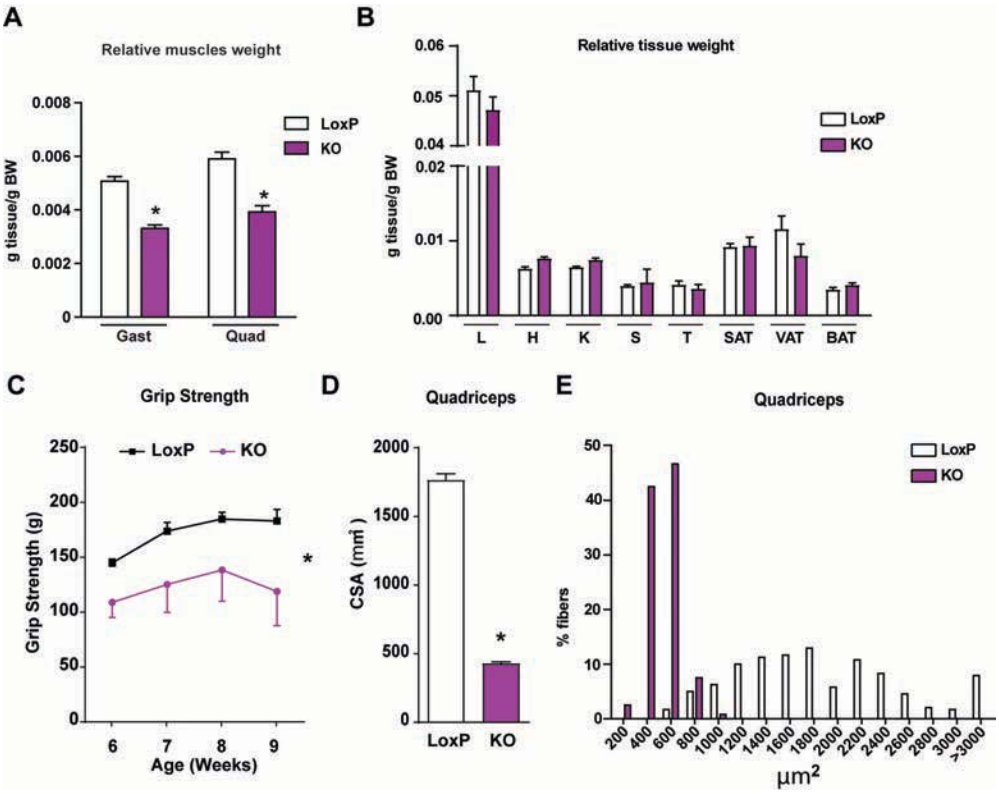

Figure 13. OPA1 loss-of-function in muscle results in reduced muscle size and strength. (A-B) Relative weight of muscles (gastrocnemius (Gast) and quadriceps (Quad)) (panel A) (n=18) and organs (liver (L), heart (H), kidney (K), spleen (S), T thymus (T), subcutaneous adipose tissue (SAT), visceral adipose tissue (VAT), and brown adipose tissue (BAT)) (panel B) (n=32) of 9-week-old loxP and KO mice. These data are expressed as g of tissue/g of body weight (BW). (C) Grip strength in loxP and KO mice. (D) Mean cross-sectional area (CSA) of 150 myofibers in quadriceps muscle. (E) Distribution of myofiber size of 150 myofibers in quadriceps muscle. Data represent mean ± SEM. * $p<0.001$ vs. control loxP mice.

Consistent with altered diaphragm morphology, OPA1 KO animals present extensive congestion and atelectasis in the lungs of these mice. In keeping with the reduced growth, plasma levels of GH were high in OPA1 KO mice (Figure 14). Characterization of the hepatic profile of OPA1 KO mice showed reduced phosphorylation of STAT5, and decreased expression of its target genes *Igf1* and *Fos*. Also, it

revealed reduced expression of growth hormone receptor (*Ghr*) and increased expression of the STAT5 inhibitor *Socs3* (Figure 14). As a result, OPA1 KO mice showed low plasma levels of IGF1 (Figure 14).

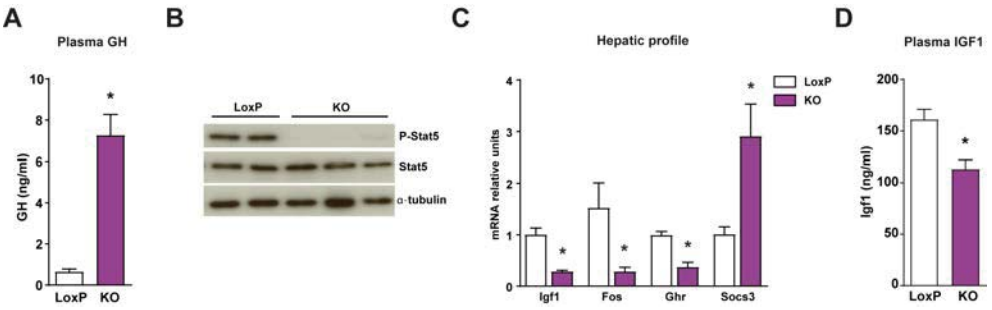

Figure 14. OPA1 loss-of-function ins muscle causes growth impairment. (A) Plasma concentration of growth hormone (GH) of loxP (n=8) and KO mice (n=10). (B) Stat5 phosphorylation in livers of loxP and KO mice (n=10). (C) mRNA levels of *Igf1*, *Fos*, growth hormone receptor (*Ghr*), and *Socs3* in liver of loxP and KO mice. (D) Plasma concentration of IGF1 of loxP (n=8) and KO mice (n=10). Data represent mean ± SEM. * p<0.001 vs. control loxP mice.

Previous studies in the lab included transcriptomic analysis of muscles of control and OPA1 KO mice. Gene set enrichment analysis of genomic profiling in revealed the up-regulation of ATF4 target genes in muscles of OPA1 KO mice. Additionally, among the large number of genes with deregulated expression (486 genes up-regulated and 175 repressed) *Fgf21* was found to be greatly increased in OPA1-deficient muscles. *Fgf21* has been described to be target of ATF4 (Kim *et al.*, 2013). In parallel, circulating FGF21 levels were 4-fold greater in these animals.

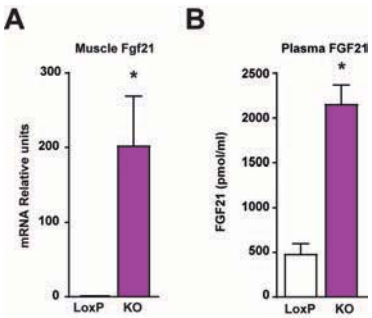

Figure 15. FGF21 enhancement under OPA1 loss-of-function. (A) *Fgf21* gene expression in muscle of loxP and KO mice (n=8). (D) FGF21 levels in plasma of loxP (n=8) and KO mice (n=10). Data represent mean ± SEM. * p<0.05 vs. control loxP mice.

Lastly, and given the preliminary data obtained from the CTX-treated muscles, the impact of OPA1 deficiency on muscle inflammation was analyzed. Nonspecific esterase (NSE) and Major Histocompatibility Complex (MHC) Class I staining revealed severe inflammation in muscles from OPA1 KO mice (Figure 16).

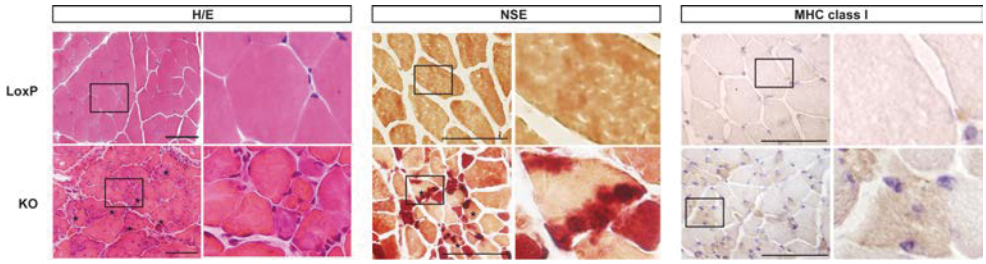

Figure 16. Histological analysis of inflammation is skeletal muscle. Representative images of hematoxylin and eosin (H/E) staining, non-specific esterase (NSE) staining and MHC class I expression in gastrocnemius muscle sections of 6 weeks old loxP and skeletal muscle specific OPA1 KO mice. Inset panels are 4x magnification of the outlined areas. Asterisks in H/E indicate necrotic fibers. Asterisks in NSE indicate the presence of macrophages. Scale bar, 100 μm.

In addition, the expression of NF-κB target genes was also induced, as well as the plasma levels of pro-inflammatory cytokines IL-1β and IL-6 (Figure 17).

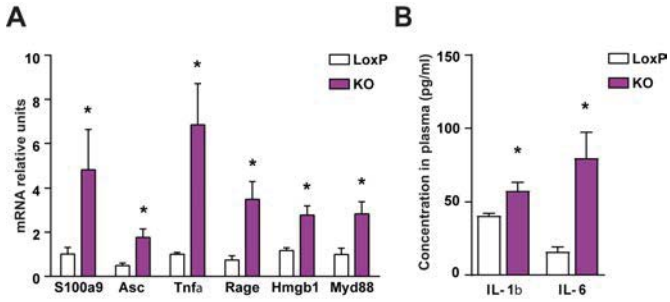

Figure 17. OPA1 deficiency results in NF-κB activation and cytokine secretion. (A) Expression of NF-κB target genes in muscles of loxP and KO mice (n=7). (B) Circulating IL-1β and IL6 measured in plasma of 8- to 10-week-old loxP and KO mice (n=9). Data represent mean ± SEM. * p<0.05 vs. loxP mice.

Based on the observations of previous studies in the lab indicating that OPA1 deficiency in skeletal muscle leads to a systemic pathology characterized by growth defects and muscle and systemic inflammation, in this study we aim to understand the link between defective OPA1 function in the muscle and the systemic component, and the specific cellular pathways involved in the development of the condition.

OBJECTIVES

Previous data gathered by Dr Àngels Díaz Ramos and Dr Eduard Noguera in the group provided promising results on the role of OPA1 in muscle that deserved further study. The initial characterization of the skeletal muscle specific OPA1 KO mouse model revealed a dramatic reduction in the lifespan of the animals. This phenotype was accompanied with defects in growth, including high levels of growth hormone and low levels of IGF-1 in plasma, compatible with growth hormone resistance. OPA1 knockout mice presented high plasma levels of IL-1β and IL-6, enhanced non-specific esterase staining and increased MHC class I labelling, suggesting a role of OPA1 deficiency in muscle inflammation.

The results compiled prior to this thesis work, motivated the present study with the goal to deeper understand the mechanisms linking OPA1 deficiency to the systemic inflammation detected in mice. The following specific objectives have been pursued:

1. To study the systemic effects induced by OPA1 depletion in skeletal muscle. To understand how the depletion of OPA1, just in skeletal muscle, results in a critically significant whole-body effect.

2. To characterize the muscle inflammatory state and to determine the origin of the systemic inflammation. To assess whether the inflammation is produced autonomously in the muscle and the contribution of cell death.

3. To identify the key players responsible for the inflammatory response. To determine the sequence of events at the molecular level that lead to inflammation.

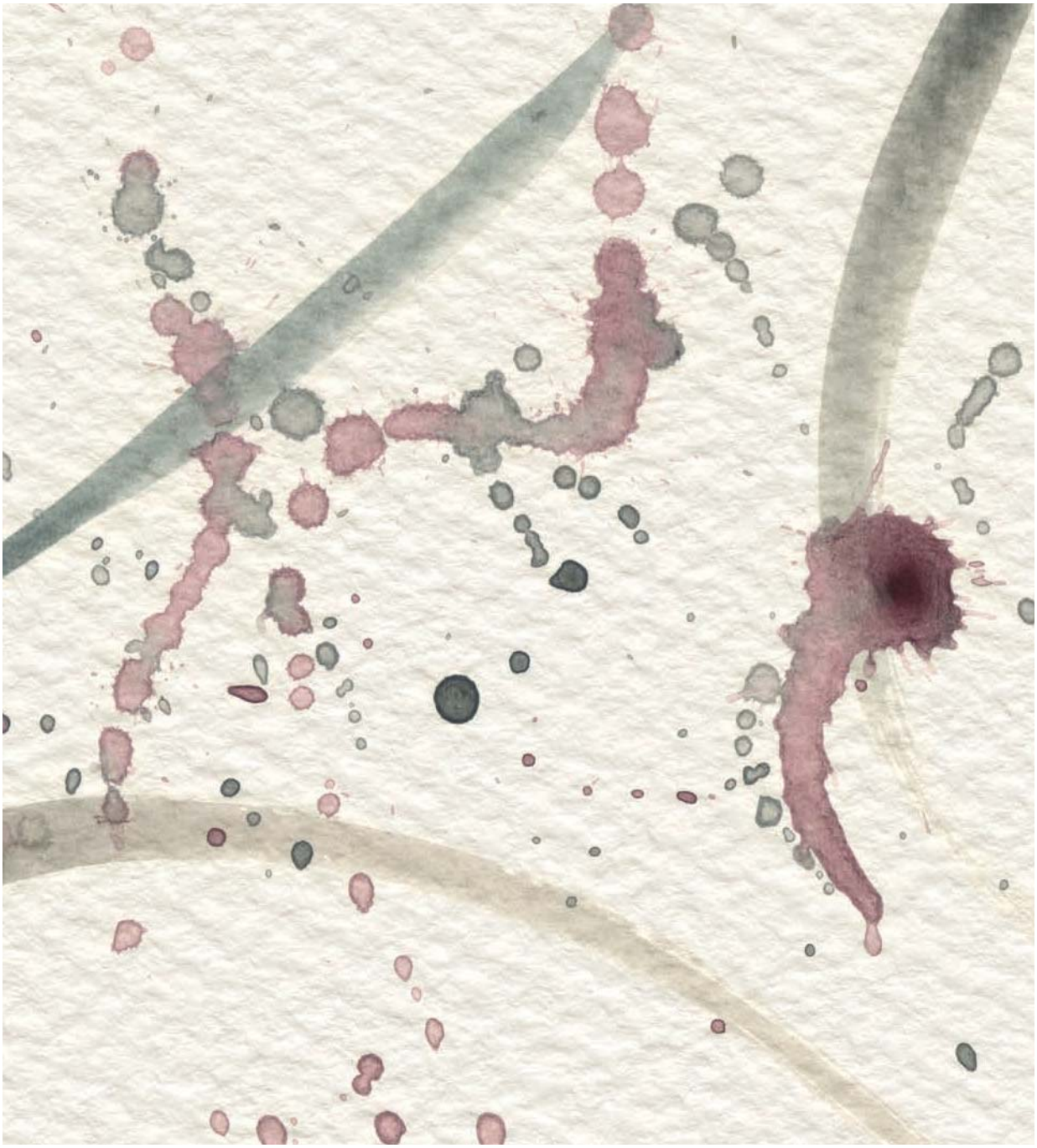

RESULTS

4.1. Systemic effects caused by skeletal muscle-specific OPA1 ablation

The characterization of the skeletal muscle-specific OPA1 KO mice revealed a severe growth impairment. Considering that the genetic manipulation is performed only in the skeletal muscle, we aimed to determine which of the different muscle secreted signals were involved in the growth defects. Previous studies documented high plasma levels of FGF21, and pro-inflammatory cytokines IL-1β and IL-6. Therefore, we aimed to identify the contribution of these altered parameters in the systemic profile.

4.1.1. Study of FGF21 as the factor responsible for the growth defects in OPA1 KO mice

Previous data determined a robust upregulation of the expression of the mitokine FGF21 in muscle, as well as increased levels in circulation (chapter 2.9, Figure 15). Different studies have identified this hormone as a negative regulator of growth. In situation of malnutrition, in which mitochondria are dysfunctional, FGF21 is highly expressed and it is described to inhibit the GH-IGF1 axis to minimize the metabolic requirements (Kubicky *et al.*, 2012; Guasti *et al.*, 2014; Ozaki *et al.*, 2015), by blocking the translocation of GHR to the plasma membrane (Inagaki *et al.*, 2008). Given that OPA1 loss-of-function results in growth impairment in a highly expressed FGF21 context, we explored the possibility of FGF21 being the driver of the growth defects.

In order to characterize the contribution of FGF21 to OPA1 KO phenotype, double knockout mouse model was generated by crossing *Opa1*$^{loxP/loxP}$ mice with FGF21 total KO mice (B6N;129S5-Fgf21^{tm1Lex}/Mmcd) to obtain *Opa1*$^{loxP/loxP}$ *Fgf21*$^{-/-}$ animals. The resulting generation was then crossed with the transgenic Myo-Cre-expressing mice. Hence, we generated two groups: FGF21 total KO animals with OPA1 depleted in skeletal muscle, hereafter double KO (DKO), and FGF21 KO only, as a control. The mRNA levels of these groups together with control (LoxP) and OPA1 KO (KO) mice showed a significant reduction in *Opa1* levels in tibialis muscles of both KO and DKO mice (Figure 18A). *Fgf21* mRNA levels

were knock out globally. No significant expression of the mitokine was detected in muscle or liver of DKO and FGF21 KO mice (Figure 18B and Figure 18C).

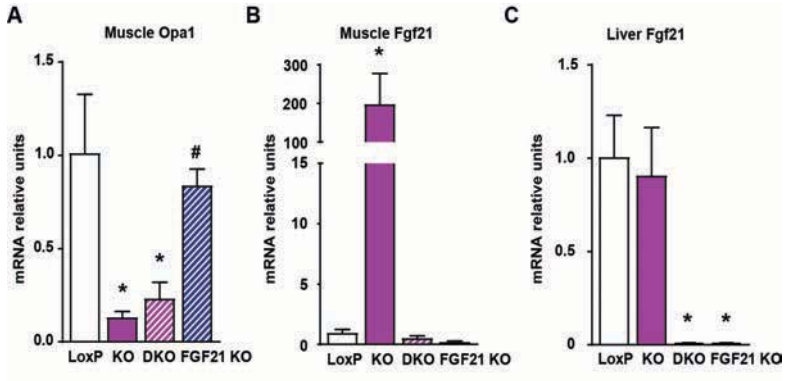

Figure 18. Validation of OPA1-FGF21 Double KO mice. (A) *Opa1* mRNA levels in muscle, (B-C) and *Fgf21* gene expression in muscle (B) and liver (C) of loxP, OPA1 KO, FGF21 KO and double KO (OPA1 + FGF21 KO, DKO) (n=8). Data represent mean ± SEM. * p<0.05 vs. control loxP mice. # p<0.05 vs. DKO mice.

Unexpectedly, the weight of gastrocnemius and quadriceps muscles were unchanged when we compare KO and DKO animals, and remained significantly reduced compared to either loxP or FGF21 KO (Figure 19A), suggesting that the reduction of organ weight was dependent on skeletal muscle-specific OPA1 ablation rather than increased circulating levels of FGF21. As it happened with OPA1 KO mice, DKO mice did not present changes in the weight of other tissues (liver, heart, kidney and spleen) (Figure 19B).

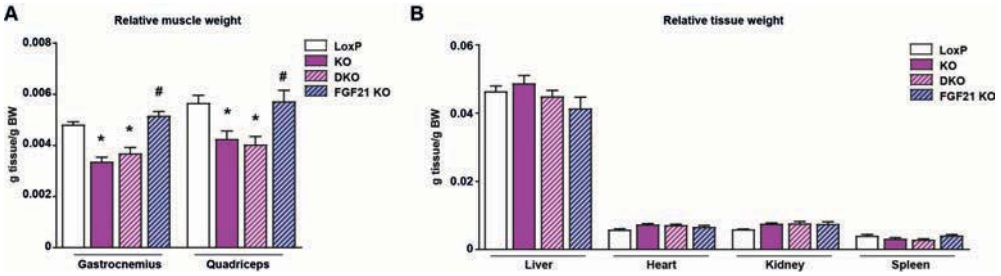

Figure 19. Relative muscle and tissue weights. Relative weight of gastrocnemius and quadriceps muscles (A), and organs (B) of loxP, OPA1 KO, DKO and FGF21 KO mice (n=10). Data represent mean ± SEM. * p<0.05 vs. control loxP mice. # p<0.05 vs. DKO mice.

We then analyzed the hepatic growth hormone axis and, in keeping with the previous observation, expression levels of insulin-like growth factor-1 (*Igf-1*) stayed significantly lower (Figure 20). The profiles of *Fos* and growth hormone receptor (*Ghr*), two other relevant proteins for the growth axis, were not

as clear. In these cases, we could observe a significant reduction of the mRNA levels in DKO compared to FGF21 KO (Figure 20). Moreover, in the case of *Fos*, although not statistically significant, there is a tendency of both OPA1 KO and DKO to be downregulated compared to loxP levels. However, the hepatic expression of *Ghr* in DKO was significantly increased compared to loxP animals (Figure 20).

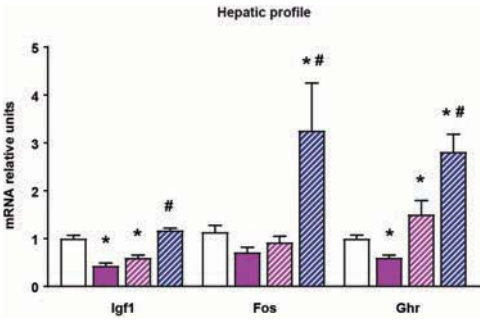

Figure 20. Hepatic expression of GH related genes. *Igf1*, *Fos* and *Ghr* mRNA levels in the livers of of loxP, OPA1 KO, DKO and FGF21 KO mice (n=10). Data represent mean ± SEM. * p<0.05 vs. control loxP mice. # p<0.05 vs. DKO mice.

These observations suggest that FGF21 global KO has a partial impact on, at least, the hepatic expression of these genes that can influence the phenotype due to skeletal muscle OPA1 ablation, because, although in *Ghr* case there is a slight increase in the DKO group, it is not comparable to the one seen in FGF21 KO alone.

FGF21 has been shown to have a regulatory role on the hepatic expression of *Pgc1α* (Potthoff et al., 2009). Aiming to identify a process driven by the increased plasma levels of FGF21, we screened for PGC1α target genes (Badman et al., 2009; Estall et al., 2009; Fisher et al., 2014). The data show a clear regulation of genes encoding *Pgc1α*, respiratory complex IV subunit *Cox7a1*, fatty acid oxidation components (*Cpta1, Mcad and Vlcad*) and gluconeogenic enzymes (*Pepck and G6p*) (Figure 21).

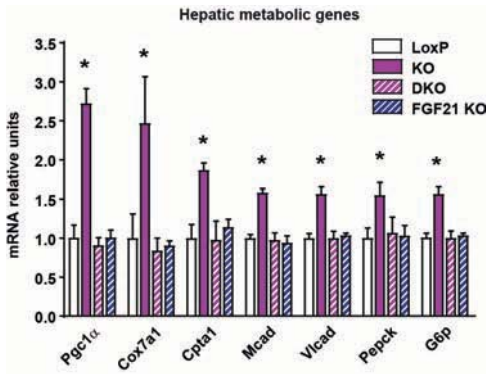

Figure 21. Hepatic expression of genes encoding *Pgc1α*, and its target genes. mRNA relative levels of *Pgc1α,* respiratory complex IV subunit *Cox7a1*, fatty acid oxidation components (*Cpta1*, *Mcad* and *Vlcad*) and gluconeogenic enzymes (*Pepck* and *G6p*) in loxP, OPA1 KO, DKO and FGF21 KO mice (n=7) Data represent mean ± SEM. * p<0.05 vs. control loxP mice. # p<0.05 vs. DKO mice.

All these genes present a conserved profile of expression characterized by a significant upregulation of the expression in OPA1 KO mice, which have increased levels of FGF21; and normalized to loxP levels in DKO and FGF21 KO mice, models with null levels of FGF21 in plasma (Figure 21). These last piece of data is consistent with FGF21 driving *Pgc1α* expression in liver, and in turn, upregulating of the oxidative metabolism.

Despite the direct regulation regarding *Pgc1α*, in skeletal muscle-specific OPA1 KO context, FGF21 is not involved in the dysregulation of the hepatic growth axis induced by OPA1 ablation in skeletal muscle, neither it is responsible for the growth defects.

4.1.2. Study of inflammation as the factor responsible for the growth defects in OPA1 KO mice

Based on the data excluding FGF21 as responsible for the growth impairment in OPA1 KO mice, we analyzed our second candidate: inflammation. Previous studies in our group showed a high inflammatory component in OPA1 KO mice (chapter 2.9, Figure 16 and Figure 17). Inflammation has been reported to regulate growth by different types of studies. Models of chronic inflammation such as juvenile idiopathic arthritis, chronic kidney disease or chronic inflammatory bowel disease (Wong et al., 2016), present severe growth impairment. Specifically, these patients present high plasma levels of the pro-inflammatory cytokines IL-1β and IL-6 (Kutukculer, Caglayan and Aydogdu, 1998; Ji et al., 2002). Studies in mouse models also report the impact of pro-inflammatory cytokines on growth. De Benedetti et al., described that overexpression of IL-6 reduced the circulating levels of IGF-1 and these phenotype could be rescued by the use of blocking antibodies for the cytokine (De Benedetti et al., 1997; De Benedetti, 2009). Interestingly, Zhao et al. reported repression of the GH-IGF-1 axis at different levels depending on the pro-inflammatory cytokine studied. On one hand, IL-1β and TNF-α, inhibit the expression of *Ghr*, on the other hand. IL-6 induced the hepatic expression of *Socs3*, which is a known inhibitor of the GH-IGF-1 axis, thus inhibiting the pathway, as well (Denson *et al.*, 2003; Lieskovska, Guo and Derman, 2003; Zhao *et al.*, 2014).

In order to elucidate the relevance of inflammation in the growth impairment phenotype we used an anti-inflammatory treatment. Salicylate is a well-known NF-κB inhibitor (Kopp and Ghosh, 1994; M. J. Yin, Yamamoto and Gaynor, 1998).

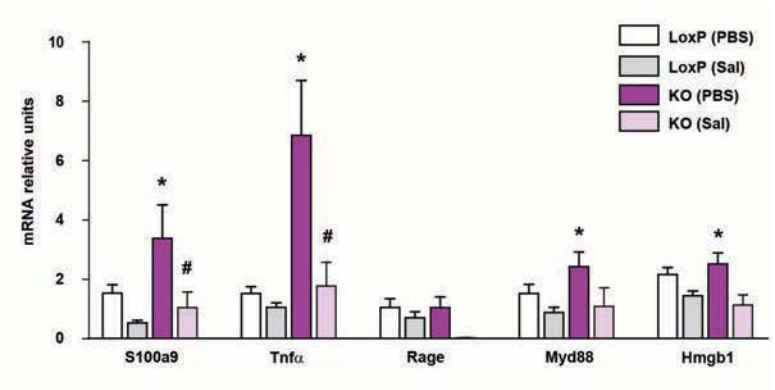

Figure 22. Anti-inflammatory treatment normalizes the OPA1-deficient-associated enhanced NF-κB target gene expression. Expression of NF-κB target genes in muscles of loxP and KO mice treated with sodium salicylate (Sal) or with PBS (PBS). Data represent mean ± SEM. * p<0.05 vs. control loxP mice. # p<0.05 vs. KO mice. Data were obtained from 8- to 10-week-old loxP and KO mice (n=6).

OPA1 KO and loxP were treated for 30 days with sodium salicylate or vehicle (in this case PBS), to equate the stress of the daily intraperitoneal administration. The efficiency of the treatment was examined by the assessment of the expression of NF-κB target genes and plasma levels of IL-6 and IL-1β. Different pro-inflammatory genes that were upregulated in PBS treated OPA1 KO mice were normalized by the administration of the anti-inflammatory treatment (Figure 22). Likewise, IL-6 and IL-1β circulating levels were restored after sodium salicylate treatment (Figure 23).

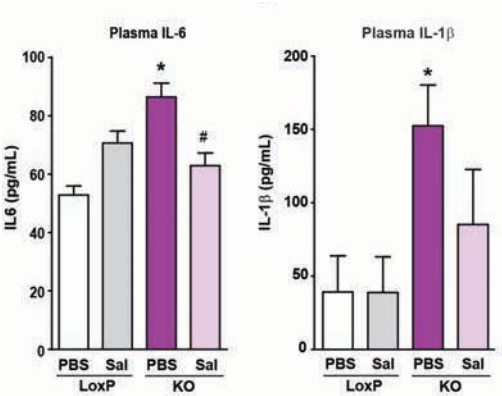

Figure 23. Anti-inflammatory treatment normalizes cytokine circulating levels. Circulating IL-6 and IL-1β measured in plasma of loxP and KO mice treated or not with sodium salicylate. Data represent mean ± SEM. * p<0.05 vs. control loxP mice. # p<0.05 vs. KO mice. Data were obtained from 8- to 10-week-old loxP and KO mice (n=6).

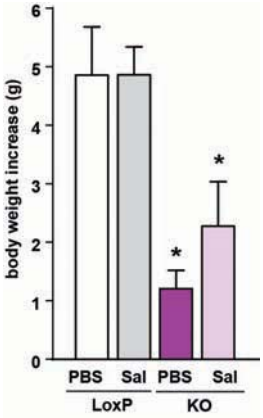

Figure 24. Salicylate-induced body weight increase. Increment of body weight of loxP and KO mice treated or not with salicylate for 30 days. Data represent mean ± SEM. * p<0.05 vs. control loxP mice. Data were obtained from 8- to 10-week-old loxP and KO mice (n=6).

After 30 days of salicylate treatment, loxP treated and not treated mice increased around 5 grams their body weight (Figure 24), which indicates that in healthy conditions anti-inflammatory treatment is innocuous, at least for the growth of a mouse. PBS-treated OPA1 KO mice had a body weight increase of only 1g. Although not statistically significant OPA1 KO treated animals, presented an improvement of growth reflected in a greater increase in body weight during the salicylate treatment (Figure 24). Despite this represents an amelioration of the severe phenotype, adjustments in the treatment such as earlier administration, prolonged treatment and different way of administration may improve even more the growth of OPA1 KO mice.

In parallel to the modest body weight increase, there was a notable improvement in the skeletal muscles of OPA1 KO salicylate treated animals. Gastrocnemius and quadriceps muscles weights were recovered (Figure 25A). Moreover, histological inspection of quadriceps muscle revealed significant improvement (Figure 25B). Cross-sectional area (CSA) quantification revealed that the anti-inflammatory treatment resulted in the recovery of nearly normal fiber size (Figure 25C). The study of the fiber size distribution documented that, beyond having an increased average CSA, the composition of the muscle was further improved, which include fibers of more than 3000 µm2, whereas the quadriceps fibers of OPA1 KO mice treated with PBS only reached 100 µm2 (Figure 25D).

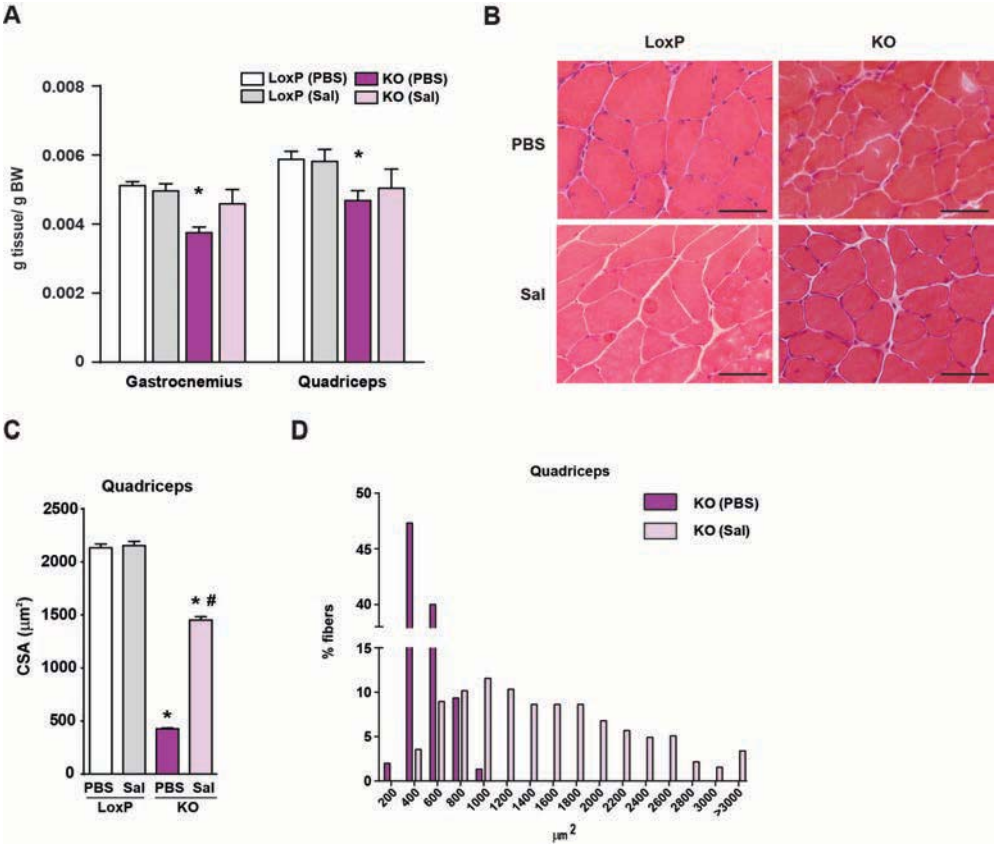

Figure 25. Anti-inflammatory treatment rescues muscle fiber size. (A) Relative weight of gastrocnemius and quadriceps muscles of loxP and KO mice treated with sodium salicylate (Sal) or PBS (PBS) for 30 days. (B) Representative H/E staining of quadriceps muscles of loxP and KO mice treated with salicylate or PBS. Scale bar, 50 µm. (C) Mean CSA of 150 myofibers in quadriceps muscles. (D) Distribution of myofiber size in quadriceps muscles from loxP and KO mice treated or not with salicylate. Data represent mean ± SEM. * p<0.05 vs. control loxP mice. # p<0.05 vs. KO mice. Data were obtained from 8- to 10-week-old loxP and KO mice (n=6).

Salicylate treated OPA1 KO mice also recovered muscle necrosis assessed by creatine kinase (CK) activity in plasma (Figure 26).

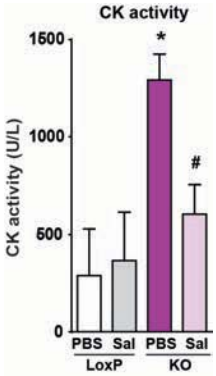

Figure 26. Muscle necrosis is reversed by anti-inflammatory treatment. Creatine kinase (CK) activity measured in plasma of salicylate-treated and PBS-treated mice. Data represent mean ± SEM. * p<0.05 vs. control loxP mice. # p<0.05 vs. KO mice. Data were obtained from 8- to 10-week-old loxP and KO mice (n=6).

Regarding the hepatic expression of the genes involved in growth, salicylate treatment was able to restore the expression levels of pro-growth factor *Ghr*, *Igf1* and *Fos* (Figure 27A, Figure 27B and Figure 27C). Also, treated animals had normalized expression levels of the inhibitor *Socs3* (Figure 27D). Accordingly, growth hormone (GH) circulating levels were also restored (Figure 27E), suggesting and amelioration of the growth hormone resistance profile.

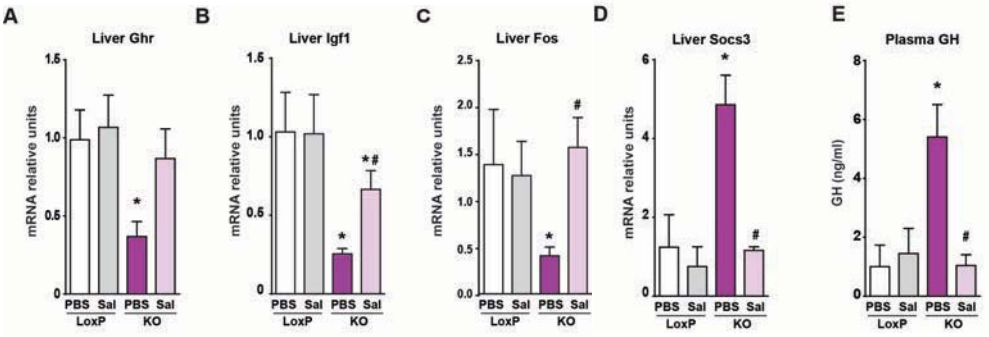

Figure 27. Growth impairment is ameliorated by anti-inflammatory treatment. Hepatic expression of *Ghr* (A), *Igf1* (B), *Fos* (C), and *Socs3* (D) in treated and PBS-treated loxP and OPA1 KO animals. (E) Circulating GH levels from salicylate-treated and PBS-treated animals. Data represent mean ± SEM. * p<0.05 vs. control loxP mice. # p<0.05 vs. KO mice. Data were obtained from 8- to 10-week-old loxP and KO mice (n=6).

4.1.3. OPA1 loss-of-function results in ATF4 activation through inflammation

Interestingly, skeletal muscle expression of Fgf21 was reduced back to nearly normal levels in salicylate treated OPA1 KO mice (Figure 28A), and so did FGF21 plasma levels (Figure 28B).

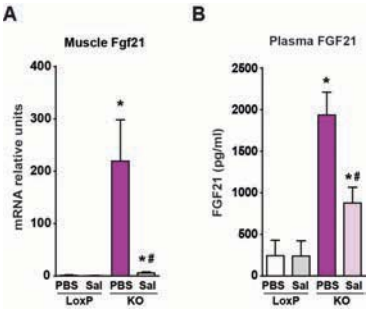

Figure 28. Anti-inflammatory treatment improves FGF21 profile induced by OPA1 deficiency (A) *Fgf21* mRNA levels measured in tibialis muscle of salicylate-treated and PBS-treated mice. (B) Concentration of FGF21 in plasma of loxP and OPA1 KO animals treated or not with salicylate. Data represent mean ± SEM. * p<0.05 vs. control loxP mice. # p<0.05 vs. KO mice. Data were obtained from 8- to 10-week-old loxP and KO mice (n=6).

We postulate that in skeletal muscle-specific OPA1 KO mice FGF21 expression is induced by ATF4, because the ATF4 target genes gene set was significantly upregulated according to the GSEA of control and OPA1-deficient muscles. ATF4 is a transcription factor activated when general translation is blocked by the phosphorylation of eIF2α. Although we did not further pursue this line of investigation, it is worth mentioning that very preliminary results show that OPA1 KO mice present increased phosphorylation of the stress kinase eIF2α. Interestingly, the increased activation of this kinase was restored upon salicylate treatment (Figure 29A).

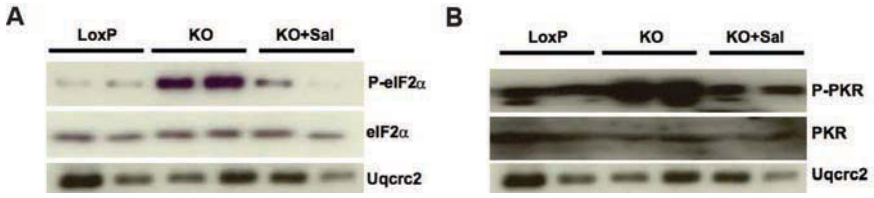

Figure 29. Anti-inflammatory treatment rescues OPA1 ablation-induced PKR and eIF2α phosphorylation. (A-B) Representative image of immunoblot of phosphrilated-eIF2α (P-eIF2α), total eIF2α (A); and phosphorylated-PKR (P-PKR) and total PKR (B) in loxP, OPA1 KO (KO) and OPA1 KO animals treated with salicylate (KO+Sal).

There are 4 kinases that phosphorylate eIF2α: GCN2 (triggered upon nutrient starvation), HRI (activated by heme deprivation, oxidative stress or heat shock), PERK (activated upon ER stress), and PKR (triggered upon viral infection or cytokine signaling) (Wek, Jiang and Anthony, 2006; Deval et al., 2008; Donnelly et al., 2013). Preliminary results also show that PERK was not phosphorylated in OPA1 KO mice (data not shown), thus ER stress is not involved in the activation of ATF4 transcription factor. In fact, OPA1 loss-of-function results in increased phosphorylation of PKR, which is reverted under anti-inflammatory treatment (Figure 29B). The interpretation of this results will be examined in the discussion chapter.

4.2. Characterization of the muscle inflammatory state and the origin of the systemic inflammation.

Inflammation is crucial for the development of the phenotype induced by skeletal muscle specific OPA1 loss-of-function, hence we decided to study whether inflammation was the primary effect of OPA1 deficiency in muscles. As previous studies had shown the existence of necrosis in OPA1 KO animals, we assessed whether necrosis or cell death was the cause or the consequence of this inflammation. Another very relevant aspect was to examine if this inflammation was intrinsic of the skeletal muscle, and not originated from resident immune cells in the tissue. To elucidate these questions, we used different approaches: First, we performed time course histological examination of muscles from very young mice for cytokine production (IL-1β) and macrophage infiltration (CD68), in parallel of the assessment of muscle necrosis using plasma creatine kinase activity. Second, we used a tamoxifen inducible OPA1 KO model and the determination of expression levels of different pro-inflammatory factor and CD68 as a pro-inflammatory macrophage marker. Third, we obtained and characterized the inflammation of a cellular model in culture to subtract any possible contribution of the immune system.

4.2.1. Inflammation, necrosis and macrophage infiltration during the early life of OPA1 KO mice

Using the skeletal muscle-specific OPA1 KO model, by which OPA1 ablation is performed at day 8.5 of embryonic development, we studied the presence of inflammation, necrosis and macrophage infiltration starting at weaning up to 3 months old mice. Muscle sections of 3-, 7-, 10- and 13-week-old loxP and OPA1 KO mice were immunostained for IL-1β, as a marker of inflammation, and CD68, as a marker of macrophage infiltration (Figure 30). Automated quantification of the positive labelling 5 images per group was performed using ImageJ software and trainable Weka plugin. Plasma of the same time points was examined for creatine kinase activity as a marker of muscle necrosis.

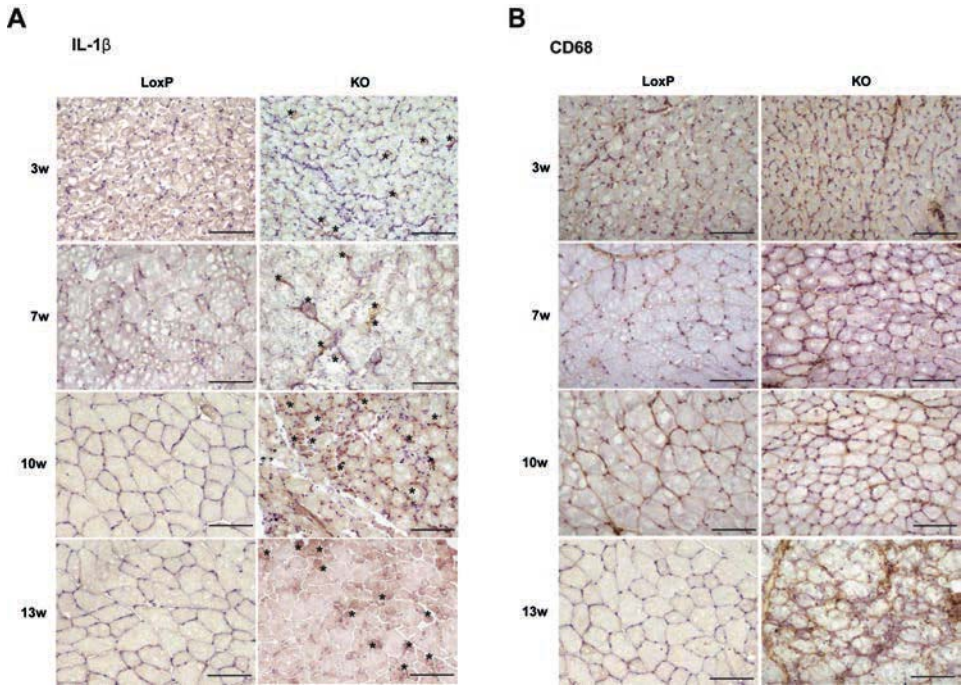

Figure 30. Immunohistochemical detection of IL-1β and CD68 in muscles from control and OPA1 KO mice. (A-B) Representative images of IL-1β (A) and CD68 immunohistochemistry (B) in muscle in 3-, 7-, 10- and 13-week-old loxP and KO mice. Scale Bar, 100 µm.

The results depicted in Figure 31 represent both the quantification of Figure 30 and the creatine kinase activity, and are expressed as fold change relative to loxP animals. LoxP level is represented as a dashed line at a value of 1 (Figure 31).

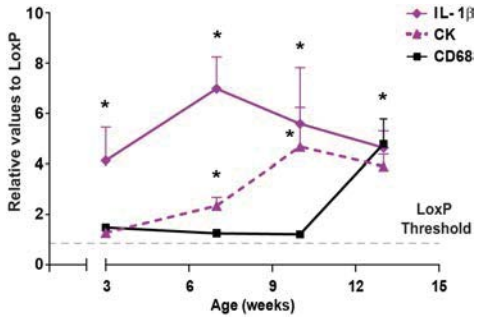

Figure 31. OPA1 deficiency results in inflammation, necrosis and macrophage infiltration, sequentially. Quantification of IL-1β and CD68 expression in gastrocnemius, and CK activity in plasma of loxP and OPA1 KO animals at 3, 7, 10, and 13 weeks of age. Values of OPA1 KO mice are represented relative to the loxP group. The staining quantification was performed using Trainable Weka Segmentation plugin from ImageJ (5 images per group). Data represent mean ± SEM. * $p<0.05$ vs. control groups.

Already at 3 weeks of age, OPA1 KO animals presented highly positive labelling for IL-1β, 4-folds from loxP. However, CD68 signal and creatine kinase activity did not differ from the loxP values. At 7 weeks of age, creatine kinase activity was significantly increased in two folds. This parameter reached 4-fold

increase in 10 weeks old animals. On the contrary CD68 labelling remained unchanged until week 13 of age, when it got to 4-fold increase from loxP values (Figure 31). These data indicate that intrinsic muscle inflammation preceded muscle necrosis, which in turn occurred before pro-inflammatory macrophage infiltration.

Apoptosis was excluded to be relevant in the phenotype because cleaved caspase 3 was not detected in gastrocnemius muscles (Figure 32). These results were obtained in collaboration with Dr Díaz-Ramos.

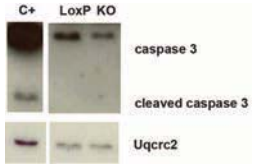

Figure 32. Apoptosis is not induced in OPA1-deficient muscles. Representative western blots of the levels of caspase 3 and cleaved caspase 3 in loxP and skeletal muscle-specific OPA1 KO mice. Apoptosis-positive control was obtained by treating C2C12 myoblasts with 10 µm staurosporin for 4h.

The results of this chapter indicate that the contribution of the immune system to the pro-inflammatory phenotype, at least of the pro-inflammatory macrophages, is secondary to muscle inflammation and necrosis, and this occurs in an apoptosis-independent manner.

4.2.2. Effects of OPA1 ablation in adult muscle on inflammation and macrophage infiltration

Aiming to obtain further proof of inflammation being a primary event in the muscle after OPA1 depletion, we used a different mouse model. In this case OPA1 ablation was performed postnatally by tamoxifen administration to *Opa1*$^{loxP/loxP}$ strain expressing Cre-ER under de control of Human Skeletal Actin (HSA) promoter, to target the deletion to mature skeletal muscle. Cre-negative littermates also received tamoxifen treatment, and were used as controls. This model allows the assessment of inflammatory markers right after OPA1 is ablated from adult muscle. Skeletal muscle samples were collected at 30, 50 and 90 days after the onset of tamoxifen treatment. Muscle mass in this model was not detectable before 50 days after tamoxifen onset (data not shown). Expression levels of different NF-κB target genes as well as *Cd68* as pro-inflammatory macrophage marker were measured.

At 30 days after the onset of tamoxifen treatment, when OPA1 is already ablated but muscle mass was still normal, *Nlrp3* and *Asc* gene expression were significantly increased in muscles form OPA1 KO animals (Figure 33).

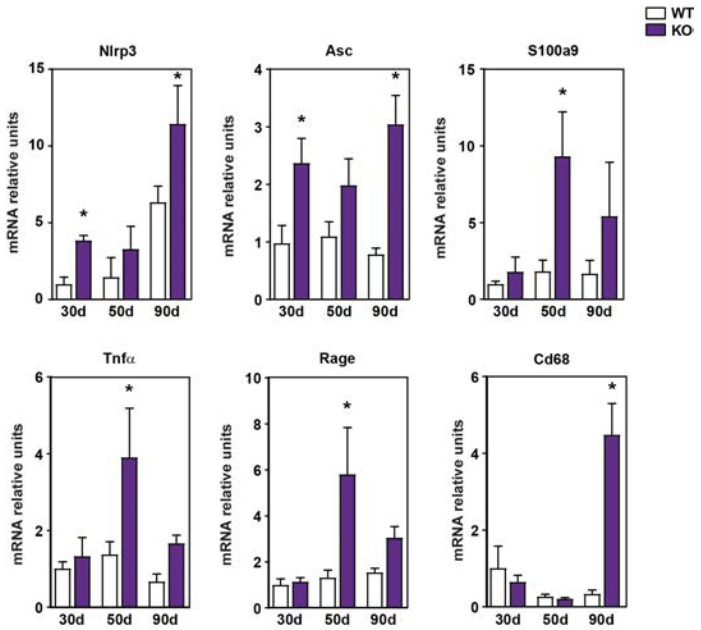

Figure 33. Adult OPA1 ablation results in muscle inflammation. Expression of NF-κB target genes in muscles of control and inducible skeletal muscle-specific OPA1-KO mice at 30, 50 and 90 days after tamoxifen treatment (n=6). Data represent mean ± SEM. * p<0.05 vs. wt.

Fifty days after the onset of tamoxifen treatment, when muscle mass was starting to be apparent, *S100a9*, *Tnf*-α and *Rage* were found to be upregulated in OPA1-ablated muscles. Only at 90 days after the onset of tamoxifen treatment was *Cd68* enhancement detectable, suggesting again that macrophage infiltration occurred in response to muscle inflammation (Figure 33). Moreover, these results indicate that OPA1 ablation is able to induce muscle inflammation even if the depletion is performed once the muscle is already formed. These studies were performed in collaboration with Dr Sandri's group in the University of Padova. Altogether, our data indicate that OPA1 loss-of-function was able to induce a pro-inflammatory state characterized by induction of NF-κB target gene expression, which preceded muscle necrosis and pro-inflammatory macrophage infiltration.

4.2.3. Evaluation of the capacity of C2C12 myoblasts to induce an inflammatory profile

Although the first two approaches offered very helpful information regarding the timeline of events, they did not irrefutably demonstrate that, within the muscle tissue, the muscle cells are the ones producing the inflammatory profile. To determine the upstream mechanism of inflammation it was critical to determine whether the muscle cells were able to induce a pro-inflammatory response, and whether this happened in a cell death-free scenario. In this regard, we decided to use a C2C12 muscle cells as the cellular model. We used these muscle cells in a myoblastic stage to avoid the differences due to OPA1 loss-of-function effects on myogenic differentiation, previously reported by Dr Noguera in the laboratory (Noguera, 2014).

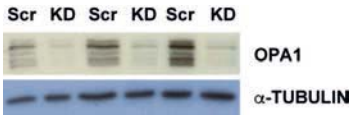

Figure 34. Validation of OPA1 depletion in C2C12 myoblasts. OPA1 protein levels in C2C12 control myoblasts (Scr) and in stably depleted OPA1 myoblasts (KD)

Stable OPA1 knock-down (OPA1 KD) C2C12 cell line were obtained using lentiviral infection of a shRNA targeting *Opa1* mRNA. Infected cells were selected by puromycin treatment. As a control, C2C12 cells were infected and selected for scramble shRNA (Scr) (Figure 34).

Previous studies compiled in Dr Noguera PhD thesis revealed a significant upregulation of the transcriptional activity of the NF-κB promoter (Figure 35A). Accordingly, a set of NF-κB target genes were found to have and upregulated expression in OPA1 KD cells (Figure 35B). Lastly, detection of IL-1β

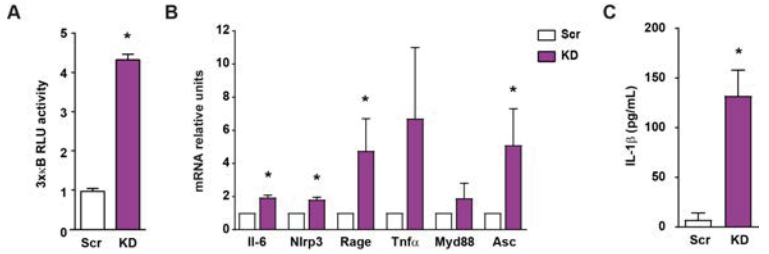

Figure 35. NF-κB activation in OPA1-deficient C2C12 myoblasts. (A) Transcriptional activity of NF-κB in myoblast expressing scramble shRNA (Scr) or shRNA against OPA1 KD (KD) (n=5). (B) Expression of NF-κB target genes in Scr and KD myoblasts (n=6). (C) Levels of IL-1β in culture media from C2C12 myoblasts (n=6). Data represent mean ± SEM. * p<0.05 vs. control groups.

in the culture media revealed and increased concentration in the media of OPA1 KD myoblasts (Figure 35C).

The detection of IL-1β in culture media using a standard sandwich enzyme-linked immune-sorbent assay (ELISA) is unable to discriminate between the immature pro-form and the cleaved active form. Hence, it was essential to quantitatively discard cell death as a player in the phenotype, which would lead to extrusion of cellular materials including inactive IL-1β. Visual monitoring of the cells in culture did not indicate any abnormalities regarding the number of dead-floating cells, nevertheless we studied necrosis and apoptosis. The presence of necrosis was assessed using lactate dehydrogenase activity assay in culture media. The results showed no differences between Scr and OPA1 KD cells (Figure 36A). We treated control cells with staurosporine to induce apoptosis and obtain a positive control. Despite of using a moderately high concentration, the induction was mild (Figure 36B and Figure 36C). Nevertheless, untreated Scr or OPA1 KD cells did not present the cleaved active for of neither caspase 3 nor Parp, arguing again in favor of a phenotype independent of cell death (Figure 36B and Figure 36C).

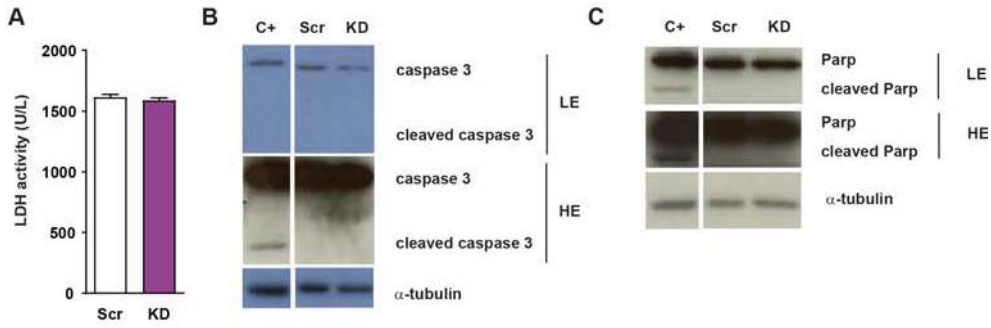

Figure 36. Necrosis and apoptosis is not induced in OPA1 loss-of-function myoblasts. (A) LDH activity in cultured media of Scr and OPA1 KD myoblasts. (B-C) Caspase 3 (B) and Parp (C) expression in Scr and OPA1 KD myoblasts. Apoptosis-positive control was obtained by treating C2C12 myoblasts with 10µm staurosporine for 4h. Data represent mean ± SEM. * $p<0.05$ vs. control group.

In all, our data indicate that OPA1 loss-of-function in myoblasts activate NF-κB transcriptional program, which leads to a pro-inflammatory state reassembling the skeletal muscle profile; and this profile appears independently of cell death.

Once cell death was discarded to play a relevant role in the phenotype, the presence of extracellular IL-1β suggested an active secretion of the cytokine. The secretion of IL-1β is the result of a complex pathway which involve inflammasome activation (Lamkanfi, 2011). Classically, inflammasome needs two signals to result in IL-1β cleavage, and thus secretion. The first signal, or priming signal, is the engagement of a PRR that cause NF-κB activation which results in the expression of inflammasome component and pro-forms of cytokines, mainly IL-1β. The second signal, or activation signal, has been describes to be very diverse in nature depending on the type of inflammasome, particularly NLRP3 is thought to be activated by a wide range of different triggers (Sutterwala, Haasken and Cassel, 2014). Typically, inflammasome activation and assembly entails caspase 1 cleavage, which in turn can cleave IL-1β, activating it to be secreted. Although in this PhD thesis work we have not further characterized the type, trigger or activation state of inflammasome we do have assessed cleavage of IL-1β. OPA1-deficient myoblasts showed increased levels of pro-IL-1β and very reduced levels of cleaved IL-1β, compared to Scr cells (Figure 37).

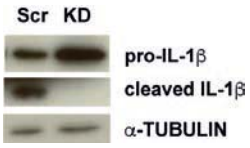

Figure 37. IL-1β protein levels in control and OPA1-deficient cells. Representative western blot of inactive pro-IL-1β and cleaved IL-1β.

We can only speculate with the few data that we have, that if the inflammasome is active, activated IL-1β might be actively secreted and we would do not detect it in total homogenates since it would be increased in the extracellular media (Bergsbaken, Fink and Cookson, 2009). Classically, inflammasome has only been studied in macrophages and other inflammatory cells, but recently several studies have reported inflammasome activation in non-immune cells, like podocytes or hepatocytes (Kawaguchi *et al.*, 2011; Wree *et al.*, 2014; Boaru *et al.*, 2015; Kanneganti, 2015; Shahzad *et al.*, 2015; Zhuang *et al.*, 2015). Moreover, there is another study in which it has been described inflammasome activation upon dysferlin deficiency in human muscle biopsies, mouse skeletal muscle, and mouse primary myoblasts and myotubes (Rawat *et al.*, 2010). Further studies in the lab will determine whether there is an activation of the any kind of inflammasome and will elucidate the type of inflammasome responsible.

4.3. Identification of the key players and the mechanism of the triggered inflammatory response

4.3.1. Characterization of the mitochondrial dysfunction caused by OPA1 loss-of-function

The importance of inflammation was examined in the previous chapter. In the present section the aim was to determine the molecule or molecules responsible for the induction of the pro-inflammatory profile. Therefore, mitochondrial homeostasis was assessed to identify possible dysregulated DAMPs that could be triggering the inflammatory response.

Skeletal muscles of OPA1 KO and loxP mice were examined for different mitochondrial parameters. As OPA1 is the protein responsible for the inner mitochondrial membrane fusion, and a correct balance of mitochondrial dynamics is essential to maintain a well fit mitochondrial network, we suspected that OPA1 KO mice may present a disrupted mitochondrial network. In order to analyze mitochondrial morphology in the muscle, tibialis anterior muscles were electroporated with mitochondrial-targeted red fluorescent protein, mitoDsRed. Results displayed in Figure 38, clearly show a complete disarrangement of the mitochondrial network in the muscles of mice depleted of OPA1, compared to the well-structured mitochondrial network of loxP mice.

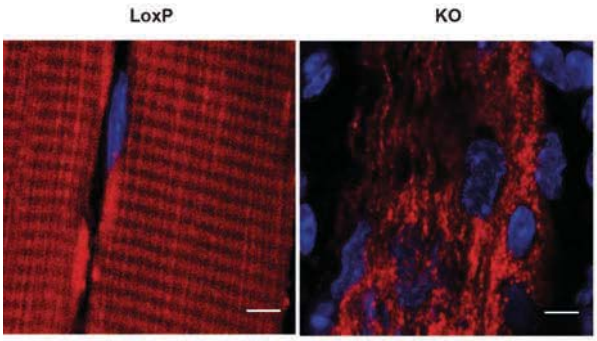

Figure 38. OPA1 loss-of-function results in mitochondrial network disarrangement. Representative images of mitochondrial network of tibialis muscles of loxP and KO mice electroporated with cDNA encoding DsRed2-Mito vector Mitochondria in red and nuceli in blue (n=3). Scale bar, 5 µm.

Mitochondrial protein levels analysis showed different profiles, neither of them showed a reduction in mitochondrial protein levels (Figure 39A and Figure 39B). Functional proteins of the different mitochondrial oxidative phosphorylation (OXPHOS) complexes remained unchanged between loxP and

OPA1 KO muscles. However, we found increased levels of structural proteins like Porin or proteins involved in mitochondrial dynamics like DRP1, MFN1, MFN2 (Figure 39A and Figure 39B). Skeletal muscle gene expression of *Pgc1α* as a master regulator of mitochondrial biogenesis was also unchanged (Figure 39C).

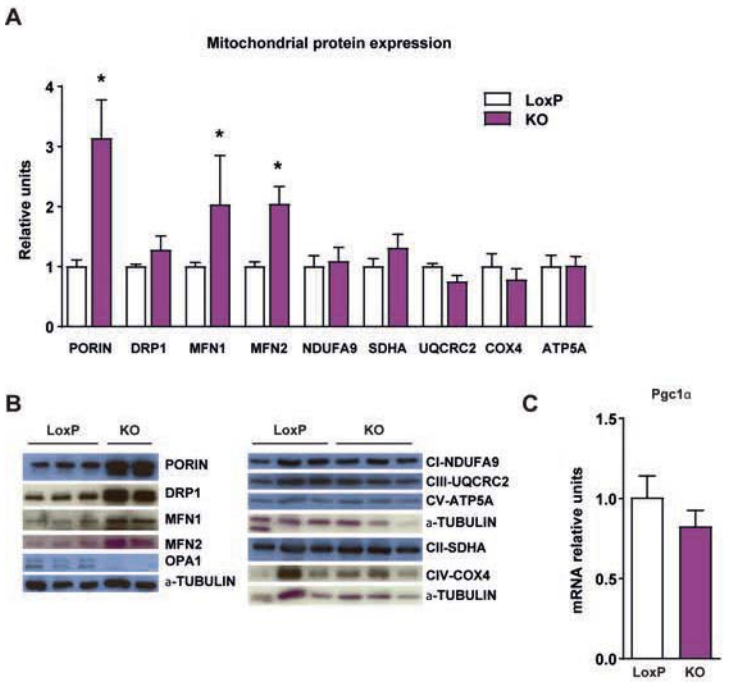

Figure 39. Mitochondrial protein content and PGC-1α expression. (A) Relative mitochondrial protein expression of gastrocnemius muscles of loxP and KO mice. Values were corrected by α-tubulin (n=10). (C) *Pgc-1α* expression in muscles of loxP and KO mice (n=7). Data represent mean ± SEM. * p<0.05 vs. loxP

OPA1 is not only essential for inner mitochondrial membrane fusion but it is also involved in cristae morphology maintenance, and this, in turn is crucial supercomplexes formation and for electron transport chain functionality. Thus, we assessed the skeletal muscle OXPHOS capacity using the respirometry technology (OROBOROS). Mitochondrial respiration in permeabilized muscles displayed an overall reduction in the ability of OPA1 KO muscles to oxidize different substrates (Figure 40). In the absence of ADP, when glutamate-malate was used as a substrate, OPA1 KO muscle showed no difference in oxygen consumption (State 4).

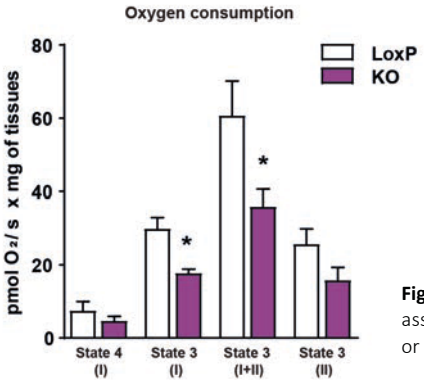

Figure 40. Mitochondrial respiration. Oxygen consumption assayed in isolated myofibers of tibialis muscles (2-4 mg) from loxP or KO mice (n=6). Data represent mean ± SEM. * p<0.05 vs. LoxP.

However, after the addition of ADP (as a substrate for ATP conversion), which measures the respiration linked to complex I (CI) activity, there was a significant reduction in the oxygen consumption of OPA1-depleted mitochondria (State 3-I). After the subsequent addition of pyruvate to measure CII and CI dependent OXPHOS, there was also a significant reduction of oxygen consumption (State 3-I+II). Finally, in order to subtract the contribution of CI, rotenone was added and oxygen consumption was not significantly reduced (State 3-II), although there was a tendency (Figure 40).

After assessing mitochondrial function in OPA1-deficient skeletal muscles we also analyzed mitochondrial health in OPA1-deficient cellular model. The absence of OPA1 in myoblasts induced a comparable type of mitochondrial dysfunction. C2C12 expressing mitoDsRed showed a completely fragmented mitochondrial network (Figure 41).

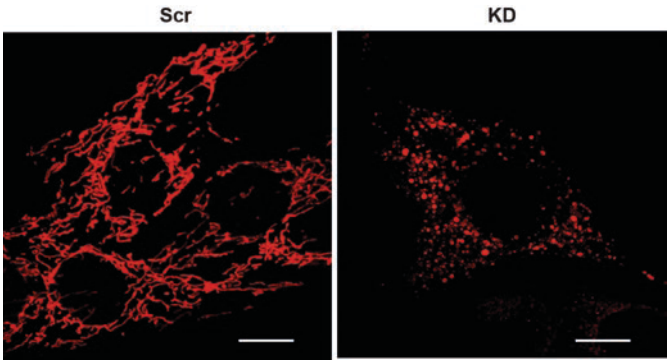

Figure 41. OPA1 loss-of-function results in mitochondrial network fragmentation. Confocal microscopy examination of mitochondrial morphology of control (Scr) and OPA1 KD (KD) C2C12 myoblasts assessed by mitochondrial targeted DsRed protein fluorescence. Scale bar, 10µm.

Data from Eduard Noguera thesis studies we know that this fragmentation is indeed due to the lack of fusion. He performed fusion studies by expressing a photoactivable mitochondrial targeted GFP. Thus, he could measure the degree of fusion by inducing fluorescence in delimitated area of the mitochondrial network and quantifying how fluorescence fade through its dilution throughout the mitochondrial network.

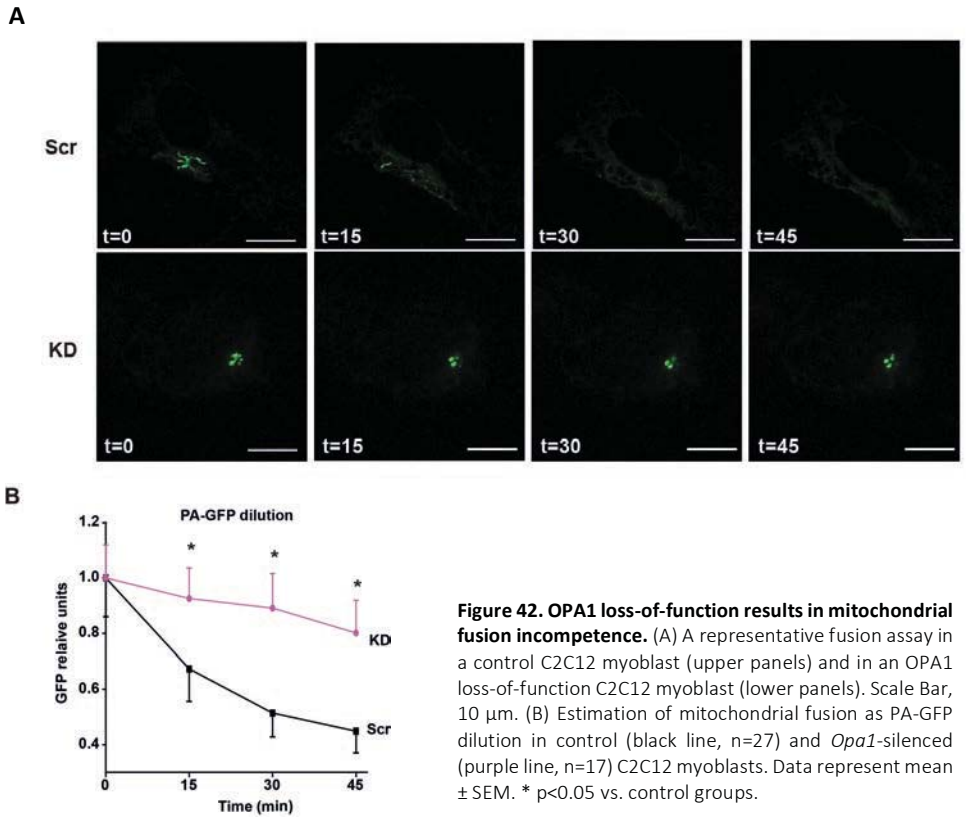

Figure 42. OPA1 loss-of-function results in mitochondrial fusion incompetence. (A) A representative fusion assay in a control C2C12 myoblast (upper panels) and in an OPA1 loss-of-function C2C12 myoblast (lower panels). Scale Bar, 10 µm. (B) Estimation of mitochondrial fusion as PA-GFP dilution in control (black line, n=27) and *Opa1*-silenced (purple line, n=17) C2C12 myoblasts. Data represent mean ± SEM. * p<0.05 vs. control groups.

He reported that while Scr myoblasts present half of the fluorescence in 45 min after the activation, OPA1 KD cells did not even achieve a 20% reduction (Figure 42).

Regarding mitochondrial mass, there was no reduction of protein markers, such as TIM44, SDHA or TOM20, while there was a significant increase in Porin levels (Figure 43).

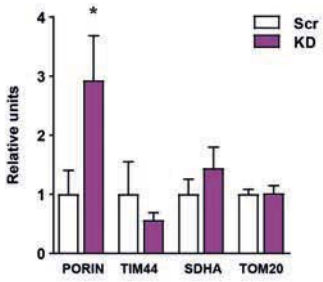

Figure 43. Mitochondrial protein levels. Expression of mitochondrial proteins in Scr and OPA1 KD myoblasts (n=4). Data represent mean ± SEM. * p<0.05 vs. control groups.

Correspondingly to the *in vivo* data, there was a reduction in mitochondrial respiration in OPA1-deficient muscle cells, measured by using Seahorse technology. The protocol uses the oxygen consumption upon different treatments that inhibit different electron transport chain complexes to assess the overall OXPHOS functionality of the cell.

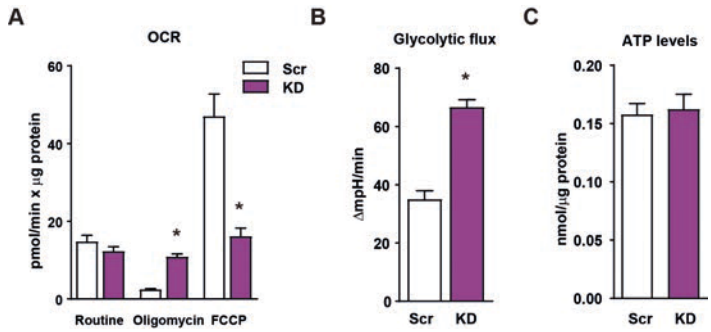

Figure 44. OPA1-deficient myoblast present reduced OXPHOS capacity and enhanced glycolysis. (A) Mitochondrial oxygen consumption rates (OCR) measured in intact Scr or *Opa1*-silenced C2C12 myoblasts (n=5). Five mM glucose was used as a substrate. Proton leak (respiration independent of ATP synthesis) was induced by 1.25 µM oligomycin (complex V inhibitor). Respiratory electron transfer system (ETS) capacity was analyzed using 1 µM FCCP. Non-mitochondrial electron transport OCR was determined by the addition of the complex III inhibitor antimycin A (0.1 µM) and subtracted from the total OCR in order to obtain mitochondrial OCR. (B) Glycolytic flux assessed as extracellular acidification rates were measured in intact Scr or OPA1 KD C2C12 myoblasts (n=5). Five mM glucose was used as a substrate. (C) ATP content in Scr and OPA1 KD cells. Data represent mean ± SEM. * p<0.05 vs. control groups.

Oxygen consumption in routine conditions was unchanged (Figure 44). In order to measure the proton leak, cells were treated with oligomycin A, a reagent that inhibit complex V ATP synthase. Therefore, the oxygen consumed in this condition is the respiration uncoupled to the production of ATP or the proton leak. In order to determine the maximal respiratory capacity, membrane potential was abolished by the treatment with FCCP, an ionophore that permeabilizes de inner mitochondrial membrane to

protons. Thus, the oxygen consumed in this condition represents the maxim respiratory capacity of the system. The data shown in Figure 44 indicate that OPA1 KD have similar routine, higher proton leak and very low maximal respiratory capacity. Therefore, the data point out that OPA1-deficient mitochondria have very little spare respiratory capacity, they are already working at the highest levels they can and in fact this respiration is not very efficient in terms of ATP production. ATP levels were unaltered (Figure 44), and in these conditions, a 2-fold increase in the ECAR or Glycolytic flux was observed in OPA1 KD cells (Figure 44).

We then analyzed of the mitochondrial DNA (mtDNA) status, a crucial component of mitochondria. Importantly, the third OPA1 attributed function is its involvement in mtDNA stability. OPA1 loss-of-function have been reported to induce a reduction in mtDNA copy number and mtDNA deletions (Hudson *et al.*, 2008; Elachouri *et al.*, 2011; Amati-Bonneau *et al.*, 2018) .

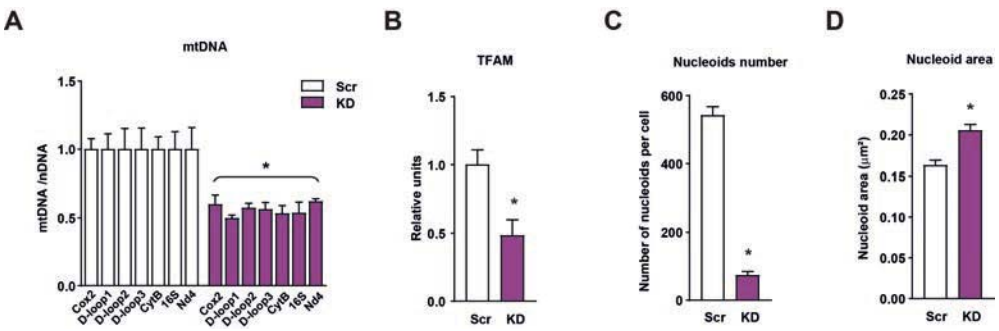

Figure 45. OPA1 loss-of-function induces mtDNA stress. (A) mtDNA levels relative to nuclear DNA (Tert) (n=4). (B) TFAM protein levels (n=4). (C-D) Nucleoid composition in Scr and OPA1 KD myoblasts. Number of mtDNA nucleoids per cell (C) and area of each nucleoid (D). Data are from a representative experiment with 20 cells randomly quantified per condition. Data represent mean ± SEM. * p<0.05 vs. control groups.

OPA1-deficient myoblast showed a reduction of the 50% in mtDNA content relative to nuclear DNA as assessed by the amplification of 7 different regions of the mtDNA using real-time PCR (Figure 45A). In keeping with this, TFAM levels were also reduce to a half (Figure 45B). TFAM is a crucial protein in mtDNA nucleoid organization and replication. Thus, we analyzed mtDNA morphology and distribution using confocal microscopy. After immunofluorescence labelling of dsDNA in Scr and OPA1 KD cells, the number of nucleoids and the area of each nucleoid was quantified in 20 random cells for three

independent experiments. Data shown in Figure 45C indicate a reduction from 550 nucleoids per cell in control conditions to less than 100 nucleoids per cell in OPA1 KD conditions. Moreover, the size of each nucleoid was enhanced in OPA1-deficient cells (Figure 45D). These changes in the mtDNA composition and morphology are described as mtDNA stress are similar to the ones produces by TFAM reduction in MEF cells (West *et al.*, 2015).

4.3.2. Study of the role of mtDNA in OPA1-driven inflammation

Base on the observation that mtDNA is notably depleted in OPA1 KD cells, not only in copy number but also and more importantly in nucleoid abundance, and given the involvement of OPA1 in mtDNA stability we explored the possibility that mtDNA itself was the triggering signal of the inflammatory profile seen in these cells. In order to answer these questions, we performed rescue studies by ablating mtDNA. To do so, we treated the cells with ethidium bromide (EtBr) for 30 days to avoid mtDNA correct replication and thus achieve a profound reduction of mtDNA copy number in these cells.

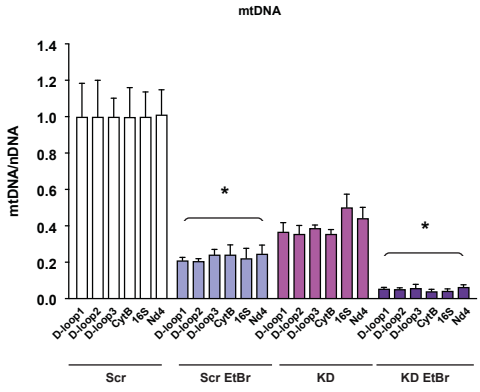

Figure 46. Depletion of mtDNA upon EtBr treatment. mtDNA levels relative to nuclear DNA (Tert). Values of mtDNA in Scr and OPA1 KD cells treated or not with EtBr, represented relative to Scr untreated values. Data represent mean ± SEM. * p<0.05 vs. untreated.

In the case of Scr cells the depletion was not achieved totally, Scr treated cells presented a 20% of the mtDNA of untreated Scr cells, while in the case of OPA1, EtBr treatment reduced to a 5% of a control cells the levels of mtDNA (Figure 46). These cells were used to analyze the expression of NF-κB target genes by real-time PCR, as inflammatory markers.

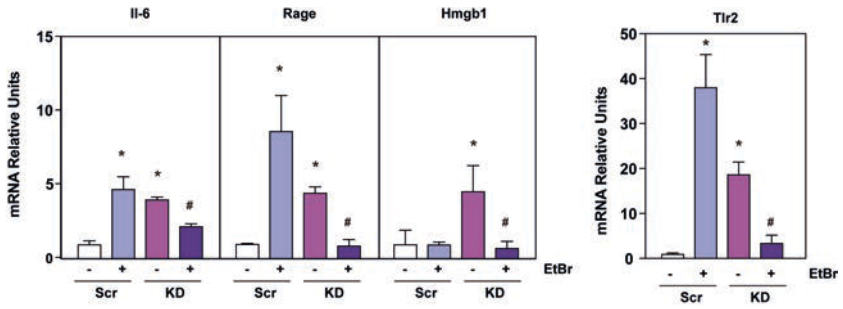

Figure 47. mtDNA depletion rescues the expression of NF-κB target genes. mRNA relative units of NF-κB target gene expression of Scr and OPA1 KD (KD) treated or not with EtBr. Relative values to untreated Scr (n=3). Data represent mean ± SEM. * p<0.05 vs. untreated Scr, # p<0.05 vs. untreated OPA1 KD.

Data represented in Figure 47 shows some interesting results. On one hand, if we focus on untreated Scr cells, and both OPA1 KD cells groups, we can clearly appreciate the normalization of the genes assessed, which indicate that most probably mtDNA is the one triggering the inflammatory response because when it is removed, inflammation levels are rescued. On the other hand, if we now include Scr treated cells, we can see that there is higher expression of NF-κB target genes (Figure 47). Probably, as in Scr it was not achieved a strong enough reduction, the mtDNA instability induced by EtBr treatment can phenocopy the instability seen in OPA1 KD cells, in some cases such as Il-6, Rage and Tlr2. Longer EtBr treatment might be better to achieve a better depletion of the mtDNA in Scr cells thus, being able to abolish the stress signal itself.

4.3.3. Assessment of the cytosolic induction of mtDNA-dependent inflammation

Our aim in this specific chapter was to elucidate which is the pathway recognizing this mtDNA and inducing the inflammatory response. Among the different patter recognition receptors (PRR) that are know, there are several known to be activated by mtDNA: AIM2, NLRP3, TLR9 and cGAS. However only two of those are able to induce a NF-κB type of response. Given that West *et al* found a cGAS type of response upon TFAM reduction and mtDNA stress, we first studied the implication of these system in our conditions. As reviewed in the introduction section, cGAS is cytosolic a sensor of mtDNA, which leads preferentially to a type I interferon response (Rongvaux *et al.*, 2014; White *et al.*, 2014). However, it is

also capable to induce an NF-κB type of pro-inflammatory response. We first examined the presence of mtDNA in the cytosol. Cellular plasma membrane was carefully permeabilized with digitonin detergent to induce pores in the plasma membrane, in order to the separate soluble cytosolic content from the membrane bound pellet fraction by centrifugation (West *et al.*, 2015).

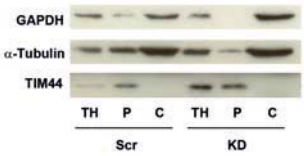

Figure 48. Cytosolic fraction extraction. Representative experiment of cytosolic extraction by digitonin protocol of Scr and OPA1 KD myoblasts. Total homogenate (TH), pellet fraction after cytosolic extraction (P) and cytosolic extract (C).

Figure 48 shows a representative immunoblotting of different markers. Cytosolic markers such as α-tubulin or GAPDH were enriched in the cytosolic fraction whereas inner mitochondrial membrane marker TIM44, was retained in the pellet (P) fraction.

Total DNA was extracted from the two subcellular fractions and the total homogenate fraction. Next, mtDNA copy number was analyzed in the different fractions (Figure 49).

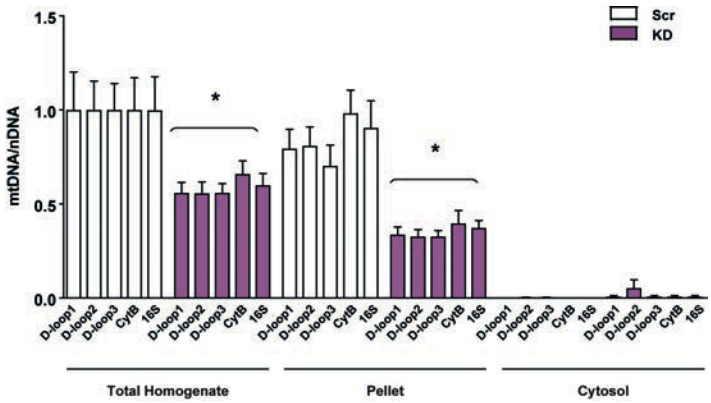

Figure 49. Absence of mtDNA in the cytosolic fraction. mtDNA levels relative to nuclear DNA (Tert) in total homogenate, pellet and cytosolic fraction of Scr and OPA1 KD (KD) cells (n=3). Data represent mean ± SEM. * $p<0.05$ vs. Scr.

Consistent with previous observations, OPA1 KD cells present 50% of mtDNA copies, this is conserved in the pellet fraction. There is no relevant amplification of mtDNA in the cytosolic fraction, which suggest that there is no leakage of mtDNA to the cytosol (Figure 49).

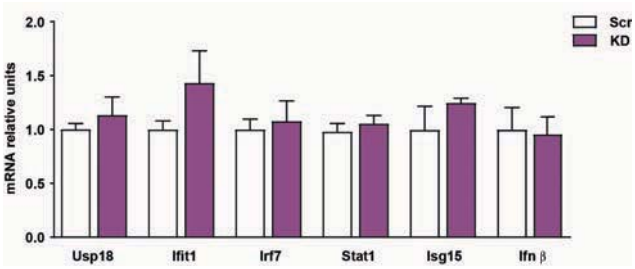

Figure 51. Type I interferon response. mRNA expression of interferon-stimulated genes (ISG) and Ifnβ in Scr and OPA1 KD (n=6). Data represent mean ± SEM. * p<0.05 vs. Scr.

Also, given that cGAS preferentially courses through type I IFN responses, we examined the expression of interferon stimulates gens (ISG) or Ifn-β between in control and OPA1-deficient cells. No differences were detected between the two groups, suggesting that the cGAS pathway was inactive (Figure 51).

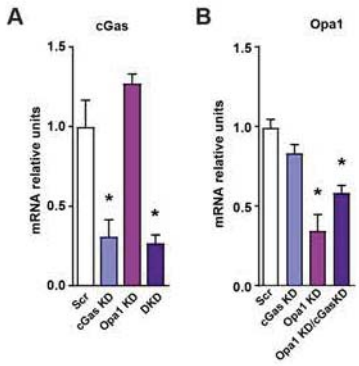

Figure 50. Validation of single and double cGAS-OPA1 depletion. Expression of cGAS (A) and OPA1 (B) upon single or double knock-down of cGAS and OPA1. Data represent mean ± SEM. * p<0.05 vs. Scr.

To robustly rule out cGAS as key player in OPA1 deficiency-induced inflammation, we performed cGAS loss-of-function on Scr and OPA1 KD cells, thus obtaining fours groups: control (Scr), single OPA1 KD (OPA1 KD), single cGAS KD (cGAS KD), and double OPA1-cGAS KD (DKD) (Figure 50).

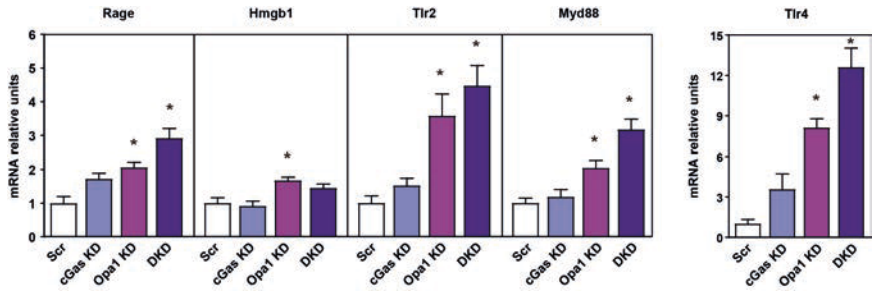

Figure 52. NF-κB target genes expression upon cGAS depletion. mRNA relative expression of NF-κB target genes in control (Scr), cGAS-depleted (cGAS KD), OPA1-depleted (OPA1 KD) and double cGAS-OPA1-ablated (DKD) cells (n=6). Data represent mean ± SEM. * p<0.05 vs. Scr.

The analysis of the expression of NF-κB target genes in these cells show no signs of rescue of the inflammatory phenotype in DKD cells (Figure 52). The absence of mtDNA in the cytosol, the constant expression of ISG and the lack of normalization of NF-κB target gene expression argue against of cGAS playing any role in the inflammatory profile of OPA1 KD cells.

4.3.4. Examination of the mitochondrial quality control system functionality

Based on the data indicating that OPA1 deficiency does not lead to mtDNA leakage to the cytosol or engagement of cGAS signaling, we analyzed whether mtDNA was maintained in mitochondria, using an imaging approach.

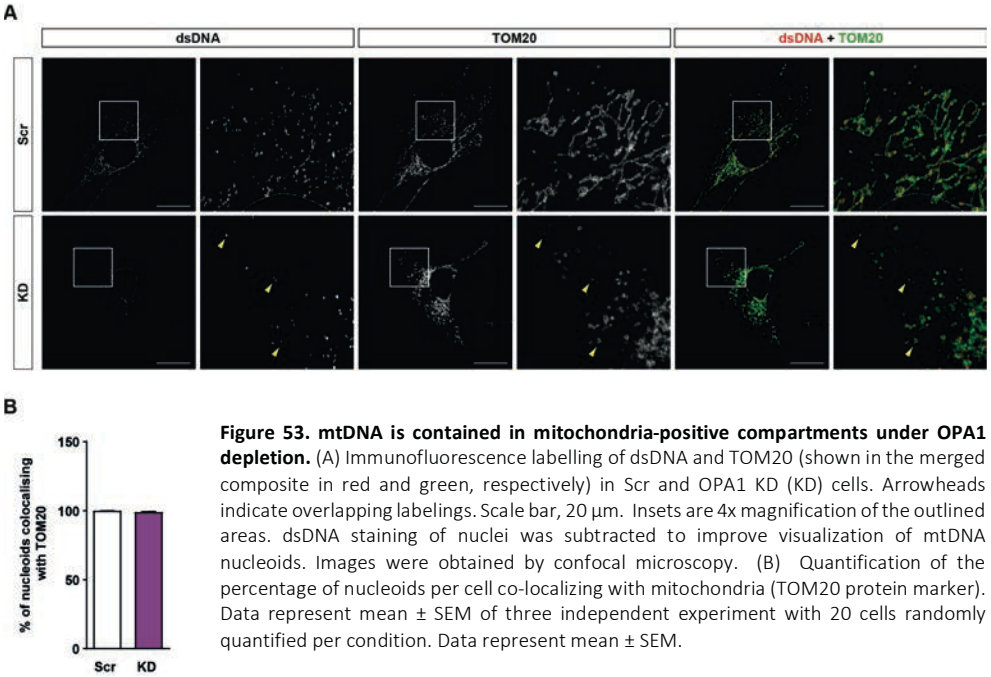

Figure 53. mtDNA is contained in mitochondria-positive compartments under OPA1 depletion. (A) Immunofluorescence labelling of dsDNA and TOM20 (shown in the merged composite in red and green, respectively) in Scr and OPA1 KD (KD) cells. Arrowheads indicate overlapping labelings. Scale bar, 20 µm. Insets are 4x magnification of the outlined areas. dsDNA staining of nuclei was subtracted to improve visualization of mtDNA nucleoids. Images were obtained by confocal microscopy. (B) Quantification of the percentage of nucleoids per cell co-localizing with mitochondria (TOM20 protein marker). Data represent mean ± SEM of three independent experiment with 20 cells randomly quantified per condition. Data represent mean ± SEM.

To detect mtDNA, we immunostained total dsDNA using an antibody in combination with Hoechst 33342 staining, which specifically detects nuclear DNA. The composite of both labeling allow for the subtraction of the nuclear staining from the dsDNA labelling, thus maintaining only the dsDNA corresponding to the mtDNA, forming nucleoids. To assess the localization of these nucleoids in mitochondria, we performed immunofluorescence of mtDNA together with immunofluorescence of an

outer mitochondrial membrane protein marker, TOM20 (Figure 53A). Quantification of 20 cells per condition for three independent experiments indicate that 100% of mtDNA nucleoids are localized in mitochondrial-positive compartments both in Scr and OPA1 KD cells. (Figure 53B).

Moreover, we used another mitochondrial marker, this time mitotracker deep red was used to detect mitochondria (Figure 54). In combination with dsDNA labelling and Hoechst staining, we were able to corroborate that there is no divergence of the localization of mtDNA and mitochondria (Figure 54).

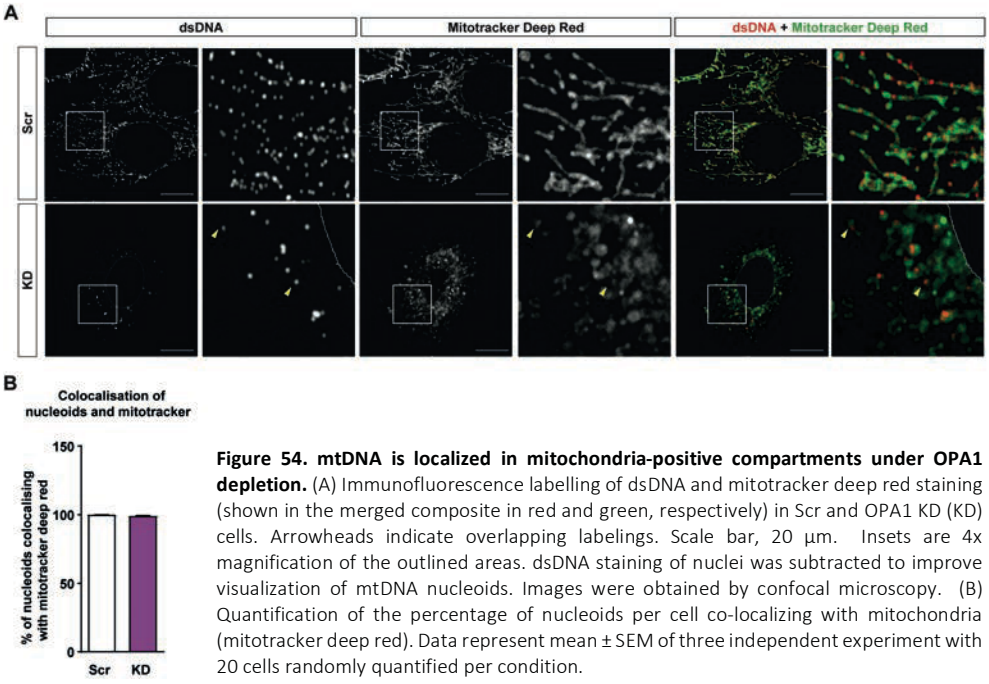

Figure 54. mtDNA is localized in mitochondria-positive compartments under OPA1 depletion. (A) Immunofluorescence labelling of dsDNA and mitotracker deep red staining (shown in the merged composite in red and green, respectively) in Scr and OPA1 KD (KD) cells. Arrowheads indicate overlapping labelings. Scale bar, 20 µm. Insets are 4x magnification of the outlined areas. dsDNA staining of nuclei was subtracted to improve visualization of mtDNA nucleoids. Images were obtained by confocal microscopy. (B) Quantification of the percentage of nucleoids per cell co-localizing with mitochondria (mitotracker deep red). Data represent mean ± SEM of three independent experiment with 20 cells randomly quantified per condition.

The mechanisms of the cell to target damaged mitochondria, like OPA1-deficient mitochondria, is described as the mitochondrial quality control system. Classically referred to mitochondrial autophagy only, however now this quality control system has expanded to include also the production of mitochondrial-derived vesicles. In this study we are going to focus on the major pathway which is mitochondrial autophagy or mitophagy, due to the observation that autophagy malfunction caused mtDNA-mediated inflammation (Nakahira *et al.*, 2011; Oka *et al.*, 2012).

We assessed the functionality of mitophagy at two levels: at the early stages of mito-autophagosome formation, and at the final steps involving fusion to the lysosome and content degradation.

Firstly, we examined mitophagy initiation by treating Scr and OPA1 KD cells with the ionophore CCCP for 30min to induce mitochondrial membrane depolarization, thus mitochondrial damage and mitophagy induction. Mitochondrial enriched fractions were obtained from treated and untreated cells, then lipidated, membrane bound LC3 or LC3-II levels were determined in these conditions (Figure 55). The recruitment of LC3-II to the mitochondrial fraction is comparable between Scr and OPA1 KD myoblasts conditions (Figure 55). The results indicate that the mitophagy machinery is able to detect damaged mitochondria and start the engulfment of these mitochondria into mito-autophagosomes containing LC3-II.

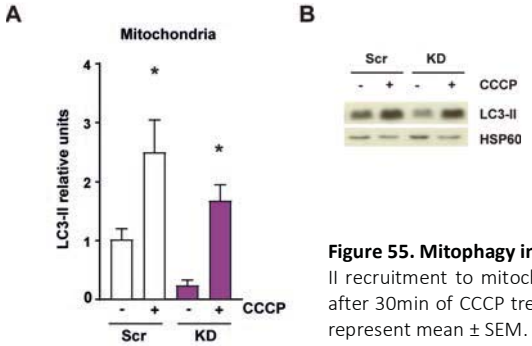

Figure 55. Mitophagy initiation is unaltered in OPA1 KD myoblasts. (A) LC3-II recruitment to mitochondrial enriched fractions in Scr and KD myoblasts after 30min of CCCP treatment (n=4). (B) Representative western blot. Data represent mean ± SEM. * p<0.05 vs. untreated group.

In parallel, with the aim of assessing the importance of mitophagy induction for the development of the specific response detected in OPA1 KD conditions, we obtained single and double PINK1-OPA1 stable knock down cells (Figure 56).

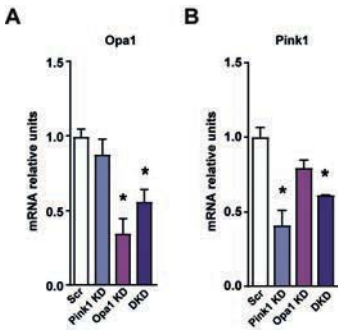

Figure 56. Validation of single and double (DKD) PINK1-OPA1 depletion. Expression of PINK1 (A) and OPA1 (B) upon single or double knock-down of PINK1 and OPA1. Data represent mean ± SEM. * p<0.05 vs. Scr.

The study of these four groups of cells revealed very interesting observations. On one hand, single PINK1 KD resulted in the induction of a very strong type I interferon response (Figure 57). In all the genes analyzed OPA1-PINK1 DKD cells presented this induction, moreover some genes like *Ups18*, *Ifit1* or *Ifnβ* were further increased (Figure 57).

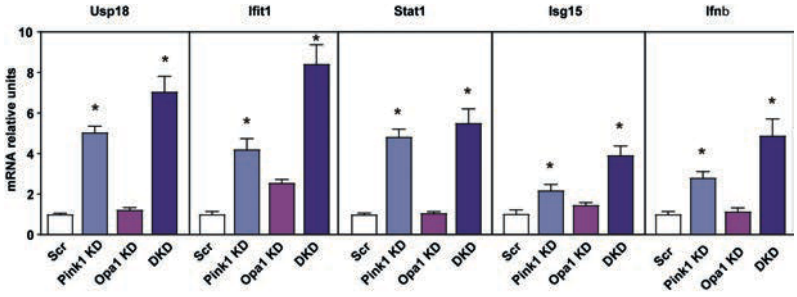

Figure 57. PINK1 deficiency induces a type I interferon response. mRNA relative expression of ISG and Ifnb in Scr, PINK1 KD, OPA1 KD and PINK1- OPA1 double KD (DKD). Data represent mean ± SEM. * p<0.05 vs. Scr.

On the other hand, the expression of NF-κB target genes was very variable. The depletion of PINK1 did not cause a clear regulation of the expression of these genes (Figure 58).

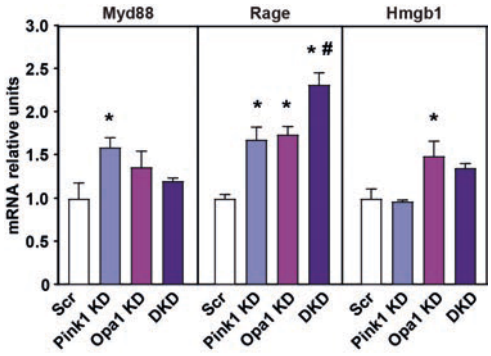

Figure 58. PINK1 deficiency does not restore the expression of NF- κB target genes induced by OPA1 deficiency. Expression of NF-κB target genes in control (Scr), PINK1-depleted (PINK1 KD), OPA1-depleted (OPA1 KD) and double PINK1-OPA1-ablated (DKD) cells (n=3). Data represent mean ± SEM. * p<0.05 vs. Scr or # p<0.05 vs. OPA1 KD cells.

Moreover, another very intriguing observation was made. PINK1 KD alone induced the leakage of mtDNA to the cytosol, both in Scr and OPA1 KD cells (Figure 59). This kind of response is probably due to the lack of contention once performed by the mitochondrial quality control system, thus damaged mitochondria remain free and undegraded, thus extruding any material to the cytosol, in this study we detected mtDNA.

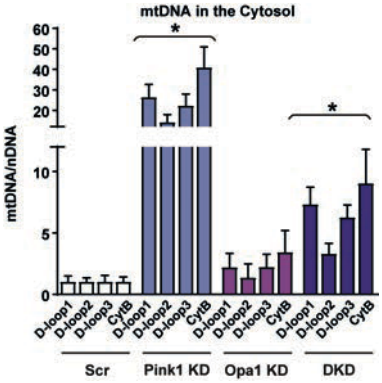

Figure 59. PINK1 deficiency induces mtDNA leakage to the cytosol. mtDNA levels relative to nuclear DNA (Tert) in digitonin-extracted cytosolic fractions of Scr, PINK1 KD, OPA1 KD and Pink-OPA1 double Knock-down (DKD) C2C12 myoblasts (n=3). Data represent mean ± SEM. * p<0.05 vs. Scr.

The studies regarding Pink loss-of-function need further research to be explained. However, these results revealed a very important aspect for our project: mitophagy initiation is essential to prevent a cytosolic type of response, which in combination with normal mitophagy initiation detected in OPA1 KD cells, suggest that mitochondrial damages are indeed contained inside autophagosomes.

Next, alterations in mitophagy resolution were assessed by inducing mitochondrial damage for longer times and analyzing the rate of mitochondrial nucleoid disappearance (Lazarou *et al.*, 2015). Cells were treated with CCCP for 9h or 16h and then immunolabeled with anti-dsDNA antibody and Hoechst 33342, which is the delineated area in the representative images (Figure 60). Quantification of 20 random images per condition and three independent were performed using a macro designed by Anna Lladó from the Advanced Digital Microcopy core facility at IRB Barcelona. Scr cells present a profile of reduction from 500 nucleoids per cell to 250 after 9h of treatment and then at 16h of treatment there is a significant recovery of the nucleoid number due to the mitochondrial biogenesis force (Figure 60).

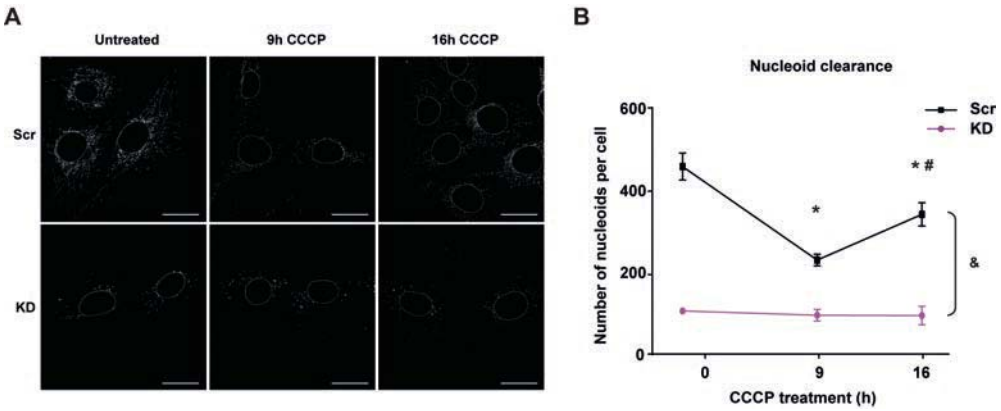

Figure 60. OPA1 deficiency results in nucleoid clearance defects. (A) Representative images of dsDNA labelling in the study of mitophagy completion by mtDNA nucleoid clearance upon long CCCP treatment in Scr and KD cells. Hoechst staining area is delimited by a white line. Scale bar, 20 µm. (B) Quantification of the number of nucleoids per cell at 0, 9, and 16h of CCCP treatment. Data represent mean ± SEM of three independent experiment with 20 cells randomly quantified per condition. * $p<0.05$ vs. Scr untreated, # $p<0.05$ vs. 9h of treatment, and & $p<0.05$ KD vs. Scr

The profile shown by Scr cells is notably different to the quantification of OPA1 KD cells, which show a constant number of nucleoids around 100 nucleoids per cell (Figure 60). These data suggest that the degradation of the nucleoids by the lysosome is not occurring in OPA1-deficient cells. Therefore, OPA1 loss-of-function results in mitophagy completion defects.

In order to study mitophagy at the skeletal muscle level of loxP and OPA1 KO animals, mice were treated for 5 days with Chloroquine (CQ) an agent preventing the fusion of the autophagosome and the lysosome, thus ablating the degradation of cellular material through this compartment.

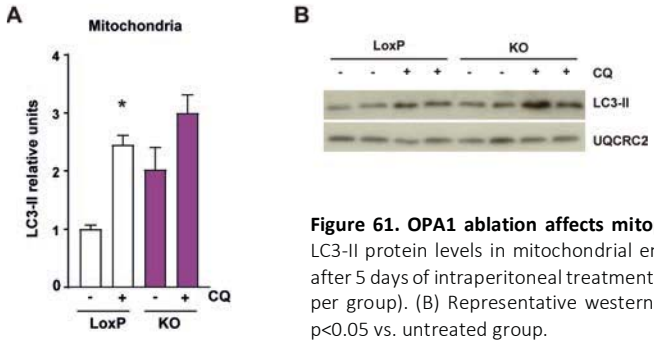

Figure 61. OPA1 ablation affects mitophagy in skeletal muscle. (A) Relative LC3-II protein levels in mitochondrial enriched fractions of quadriceps muscle after 5 days of intraperitoneal treatment with chloroquine (CQ) (10 observations per group). (B) Representative western blots. Data represent mean ± SEM. * $p<0.05$ vs. untreated group.

Quadriceps muscles of these animals were homogenized, mitochondrial enriched fraction was obtained, and LC3-II levels were assessed in these fractions. Control animals presented a normal profile characterized by the buildup of LC3-II in treated conditions (Figure 61). On the contrary, OPA1 KO muscles present already at basal conditions significantly increased levels of LC3-II in mitochondrial enriched fraction and the CQ treatment did not significantly impact on this amount (Figure 61), suggesting that lysosomal degradation is already blocked in basal conditions.

Consistent with these data, transmission electron microscopy studies revealed an accumulation of aberrant mitochondria encapsulated in double or single membrane structures (Figure 62). All these supporting the idea of mitochondrial accumulation and impairment of mitophagy completion. Regarding this electron microscopy micrographs, it is interesting to note a marked dilatation of the sarcoplasmic reticulum in OPA1-deficient muscles (Figure 62, lower panels). The type of swelling resembles the one observed in initial stages of vacuole formation in Mg56-knockout muscle (Van *et al.*, 2015), in which is associated with ER stress and UPR response. ER stress has been associated with ER swelling also in pancreatic β cells (Riggs *et al.*, 2005; Akiyama *et al.*, 2009).

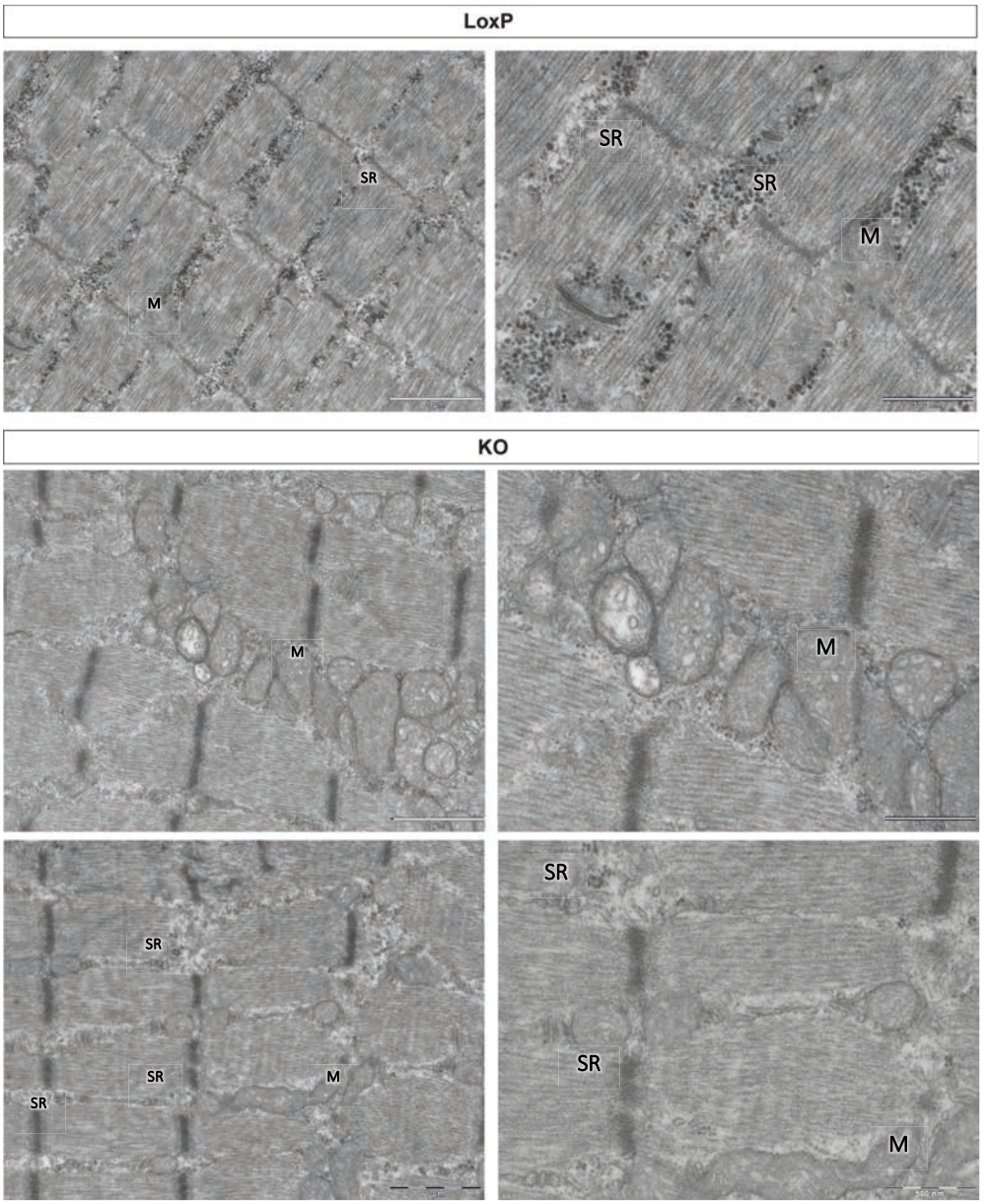

Figure 62. Electron micrographs of gastrocnemius muscles from 3-weeks old loxP and KO mice. (M) mitochodnria. (SR) Sacoplasmic reticulum. Scale bar, 1 µm in left panels, and 500 nm in right panels.

We wanted to assess whether this was restricted to mitophagy or was relevant to the general autophagy of the cell, so we performed further studies in this regard. Using the cellular model, we assessed the response of Scr and OPA1 KD myoblasts to CQ treatment during time, regarding LC3-II accumulation.

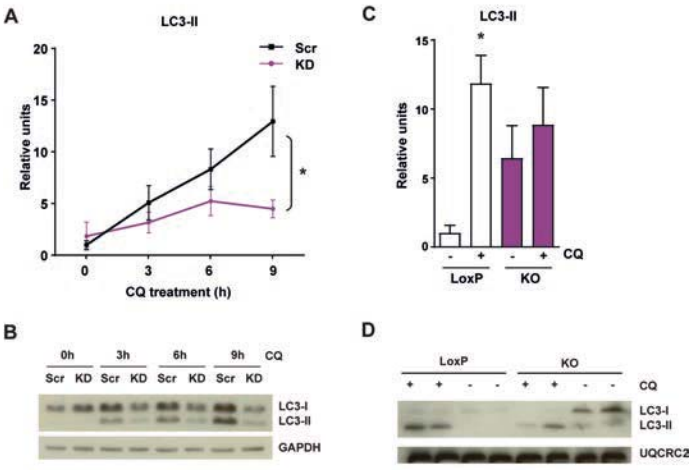

Figure 63. Autophagy is altered in OPA1-deficient conditions. (A) Time course study of LC3-II protein levels in Scr and KD C2C12 myoblasts under CQ treatment (n=6). (B) Representative western blot. (C) Relative LC3-II protein levels in total homogenates of gastrocnemius muscle after 5 days of intraperitoneal treatment with CQ (6 observations per group). (D) Representative western blot. Data represent mean ± SEM. * $p<0.05$ vs. control group.

While Scr cells linearly accumulate LC3-II due to the blockage of lysosomal degradation, OPA1 KD cells do not induce such a buildup, or at least the buildup is much lower, suggesting that the pathway it is probably already dysfunctional (Figure 63A and Figure 63B). The assessment of LC3-II levels in total homogenates of muscles from loxP or OPA1 KO animals treated or untreated with CQ depicted a similar scenario than mitochondrial enriched fractions, this time of higher magnitude (Figure 63C and Figure 63C). LoxP treated increased 12-fold the levels of LC3-II, while OPA1 KO muscle already have 6.4-fold increased its levels under CQ treatment did not significantly impact on these levels.

Time course studies of muscle sections at different ages from 3 to 20 weeks old mice of p62 revealed an enhanced staining for this autophagy marker in OPA1 KO mice (Figure 64A). The same occurred when muscle sections were stained with Gomori's trichrome staining, which labels ragged red fiber, i.e., fibers containing damaged mitochondria (Figure 64B). Histological studies were performed in collaboration with Dr Diaz Ramos.

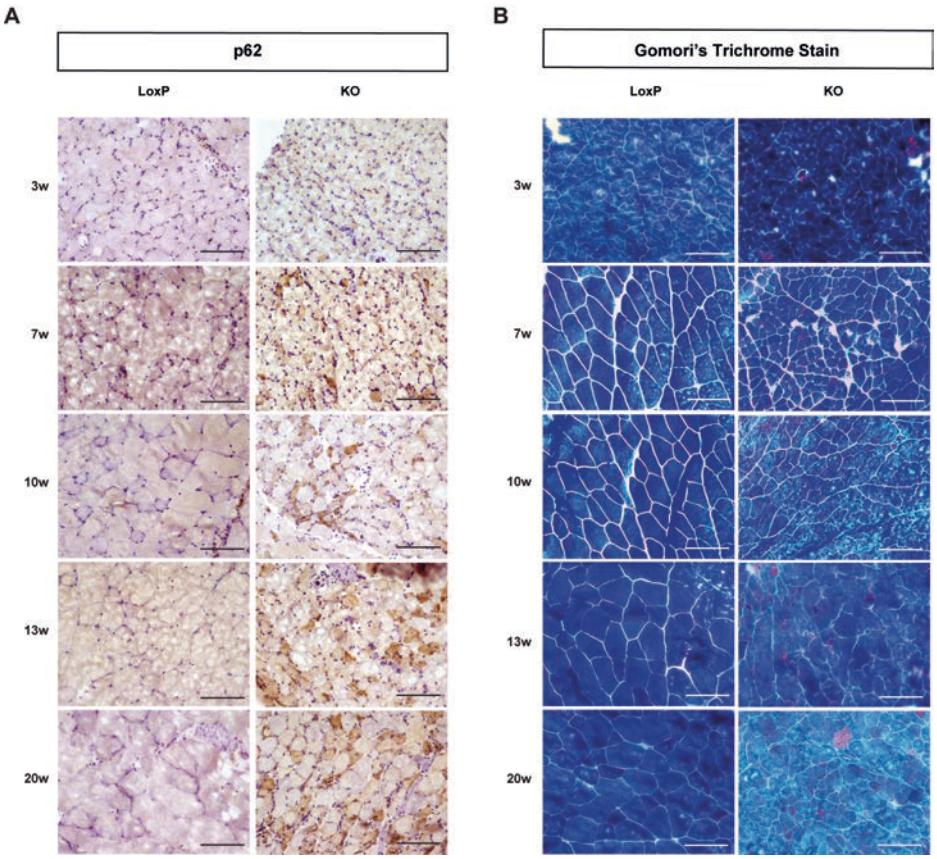

Figure 64. OPA1 depletion induces accumulation of p62 and damaged mitochondria in skeletal muscle. Representative images of p62 (A) and Gomori's Trichrome Staining (B) in muscles of 3-, 7-, 10-, 13-, and 20-week cold loxP and KO animals. Scale bar, 100 µm.

Automated quantification of the histological studies revealed that, both p62 and Gomori's trichrome staining were already statistically significant at 3 weeks old, and further accumulate as the animals aged

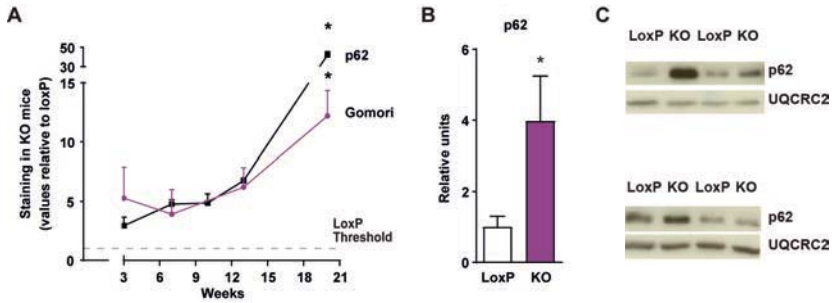

Figure 65. OPA1-deficient muscles accumulate damaged mitochondria and p62. (A) Relative expression of 3 weeks old mice of p62 (n=5). (B) Quantification of p62 expression and Gomori's Trichrome staining in gastrocnemius muscle of OPA1 KO animals at 3, 7, 10, 13 and 20 weeks of age. Values of OPA1 KO mice are represented relative to the loxP group. This quantification was performed using Trainable Weka Segmentation plugin from ImageJ (5 images per group). Data represent mean ± SEM. * p<0.05 vs. loxP.

(Figure 65A). Furthermore, immunoblot analysis of p62 in skeletal muscle total homogenates confirmed that p62 protein levels were already significantly increased at 3 weeks of age (Figure 65B and Figure 65C).

4.3.5. Characterization of the mtDNA localization

Recent data have established a relationship between autophagy malfunction and the presence of undegraded mtDNA, which is recognized by TLR9 and results in inflammation (Nakahira *et al.*, 2011; Oka *et al.*, 2012). Based on those observations indicating that OPA1 deficiency causes an impairment in the resolution of mitophagy, the presence of TLR9 in the endolysosomal pathway and the close cross-talk between the two vesicular systems, next we explored whether mitochondrial-containing autophagosomes are being re-routed to the endosomal pathway, which would enable the recognition of mtDNA by TLR9. To this end, we analyzed the cellular localization of mtDNA regarding the different endo-lysosomal compartments.

First, we studied whether mtDNA distribution with an early endosome localization. Thus, we immunostained for dsDNA and EEA1 (early endosome protein marker).

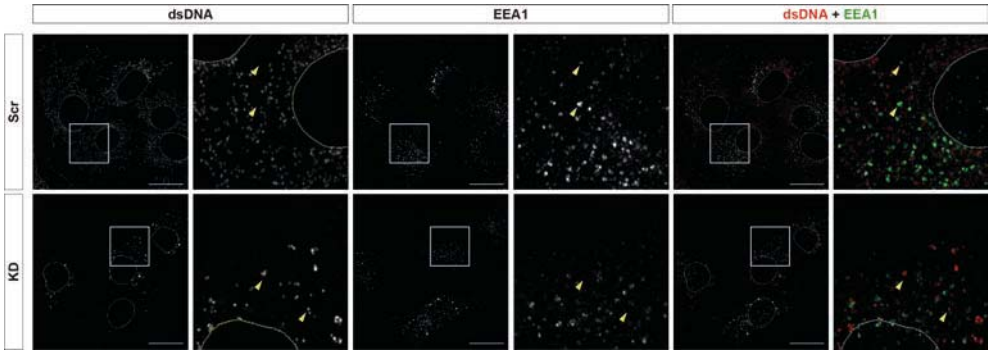

Figure 66. mtDNA does not co-localize with early endosomes. Immunofluorescence labelling of dsDNA and EEA1 (shown in the merged composite in red and green, respectively) in Scr and OPA1 KD (KD) cells. dsDNA staining of nuclei was subtracted to improve visualization of mtDNA nucleoids. Insets are 4x magnification of the outlined areas. Images were obtained by confocal microscopy. Arrowheads indicate exclusion labelings. Scale bar, 20 µm.

Both in Scr and OPA1 KD cells dsDNA and EEA1 staining were completely exclusive (Figure 66). There was no co-localization detected.

Then we screened for other late endosomes or multivesicular bodies markers and found a relevant correlation between the staining for VPS4 and dsDNA (Figure 67). Vps4 is a subunit of ESCRT-III complex, involved in the formation of multivesicular bodies.

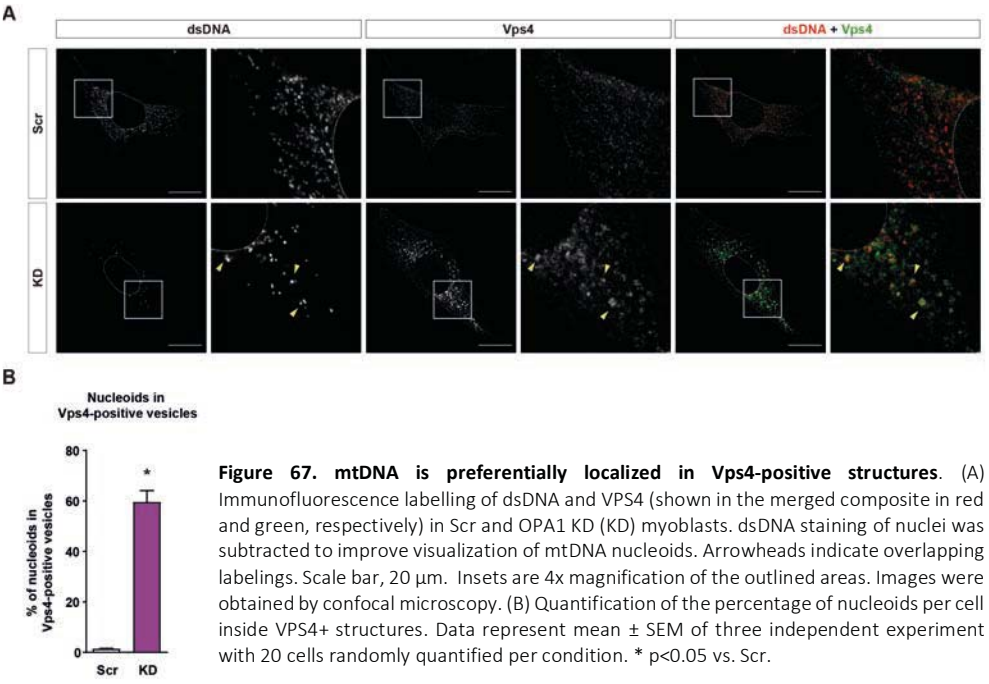

Figure 67. mtDNA is preferentially localized in Vps4-positive structures. (A) Immunofluorescence labelling of dsDNA and VPS4 (shown in the merged composite in red and green, respectively) in Scr and OPA1 KD (KD) myoblasts. dsDNA staining of nuclei was subtracted to improve visualization of mtDNA nucleoids. Arrowheads indicate overlapping labelings. Scale bar, 20 µm. Insets are 4x magnification of the outlined areas. Images were obtained by confocal microscopy. (B) Quantification of the percentage of nucleoids per cell inside VPS4+ structures. Data represent mean ± SEM of three independent experiment with 20 cells randomly quantified per condition. * $p<0.05$ vs. Scr.

These images revealed two kinds of information. On one hand, we detected the presence of aggregated structures positive for VPS4 in OPA1 KD cells compared to a diffuse cytosolic, barely noticeable in control cells (Figure 67). On the other hand, we found clustered mtDNA nucleoids in this VPS4$^+$ structures (Figure 67). The quantification shows that 60% of nucleoids present in an OPA1 KD myoblast are present in VPS4$^+$ structures (Figure 67).

Given the reported presence of TLR9 in the lysosomes (Oka *et al.*, 2012; De Leo *et al.*, 2016), we examined whether this could be a relevant compartment together with VPS4⁺ late endosomes. To this end, we performed double and triple staining using LAMP1 as a lysosomal marker. These studies showed no co-localization between LAMP1 and TOM20 (containing 100% of mtDNA nucleoids) (Figure 68).

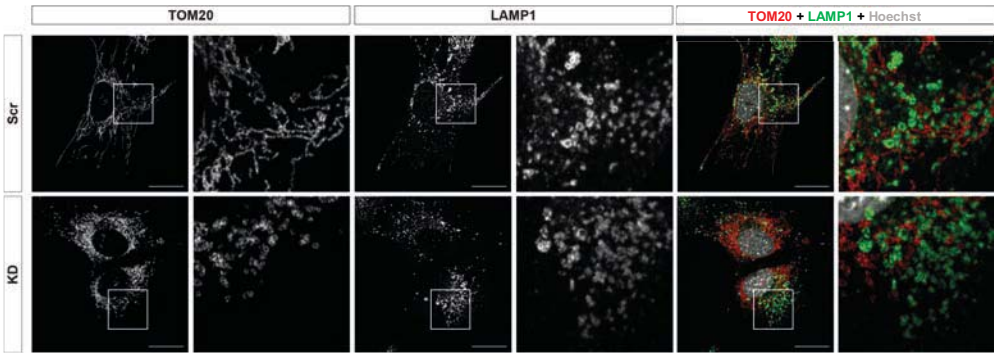

Figure 68. Mitochondria and lysosomes labelings are exclusive. Immunofluorescence labelling of TOM20 and LAMP1 (shown in the merged composite in red and green, respectively, together with Hoechst 33342 in grey) in Scr and OPA1 KD (KD). Insets are 4x magnification of the outlined areas. Images were obtained by confocal microscopy. Scale bar. 20 um.

Likewise, there was no co-localization between LAMP1 and VPS4 (the latter containing around 60% of the nucleoids), thus we suggest the structures labelled by these markers are close yet separated (Figure 69).

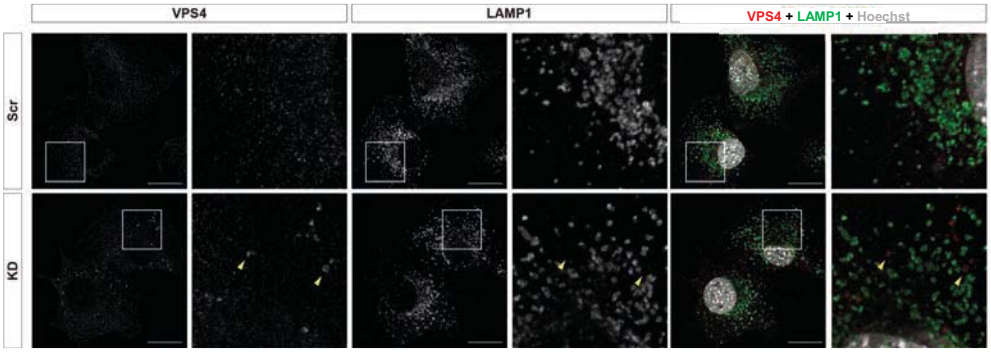

Figure 69. VPS4 does not co-localize with LAMP1. Immunofluorescence labelling of VPS4 and LAMP1 (shown in the merged composite in red and green, respectively, together with Hoechst 33342 in grey) in Scr and OPA1 (KD). Insets are 4x magnification of the outlined areas. Images were obtained by confocal microscopy. Arrowheads indicate exclusion labelings. Scale bar, 20 µm.

Triple labeling of mtDNA, LAMP1 and VPS4 in control and OPA1-deficient cells showed exclusion localization between mtDNA and LAMP1, and localization of mtDNA inside VPS4⁺ structures (Figure 70).

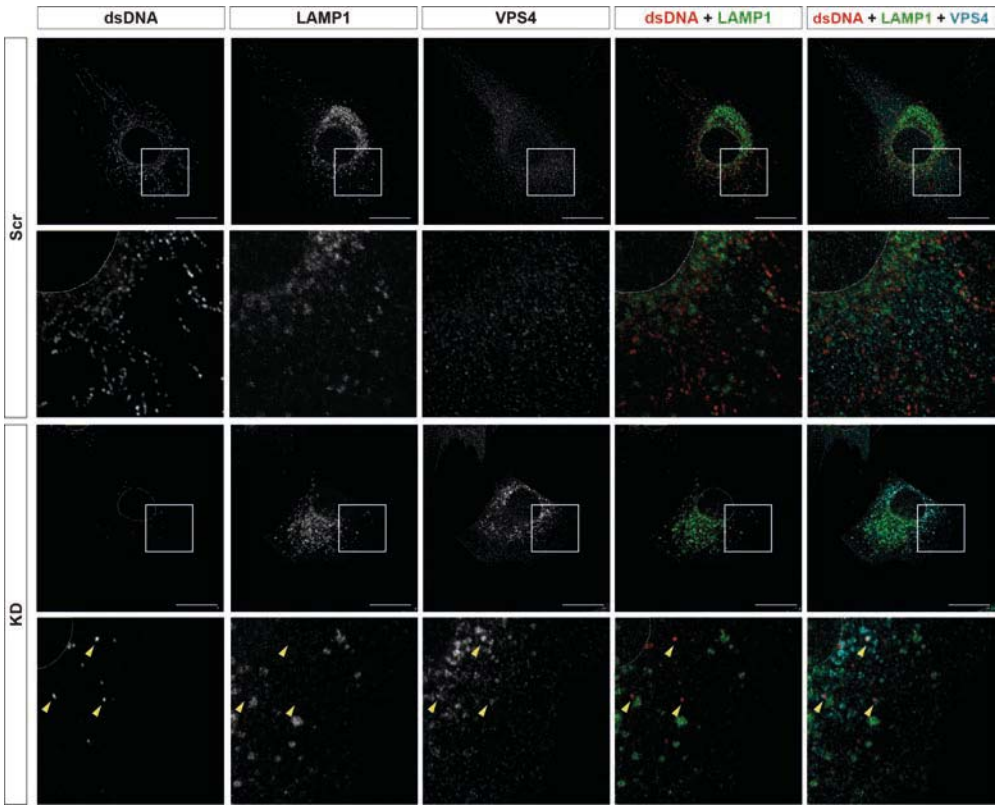

Figure 70. mtDNA localization upon OPA1 deficiency. Immunofluorescence labelling of dsDNA, LAMP1 and VPS4 (shown in the merged composites in red, green and cyan, respectively) in Scr and OPA1 KD (KD) cells. dsDNA staining of nuclei was subtracted to improve visualization of mtDNA nucleoids. Insets are 4x magnification of the outlined areas. Images were obtained by confocal microscopy. Arrowheads point at nucleoids of interest. Scale bar, 20 µm.

These data suggest that a substantial proportion of mitochondria are localized in late endosomes upon OPA1 depletion.

4.3.6. Assessment of the TLR9 localization and its involvement in OPA1 deficiency-induced inflammation

Most mtDNA co-localizes with the mitochondrial protein TOM20 and it is not present in lysosomes in control and OPA1 KD cells. Based on that we next analyzed whether mtDNA co-localizes with TLR9 in OPA1-deficient muscle cells.

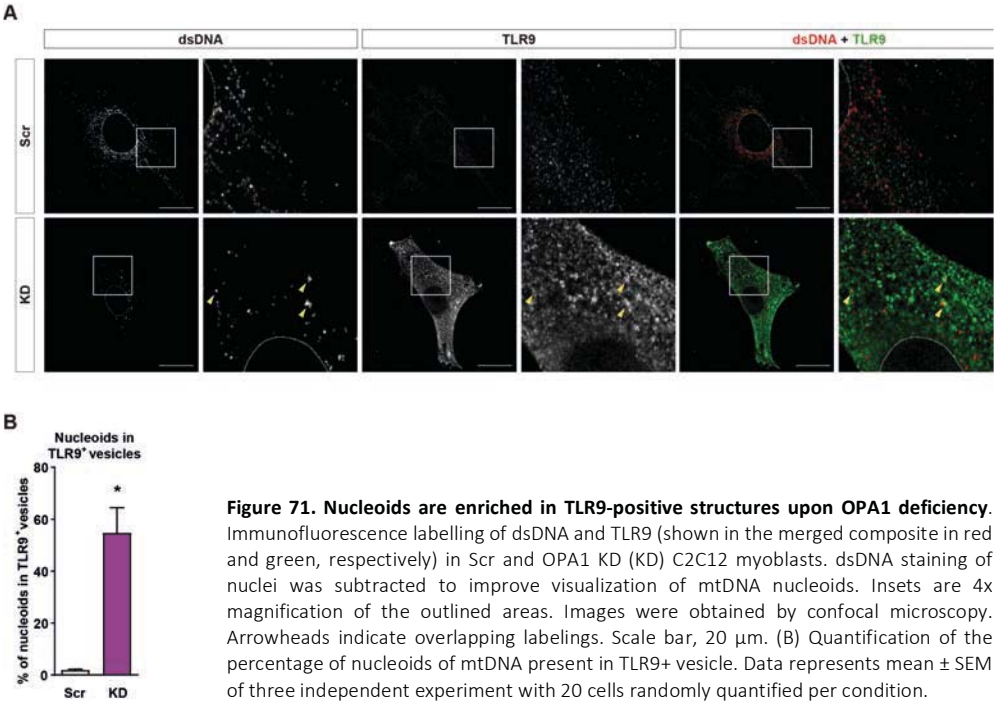

Figure 71. Nucleoids are enriched in TLR9-positive structures upon OPA1 deficiency. Immunofluorescence labelling of dsDNA and TLR9 (shown in the merged composite in red and green, respectively) in Scr and OPA1 KD (KD) C2C12 myoblasts. dsDNA staining of nuclei was subtracted to improve visualization of mtDNA nucleoids. Insets are 4x magnification of the outlined areas. Images were obtained by confocal microscopy. Arrowheads indicate overlapping labelings. Scale bar, 20 µm. (B) Quantification of the percentage of nucleoids of mtDNA present in TLR9+ vesicle. Data represents mean ± SEM of three independent experiment with 20 cells randomly quantified per condition.

In control cells, TLR9 was barely detectable, which was markedly enhanced in OPA1-deficient cells (Figure 71). In addition, OPA1 KD cells showed presence of mtDNA in $TLR9^+$ structures (Figure 71). The quantification of these images reflects that 50% of mtDNA was found in $TLR9^+$ structures (Figure 71). Also, there is some enrichment in structures positive for both TLR9 and LBPA (a marker of the intraluminal vesicle of multivesicular bodies or late endosomes) (Figure 72).

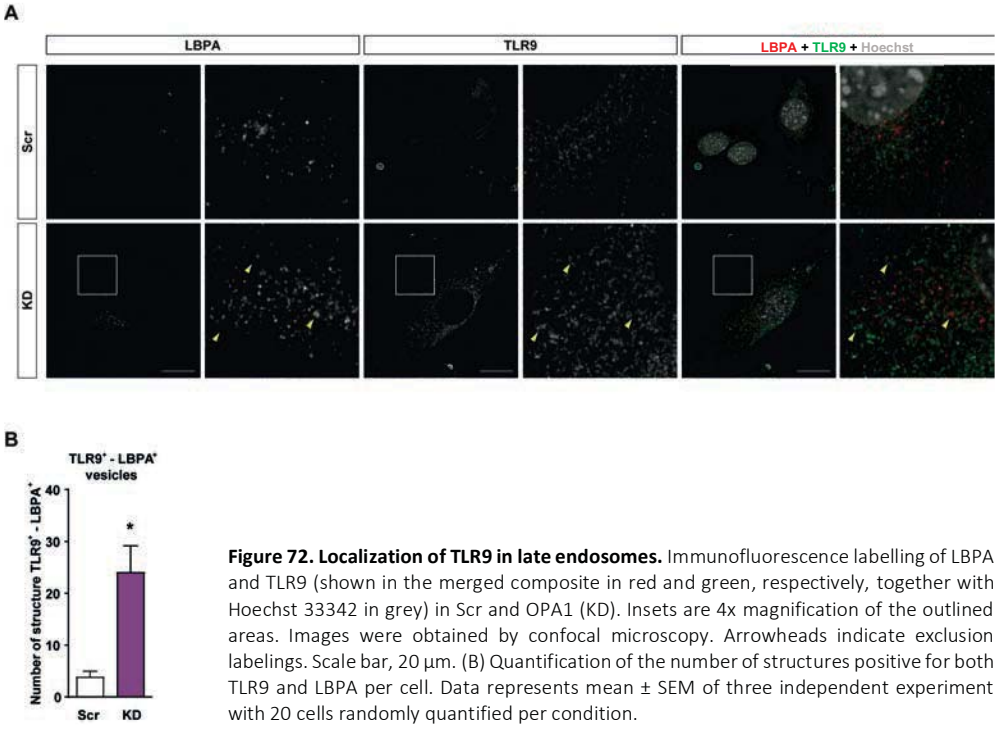

Figure 72. Localization of TLR9 in late endosomes. Immunofluorescence labelling of LBPA and TLR9 (shown in the merged composite in red and green, respectively, together with Hoechst 33342 in grey) in Scr and OPA1 (KD). Insets are 4x magnification of the outlined areas. Images were obtained by confocal microscopy. Arrowheads indicate exclusion labelings. Scale bar, 20 µm. (B) Quantification of the number of structures positive for both TLR9 and LBPA per cell. Data represents mean ± SEM of three independent experiment with 20 cells randomly quantified per condition.

In addition, and aiming to completely discard the possibility of TLR9 being in a compartment with lysosomal characteristics, we performed double staining of TLR9 and LAMP1 and the staining are completely exclusive. TLR9^{+} structures did not co-localize with lysosomes, when using LAMP1 as a marker, in control or in OPA1-deficient cells (Figure 73).

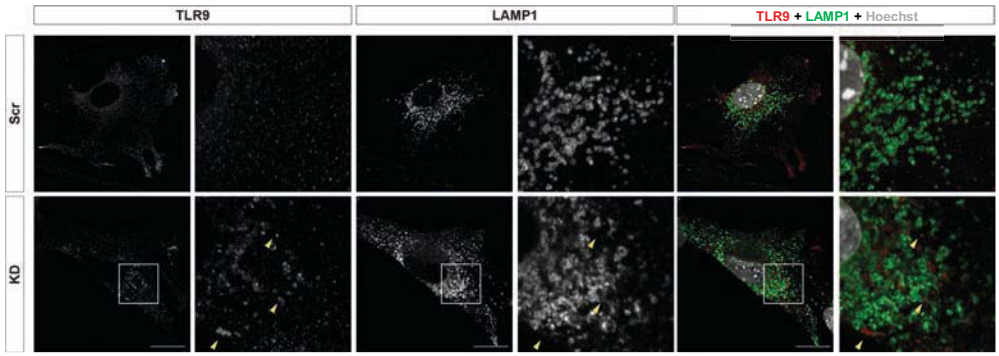

Figure 73. TLR9 and LAMP1 labelings are exclusive. Immunofluorescence labelling of TLR9 and LAMP1 (shown in the merged composite in red and green, respectively, together with Hoechst 33342 in grey) in Scr and OPA1 KD (KD) cells. Insets are 4x magnification of the outlined areas. Images were obtained by confocal microscopy. Scale bar, 20 µm.

Furthermore, in skeletal muscle specific OPA1 KO mice the expression of TLR9 was already double at weaning and further increased with age compared to controls (Figure 74). The quantification shows 2-fold from 3 weeks of age and an abrupt increase after week 13 in OPA1 KO mice. These data support the concept that TLR9 is activated upon OPA1 deficiency.

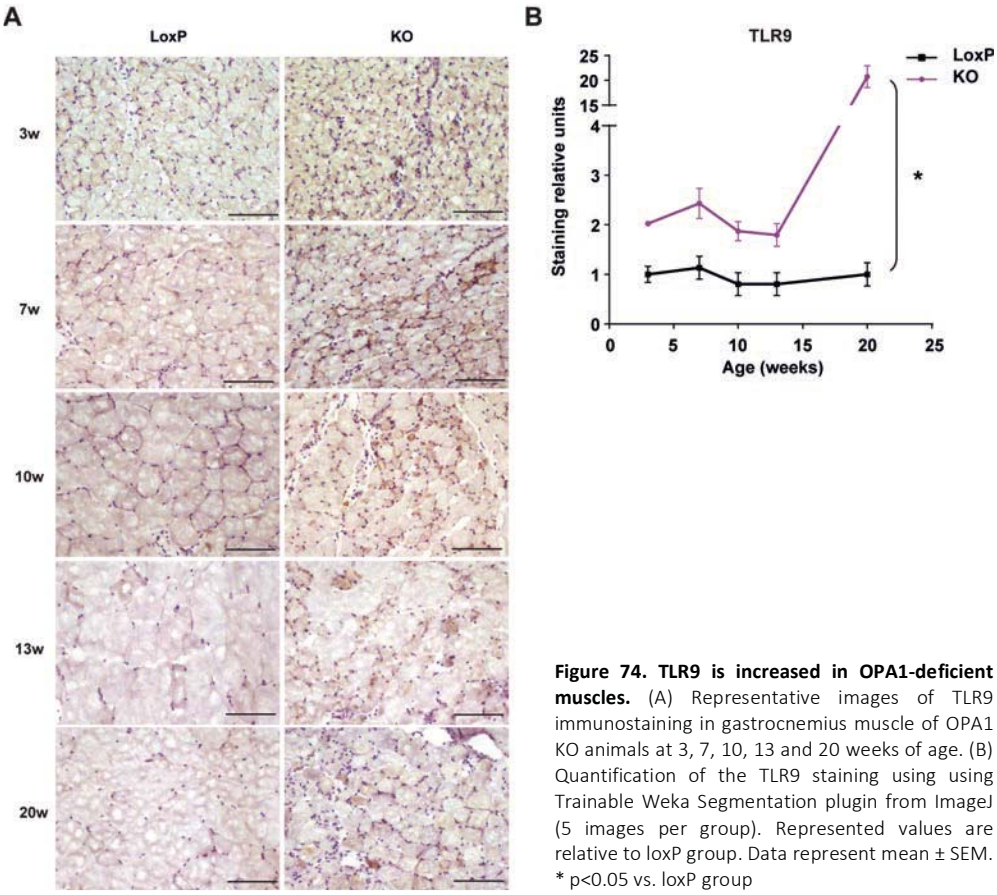

Figure 74. TLR9 is increased in OPA1-deficient muscles. (A) Representative images of TLR9 immunostaining in gastrocnemius muscle of OPA1 KO animals at 3, 7, 10, 13 and 20 weeks of age. (B) Quantification of the TLR9 staining using using Trainable Weka Segmentation plugin from ImageJ (5 images per group). Represented values are relative to loxP group. Data represent mean ± SEM. * $p<0.05$ vs. loxP group

All these suggest that mtDNA comes to proximity and share the same type of vesicular compartment with TLR9, which could entail a response through this receptor. To prove the involvement of TLR9 in the NF-κB response characteristic of OPA1-deficient context, two approaches were taken to ablate TLR9 function and assess NF-κB target gene expression normalization. First, cells were treated with the TLR9 antagonist ligand ODN2088 or with the corresponding negative control.

Incubation of OPA1 KD muscle cells with ODN2088 attenuated the expression of NF-κB target genes, Myd88, S100a8, Hmgb1 or Rage (Figure 75). In addition, the enhanced release of IL-6 of OPA1-deficient cells was inhibited by incubation with ODN2088 compared to the negative control (Figure 75).

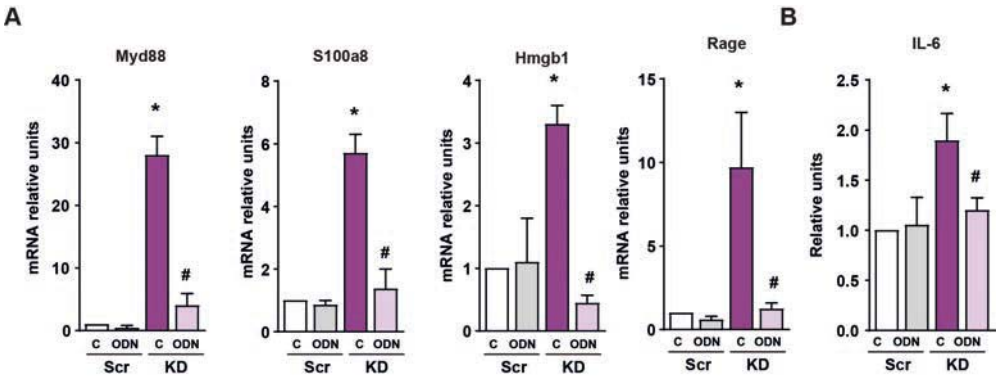

Figure 75. Normalization of NF-κB target genes expression upon TLR9 antagonist treatment. (A) MyD88, S100A8, HMGB1 and RAGE expression in Scr and KD myoblasts treated with ODN2088 (ODN) or ODN2088 negative control (C) 1 μM (n=9). (B) IL-6 levels detected in cultured medium of myoblasts (Scr and KD) treated with ODN2088 (ODN) or ODN2088 negative control (C) (n=9). Data represent mean ± SEM. * p<0.05 when comparing the effect of OPA1 deficiency or # p<0.05 when comparing the effects of ODN2088.

Lastly, we analyzed whether similar effects were detected upon genetic depletion of TLR9. To this end, TLR9 was depleted in scramble or OPA1-depleted muscle cells (Figure 76).

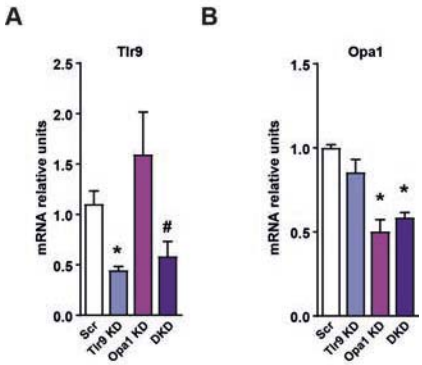

Figure 76. Validation of single and double OPA1-TLR9 knock-down myoblasts. Expression of TLR9 (A) and OPA1 (B) upon single or double knock-down. Data represent mean ± SEM. * p<0.05 vs. Scr. # p<0.05 vs. OPA1 KD.

Depletion of TLR9 markedly reduced the induction of NF-κB genes in OPA1-deficient cells (Figure 77), in agreement with the data obtained by the treatment with TLR9 antagonists. In all, our data are coherent with a TLR9 activation mediated by OPA1 deficiency.

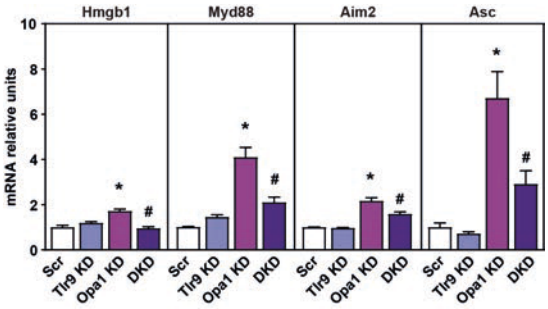

Figure 77. Recovery of OPA1 deficiency-dependent NF-κB target genes expression upon TLR9 depletion. Expression of NF-κB target genes in control (Scr), Tlr9-depleted (Tlr9 KD), OPA1-depleted (OPA1 KD) and double Tlr9-OPA1-ablated (DKD) cells (n=3). Data represent mean ± SEM. * $p<0.05$ vs. Scr or # $p<0.05$ vs. OPA1 KD cells.

DISCUSSION

The results of the present work can be synthesized in these three concepts depicted in Figure 78:

1. Skeletal muscle-specific OPA1 loss-of-function leads to the secretion of FGF21 and pro-inflammatory cytokines, the latter causing severe growth impairment.
2. OPA1 deficiency in the muscle context causes inflammation in muscle.
3. OPA1 ablation results in mitochondrial dysfunction, mtDNA stress and mitophagy alterations, all of which leads to TLR9 activation, and in turn, to inflammation.

In this discussion chapter I am going to dissect and analyze the possible interpretations of the results obtained during the course of this PhD thesis. Also, at the end, I will discuss globally my working model.

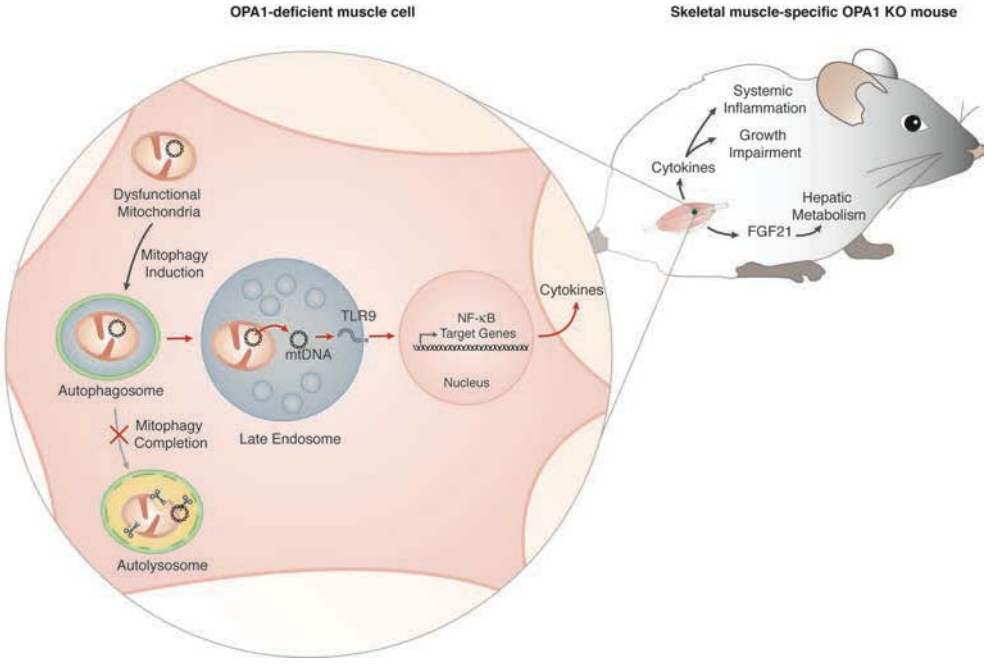

Figure 78. Working model of the mechanisms leading to the OPA1-deficiency phenotype.

5.1. Systemic effects caused by OPA1 depletion in skeletal muscle

OPA1 is a dynamin-related protein that is responsible for inner mitochondrial membrane fusion, essential for mitochondrial cristae morphology maintenance, and involved in mtDNA stability. In this study we have explored the effects of the depletion of OPA1 in early developmental stages. The model of study was obtained in the laboratory by crossing *Opa1* floxed animals with transgenic animals expressing Cre recombinase under the control of the promoter of the muscle developmental protein myogenin and the enhancer MEF2C. The basic characterization of the skeletal muscle-specific OPA1 KO (OPA1 KO) mice stablished the foundation of this study. Previous results revealed a dramatic reduction in lifespan of the OPA1 KO animals and severe growth defect. Consistent with the growth defects, the hepatic growth hormone (GH) – insulin-like growth factor 1 (IGF-1) axis was altered. Further analysis of histological markers and circulating parameters revealed a systemic pro-inflammatory state. Moreover, muscle expression of FGF21 and plasma levels of the mitokine were increased. In this study we explored two paths to explain the growth impairment: FGF21 and inflammatory cytokines.

First, we focused on the role of FGF21 in the systemic effects reported in the skeletal muscle-specific OPA1 KO mice. FGF21 is a factor secreted by cells and tissues when suffering from mitochondrial dysfunction. Although skeletal muscle is not usually the primary source of FGF21, in specific OPA1 KO mice we detected a high expression. This result together with its notably high plasma levels, suggested a relevant role for the mitokine in the phenotype. Thus, we hypothesized that OPA1 loss-of-function induced mitochondrial dysfunction which increased the expression of FGF21, via ATF4 transcription factor activation.

FGF21 has been described to play an important role in growth regulation. Several studies assigned FGF21 as the link between malnutrition and growth defects (Kubicky *et al.*, 2012; Guasti *et al.*, 2014; Ozaki *et al.*, 2015), it is described to impair the GH-IGF-1 axis by inhibiting the translocation of growth hormone receptor (GHR) to the plasma membrane, thus inhibiting its signaling (Inagaki *et al.*, 2008).

FGF21-induced inhibition of IGF-1 action limits the growth of the overall organism, thus limiting metabolic requirement with the aim to ensure organism survival in low nutrient availability conditions.

Aiming to determine the contribution of FGF21 to the growth defects in OPA1 KO mice we generated double knock-out mice (DKO), global FGF21 KO and skeletal muscle specific OPA1 KO. DKO mice did not either improved body weight, or normalized the expression of hepatic genes involved in the GH-IGF-1 axis, specifically when compared with FGF21 KO control mice. In this regard, we made an interesting observation, FGF21 global ablation increased the hepatic expression of *Fos* and *Ghr*, but not that of *Igf1*. The data obtained from these experiments refute the idea of FGF21 being the driver of growth impairment. Nevertheless, FGF21 KO did rescue the expression of PGC-1α target genes. This is in keeping with the observation that FGF21 induces PGC1α in liver which results in upregulation of its target genes, including mitochondrial biogenesis, lipid transport and lipid oxidation (Badman *et al.*, 2009; Estall *et al.*, 2009; Potthoff *et al.*, 2009; Fisher *et al.*, 2014). The hepatic pattern of gene expression detected in OPA1 KO animals suggests that the liver represents a major organ to sustain the metabolic response to FGF21, probably together with white adipose and brown adipose tissues.

Although we excluded FGF21 from having a major contribution in OPA1 KO mice growth impairment, other groups have proposed a more relevant role for this myokine. Tezze and colleagues reported that skeletal muscle ablation of FGF21 on OPA1-ablated muscles was able to restore metabolic status and recover lifespan (Tezze *et al.*, 2017). Furthermore, Pereira and colleagues stated that OPA1 ablation in mature muscle elicit age- and diet-induce weight gain through FGF21 upregulation (Pereira *et al.*, 2017). The comparison of our work with these studies unveils different phenotypes in response to similar gene manipulations in skeletal muscle.

For instance, Tezze *et al.* showed that OPA1 ablation in adult muscle resulted in ATF4 activation and alternative splicing of Xpb1, which was rescued by chemical chaperon administration. These data support the idea of ER stress response activation in this model. Differently, we reported eIF2α phosphorylation independent on ER stress (no PERK induction). However, we did not examine IRE1 or

ATF6 ER-stress branches, thus it is possible that ER stress is contributing to the phenotype. In fact, electron microscopy examination of OPA1-ablated muscles revealed dilated sarcoplasmic reticulum, similarly to the initial states of vacuoles formation in Mg56 KO skeletal muscles, which is associated with ER stress (Van et al., 2015). Despite we did not detect PERK phosphorylation to be increased, the two other branches of the integrated stress response of ER stress will need to be assessed in future experiments.

The specific details of the two models could be the key for the different pathways affected, and while our model ablates OPA1 at very early stages of muscle formation, both Abel and Sandri studied models in which OPA1 was depleted in adult muscle. From previous data gathered in our laboratory (Noguera, 2014), we know that OPA1 is essential for proper myogenic differentiation of C2C12 myoblasts, thus the inability to differentiate might be leading to further devastating effects than adult OPA1 ablation. Nevertheless, as it will be discussed below, anti-inflammatory treatment of control and OPA1 KO mice was able to rescue not only growth parameters but also FGF21 expression and circulating levels, which suggests inflammation playing a role in the enhancement of the mitokine.

Having discarded FGF21 as a major player in the growth defects, we focused on the inflammation as the cause of growth impairment. Different types of chronic inflammation in children, i.e. juvenile idiopathic arthritis, chronic kidney disease or chronic inflammatory bowel disease; have been associated with reduced growth (Wong et al., 2016). The cytokines reported to be responsible for the growth impairment are IL-6, IL-1β (Kutukculer, Caglayan and Aydogdu, 1998; Ji et al., 2002). The correlation of inflammation and growth defects have been corroborated using several animal models. Overexpression of IL-6 causes reduced circulating levels of IGF-1, and it is normalized by treatment with neutralizing antibodies specific for IL-6 (De Benedetti et al., 1997; De Benedetti, 2009). Another study explored the different pathways by which IL-6, IL-1β and TNF-α can block the GH-IGF-1 axis (Zhao *et al.*, 2014). The first one inhibits the expression of GHR, while the two latter enhance expression of SOCS3 inhibitor, the three leading to a reduced expression of IGF-1 and, thus growth defects (Denson *et al.*, 2003; Lieskovska, Guo and Derman, 2003; Zhao *et al.*, 2014). Previous data revealed increased plasma levels of both IL-6

and IL-1β in OPA1 KO mice. In fact, the hepatic expression of growth-related genes was characterized by reduced expression of *Fos*, *Ghr* and *Igf1* and increased expression of the inhibitor *Socs3*, coherent with the idea that IL-6 and IL-1β have a hepatic effect that reduces global growth Figure 78.

To assess the importance of inflammation in the skeletal muscle-specific OPA1 KO growth defects we treated control and OPA1 KO mice with sodium salicylate or vehicle (PBS) for 30 days. Chronic treatment with anti-inflammatory agent resulted in substantial amelioration of muscle mass, body weight, muscle necrosis and hepatic growth hormone resistance. Based on these data, we support the view that reduced growth in OPA1 KO mice is, at least in part, secondary to systemic inflammation. The improvement in body weight increase is modest, hence we propose that variation of the treatment may produce better improvement in whole body growth. Given that OPA1 depletion is performed at day 8.5 of embryonic development it might be a good idea to supplement the mothers diet with a low-dose anti-inflammatory treatment. In the same line, a change in the type of administration to one with less intervention and stress could depurate the beneficial effects linked only to the anti-inflammatory therapy in OPA1 KO mice. Another important consideration for future studies is the specificity of the anti-inflammatory agent. Sodium salicylate is a molecule, which although it is a very efficient broad anti-inflammatory drug it has plenty off target effects. Thus, it might be advisable to select a more specific treatment. Neutralizing antibodies have been proven efficient on preventing growth defects induced by high circulating cytokine levels, thus it would be interesting to treat with antibodies against IL-6 and/or IL-1β, and to determine whether there are equally responsible or even participating in the growth defects caused by OPA1 ablation in skeletal muscle.

Lastly regarding anti-inflammatory treatment, it is worth mentioning the rescue that we reported on FGF21 expression and circulating levels upon salicylate administration. Although we directed our efforts in another direction it is interesting to note what we learned from this and perhaps speculate on the mechanism or pathways involved. The few pieces of data that we generated in this regard include a very robust induction of activating transcription factor 4 (ATF4) target gene signature, and in turn FGF21 upregulation in skeletal muscle of OPA1-deficient mice, as an ATF4 target gene (Kim *et al.*, 2013). Also,

OPA1 ablation results in increased phosphorylation of the viral double-stranded RNA binding protein kinase R (PKR), and of its target: the stress kinase eIF2α. ATF4 is described to be activated by eIF2α. Phosphorylation of eIF2α inhibits the loading of methioninyl-tRNAs thus preventing normal translation initiation by reducing the availability of this kind of tRNA. This favors the expression of ATF4 due to its double regulatory translation initiation regions which enables the translation of the ATF4 protein only in situation of low $tRNA^{Met}$ availability (Wek, Jiang and Anthony, 2006). Interestingly, anti-inflammatory treatment efficiently restored both eIF2α and PKR increased phosphorylation to normal levels in OPA1 KO muscles, which is coherent with the normalization of FGF21 expression levels. These data suggest that PKR activation, which is the most upstream factor of the pathways that we have examined, is downstream of inflammation (Figure 79).

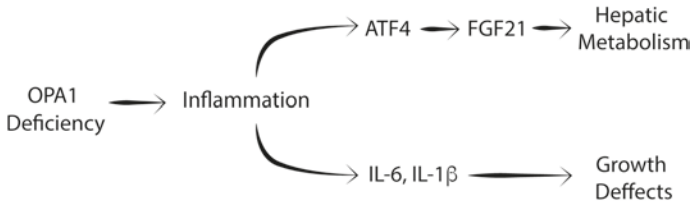

Figure 79. Proposed model for the systemic effects caused by OPA1 depletion in skeletal muscle

This is in contrast with the literature describing PKR as an upstream regulator of NF-κB or inflammasome activation (Goh, deVeer and Williams, 2000; Lu *et al.*, 2012; Yim and Williams, 2014; Yoshida *et al.*, 2017). One study has reported that it might be involved in the discrimination between different TLRs and their downstream pathways to NF-κB. Asakura and colleagues stated that PKR is essential for the delivery of signal from TLR3, TLR9 and also TNFR; and dispensable in TLR4 signaling (Asakura *et al.*, 2007). Therefore, we can speculate the interconnection of those pathways in OPA1-deficient muscle cells so TLR9 activation induces PKR, and this in turn eIF2α, and ATF4, finally leading to FGF21 expression. However, this is only a hypothesis at this point. The activation of PKR - FGF21 axis should be assessed in OPA1-TLR9 double knock-down cells.

Consequently, it would be interesting for future studies to explore the connection between TLR9 and PKR-dependent FGF21 expression, and if the contribution of PKR to the signal transduction from TLR9 to NF-κB is compatible with a rescue of the anti-inflammatory drug sodium salicylate. We have to consider, as well, that as salicylate is a molecule which has been described to act at different level besides NF-κB inhibition (Kopp and Ghosh, 1994; M. J. Yin, Yamamoto and Gaynor, 1998). Many studies have shown that salicylate targets other pathways besides the cyclo-oxigenase inhibition, which was first described for acetylsalicylic acid, the metabolic precursor of salicylate (Vane, 1971). There are some studies linking salicylate to ER stress regulation (Silva *et al.*, 2007; Gentz *et al.*, 2013; Mügge and Silva, 2017). There are some other studies that show regulation of different cellular kinases like MAPK (Amann and Peskar, 2002). The plural variety of effects of salicylate permits to consider another possibility in which there is no lineal sequence between NF-κB, PKR and FGF21 production, hence caution is mandatory when working and analyzing results with such a drug.

5.2. Characterization of the muscle inflammatory state and the origin of the systemic inflammation

In the previous chapter it has been argued that inflammation is responsible for the growth impairment. In this section, we will discuss the origin of the systemic inflammation and whether it is the primary event that connects local OPA1 deficiency in skeletal muscle to the systemic phenotype.

Once inflammation was proved to be crucial for the growth defects detected in OPA1 KO mice a question arose. Given that in OPA1 KO mice the genetic manipulation is restricted to the muscle fiber, we wondered whether the muscle fiber itself was producing the initial inflammatory signals. Importantly, OPA1 KO mice were reported to have high levels of creatine kinase when examined in the plasma of 8- to 10-weeks old mice. Also, histological examination of muscle section reported the higher presence of necrotic fibers in OPA1 KO mice. Although we have documented that skeletal muscle necrosis is a relevant feature of OPA1 deficiency, it was important to assess whether it was the primary triggering event in the muscle fiber. Extrusion of fiber content would induce an inflammatory response similar, to

some extent, to the one seen upon cardiotoxin-induced injury, thus it could be the driving force of inflammation with the recruitment of the immune system. To analyze inflammation, necrosis and immune system recruitment *in vivo* we designed two approaches, first a time course study of different parameters in young mice, and then similarly studies of pro-inflammatory markers in a model of adult ablation of OPA1.

The first approached revealed that OPA1 depletion at embryonic stages resulted in a statistically significant increase of IL-1β assessed by immunohistochemical staining of muscle sections. Also, muscle necrosis assessment showed that while there were no differences detected at 3 weeks old mice, when mice were 7 weeks-old OPA1 deficiency had induced a statistically significant higher plasma activity of creatine kinase, indicating increased muscle necrosis. Finally, with this time course study we reported that CD68, a marker of pro-inflammatory macrophages (Taylor *et al.*, 2005), was only significantly increased in muscle sections at week 13 of age. The assessment of caspase 3 cleavage as a marker of apoptosis revealed that there is no programmed cell death in either loxP or in OPA1 KO muscles.

It is very surprising that the immune system delays its appearance so much. Only at week 13 there is upregulation of the CD68 labelling, thus this topic need to be further investigated to understand whether is a problem of sensitivity of our technique or in fact the cellular recruitment to the damaged muscle takes 10 weeks to occur. Future studies should include other markers of immune infiltrates, to ensure that there is no contribution of the immune system in early stages. However, if we consider the data on CD68 recruitment in 3 months-old mice, we can speculate for the reason of this delay. Some studies have reported a role for FGF21 in macrophage function modulation. Guo *et al.* reported the involvement of FGF21 in macrophage actions and maturation through microRNA-33 regulation (Guo *et al.*, 2016). Moreover, Yu *et al.* documented the induction of NRF2 and suppression of NF-κB in RAW264.7 macrophages upon treatment with FGF21. These studies suggest that the high circulating FGF21 levels in OPA1 KO mice might be preventing the immune system, specially macrophages, to response promptly and efficiently to the muscle inflammation and necrosis caused by the ablation of OPA1. To explored this possibility, future studies could analyze CD68 labeling in OPA1-FGF21 double KO

mice. If FGF21 has any effect on macrophage recruitment, this experiment should unveil a faster recruitment of pro-inflammatory macrophages to skeletal muscle in an FGF21 KO context.

The second approach was designed to detect early changes upon OPA1 depletion in adult muscles. Real time PCR studies measured the expression of NF-κB target genes and *Cd68* also confirmed the early onset of inflammation, before muscle mass loss and in turn preceding *Cd68* upregulation. Further analysis of this model is required to perfectly determine the time point at which OPA1 is ablated and to be able to perform biochemical analysis of the pathways induced at very early stages of OPA1 deficiency.

Inflammation has not been described in ADOA patients. The study of the OPA1 heterozygous animals might give a closer phenotype to the skeletal muscle pathology reported in ADOA *plus* syndrome. Nevertheless, regarding muscle pathologies that involves inflammation, there is a group of disease called idiopathic inflammatory myopathies (IIMs), which include polymyositis (PM), dermatomyositis (DM) and sporadic inclusion body myositis (sIBM) (Temiz, Weihl and Pestronk, 2009). IIMs patients show muscle weakness, fatigue and elevated muscle enzymes in serum, and their histological characteristics include mononuclear cell infiltration and myofiber degeneration, with unusual over-expression of major histocompatibility complex (MHC) class I molecules on the surface of the affected myofibers (Malik *et al.*, 2016). OPA1 KO mice show several of these characteristics: MHC class I enhancement, fiber degeneration, muscle weakness, mononuclear infiltrates and circulating creatine kinase. Furthermore, IIMs are correlated with mitochondrial pathology with depletion of COX and the presence of mtDNA deletions (Lindgren *et al.*, 2015; Catalan-Garcia *et al.*, 2016). For future studies it might be worth assessing OPA1 levels and isoform composition in samples from these patients, or perhaps to further characterize OPA1 KO models to determine whether they could serve as an animal model for the study of inflammatory myopathies.

Lastly, with the aim of irrefutably assessing whether OPA1 deficiency caused a cell-autonomous inflammatory profile in the muscle context, OPA1 was knocked-down in C2C12 myoblasts. We decided to use lentiviruses to deliver shRNA to C2C12 for different technical issues. Transfection was discarded

due to the low efficiency achieved in muscle cells. Adenoviral delivery was also discarded because first, we were afraid that the infection itself could have an impact on the priming state of muscle cells and thus could be generating background inflammation that could corrupt our data. In addition, we wanted to maintain and study cells in an undifferentiated state, thus it was necessary to produce a cell line stably expressing the targeting shRNA. Moreover, during the course of this study we found that the optimal time for the study of effects of OPA1 ablation was between 1 and 3 weeks after the cells were selected, thus expressing shRNA targeting OPA1. That time frame was stablished because before one week the mtDNA features were not present yet; and after 3 weeks, OPA1 ablation reverted, perhaps due to the better fitness of cells that did not express the shRNA. For those reasons, we needed a cheap and easy way to repeat technique, and the lentiviral infection seemed fully appropriate.

In these conditions, OPA1 deficiency induced the activation of NF-κB as a transcription factor, the expression of NF-κB target genes and the secretion of IL-1β in C2C12 cells. Neither necrosis nor apoptosis were detected in OPA1-deficient C2C12 myoblasts. These data support the idea that OPA1 loss of function induces a cell-autonomous pro-inflammatory response which is independent of cell death (Figure 78). An unexplored part of this chapter is how is IL-1β is secreted from the myoblasts if there is no necrosis. There are different types of IL-1β secretion independent of cellular content extrusion (Bergsbaken, Fink and Cookson, 2009; Piccioli and Rubartelli, 2013). Most of them are accompanied by the activation of the cytokine by an oligomeric complex named the inflammasome, which upon activation proteolytically cleaves caspase 1 and this in turn cleaves IL-1β (Lamkanfi and Dixit, 2014). The inflammasome is not only triggered by pathogen-associated molecular patterns (PAMPs) as flags of pathogen infection, but also it is activated by damage-associated molecular patterns (DAMPs), which flag cellular malfunction or stress. There are two signals involved in the activation of the inflammasome. The priming signal, which leads to NF-κB activation including the expression of inflammasome components and inactive forms of the cytokines. This signal prepares the cell for a possible activation of the pathway upon, for instance, pathological infection. Typically, this first signal is the engagement of a membrane pattern recognition receptor (PRR) for example TLR4, but also it is

activated by intracellular receptors like intraluminal TLRs like TLR7 and TLR9. Experimentally LPS is widely used to prime cells for inflammasome activation. The second signal is the proper trigger, which interacts with the recognition part of the complex and leads to the oligomerization and activation of the inflammasome particle. Besides the recognition protein, which is specific for each type of inflammasome, there is a scaffold protein common to all of them. The adaptor protein known as ASC, which functions as a bridge from the upstream inflammasome sensor molecule to caspase 1. Inflammasome assembly and oligomerization results in the cleavage of caspase 1, which in turn causes a fast and efficient activation and secretion of large amounts of IL-1β, which were already expressed because of the priming signal. There are different types of inflammasomes, Broz and Dixit classified the inflammasomes in: the nucleotide-binding oligomerization domain (NOD), leucine- rich repeat (LRR)-containing protein (NLR) or NLR inflammasomes, the absent in melanoma 2 (AIM2) and pyrin inflammasomes, which are canonical inflammasome; and a third group of non-canonical inflammasomes (Broz and Dixit, 2016). NLRP3 is the most studied type of inflammasome, yet the mechanisms of activation are so diverse that there is no consensus on whether it has affinity for a wide range of molecules or rather there is an unknown intracellular signal that converges all the different triggers into NLRP3 activation (Man and Kanneganti, 2015; Jo *et al.*, 2016). The only data that we have in this regard is an upregulation of inflammasome component, which are NF-κB target genes (*Nlrp3* and *ASC*), by immunoblot we detect increased levels of the uncleaved forms of IL-1β and no cleaved for of IL-1β at all. We think that further studies should elucidate whether there is activation of the inflammasome in OPA1-deficient conditions, if so, what type of inflammasome is activated and by what kind of trigger. In order to determine whether there is inflammasome activation in general it would be worth it to analyze ASC oligomerization, caspase 1 cleavage by western blot or using FAM-Flica assay. Because, up to date, there is only one study documenting inflammasome activation in skeletal muscle and it would be worth knowing the importance of this auto-inflammatory response in our tissue of study (Rawat *et al.*, 2010).

5.3. Identification of the key players and the mechanism of the triggered inflammatory response

Based on the data linking OPA1 deficiency and muscle inflammation, we next aimed to identify the proteins and molecules responsible for the phenotype, and to explain the mechanisms by which inflammation is triggered. To do so, we characterize the mitochondrial defects associated with the loss of OPA1 functionality. Mitochondrial network organization and mitochondrial respiratory capacity were affected both in OPA1 KO skeletal muscles and in OPA1-deficient myoblasts. These effects have been extensively explored regarding OPA1 functions in inner membrane fusion and cristae morphology maintenance. In our cellular model ATP levels are unchanged relative to control cells. These data, together with the observation that OPA1 deficiency results in an increase of the glycolytic flux, support the idea that OPA1 KD cells are able to compensate the lack of mitochondrial derived ATP with an increase of the glycolytic capacity. The glycolytic flux is assessed by the acidification of the extracellular media with the Seahorse technology. We have confirmed this result daily by comparison of the media of similarly-confluent cells. As the medium contains phenol red indicator, OPA1 KD cells showed a more acidic media (tend to orange-yellow) than Scr (tend to red-pink).

Additionally, OPA1 is involved in mtDNA stability (Hudson *et al.*, 2008; Amati-Bonneau *et al.*, 2018). Here we document that OPA1 deficiency was characterized by reduced mtDNA copy number, parallel to diminished TFAM protein abundance, reduced number of nucleoids, and increased nucleoid size. OPA1 deficiency has been reported to induce low mtDNA copy number and nucleoids abundance in human fibroblasts, which suggests that those alterations are not just restricted to muscle cells (Liao *et al.*, 2017). Our data support the existence of mtDNA stress induced by OPA1 deficiency, which includes mtDNA loss, reduced nucleoids number, and increased nucleoid size.

Interestingly, the reduction in nucleoid number per cell is far more pronounced than the reduction in mtDNA copy number. There is a 50% reduction in mtDNA, assayed by amplification of 6 different regions (coding and non-coding). Differently, the number of nucleoids per cell was reduced from around 550

nucleoids per cell in control cells to less than 100 in OPA1 KD cells. While it is tempting to speculate that OPA1 deficiency results in an increment in the number of copies per nucleoid, perhaps due to replication resolution problems because of mtDNA instability; it is also possible that the limitation of the techniques used to obtain these data result in these notably different values. On one hand, RT-PCR is used to determine the number of mtDNA copies by amplification of different regions of the genome, thus it is not quantifying nucleoids, rather than actual DNA copies. On the other hand, nucleoid quantification is performed using an antibody against dsDNA for immunofluorescence staining, then nucleoids are quantified in images taken with confocal microscopy, which has a resolution capacity of 250 nm while nucleoids are describe to be 80-100 nm in size (Brown *et al.*, 2011; Kukat *et al.*, 2011, 2015). Therefore, the sensibility and resolution of confocal microscopy might not be enough to detect small fragments of mtDNA that are amplified by PCR but might not be structured as a mtDNA nucleoid, also the resolution limitation may underestimate the number if more than one nucleoids are very close together.

The 50% reduction in TFAM levels go parallel the reduction in mtDNA copy number. Since it is described that *Tfam*$^{+/-}$ results in mtDNA stress (West *et al.*, 2015), future studies will need to investigate whether OPA1 deficiency results in mtDNA instability directly or it is through TFAM reduction. In this regard, it is important to note that besides ATF4 induction, as we reported in OPA1-deficient cells; the phosphorylation of the stress kinase eIF2α is described to activate CHOP and ATF5. The three transcription factors are the pillars of the mitochondrial unfolded protein response (UPR^{mt}). The induction of this response results in the activation of number of genes to promote the recovery of OXPHOS complexes, mitochondrial proteostasis. In mammals, this response induces, among others, the expression of *Lonp1* gene, encoding the mitochondrial LON protease, which is the protease responsible for the degradation of TFAM. Therefore, it is possible that mitochondrial OXPHOS dysfunction, caused by OPA1 deficiency, results in UPR^{mt} which activates LON, that degrades TFAM, and in turn results in the reduction of mtDNA copy number (Matsushima, Goto and Kaguni, 2010). However, TFAM levels are also regulated by the amount of mtDNA. Unbound TFAM is rapidly degraded by LONP1, thus it is possible that, per se, the mtDNA instability contributes to the reduction of TFAM protein levels (Lu *et al.*, 2013).

To sum up, future studies need to discriminate whether TFAM or mtDNA are the cause of the reduction of the other, perhaps by assessing how the overexpression of TFAM impacts on the OPA1-deficient cells phenotype.

Damaged mitochondria have been implicated in the induction of inflammation through the production of reactive oxygen species and the release of damage-associated molecular patterns (DAMPs) (Zhang *et al.*, 2010; Arnoult *et al.*, 2011; Krysko *et al.*, 2011; Oka *et al.*, 2012; Wenceslau *et al.*, 2013; Yu and Bennett, 2014; Nakahira, Hisata and Choi, 2015). In this connection, we document that the inflammation detected in OPA1-deficient muscle cells requires the presence of mtDNA. Nearly total depletion of mtDNA in OPA1 KD cells was achieved using ethidium bromide to prevent mtDNA replication. NF-κB target genes were normalized in OPA1 KD cells when mtDNA was almost ablated. However, the partial depletion of mtDNA performed in Scr cells increased expression of some NF-κB target genes. The instability induced by EtBr treatment could induce an inflammatory response comparable or even higher than the one elicited by OPA1 loss-of-function. Future experiments should be performed to achieve total depletion of mtDNA in control cells, for instance, with longer time of exposure to EtBr or with higher dose. However, it may be even more exciting is to understand the type of inflammatory response that might be promoted by EtBr treatment in control myoblasts, and whether it is phenocopying the OPA1-deficiency mtDNA stress.

Once determined that mtDNA was essential for the activation of NF-κB in OPA1 loss-of-function myoblasts, two dsDNA sensors were chosen as candidates to link mtDNA and NF-κB: (i) the cytosolic sensor cGAS and (ii) the intraluminal sensor TLR9. We also considered the inflammasome recognition protein AIM2 because it is capable to sense dsDNA in the cytosol. However, it does not result in NF-κB activation. The engagement of dsDNA or mtDNA to AIM2 will constitute the inflammasome second signal (Man, Karki and Kanneganti, 2016), which means that NF-κB should have been activated previously and that is the reason why it was discarded.

MtDNA stress triggered by TFAM deficiency has been reported to release mtDNA to the cytosol causing the activation of the DNA sensor cGAS, and to promote STING-IRF3-dependent signaling to induce interferon-stimulated genes (West *et al.*, 2015). However, here we report that OPA1 depletion causes mtDNA stress but this occurs in the absence of leakage of mtDNA to the cytosol, and with no induction of interferon-stimulated genes. To further confirm that cGAS was not important in the development of OPA1-deficiency induced inflammation, we obtained cGAS silenced stable cells on Scr and OPA1 KD cells. The depletion of cGAS did not rescue the induction of NF-κB target gene expression, thus indicating that cGAS was not essential for the development of the inflammatory profile. A potential explanation for these different cellular responses under condition of mtDNA instability may lie on mitochondrial morphology. West and colleagues showed a hyperfused phenotype of the mitochondrial network (West *et al.*, 2015), and it has been reported the need for mitochondria to be fragmented prior to undergo mitophagy (Twig *et al.*, 2008). Therefore, TFAM-deficient mitochondria may not be included into autophagosomes, thus enabling mtDNA leakage to the cytosol. On the contrary, OPA1-deficient mitochondria are completely fragmented, which favors their entry into the mitophagic pathway thus restraining the potential leakage to the inside of the vesicular system. Furthermore, mtDNA nucleoids were found co-localizing with mitochondria, which suggests that mtDNA does not leak and it is retained together with mitochondria (Figure 78).

Next, we explore how important was the mitophagy process for the development of the inflammatory response upon OPA1 deficiency. To do so, we silenced a protein essential for the mitophagic process to initiate, PINK1. We generated PINK1-silenced cells on Scr and OPA1 KD. When screened for different response we detected a marked upregulation of interferon stimulated genes (ISG) and *Ifnβ*. Although we did not further characterize the huge upregulation in these genes only by PINK1 deficiency, we analyzed the mtDNA content in the cytosolic fraction of these cells. There was a clear contribution of PINK1 loss-of-function to the presence of mtDNA in the cytosol. Intriguingly, while PINK1-OPA1 DKD cells contain less copies of mtDNA in the cytosol the type of response tends to be higher than in single

PINK1 KD cells. This fact could be attributed to several factors, namely a) that mtDNA in OPA1 KD cells was more immunogenic; b) that OPA1-deficient cells become more susceptible to additional cell stress.

This experiment allows us to state that PINK1-dependent mitophagy initiation is crucial for the kind of response that we detect in OPA1-deficient cells. Thus, we investigated the state of mitophagy in OPA1 deficiency in muscle cells *in vitro* and *in vivo.* To do so, we assessed LC3-II abundance in the mitochondrial fraction of control and OPA1-deficient cells treated with CCCP for 30 min. The build-up of LC3-II comparing treated to untreated condition was found to be comparable in both groups, which suggests that mitophagy initiation is functional in OPA1-deficient cells. This indicates that the mitophagy machinery is capable to detect mitochondrial damage and engulf mitochondria into a LC3-II containing double membrane structure, or mito-autophagosome.

Aiming to study mitophagy resolution, defined as the degradation and recycling of the mitochondrial material by the lysosome, we analyzed mitochondrial protein levels at different time points in cells treated or not with inhibitors of lysosomal fusion, or with mitochondrial damage agents. None of these experiments showed a profile of mitochondrial protein levels corresponding with a time-dependent decrease due to lysosomal degradation. We reckon that probably, we were not able to discriminate mitochondrial degradation from mitochondrial biogenesis. However, when we studied mtDNA nucleoid clearance we found it to be very responsive to mitochondrial damage (Lazarou *et al.*, 2015). Long treatment with CCCP induced a reduction of 50% of the number of nucleoids per cell in control cells, while OPA1-deficient cells presented an invariable number of nucleoids throughout the 16h of treatment. We understand that the differences are due to the lack of mitophagy completion (Figure 78). It may be relevant to monitor mitophagy progression using mitochondrial-targeted proteins that change the fluorescence excitation range with pH acidification, for instance mt-Keima.

In parallel, we studied mito-autophagosome accumulation in skeletal muscles of mice treated with chloroquine (CQ). As a lysosomotropic agent, CQ prevents endosomal acidification, thus when comparing basal and CQ treated samples, the autophagic flux can be inferred. In this case, we obtained

mitochondrial enriched fraction from the quadriceps of loxP or OPA1 KO mice. On one side, CQ treatment of control animals resulted in the build-up of LC3-II in mitochondrial fraction due to the lack of degradation. On the other side, OPA1 KO animals presented higher levels of LC3-II in the mitochondrial fraction already in basal conditions., and CQ did not induce further accumulation of the autophagic marker which suggests that mitochondrial autophagy is blocked. Although we cannot determine whether there was a blockage of mitophagy completion in the moment of the assay, we determined that the mitochondrial fraction contained higher levels of LC3-II, the membrane bound form, which suggests that there is higher presence of mito-autophagosmes in the fraction (Sebastián *et al.*, 2016). Alternative approaches need to be performed to determine the extent of the alteration in mitophagy, because mitochondrial enriched fractions are obtained by sequential centrifugations and thus mitochondrial morphology differences could impact in the population obtained and thus affect the overall results. Nevertheless, electron microscopy examination of muscle section of control and OPA1 ablated muscles revealed accumulation of mitochondria engulfed in single or double membrane structures which resemble mito-autophagosomes, supporting the idea of normal mitophagy initiation and blockage of autophagy completion.

Autophagy was also impaired in cells and in tissues. Measurement of LC3-II in basal and CQ treated conditions revealed a defect in the build-up of LC3-II. Also, the presence of ragged red fibers was increased in OPA1-deficient muscles from 3 weeks of age. The levels of p62 presented the same profile. Immunoblot analysis of the protein levels of this autophagy cargo recognition receptor showed that it was increased 4 times, although there was a lot of variability. These data suggest that the alterations are affecting the autophagy machinery in general.

Further studies regarding when and how mtDNA is released from mitochondria should be performed not only to understand whether there is an active form of transport of this mtDNA, but also to understand if mtDNA has any control on the destination of the mito-autophagosome. In this regard, it remains unclear the nature of the mechanisms by which OPA1 deficiency causes alterations in late stages of mitophagy, as well as in autophagy. It has been described that the mitophagy receptor can

bind to OPA1 to induce disruption of inner mitochondrial cristae junction and release of pro-apoptotic factors (Landes *et al.*, 2010; Quinsay *et al.*, 2010). Hence, it is possible that OPA1 interacts with other factors of the mitophagy machinery throughout the mitophagy route to lysosomes. Therefore, it would be important to understand if this blockage of mitophagy completion is a consequence of general autophagy alterations, meaning that there are common players directly affected by OPA1 deficiency, or whether there are distinguishable defects for each pathway.

Confocal microscopy analysis revealed that mtDNA is enriched in vesicles positive for the vacuolar protein sorting-associated protein 4 (VPS4), a marker of multivesicular bodies (MVB) (Figure 78). The localization in early endosomes and lysosomes was discarded. As mitochondrial-derived vesicles (MDV) have been reported to deliver mitochondrial material to the lysosome, multivesicular body and peroxisome, thus we cannot discard them as a possible mechanisms, in spite of being described to bud from elongated mitochondria (Neuspiel *et al.*, 2008; Soubannier *et al.*, 2012; Mclelland *et al.*, 2014; McLelland *et al.*, 2016). Something very interesting derived from the localization studies is the type of staining detected for VPS4. This protein is an ATPase subunit of ESCRT-III complex, which is the responsible for the disassembly of the complex and closure once the intraluminal vesicle (ILV) is formed. It is mainly cytosolic, however in OPA1-deficient conditions appears accumulated in vesicular structures, and co-localizing with mtDNA.

Based on the pattern of alterations detected, we propose that in OPA1-deficient cells, mitochondria-containing autophagosomes are mainly diverted into the formation of amphisomes or amphisome-like organelles, which is linked to the activation of TLR9 (Figure 78). In this connection, further studies are required to address whether the re-routing of the mito-autophagosome to the endosomal pathway may be an active programmed cause-response mechanism or rather a consequence of the saturation of the lysosomal capacity due to the large amount of material to be degraded in an OPA1-deficient context. In this relation, the existence of communication mechanisms linking mitochondria and lysosomes and *vice versa* may be responsible for some of the alterations detected in OPA1-deficient cells (Raimundo *et al.*, 2016). On one hand, mitochondrial dysfunction has been reported to promote enhanced lysosomal

biogenesis in some conditions, and reduced lysosomal function (Baixauli *et al.*, 2015; Demers-Lamarche *et al.*, 2016; Fernández-Mosquera *et al.*, 2017). On the other hand, lysosomal defects have also been described to affect mitochondrial function. Besides the implications of failed degradation of damaged mitochondrial, lysosomal malfunction can lead to the increase of cytosolic calcium which in turn induces mitochondrial fragmentation via DRP1 phosphorylation and recruitment to mitochondria (Cereghetti *et al.*, 2008). Also, we cannot exclude the possibility that OPA1 deficiency causes the activation of TLR9 by mtDNA through the formation of mitochondrial-derived vesicles, in spite of being reported under conditions of mitochondrial elongation (Neuspiel *et al.*, 2008; Soubannier *et al.*, 2012; Mclelland *et al.*, 2014; McLelland *et al.*, 2016). It will be very informative to know the functional state of lysosomes, and in the case of dysfunction study whether restoration of lysosomal function is enough to resolve mitophagy and thus prevent undegraded mtDNA to trigger the pro-inflammatory response. Moreover, we reckon that it will be worth determining whether lysosomal impairment together with mtDNA instability induce a pro-inflammatory response similar to the one we report in OPA1-deficient cells. Furthermore, given that we have studied this process in the muscle context, it will be revealing to determine if it is a common mechanism for different cell types or it is preferentially active in certain cells, for instance the one relying on more mitophagy as a quality control system. In this regard, we need to answer whether we can achieve TLR9 activation by mitochondrial dysfunction in combination to mtDNA stress, which would mean that is something independent on OPA1. Now, another question is whether this could be replicated in other cell types or whether it is a mechanism specific of muscle cells.

The existence of TLR9 activation is mainly supported by the normalization of NF-kB target gene expression either when cells were treated with a TLR9 antagonist or in TLR9 KD conditions. The additional data that we have gathered include an enhanced expression under OPA1-deficient conditions, and co-localization with mtDNA. Because, more that 50% of mtDNA is localized in $TLR9^{+}$ vesicles, and neither mtDNA nor TLR9 are found in lysosomes in OPA1-deficient cells, we favor the view that TLR9 localizes in amphisome-like compartment, where it can interact with mtDNA leaking from mitochondria delivered by the mitophagy machinery. However, further work is required to precisely

assess the recruitment of TLR9 from the ER, its localization and whether it directly interacts to mtDNA. For instance, co-localization of TLR9 and ER markers by confocal microscopy, or prevention of NF-κB by ablation of the protein responsible for TLR9 trafficking from the ER to the endo-lysosomal pathway (UNC93B1). Also, it would be worth it to co-immunoprecipitate TLR9 and sequence the type of dsDNA that it is binding to directly identify mtDNA as the trigger signal.

In this PhD thesis we document that OPA1 is required for mtDNA stability, and mitochondrial quality control. As a result, we propose that OPA1 deficiency leads to presence of mtDNA and mitochondria in multivesicular bodies or amphisome-like organelles, and to the engagement of TLR9 resulting in the activation of NF-κB inflammatory program. This is the mechanism by which OPA1 deficiency triggers muscle inflammation, which eventually becomes systemic, and leads to altered GH-IGF-1 axis, and reduced growth. In parallel, inflammation induces FGF21 secretion from the muscle, which has an impact of hepatic metabolism (Figure 78). We propose that a deficient OPA1 activity may participate in the development of human inflammatory myopathies.

We think that given the data compiled in this study it is important to focus future studies in how mtDNA can be delivered to late endosomes, how essential is mitophagy and how opportunistic or deliberated is the re-routing. In other words, the main questions that need to be answer in future research include: 1) Is the cell capable to detect the amount of mitochondrial damage and thus trigger differential types of processing that might not always include total lysosomal degradation? 2) Is this something specific of mtDNA instability, or even specific of OPA1 deficiency? 3) Do mtDNA instability inducers generate a similar type of response? Does this response require mitophagy? 4) What happens when mitophagy is dysfunctional? These are relevant questions and will help to understand the pathologies linked to mitochondrial dysfunction and mtDNA stress. Furthermore, studies with different cell lines, screening for several types of mitochondrial dysfunction in combination with mtDNA instability with fit mitophagy machinery or ablation of key mitophagy/autophagy components could be very informative.

In this study I provide evidence for a link between OPA1 deficiency and the triggering of local muscle inflammation, which later on becomes systemic. From a translational perspective, it will be key to analyze whether specific OPA1-carrying ADOA patients show chronic inflammation even at a subclinical level or are more susceptible to inflammation in response to certain conditions. Similarly, it will be relevant to determine whether inflammatory myopathies are triggered at least in some patients as a consequence of a defective OPA1 function.

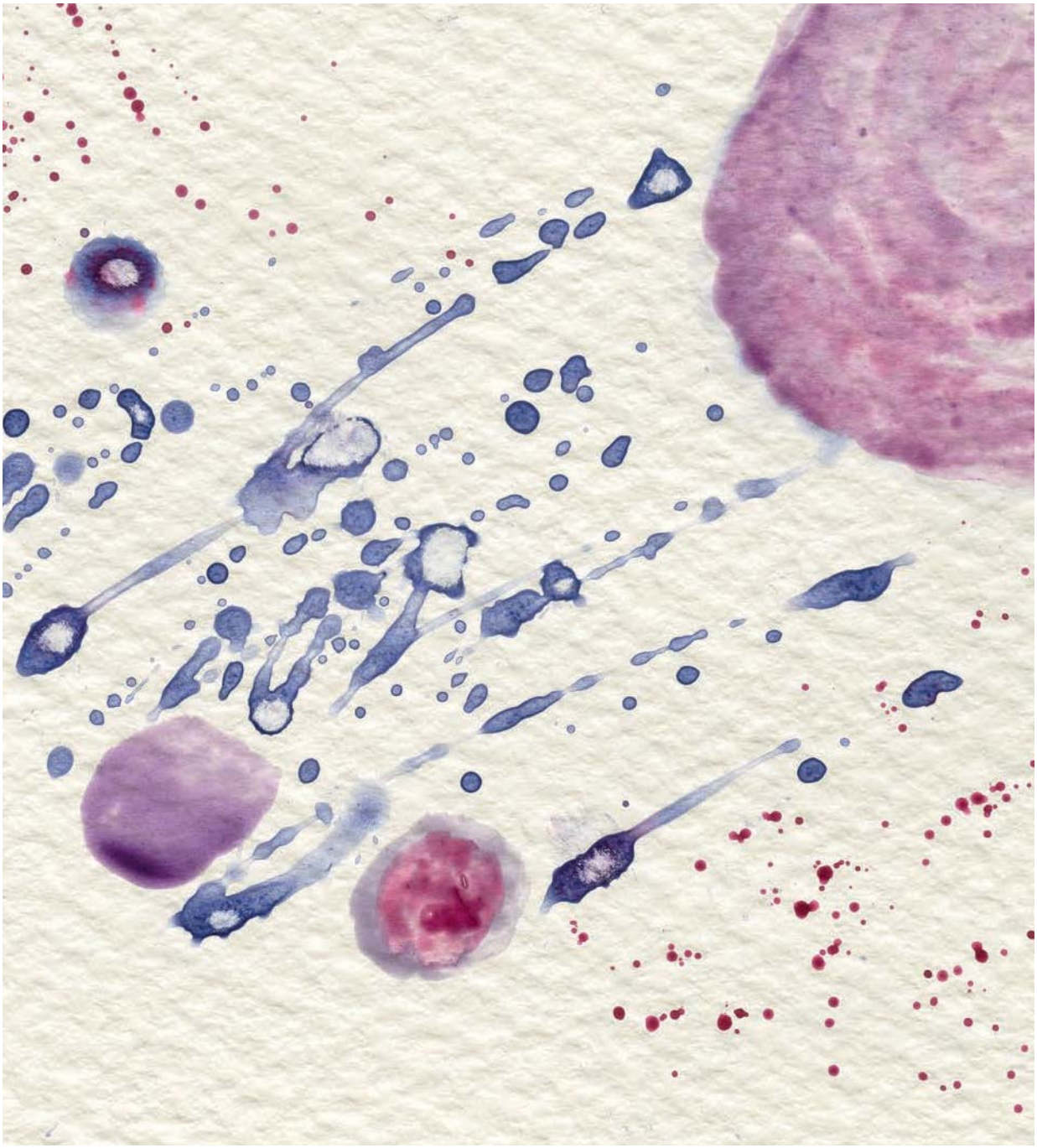

CONCLUSIONS

The data compiled in this study allow us to conclude:

1. Muscle OPA1 deficiency causes strong growth defects and reduced lifespan in mice. Those growth defects are independent of the muscle overexpression of FGF21 and enhanced plasma levels.

2. Muscle OPA1 ablation also causes local and systemic inflammation. The systemic inflammation is responsible for the body growth impairment seen in OPA1 knockout mice. This inflammation is local, cell autonomous and independent of cell death.

3. OPA1 deficiency results in mitochondrial dysfunction. In addition, OPA1-deficient muscle cells are characterized by reduced mtDNA copy number, and mtDNA stress.

4. In OPA1-deficient cells, mtDNA depletion cancels inflammation, which supports the idea that mtDNA is the trigger of the inflammatory response. This response is independent of cGAS and is characterized by impaired mitophagy completion in muscle cells.

5. Under OPA1-deficient conditions, TLR9 becomes activated and is responsible for the inflammatory response detected in muscle cells, which involves NF-κB activation and cytokine secretion.

6. We propose a model in which OPA1 deficiency causes the formation of amphisome-like organelles which allows the activation of TLR9, potentially leading to systemic inflammation.

MATERIALS AND METHODS

7.1. Materials

The materials used in the development of this thesis are included in the following tables, classified in four different categories: reagents, plasmids, antibodies and primers.

Table 1. Details of reagents used

Name	Working conditions	Application	Source
Antimycin A	For muscles: 2.5 µM For cells: 0.1 µM	Complex III inhibitor	Sigma-Aldrich
CCCP	30 µM	Loss of mitochondrial membrane potential	Sigma-Aldrich
Chloroquine	For mice: 50 mg/Kg For cells: 30 µM	Autophagy completion inhibitor	Sigma-Aldrich
Ethidium bromide	100nM	mtDNA depletion	Sigma-Aldrich
FCCP	1 µM	Loss of mitochondrial membrane potential	Sigma-Aldrich
Hoechst 33342	2.5 µg/mL	Nucleus staining	Thermo Fisher Scientific
Hygromycin	400 µg/mL	Stable cell line selection	Thermo Fisher Scientific
Mitotracker Deep Red	100 nM	Mitochondrial staining	Thermo Fisher Scientific
Oligomycin A	1.25 µM	Complex V inhibitor	Sigma-Aldrich
Puromycin	2.5 µg/mL	Stable cell line selection	Sigma-Aldrich
Rotenone	0.5 µM	Complex I inhibitor	Sigma-Aldrich
Salicylate	200mg/Kg	Anti-inflammatory drug	Sigma-Aldrich

Table 2. Plasmids for the production of lentiviruses carrying shRNA sequences.

Packaging vectors

Name	Vector	Bacterial Selection	Function
pMD2.G	Addgene: #12259	Ampicillin	VSV-G envelope expressing plasmid
psPAX2	Addgene: #12260	Ampicillin	2nd gen. lentiviral packaging plasmid
pLKO.1-hygro	Addgene: #24150	Ampicillin	Plasmid backbone with hygromicin resistance

pLKO.1 shRNA containing vectors, from MISSION library, Sigma-Aldrich

Target	Target sequence	Bacterial Selection	Mammalian Selection
Opa1	CCGACACAAAGGAAACTATTT	Ampicillin	Hygromycin
Opa1	CCGACACAAAGGAAACTATTT	Ampicillin	Puromycin
cGas	GATGCTGTCAAAGTTTAGGAA	Ampicillin	Puromycin
Pink1	GCGGTAATTGACTACAGCAAA	Ampicillin	Puromycin
Tlr9	CCGCCACTTCTATAACCAGAA	Ampicillin	Puromycin

Table 3. Antibodies used and details of usage.

PRIMARY ANTIBODIES

Target	Raised in	Working conditions	Cat. number	Source
ATP5A1 (CV)	Mouse	WB: 1/1000; 4 °C O/N	459240	Thermo Fisher Scientific
α-TUBULIN	Mouse	WB: 1/8000; 4 °C O/N or RT 1h	T5168	Sigma-Aldrich
CASPASE3	Rabbit	WB: 1/1000; 4 °C O/N	9661	Cell Signaling
COX IV (CIV)	Mouse	WB: 1/1000; 4 °C O/N	459600	Thermo Fisher Scientific
DRP1	Mouse	WB: 1/1000; 4 °C O/N	611738	BD Bioscience
DSDNA	Mouse	IF: 1/400MHC; 30min RT	ab27156	Abcam
EEA1	Rabbit	IF: 1/400; 30min RT	3288	Cell Signaling
GAPDH	Mouse	WB: 1/1000; 4 °C O/N	AM4300	Thermo Fisher Scientific
HSP60	Rabbit	WB: 1/1000; 4 °C O/N	4870	Cell Signaling
IL-1ß	Rabbit	WB: 1/1000; 4 °C O/N	ab9722	Abcam
LAMP1	Rat	IF: 1/400; 30min RT	sc-19992	Santa Cruz
LC3	Rabbit	WB: 1/1000; 4 °C O/N	2775	Cell Signaling
MFN1	Rabbit	WB: 1/1000; 4 °C O/N		kindly provided by Dr. Manuel Rojo
MFN2	Mouse	WB: 1/1000; 4 °C O/N	ab56889	Abcam
NDUFA9 (CI)	Mouse	WB: 1/1000; 4 °C O/N	459100	Thermo Fisher Scientific

OPA1	Mouse	WB: 1/1000; 4 °C O/N	612607	BD Bioscience
P62	Guinea Pig	WB: 1/1000; 4 °C O/N	GP62-C	Progen
PARP	Rabbit	WB: 1/1000; 4 °C O/N	9542	Cell Signaling
PORIN	Mouse	WB: 1/1000; 4 °C O/N	ab14734	Abcam
P-STAT5	Rabbit	WB: 1/1000; 4 °C O/N	4322	Cell Signaling
SDHA (CII)	Mouse	WB: 1/1000; 4 °C O/N	459200	Thermo Fisher Scientific
STAT5	Rabbit	WB: 1/1000; 4 °C O/N	94205	Cell Signaling
TFAM	Rabbit	WB: 1/1000; 4 °C O/N	ab131607	Abcam
TIM44	Mouse	WB: 1/1000; 4 °C O/N	t14720	BD Bioscience
TLR9	Rabbit	WB: 1/1000; 4 °C O/N IF: 1/800; 30min RT	76680	Novus
TOM20	Rabbit	WB: 1/1000; 4 °C O/N IF: 1/400; 30min RT	sc-11415	Santa Cruz
UQCRC2 (CIII)	Mouse	WB: 1/1000; 4 °C O/N	459140	Thermo Fisher Scientific
VPS4	Rabbit	IF: 1/400; 30min RT	SAB4200025	Sigma-Aldrich

SECONDARY ANTIBODIES

Target	Conjugated	Working conditions	Cat. number	Source
Mouse	HRP	WB: 1/10,000; 1h RT	715-035-150	Jackson Immuno Research
Mouse	Alexa-488	IF: 1/800; 30min RT	A11029	Thermo Fisher Scientific
Mouse	Alexa 568	IF: 1/800; 30min RT	A11004	Thermo Fisher Scientific
Mouse	Alexa-647	IF: 1/800; 30min RT	A31571	Thermo Fisher Scientific
Rabbit	HRP	WB: 1/10,000; 1h RT	711-035-152	Jackson Immuno Research
Rabbit	Alexa-488	IF: 1/800; 30min RT	A11034	Thermo Fisher Scientific
Rabbit	Alexa 568	IF: 1/800; 30min RT	A11036	Thermo Fisher Scientific
Rabbit	Alexa-647	IF: 1/800; 30min RT	A21443	Thermo Fisher Scientific
Rat	HRP	WB: 1/10,000; 1h RT	712-035-153	Jackson Immuno Research
Rat	Alexa-647	IF: 1/800; 30min RT	A21247	Thermo Fisher Scientific
Guinea Pig	HRP	WB: 1/10,000; 1h RT	sc-2438	Santa Cruz

Table 4. Primers used in these thesis

Real time PCR Sybr Green primers

Symbol	Forward	Reverse
Aim2	GGAGGTCACCAGTTCCTCAG	TTGTTTTGCTTGGGTTTCC
Arp	GAGCCAGCGAAGCCACACT	GATCAGCCCGAAGGAGAAGG
Asc	GAAGCTGCTGACAGTGCAAC	GCCACAGCTCCAGA CTCTTC
Actin	GGTCATCACTATTGGCAACGA	GTCAGCAATGCCTGG
Fos	ACCAGTGTCTACCCCTGGAC	GCTGGGGAATGGTAGTAGGA
Cd68	CCAATTCAGGGT GGAAGAAA	CTCGGGCTCTGATGTAGGTC
CGas	GGAAGTCCCCAGGATTGAGC	TGACTCAGCGGATTTCCTCG
Cox7a1	GCTCTGGTCCGGTCTTTTAGC	GTACTGGGAGGTCATTGTCGG
Fgf21	ATGGAATGG ATGAGATCTAGAGTTGG	TCTTGGTGGTCATCTGTGTAGAGG
G6p	TCCTGGGACAGACACACAAG	CAACTTTAATATACGCTATTGG
Hmgb1	CGCGGAGGAAAATCAACTAA	TCATAACGAGCCTTGTCAGC
Ifit1	CTGAGATGTCACTTCACATGGAA	GTGCATCCCCAATGGGTTCT
Ifnb	CCCTATGGAGATGACGGAGA	CCCAGTGCTGGAGAAATTGT
Igf-1	TGTGCTGCATCGCTGCTTAC	ACTCTTCCACGATGCCACG
Il-6	GCCCACCAAGAACGATAGTCA	CAAGAAGGCAACTGGATGGAA
Irf7	CAATTCAGGGGATCCAGTTG	AGCATTGCTGAGGCTCACTT
Isg15	GGTGTCCGTGACTAACTCCAT	TGGAAAGGGTAAGACCGTCCT
Mcad	TCGGTGAAGGAGCAGGTTTCAAGA	AAACTCCTTGGTGCTCCACTAGCA
Myd88	GAAACTCCACAGGCGAGCGTA	GTTAAGCGCGAC CAAGGGTATG
Nlrp3	CGAGACCTCTGGGAAAAAGCT	CATACCATAGAGGAATGTGATGTACA
Pepck	GTGCTGGAGTGGATGTTCGG	CTGGCTGATTCTCTGTTTCAGG
Pgc-1a	AGCCGTGACCACTGACAACGAG	GCTGCATGGTTCTGAGTGCTAAG
Pink1	TTCTTCCGCCAGTCGGTAG	CTGCTTCTCCTCGATCAGCC
Rage	GAAGGCTCTGTGGGTGAGTC	CCGCTTCCTCTGACTGATTC
S100a8	GGAAATCACCATGCCCTCTACA	GTCACTATTGATGTCCAATTCTCTGAA
S100a9	TGAGCAAGAAGGAATTCAGACAAA	TGTGTCCAGGTCCTCCATGA
Stat	CGCGCATGCAACTGGCATATAACT	ATGCTTCCGTTCCCACGTAGACTT
Tlr2	TGCTTTCCTGCTGGAGATTT	TGTAACGCAACAGCTTCAGG
Tlr4	ACCTGGCTGGTTTACACGTC	CTGCCAGAGACATTGCAGAA
Tlr9	CTCCATCTCCCAACATGGTTCT	GCCAGCACTGCAGCCTGTA
Tnfa	CACAAGATGCTGGGACAGTGA	TCCTTGATGGTGGTGCATGA
Usp18	AGAGTTAGCAAGCTCCGACAT	TGAGGTGAATGGTCAAGGTTTG
Vlcad	CGTCAGAGGTGTACTTTGATGG	CATGGACTCAGTCACATACTGC

mtDNA copy number assessment primers

Symbol	Forward	Reverse
mtDNA16S	CACTGCCTGCCCAGTGA	ATACCGCGGCCGTTAAA
mtDNACox2	CTACAAGACGCCACAT	GAGAGGGGAGAGCAAT
mtDNACytB	GCTTTCCACTTCATCTTACCATTTA	TGTTGGGTTGTTTGATCCTG
mtDNADloop1	AATCTACCATCCTCCGTGAAACC	TCAGTTTAGCTACCCCCAAGTTTAA
mtDNADloop2	CCCTTCCCCATTTGGTCT	TGGTTTCACGGAGGATGG
mtDNADloop3	TCCTCCGTGAAACCAACAA	AGCGAGAAGAGGGGCATT
mtDNAND4	AACGGATCCACAGCCGTA	AGTCCTCGGGCCATGATT
nucDNATert	CTAGCTCATGTGTCAAGACCCTCTT	GCCAGCACGTTTCTCTCGTT

Genotyping PCR primers

Symbol	Forward	Reverse
Cre	CGGTCGATGCAACGAGTGATGAGG	CCAGAGACGGAAATCCATCGCTCG
Opa1 floxed	ATTGTCTGATGGCAGTGGTG	TTCTGTGCACACTGGTGTCC
Fgf21	AGGAGGCTAGGGCTTGACTCT	TGACAGGGTCTCAGGTTCAA GCAGCGCATCGCCTTCTATC

7.2. Methods

7.2.1. Animal studies

7.2.1.1. Animal care

All animal experiments were done in compliance with the guidelines established by the Committee on Animal Care of the University of Barcelona. Mice were kept under a 12-h dark-light period and provided with a standard chow-diet and water *ad libitum.*

7.2.1.2. Generation of animal model

Opa1$^{loxP/loxP}$ mice were generated using embryonic stem (ES) cells derived from the trans-NIH Knock-Out Mouse Project (KOMP) and obtained from the KOMP Repository. C57BL/6N-*Opa1*tm1a(KOMP)Wtsi, Clone EPD0151-4-B11 was used to generate the gene-targeted mice. The Myo-Cre *Opa1* mouse line was generated by crossing homozygous *Opa1* $^{loxP/loxP}$ mice with a strain expressing Cre recombinase under the control myogenin promoter and the 1-kb mouse MEF2C enhancer, thus yielding a transgene called Myo-Cre (Li *et al.*, 2005). Myogenin is first expressed at day E8.5 of the embryonic development in mice. Mice were in a C57BL/6J pure genetic background. Cre *Opa1*$^{loxP/loxP}$ littermates were used as controls for KO animals. 8- to 10-week-old loxP and KO mice were used in all experiments, unless indicated.

Postnatal deletion of *Opa1* was achieved by crossing *Opa1*$^{loxP/loxP}$ strain with a strain of mice carrying Cre-ER under de control of Human Skeletal Actin (HSA) promoter (HSA-Cre-ER- *Opa1*$^{loxP/loxP}$/BL6). Tamoxifen-induced *Opa1* deletion was accomplished by oral administration of tamoxifen-containing chow (Tam400/Cre ER Harlan), ad libitum for 5 weeks. Cre-negative littermates, also receiving tamoxifen treatment, were used as controls.

Opa1$^{loxP/loxP}$ mice were crossed with Fgf21 total KO mice (B6N;129S5-Fgf21^{tm1Lex}/Mmcd) to obtain *Opa1*$^{loxP/loxP}$ Fgf21$^{-/-}$ animals. These were then crossed with the transgene Myo-Cre to generate FGF21 total KO animals with OPA1 depleted in skeletal muscle, hereafter double KO (DKO).

Animal genotype was assessed by PCR amplification of specific genomic fragments following the protocol detailed below:

1. Mouse tail tips (1-2mm) are obtained at weaning and kept at -20 °C until processing.
2. Digest tail tips O/N at 55 °C and 450 rpm shaking, in 500 µl of Lysis Buffer (5mM EDTA; 200mM NaCl; 0.2 % SDS; 100mM Tris-HCl (pH8.5)) + 10 µl of Proteinase K.
3. Inactivate Proteinase K by 2 min 80 °C and cool down on ice.
4. Spin at 18,000g for 15 min at RT
5. Transfer supernatant to new eppendorf tubes containing 500 µl isopropanol.
6. Shake by inversion 10 times.
7. Spin at 14,000 x g for 10 min at RT
8. Discard supernatant
9. Wash pellet with 500 µl of EtOH 70 %
10. Spin at 14,000 x g for 5 min at RT
11. Discard supernatant and let pellets dry capsized for 1h
12. Before PCR, DNA is resuspended in 500 µL of water and heated for 2 min at 65 °C
13. PCR master mix is prepared for the total number of samples of the run. Primers used are detailed in Table 4**.**
14. For each sample the mix contains: 18.8 µl H2O, 2.5 µl 10xBuffer, 0.5 µl dNTPs (10 mM each), 0.5 µl of each primer at 10 µM (Table 4), 0.125 µl DNA Pol (Biotools 5U/ µl ref. 10043) and 1.5 µl DNA.
15. The PCR program is: 4 min at 95 °C, 35 cycles of (30s 95 °C, 30s 60 °C and 3min 72 °C), 10 min 72 °C and kept at 4 °C.
16. Resolve PCR products in an agarose gel and document the resulted bands using a trans-illuminator.

The PCR products identify the different genotypes. Regarding *Opa1*: *Opa1* $^{-/-}$ resulted in a band of 800bp, Opa1 $^{loxP/loxP}$ resulted in a band of 1100bp, thus hemizygous mice showed 2 bands: 800bp and 1100bp. Regarding the Cre recombinase, the PCR assessed presence or absence of Cre, since the insertion is random and subject to recombination throughout generation: Cre negative 0bp; Cre positive 600bp.

Finally, Fgf21 total KO was assessed by the use of three primers that can result in two different PCR products depending on the scission of Fgf21. Thus, Fgf21 wild type resulted in a 620 bp band, while Fgf21 KO resulted in a 202 bp band.

7.2.1.3. Mice treatment

Sodium salicylate was administered daily by intraperitoneal injection for 30 days. Sodium salicylate (Sigma-Aldrich) was prepared at a concentration of 40 mg/mL and the daily dose was 200 mg/Kg, thus the volume injected daily was 50 µL/mg of body weight. Neither sodium salicylate nor vehicle (PBS) alone produced any apparent damage or stress response. Six mice per group were subjected to treatment.

Autophagy flux was assessed in 3 weeks old mice by chloroquine (Sigma) treatment of loxP and OPA1 KO mice. Chloroquine was administered via intraperitoneal injection twice a day during 5 days at a concentration of 50 mg/Kg. Chloroquine (Sigma-Aldrich) was prepared at a concentration of 5 mg/mL and every injection volume was of 10 µL/mg of body weight.

7.2.1.4. In vivo gene transfer

For electro-transfer studies, pDsRed2-Mito (Clontech) vectors were purified with a plasmid kit (EndoFree; Qiagen) and dissolved in 0.9 % NaCl. Seven-week-old mice (OPA1$^{loxP/loxP}$ and KO) were used for pDsRed2-Mito vector expression. Mice were anesthetized with ketamine/xylazine, and 1 h before electrotransfer muscles were pretreated with hyaluronidase (10 U per muscle) (Kherif et al, 1999; Kuznetsov et al, 2008). Afterwards, the left tibialis anterior was injected with the empty vector, while pDsRed2-Mito was injected in the right muscle. We established that the optimal amount of plasmid to inject to achieve acceptable protein expression was 60 µg and 100 µg DNA in the former and latter, respectively. Ten pulses of 20 ms each were applied to each hind limb at 175 V/cm and 1 Hz using an electroporator (ECM 830; BTX). Experiments were performed 8 days after electro-transfer of pDsRed2-Mito vector.

7.2.1.5. Fluorescence microscopy in muscle sections

Tibialis anterior muscles were removed and fixed in PFA 4 % (Santa Cruz) and left to rotate for 1 h and 30 min at 4 °C. After being passed through a sucrose gradient from 10 % to 30 %, muscles were embedded in OCT solution (TissueTek), immediately frozen in liquid nitrogen-cooled isopenthane (Sigma), and stored at -80 °C. 10-µm cryosections of tibialis anterior muscle transfected with DsRed2-Mito vector, which specifically labels mitochondria, were analyzed using a Leica TCS SP2 AOBS Systems confocal scanning microscope. Images were quantified using Trainable Weka Segmentation plugin from ImageJ.

7.2.1.6. Histological analysis

For light microscopy, muscles were removed, embedded in OCT solution (TissueTek), immediately frozen in liquid nitrogen-cooled isopenthane (Sigma), and stored at -80 °C. 10-µm cryosections of tibialis anterior, diaphragm, gastrocnemius and quadriceps muscles were used. Cryosections were stained with haematoxylin and eosin, Gomori's Modified Trichrome Stain. Cross-Sectional Area (CSA) was quantified using Image J software. Immunohistochemistry was performed with the indicated antibodies and labeling with the Vectastain ABC kit (Vector Laboratories), following the manufacturer's instructions.

7.2.1.7. Respiration measurements in muscle

The respiration of permeabilized muscle was measured at 37 °C by high resolution respirometry with an Oxygraph-2k (Oroboros Instruments), as described (Kuznetsov *et al*, 2008). Mice were anesthetized with ketamine/xylazine, and the tibialis muscle was removed and placed on a plastic Petri dish containing 1 mL of ice-cold isolation solution [10 mM Ca-EGTA buffer (2.77 mM of CaK_2EGTA + 7.23 mM of K_2EGTA), 20 mM imidazole, 20 mM taurine, 50 mM K-MES, 3 mM K_2HPO_4, 6.5 mM $MgCl_2$, 5.7 mM ATP, 15 mM phosphocreatine, and 0.5 mM DTT (pH 7.1)]. Individual fiber bundles were separated with two pairs of sharp forceps and then permeabilized for 30 min in 2 mL of ice-cold isolation solution containing 50 µg/mL saponin. After rinsing muscle bundles in respiration medium [0.5 mM EGTA, 3 mM $MgCl_2 \cdot 6H_2O$, 20 mM taurine, 10 mM KH_2PO_4 20 mM Hepes, 1 g/L BSA, 60 mM K-lactobionate, and 110 mM sucrose

(pH 7.1)], we weighed and transferred them (typically 2–4 mg wet weight) into the Oxygraph chamber containing 2 mL of air-saturated respiration medium. All respiration measurements were made in triplicate and using the following protocol: resting respiration (state 2, absence of adenylates) was assessed by the addition of 10 mM glutamate and 2 mM malate as the complex I substrate supply, and then state 3 respiration was assessed by the addition of 2.5 mM ADP. The integrity of the outer mitochondrial membrane was established by the addition of 10 µM cytochrome c; no stimulation of respiration was observed. The addition of 10 mM succinate provided state 3 respiration with parallel electron input to complexes I and II. We examined ADP control of coupled respiration and uncoupling control through the addition of the protonophore carbonylcyanide-4-(trifluoromethoxy)-phenylhydrazone (FCCP) (optimum concentration for maximal flux). The addition of 0.5 µM rotenone inhibited complex I, thereby allowing examination of O_2 flux with the complex II substrate alone, whereas 2.5 µM antimycin A was added to inhibit complex III in order to observe non-mitochondrial respiration. The concentrations of substrates and inhibitors used were based on prior experiments conducted to optimize the titration protocols.

7.2.1.8. Transmission electron microscopy

Right after euthanasia, quadriceps muscles were dissected and cut into pieces of about 1 mm^3. Then the pieces of interest were transferred to glass vials filled with 2 % paraformaldehyde and 2.5 % glutaraldehyde in phosphate buffer. They were kept in the fixative for 24 h at 4 °C. They were then washed with the same buffer and post-fixed with 1% osmium tetroxide in the same buffer containing 0.8% potassium ferricyanide at 4 °C. The samples were then dehydrated in acetone, infiltrated with Epon resin for 2 days, embedded in the same resin orientated for longitudinal sectioning, and polymerized at 60 °C for 48 h. Semi-thin sections were made in order to corroborate that the orientation was satisfactory under the light microscope. Ultrathin sections were obtained using a Leica Ultracut UC6 ultramicrotome (Leica Microsystems, Vienna, Austria) and mounted on Formvar-coated copper grids. They were stained with 2 % uranyl acetate in water and lead citrate. Sections were then observed under

a JEM-1010 electron microscope (Jeol, Japan) equipped with a CCD camera SIS Megaview III and the AnalySIS software.

7.2.2. Cell culture protocols

7.2.2.1. Cell Maintenance

The present work used C2C12 myoblasts a cellular model. Cells were obtained from ATCC CRL-1772™. HEK293T were also used as lentiviral producing cells, these cells were provided by Dr Daniel Bach and Dr Didier Trono from EPH Lausana. Cells were grown in DMEM (Invitrogen) with 10 % FBS and 100 U/ml of penicillin/streptomycin (Invitrogen) at 37 °C in a humidified atmosphere of 5 % CO_2/95 % O_2. OPA1-deficient cells were grown in the presence of 50 µg/ml uridine until 24h before experimental analysis, to support DNA replication independent of pyrimidine nucleotides *de novo* synthesis. Once every two weeks mycoplasma detection test was performed to ensure no contamination of the cells. In our case, when mycoplasma was detected the cells were discarded, instead of decontaminated with Plasmocin (Invivogen).

Maintenance of the different cell lines generated required regular split of the proliferating cells. Three times a week cells were split: medium was aspirated from the 75 cm^2 flasks and 10 mL PBS was added to wash the remaining media from the cells. Then, 2mL of trypsin was added and incubated for 5min at 37 °C. Trypsin was inactivated by the addition of 8mL of compete media to the flask. 10mL of cells in suspension was retrieved and the appropriate dilution was done (usually 1:3 to 1:10). In the case that a specific number of cells needed to be plated, cells were counted using Nuebauer chamber. Trypan Blue was used in a 1:1 dilution of the cell suspension to ensure the counting of only alive unstained cells.

7.2.2.2. Freeze and Thaw cell aliquots

Cellular stocks were kept at liquid nitrogen. Cell Freezing was performed by centrifugation of trypsinized cell suspension at 500 x g for 5 min and resuspension in freezing media (10% DMSO in FBS). Cells in freezing media were distributed in cryovials (2-3 million cells in 1 mL per cryovial) and placed in

stratacooler at -80 °C to achieve slow freezing. After 24 h cells cryovials can be stored at -80 °C in boxes, and after 3-5 days those can be moved into liquid nitrogen tanks. To thaw cell aliquots, cryovials are rapidly transferred from -80 °C to 37 °C water-bath to ensure rapid thawing. Cells in freezing media containing toxic DMSO are mixed in 5mL of complete media. To remove freezing media cells are spun at 600 x g for 5 min and resupended in complete media and plated in the appropriate container.

7.2.2.3. Cell treatments

C2C12 cells were treated with 10 µM staurosporine (Sigma) for 4 h to obtain an apoptosis-positive control. C2C12 mtDNA depletion was achieved by treatment with 100 nM ethidium bromide (Sigma) for 14 days. For mitophagy assessment 30 µM CCCP was used to induce mitochondrial damage at the indicated times. C2C12 cells were treated with chloroquine (CQ) at 30 µM to analyze autophagic markers accumulation at the indicated times.

7.2.2.4. C2C12 stable Knock-down generation

Short hairpin RNA (shRNA) encoding sequences were delivered to C2C12 myoblasts using lentiviral infection (Muñoz and Zorzano, 2015). Thus, the stable expression of shRNA against *Opa1* mRNA generated stable OPA1 knock-down cells (KD). C2C12 stably expressing scramble shRNA (Scr) were used in parallel in all the experiments. All the work involving lentiviral viruses was performed in a cell culture room with a biosafety level of 2 and a hood with biosafety category IIA. Lentiviruses were produced by transfection of second-generation lentiviral packing plasmids and pLKO.1 (shRNA stable expression and antibiotic selection, Sigma) into a human embryonic kidney cell line (HEK 293T), using the following protocol:

1. Day 0: 24 h before transfection, 3 million HEK293T cells are plated in a petri dish of 100 mm of diameter (p10), to achieve 70 % confluence at the moment of transfection.
2. Day 1: Mix plasmids in 1560 µL of filtered 150 mM NaCl: 5 µg of pMD2.g + 5 µg of PAX2 + 10 µg of de specific pLKO.1 (Table 2), and let the mixture equilibrate for 5 min.
3. Add 78 µL of PEI (1 mg/mL pH=7, filtered with 0,2 mm filter) to the mixture.

4. Incubate 20 min at RT to allow for the formation of DNA-PEI complexes.
5. Add the transfection mixture gently to the media of HEK293T cells.
6. After 6-8 h, change transfection media for fresh complete media
7. Place transfected cells in a 33 °C incubator to improve viral particle stability.

Lentiviral production was allowed for 48 h after transfection was performed. 24 h post transfection (Day 3) target cells, C2C12 myoblasts were plated: 200,000 cells in p10 dishes, one extra p10 was plated and not transfected, as a control. Two subsequent transfections were performed, at day 4 and day 5, following the next protocol:

1. Retrieve media containing the viral particles from HEK293T dishes
2. Filter media using a 0.45 µm filter.
3. Add polybrene to a final concentration of 2.5 µg/mL to enhance viral infection.
4. Add filtered media to target cells, C2C12 myoblasts.
5. 24 h - 48h after the second infection (Day 6-7), split cells and add the selection antibiotic to the media of the cells: 2.5 µg/mL puromycin (Sigma) or 400 µg/mL hygromycin (Thermo Fisher Scientific)

7.2.2.5. C2C12 stable double Knock-down generation

In order to generate stable double knock-down cell lines, the same protocol described above was used to infect with a pLKO.1-hygro (shRNA stable expression and hygromycin selection) for *Opa1* and for Scr, and then cells were selected with 400 µg/mL hygromycin (Thermo Fisher Scientific). Before continuing with the second infection, cells were amplified and cellular stocks were frozen. The second lentiviral infection was performed on Scr or OPA1 KD hygromycin resistant cells with pLKO.1-puro for different targets or Scr, and selected with puromycin, thus generating 4 groups: Scr/Scr, Scr/second target, OPA1/Scr, OPA1/second target (plasmids specified in Table 2). Double infected cells were grown in complete media supplemented with 2.5 µg/mL puromycin and 400 µg/mL hygromycin.

7.2.2.6. Luciferase reporter assay

C2C12 myoblasts were transfected with 0.9 µg of a plasmid encoding for p3xκB as a luciferase NF-κB transcriptional activity reporter, previously used in Espinosa et al. (Espinosa et al, 2002), and 0.1 µg CMV-Renilla, using Metafectin (Bio-Rad) and following the manufacturer´s instructions. Luciferase activity was determined with the Dual-GLO Luciferase Reporter Assay System (Promega) in a luminometer Lumat LB 9507 (Berthold Technologies).

7.2.2.7. Oxygen consumption measurements in C2C12 myoblasts

C2C12 myoblasts (Scr or OPA1 KD) were plated on SeaHorse Bioscience XF24 plates. After 48 h, oxygen consumption was measured using a Seahorse Bioscience XF24 extracellular flux analyzer. The instrument was calibrated the day before the experiment following the manufacturer's instructions. On the day of the experiment, the injection ports on the sensor cartridge were loaded with 1.25 µM oligomycin (complex V inhibitor) to distinguish the percentage of oxygen consumption devoted to ATP synthesis and the percentage required to overcome the natural proton leak across the inner mitochondrial membrane. We used 1 µM FCCP to calculate the "spare" respiratory capacity of cells, which is defined as the quantitative difference between maximal uncontrolled OCR and the initial basal OCR, and 0.1 µM rotenone (complex I inhibitor) and 0.1 µM antimycin A (complex III inhibitor) to calculate the remaining respiration caused by oxidative side reactions. During the sensor calibration, cells were kept in a 37 °C incubator without CO_2 in 700 µl of respiration buffer (DMEM, 5 mM glucose, 2 mM glutamine, 31.6 mM NaCl and Phenol Red). Plates were immediately placed in a calibrated Seahorse XF24 flux analyzer for mitochondrial bioenergetics analysis. Extracellular acidification rate of C2C12 cells (ECAR) was measured in parallel.

7.2.2.8. ATP content

ATP cellular content was measured using the ATP Determination Kit (Molecular Probes), following the manufacturer's instructions. Briefly, ATP is determined by luciferase activity due to is requirement of

ATP to produce light (emission maximum ~560 nm at pH 7.8) from the reaction. A standard curve is obtained and ATP content in samples is calculated by interpolation.

7.2.2.9. Immunofluorescence

Cells were plated on 12mm diameter coverslips in 24-well plates, 15,000 cells/well, to obtain a 50-70 % confluence upon fixation the next day. Mitotracker deep red (Thermo Fisher Scientific) loading to mitochondria was performed in live cells by incubation during 30 min with the probe at 100 nM in complete medium, then cells were washed for 10min in complete medium before fixation. Cells were fixed in 4 % paraformaldehyde (PFA) in PBS for 20 min and washed with 50 mM NH_4Cl. Immunofluorescence was performed as follows:

1. In the cases when dsDNA is the target of the immunofluorescence cells are permeabilized in buffer A (0.1 % Triton X-100, 3 % FBS in PBS) for 30 min. Alternatively, when dsDNA is not immunolabeled, in order to avoid the extraction of membrane proteins from membranes as a result of Triton X-100 action, this step with buffer A is skipped.
2. Incubate coverslips in plate for 10 min in approximately 200 µl of buffer B (0.05 % Saponin, 2 % FBS in PBS), which allow moderate permeabilization and blocking of the fixed cells.
3. Dilute all primary antibodies in buffer B (dilutions specified in Table 3) and distribute 35-40 µl drops on a flat parafilm piece.
4. Place coverslips cell-face down on primary antibody drops and incubate in a dark wet chamber for 30 min.
5. Return coverslips to plate and wash three times for 10 min with buffer B.
6. Dilute all secondary antibodies in buffer B (dilutions specified in Table 3) and distribute 35-40 µl drops on a flat parafilm piece.
7. Place coverslips cell-face down on secondary antibody drops and incubate in a dark wet chamber for 30 min.
8. Return covereslips to plate and wash three times for 10 min with buffer B.

9. Wash coverslips in plate twice for 10 min with PBS.
10. Dilute Hoechst 33342 1:7,000 in PBS and distribute 35-40 µl drops on a flat parafilm piece.
11. Place coverslips cell-face down on Hoechst drops and incubate in a dark wet chamber for 10 min.
12. Return coverslips to plate and washed twice with PBS.
13. Mount coverslips onto microscope slides using Flouromount (Sigma).
14. Let slides dry O/N at RT and then keep them in microscopy slides boxes at 4 °C

Importantly, secondary antibodies must not recognize each other. We detected that our anti-mouse antibody conjugated to alexa-568 (anti-mouse) was binding LAMP1 antibody raised in rat. To avoid cross-recognition, we examined different conditions to restrict the affinity of anti-mouse to rat IgG. First, we incubated the secondary antibodies in two steps: first anti-rat and anti-rabbit secondary antibodies and then anti-mouse secondary antibody, with the aim of covering the rat IgG. However, since the washes were doubled, the signals of rabbit- and rat-raised antibodies were weak. Thus, we chose to incubated the secondary antibodies together in a more stringent environment. We decreased the concentration of anti-mouse antibody from 1:800 to 1:1,600 and increased the concentration of FBS from 2 % to 4 % as the blocking agent to reduce unspecific binding.

Confocal images were obtained using a Zeiss LSM 780 with a PlanAchromat 63x oil objective lens with 1.40 NA, a pinhole diameter of 1 airy unit and a pixel size as small as 100 nm to meet Nyquist sampling criterion (to preserve the spatial resolution in the given image). Z-stacks were acquired with the optimal step. Zooms shown in figures were obtained in the microscope. Image processing and quantification were performed using ImageJ software.

7.2.2.10. Mitochondrial fusion assays

One µg of mtPA-GFP was transfected into C2C12 myoblasts (Scr or OPA1 KD) using Lipofectamine® 2000 (Lovy et al, 2012). Experiments were performed 48 h after transfection and the protocol was followed as described previously. This was performed in collaboration with Dr Eduard Noguera during his stay at Dr Shirihai laboratory in Boston University Medical Center (Noguera, 2014).

7.2.2.11. Mitophagy-autophagy assessment

To analyze mitophagy initiation Scr and OPA1 KD C2C12 cells were treated with 30 µM CCCP (Sigma) for 30min and LC3-II levels in mitochondrial enriched fraction were determined. Optimization experiments determined that 30 min of 30 µM CCCP was the appropriate time for the maximal recruitment of LC3-II to mitochondrial enriched fraction in control C2C12 myoblasts.

To analyze mitophagy resolution, cells were treated with 30 µM CCCP for 9 and 16h. Then, together with control untreated cells, were fixed and immunostained for dsDNA and Hoechst. MtDNA nucleoid number were quantified using ImageJ software and a macro for automated quantification using a macro designed by Anna Lladó from the Advanced Digital Microcopy core facility at IRB Barcelona. Briefly, the macro delimitates the cell area using the transmitted light image, it counts the number of cells per image using complete nucleus staining (Hoechst). At this point there is a verification step were the user can refine the area of the cells. The quantification of nucleoids will be performed in the area resulting from the subtraction of the cell area and the nuclear area. Nucleoids are quantified using the function “find maxima” which allows for the discrimination of nucleoids located very close to each other. Using this macro three independent experiments were performed, in which 20 images obtained randomly were quantified per condition.

In experiments of nucleoid characterization this was combined with the quantification of the area per nucleoid, which was obtained arithmetically by the division of total fluorescence area of the cytoplasm above a pre-set threshold divided by the number of nucleoids. Therefore, the resulting area is an average of the area of the nucleoids in the cells. Using this macro three independent experiments were performed, in which 20 images obtained randomly were quantified per condition.

7.2.3. General molecular biology protocols

7.2.3.1. Mitochondrial enriched fraction from skeletal muscle

Mitochondrial enriched fractions were obtained from quadriceps muscle using the following protocol:

1. Cut frozen muscles to obtain a 10 mg sample, on dry ice to avoid any thawing.
2. Place muscle slices in tubes containing 300 µL of solubilization buffer (0.1M KCl, 5mM $MgCl_2$, 5mM EGTA, 1 mM sodium ortovanadate, 50 mM NaF, 5 mM sodium pyrophosphate and protease inhibitors cocktail tablet; pH=7.4), and keep tube on ice.
3. Mince muscle tissue inside the tube using dissection scissors.
4. Short spin tubes were shortly spin to pellet the tissue pieces.
5. Change solubilization buffer for new one.
6. Incubate for 10 min in solubilization buffer.
7. Shortly spin tubes to pellet the tissue pieces and discard solubilization buffer.
8. Add 300 µL of Homogenization buffer (250mM sucrose, 50mM KCL, 5mM EDTA, 5mM $MgCl_2$, 1 mM sodium ortovanadate, 50 mM NaF, 5 mM sodium pyrophosphate and protease inhibitors cocktail tablet; pH= 7.4) to the fragmented tissue.
9. Transfer the tube content to a 2 cm^2 glass tube compatible with a potter pestle.
10. Homogenize the tissue by 20 up and down with the pestle rotating at 1,800rpm.
11. Transfer homogenate to a new tube using a glass pasteur.
12. Spin 10,000 x g for 15 min at 4 °C to obtain the maximum amount of mitochondrial content.
13. Keep the supernatant as mitochondria-free fraction.
14. Resuspend in 300 µL of Homogenization buffer.
15. Spin 10,000 x g for 15 min at 4 °C to obtain the maximum amount of mitochondrial content.
16. Discard supernatant.

17. Resuspend in 150 µL of Ripa buffer (50 mM Tris pH 8, 150 mM NaCl, 1% NP-40, 0.1% SDS, 1 mM EDTA, 1 mM sodium ortovanadate, 50 mM NaF, 5 mM sodium pyrophosphate and protease inhibitors cocktail tablet).

7.2.3.2. Mitochondrial enriched fraction from C2C12 myoblasts

Cells seeded on p10 dishes and treated or not for 30min with 30 µM CCCP were subjected to the following protocol:

1. Wash cell in dish with PBS
2. Add 150 µL of mitochondria extraction buffer (250mM sucrose, 10mM Hepes, 1mM EGTA, 1 mM sodium ortovanadate, 50 mM NaF, 5 mM sodium pyrophosphate and protease inhibitors cocktail tablet; pH= 7.4) to the p10 dish.
3. Scrape cells and transfer content to a 2 cm^2 glass tube compatible with a potter pestle.
4. Homogenize the tissue by 20 up and down with the pestle rotating at 1,800rpm.
5. Transfer homogenate to a new tube using a glass pasteur.
6. Spin 800 x g for 15 min at 4 °C to obtain the maximum amount of mitochondrial content.
7. Keep the supernatant as mitochondria-free fraction.
8. Resuspend in 100 µL of Ripa buffer (50 mM Tris pH 8, 150 mM NaCl, 1% NP-40, 0.1% SDS, 1 mM EDTA, 1 mM sodium ortovanadate, 50 mM NaF, 5 mM sodium pyrophosphate and protease inhibitors cocktail tablet).

7.2.3.3. Cytosolic fraction from C2C12 myoblasts

To obtain cytosolic fractions digitonin was used to slightly permeabilized the plasma membrane using the following protocol adapted from (West *et al.*, 2015):

1. Trypsinize and count cells at least 10 million cells per condition are needed.
2. Split the same number of cells into two 15mL falcon tubes: 5 million cells each.

3. Spin cells at 500 x g and wash with 1mL of PBS and transfer to 1.5mL Eppendorf tubes named: "Total homogenate" and "Pellet".
4. Dived the "total homogenate" suspension into two tubes: for western blot and genomic DNA (gDNA) analysis, 2.5 million cells each.
5. Spin all three tubes and aspirate PBS. Keep total homogenate tubes on ice or -20 °C for future processing.
6. Resuspend the pellet in "Pellet" tube with 500 µL of digitonin buffer (150 mM NaCl, 50mM Hepes pH ,4, 50 µg/mL Digitonin (Sigma))
7. Incubate end over end for 10min 4 °C to allow selective plasma membrane permeabilization.
8. Spin at 980 x g for 4 min at 4 °C.
9. Transfer the supernatant to a new tube and save the first pellet as "Pellet".
10. Spin at 980 x g for 4 min at 4 °C and transfer the supernatant to a new tube
11. Spin at 17,000 x g for 10 min at 4 °C to pellet any remaining cellular debris, yielding cytosolic preparations free of nuclear, mitochondrial and endoplasmic reticulum contamination.
12. Transfer the supernatant to a new tube named "cytosol" and save it as the cytosolic fraction.
13. Divide the three fractions (Total homogenate, pellet and cytosol) into two tubes each: for subsequent genomic DNA (gDNA) and western bolt analysis.

7.2.3.4. Protein extraction

Total cellular protein extracts for western blot analysis was performed as follows: cells were rinsed in ice-cold PBS 1X and scraped from culture plates in lysis buffer (50 mM Tris pH 8, 150 mM NaCl, 1% NP-40, 0.1% SDS, 1 mM EDTA, 1 mM sodium ortovanadate, 50 mM NaF, 5 mM sodium pyrophosphate and protease inhibitors cocktail tablet). Cellular primary homogenates from plate were further homogenized by passing them through a 25G syringe avoiding the generation of bubble or foam. Homogenates were centrifuged at 13,000 rpm for 30 min at 4 °C and supernatants protein extracts were transferred to new tubes and kept at -20 °C.

Tissue samples were homogenized in 10 volumes of lysis buffer using polytron. Homogenates were rotated for 1h at 4 °C and centrifuged at 13,000 rpm for 15 min at 4 °C. In the case of muscle samples a fiber solubilisation step was performed before homogenization using a solubilisation buffer (0.1M KCl, 5mM $MgCl_2$, 5mM EGTA, 1 mM sodium ortovanadate, 50 mM NaF, 5 mM sodium pyrophosphate and protease inhibitors cocktail tablet).

7.2.3.5. Protein quantification and sample preparation

Protein quantification was performed using the Pierce BCA Protein assay kit (Thermo Fisher Scientific). Briefly, a standard curve is generated between 0.5 mg/mL to 16 mg/mL using 2 mg/mL BSA from the kit. After sample distribution in a 96 well-plate, 200 µL of reaction mixture (A+B solutions at 50:1 ration) is added to each well using a multichannel pipette to avoid differential time of incubation throughout the plate. The plate is incubated 30min at 37 °C and absorbance at 562nm is measured and sample protein concentration is calculated by interpolation from the standard curve.

Samples were prepared by the addition of the specific volume of sample (to add from 10-50 µg of protein, depending on the protein to be assessed), dH_2O to equal the volume of every sample, and Loading Sample Buffer with 100 mM DTT to ensure denaturing of protein secondary structures and disulfur bridges. Before loading into the SDS-PAGE gel samples were boiled at 95 °C for 5min.

7.2.3.6. Western blot

Proteins were resolved by size by electrophoresis in an SDS-PAGE gel. The resolving gel had different concentrations of acrylamide depending on the size of proteins to be resolved (usually 7,5 %, 10 % 12,5 % or 15 %). Samples were run besides a molecular weight marker Spectra™ Multicolor Broad Range Protein Ladder (Thermo Fisher Scientific). Voltage was maintained at 80V until samples entered resolving gel, then voltage was increased to 120V until the blue color front given by the Loading Sample buffer escaped from the bottom part of the gel.

Next, proteins resolved in the electrophoresis gel were transferred to Immobilon PVDF membranes (Millipore) by 2 h transference at 250 mA at RT or by O/N transference at 40 V at 4 °C. Membranes were blocked in 5 % milk in TBS-Tween20 (TBST: 0,1 % Tween in TBS buffer) for 1 h at RT. Membranes were incubated in primary antibody diluted, as specified in Table 3, in TBST O/N at 4 °C. Membranes were washed three times for 5 min and then incubated 1h at RT with appropriate horseradish peroxidase (HRP)-conjugated secondary antibodies diluted in 5% milk TBST. Then, membranes were washed twice with TBST for 10min and once with TBS during 10min. Membranes were exposed to developing agents' mixture 1:1 for 2 min (Ge Healthcare), and immediately after, placed into developing cassettes. In the dark room, hypersensitive films were expose to membranes with chemiluminescent bands and developed using a HyperProcessor® Model AM4 (Amersham Pharmacia Biotech).

To reuse membranes for other antibodies, they were stripped incubating the membranes twice for 5min with boiling water. In this state, membranes needed to be blocked again. Successful films were scanned and bands were quantified using ImageJ software.

7.2.3.7. Plasma and cell culture media measurements

Plasma concentrations of IGF-1, IL-6 and IL-1β (Abnova), GH and FGF21 (Millipore) were measured by ELISA assay following the manufacturer's instructions. Briefly, a standard curve at known concentration of each factor was assayed in parallel to the samples. Samples are load to wells containing immobilized antibody, then biotinylated antibody is added to the bound samples and Avidin-Biotin-Peroxidase Complex (ABC) was added and developed with TMB and stopped using acidic stop solution. The absorbance at 450 nm was measured and sample concentration was interpolated with the standard curve. Cell culture media was concentrated and cytokine concentration was assessed in a similar way.

Creatine kinase (Thermo Scientific) and lactate dehydrogenase (LDH) (BioVision) activities were measured following manufacturers protocol. In brief, for the creatine kinase activity assay the spectrophotometer was programmed with shacking at 37 °C to read every 20s for 3 min at 340 nm (334-365 nm) and 405 nm (as a reference). Plasma samples were diluted 1/20 and 1/200 in PBS, and 10 µL of

the dilutions were added to a 96 well plate well. Then, 200 µL of CK-NAC reagent was added to each well with a multichannel pipette, and immediately after enzymatic activity was analyzed. Similarly, for lactate dehydrogenase activity samples were loaded into 96 well plate besides standard curve of known concentration of NADH. Then, reaction mix was added to wells. Absorbance at 450 nm was measured before and after the 30 min incubation at 37 °C.

7.2.3.8. RNA purification

RNA extraction from tissues was performed using a protocol that combined TRIzol reagent (Invitrogen) and RNAeasy® minikit columns (Qiagen), following the manufacturer's instructions. Briefly, tissue slices were placed in tubes containing 3 beads and 1mL of TRIzol per 50-100 mg of tissue, and 2 rounds of 30 s at maximal speed were performed. Chloroform (200 µL per every 1mL of TRIzol) was added, and tubes were mixes thoroughly to separate aqueous and organic phases. Samples were spun at 12,000 x g for 15 min at 4 °C and aqueous phase was transferred to a new tube. From this point the protocol is common to the cellular RNA extraction after cellular lysis with Kit lysis buffer containing 1 % DTT and 25G syringe homogenization. Aqueous phase or cellular homogenates followed the next protocol:

1. Add one volume 70 % ethanol in RNase-free water to each volume of cell or tissue homogenate.
2. Transfer up to 700 µL of the sample to the spin cartridge with a collection tube.
3. Centrifuge at 12,000 x g for 30 s at RT. Discard the flow-through
4. Add 700 µL Wash Buffer I to the spin cartridge.
5. Centrifuge at 12000 x g for 30 s at RT.
6. Add 80 µL of DNase solution to each spin cartridge (8 µL of Pure Link 10x DNase Buffer, 10 µL DNase stock solution (Thermo Scientific) + 62 µL RNase-free water)
7. Incubate 15min at RT.
8. Add 500 µL Wash Buffer II to the spin cartridge.
9. Centrifuge at 12,000 x g for 30 s at RT Discard the flow-through.
10. Repeat steps 8-9 once.

11. Centrifuge the spin cartridge at 12,000 x g for 1-2 min to dry the membrane with bound RNA.
12. Add 20 µL RNase-free water warmed 70 °C.
13. Incubate at RT for 1 minute.
14. Elute by centrifugation at 12,000 x g for 2 min at RT.
15. Store the purified RNA at -80 °C.

7.2.3.9. RNA reverse transcription to cDNA

RNA samples were quantified using the Nanodrop™ 2000/2000c spectrometer (Thermo Fisher Scientific) and the ND1000 software (Thermo Fisher Scientific). RNA purity was determined by the A260/A280 and A260/A230 absorbance ratio. A A260/A280 ratio of 1.8 is accepted as pure DNA, while pure RNA is at 2.0. If this ratio is lower than expected could imply sample contamination with DNA, proteins, phenol or other contaminants that absorb preferentially at or near 280nm. Also, pure nucleic acid result in a higher 260/230 ratio than 260/280 ratio. Lower ratios can be attributed to contaminants from the RNA extraction such as EDTA, carbohydrates, phenol or TRIzol.

Reverse transcription was performed using the SuperScript™ RTII kit (Invitrogen) using a 2720™ Thermal Cycler (Applied Biosystems). Briefly, 2 µg of RNA RNase-free water were added to PCR tubes to a final volume of 10 µL. Two master mixes were prepared. Master mix 1 contained: 1 µL deoxynucleotides (10mM stock 1:1:1:1 of dATP, dCTP, dGTP, dTTP) and 1 µL oligodT (500 µg/mL stock) per sample, which was added to the samples. Samples were heated at 65 °C for 5min to ensure linearization of RNA molecules. In parallel, master mix 2 was prepared: 4 µL of 5X First-Strand Buffer, 2 µL DTT 0,1M, 1 µL of RNAseOUT™ (40 U/ µL stock), and 1 µL of SuperScript™ II reverse transcriptase (200 U/ µL stock), the latter added just before addition of the master mix to the samples. After 5 min of heating, 8 µL of master mix 2 was added to each tube. Reverse-Transcription Polymerase Chain Reaction (RT-PCR) was set for 53 min at 42 °C to allow DNA polymerization. Then, samples were heated for 15 min at 70 °C to stop the reaction and cooled down to 4 °C to ensure preservation. Generated cDNA was diluted to 1/40 to 2.5 ng/ µL with Milli-Q H2O and stored at -20 °C.

7.2.3.10. Mitochondrial DNA analysis

Total genomic DNA was extracted from cells from using DNeasy® Blood & Tissue Kit columns (Qiagen) following the manufacturer's instructions:

1. Resuspend in pellet fractions or cells in 200 µL of PBS.
2. Add 20 µL of proteinase K to cytosolic enriched fractions or resuspended cell suspensions/pellet fractions.
3. Add 200 µL of Buffer AL. Mix thoroughly by vortexing.
4. Incubate the samples at 56 °C for 10 min.
5. Add 200 µL ethanol (96-100%). Mix thoroughly by vortexing.
6. Pipet the mixture into a DNeasy Mini spin column placed in a 2 mL collection tube.
7. Centrifuge at 6000 x g for 1 min.
8. Add 500 µL of Buffer AW1.
9. Centrifuge for 1 min at 6000 x g.
10. Add 500 µL of Buffer AW2
11. Centrifuge for 3 min at 20000 x g.
12. Transfer the spin column to a new 1.5 mL Eppendorf tube.
13. Elute DNA from cell suspensions/pellet fractions with 100 µL of Buffer AE, and cytosolic fraction with 50 µL of Buffer AE.
14. Incubate for 1 min at RT and centrifuge for 1 min at 6000 x g.

7.2.3.11. Quantitative real-time PCR

Assay Master Mix for SYBR Green analysis was prepared by combining 5 µL of SYBR Green PCR Master Mix (Applied Biosystems), 0.6 µL of 10 µM primer mix (forward and reverse) and 0.4 µL of Milli-Q H2O per each sample. In the case of TaqMan probes the Master mix contained 5 µL of TaqMan PCR Master Mix (Applied Biosystems), 0.5 µL of the specific TaqMan probe and 0.5 µL of Milli-Q H2O per each sample.

The reaction volume was set to 10 µL per sample. Plates of 384 wells were loaded with 6 µL of Assay Master Mix , and, in the case of mRNA expression assays, 4 µL of 2.5 ng/µL cDNAn sample was loaded. Alternatively, in the case of mtDNA copy number assessment, gDNA was diluted to achieve a concentration between 25 pg/µL a 250 pg/µL. RT-PCR negative controls were loaded to identify cross-contamination and 3 technical replicates were analyzed per sample.

Quantitative real-time PCR was performed using the ABI Prism 7900 HT real-time PCR machine (Applied Biosystems) and the SYBR® Green PCR Master Mix or the Taqman Probes 20X (Mm00439093_m1 for Ghr, Mm00453879_m1 for Opa1, and Mm00545913_s1 for Socs3) (Applied Biosystems). All measurements were normalized to β-actin and Arp. Except in the case of mtDNA copy number assessment that measurements were normalized to Tert as a nuclear gene.

7.2.3.12. Cloning

During this thesis the puromycin resistance of the plasmid pLKO.1-puro with the expression of shRNA against *Opa1* mRNA was changed to hygromycin in order to be able to use the pLKO.a-puro Sigma mission library to obtain double knock-downs. Traditional cloning methods was used to perform this resistance substitution.

The starting plasmids were:

- pLKO.1-hygro: as the source of hygromicin resistance sequence (Addgene, #24150)
- pLKO.1-puro-*Opa1*: as the receptor of the new resistance containing shRNA against *Opa1*.

First, both plasmids were amplified by transformation to bacteria, growth and DNA purification, this amplification protcolo was performed for all the plasmids used in this thesis.

Transformation was performed by heat shock using the following protocol:

1. Mix 20 ng of plasmid with 100 µL of Top10 competent Escherichia coli bacteria.
2. Place the tube 30 min on ice to allow the plasmid to contact with the bacterial wall.

3. Heat shock Top10 by 60-90 s at 42 °C. This is the transformation effective step.
4. Keep the tube on ice for 2 min.
5. Add 800 µL of LB to the tube
6. Incubate 1 h at 37 °C at 500rpm.
7. Seed 100 µL of the transformation in a LB-agar dish containing 100 µg/mL ampicillin as the bacterial selection.
8. Incubate the plate upside down at 37 °C O/N.

As we intended to perform Maxi-prep, we obtained first a starter of the culture by picking individual colonies of the dish and introducing each one into a tub containing 5mL of LB with 100 µg/mL ampicillin. Bacteria were grown for 6-8h with mild shacking, then starter was added to a 2 L Erlenmeyer containing 200 mL LB and 100 µg/mL ampicillin. Bacteria were grown O/N at 37 °C with mild shacking. Plasmid DNA purification (MaxiPrep) was performed using the NucleoBond Xtra Maxi Kit (Macherey-Nagel), following manufacturer's protocol. In brief, bacteria were pelleted, lysed and filtered through the column provided for the DNA to bind to the column. Bond fraction was washed and eluted. DNA was precipitated by isopropanol and 70 % ethanol, and DNA pellets were reconstituted in 200-500 µL of TE Buffer.

The concentration of plasmid was analyzed using the Nanodrop™ 2000/2000c spectrometer (ThermoScientific) and the ND1000 software (Thermo Scientific).

Both plasmids were digested using KpnI and BamH1 High fidelity restriction enzymes. The digestion mix contained: 2 µg plasmid DNA, 2 µL 10x Buffer High fidelity, 1 µl BamHI, 1 µL KpnI, 18 µL H2O. The digestion was performed by incubation at 37 °C for 1-2h. The controls used in this digestion contained: no restriction enzymes, or only BamHI, or only KpnI.

Digestion products were resolved in an agarose gel and check that all controls were as expected: linearization of the plasmid cut only with one restriction enzyme, circular plasmid in the case of no restriction enzymes added and two bands present in the case of double digestion. Then, the bands of

interest were cut: Hygromycin resistance: 1160 bp, and pLKO.1-puro- *Opa1* without puromycin resistance: 6353 bp.

NuceloSpin Gel and PCR clean up kit (Macherey-Nagel) was used to purify the plasmid fragments from the agarose gel following manufacturer's protocol. Briefly, DNA was excise from the solubilized gel slice, DNA was bound to the kit column, washed, and eluted in a final volume of 40 µL.

The concentration of DNA purified fragments was analyzed using the Nanodrop™ 2000/2000c spectrometer (ThermoScientific) and the ND1000 software (Thermo Scientific).

Ligation molar ration were calculated using NEBioCaluclator. We defined rations of 1:3 or 1:7 vector to insert with a DNA mass of vector of 100ng. The ligation mixture for each sample contained: 2 µL of T4 DNA ligase Buffer, 50ng of vector (pLKO.1-puro- *Opa1* without puromycin resistance), 37.5 ng of insert (hygromycin resistance), up to 20 µL with Nuclease-free water and 1 µL of T4 DNA Ligase. As we had cohesive ends, the ligation was performed by O/N incubation at 16 °C. Ligase was inactivated by heat at 65 °C for 10 min and ligation was placed on ice.

Ligation was transformed into competent cells as explained before with the exception that all cells were plated onto the LB dish. Ten different colonies were picked per condition and grown for MiniPrep DNA extraction. Plasmids purified from culture of the different clones were digested with restriction enzymes as described before, and an agarose gel was run to check the correct size of the digestion products. Clones that show a band pattern compatible with the insertion of the sequence for hygromycin resistance, were selected for sequencing using BigDye Terminator v3.1 Cycle Sequencing Kit using and the forward primer 5´GTGTTCCGCATTCTGCAAG 3´ for the Human phosphoglycerate kinase eukaryotic promoter (hPGK), which allow for the sequencing of the fragment containing the sequence encoding for the resistance of hygromycin, thus we were able to check the incorporation of the right resistance.

7.2.4. Statistics

The data presented here were analyzed using the Student *t*-test or analysis of variance (ANOVA) with an appropriate post-hoc test. Data are presented as mean ± SEM unless stated otherwise. Significance was established at $p<0.05$. Statistical analysis was only applied to data from $n\geq 3$ independent experiments.

RESUM EN CATALÀ

8.1. Introducció

Els mitocondris són orgànuls cel·lulars que tenen un paper fonamental en diversos processos de la cèl·lula, com en la respiració, la producció d'ATP, la homeòstasi del calci o l'apoptosi. En el control d'aquests processos la dinàmica mitocondrial es proposa com un component crucial en el bon manteniment de l'eficiència mitocondrial i per tant del correcte desenvolupament de totes aquest funcions derivades. La dinàmica mitocondrial engloba dos esdeveniments principals: la fusió i la fissió (Twig *et al.*, 2008; Liesa, Palacin and Zorzano, 2009; Sebastian *et al.*, 2012; Muñoz *et al.*, 2013).

La fusió mitocondri pot dividir-se en dos processos: la fusió de la membrana mitocondrial externa, esdeveniment sota el control de les proteïnes mitofusina 1 (Mfn1) i mitofusina 2 (Mfn2); i per altra banda, la fusió de la membrana mitocondrial interna controlada únicament per la proteïna OPA1 (de l'anglès "Optic Atrophy 1"), aquesta serà la proteïna central del present estudi. OPA1 és una proteïna descrita com a relacionada amb la dinàmica amb acció de GTPasa. Existeixen diferents isoformes d'OPA1 que es localitza a l'espai intermembrana o ancorades a la membrana mitocondrial interna orientades cap a l'espai intermembrana (Olichon *et al.*, 2003; Cipolat *et al.*, 2004; Griparic *et al.*, 2004; Ishihara *et al.*, 2006). Les diferents isoformes expliquen potencialment la varietat de funcions que es relacionen amb la proteïna OPA1, ja que a més de ser la responsable de la fusió de la membrana mitocondrial interna. És essencial pel manteniment de la correcta morfologia de les crestes mitocondrial (Cogliati *et al.*, 2013), la formació dels supercomplexes de la cadena de transport d'electors (Frezza *et al.*, 2006), i també ha estat relacionada amb la estabilitat del ADN mitocondrial (ADNmt) (Elachouri *et al.*, 2011). Una dinàmica mitocondrial equilibrada és crucial per mantenir la funcionalitat cel·lular.

En humans, mutacions sense sentit en OPA1 han estat descrites en pacients afectats per ADOA (OMIM #165500) (de l'anglès "Autosomal Dominant Optic Atrophy") (Alexander *et al.*, 2000; Delettre *et al.*, 2000). A més a més, el 20% dels pacients que pateixen ADOA presenten un quadre patològic més sever de manifestació prematura anomenat síndrome d'ADOA plus (OMIM #125250). Aquest desordre és multisistèmic i s'associa amb manifestacions afegides a ADOA, entre d'altres l'aparició de múltiples

delecions en el ADNmt a múscul esquelètic, el que reforça el paper d'OPA1 en l'estabilitat del ADNmt (Amati-Bonneau *et al.*, 2018).

La peculiaritat del fet que les delecions al ADNmt es detectés en múscul esquelètic va motivar que s'iniciés un estudi al grup del Dr Zorzano per veure quines implicacions tenia l'absència d'OPA1 en múscul esquelètic. Per això, es va generar un model animal amb depleció d'OPA1 específicament en múscul esquelètic (OPA1 KO), utilitzant la tecnologia Cre-LoxP. Anàlisis inicials d'aquests animals van descriure que la manca d'OPA1 en aquest teixit tenia un impacte global, els efectes no es limitaven al teixit, de fet, es va descriure que els ratolins OPA1 KO mostraven una reducció dramàtica en l'esperança de vida. Així mateix, presentaven defectes de creixement comparats amb els ratolins control. La caracterització d'aquest creixement impedit va permetre trobar que els ratolins presentaven un perfil semblant a una resistència a l'hormona del creixement: els nivells d'hormona del creixement en plasma eren molt alts, ara bé, tota la via de senyalització en fetge estava molt reprimida el que comportava una reducció significativa de IGF-1 (de l'anglès "Insulin-like Growth Factor 1"), l'hormona final d'aquesta via hepàtica, encarregada de dur la senyal de creixement a la resta de teixits.

Un altre aspecte important dels estudis previs d'aquest model va revelar que la deficiència d'OPA1 en múscul resultava en un estat pro-inflamatori sistèmic. La inspecció histològica dels músculs deplecionat va mostrar que més enllà de tenir problemes de desenvolupament presentaven una excessiva quantitat d'infiltrats. Es va detectar un increment en la tinció de la esterasa no específica i també un augment de la immunotinció per MHC classe I (de l'anglès "Major Histocompatibility Complex"). A més, es van trobar augmentat els valors de citocines pro-inflamatòries IL-1β i IL-6. Totes aquestes característiques van motivar el present estudi, per tal d'esbrinar la relació entre la deficiència d'OPA1 i la inflamació al cotext del múscul esquelètic, i si era aquesta la que desembocava en els defectes sistèmics observats en el model de ratolí OPA1 KO.

Els mitocondris, degut al seu passat com a bacteris lliures tenen motius molt semblant als d'aquest patògens que poden ser font de DAMPs (de l'anglès "Damage-Associated Molecular Patters"), que són

patrons moleculars que la cèl·lula és capaç de detectar com a senyal d'alerta d'algun tipus de disfuncionalitat o perill. Entre altres, el ADNmt ha estat descrit com una molècula immunoestimuladora, quan es troba fora de lloc pot ser reconegut per diferents receptors o sensors de la cèl·lula o PRRs (de l'anglès "Pattern Recognition Receptors"), i d'aquesta manera, desencadenar diferents tipologies de respostes immunes (Zhang *et al.*, 2010; Oka *et al.*, 2012; Wenceslau *et al.*, 2013).

D'una banda, el sensor citosòlic de cGAS (de l'anglès "cyclic GMP-AMP synthase") pot reconèixer la mtDNA que es filtra o s'escapa al citosol. La interacció de cGAS amb mtDNA produeix cGAMP, que interacciona amb STING, induint la fosforilació del factor de transcripció IRF3 o IKK que donarà lloc a una resposta interferó tipus I o resposta pro-inflamatòria, respectivament. De fet, West et al. van descriure que la inestabilitat de mtDNA induïda per la deficiència del factor de transcripció A mitocondrial (TFAM), que és un component important de l'empaquetatge de l'ADNmt per formar nucleoides, mostra una major expressió de gens estimulats per interferó (ISG) i també d'interferó β (West *et al.*, 2015).

D'altra banda, el TLR9 (de l'anglès "Toll-Like Receptor 9") es va descriure com un sensor d'àcid nucleic, específicament s'uneix a patògens motius CpG hipometilats d'ADN hipometilats, com en el cas de l'ADN mitocondrial (Zhang *et al.*, 2010; Barbalat *et al.*, 2011). En aquest cas el reconeixement no es realitza al citosol, la regió de reconeixement de TLR9 està orientada cap al lumen de la ruta endo-lisosomal. La senyalització del TLR9 es produeix a través de la proteïna MyD88, que activa diferents quinases i factors transcripcionals, entre d'altres el factor nuclear κB (NF-κB) o el factor de transcripció IRF7, el que desencadena respostes pro-inflamatòries o bé respostes interferó tipus I. El resultat de l'activació TLR9 es basa en el compartiment des del qual s'inicia la senyalització (Honda *et al.*, 2005). S'ha descrit el reconeixement de l'ADNmt per part de TLR9 tant quan el primer es troba en circulació (Zhang *et al.*, 2010) i com un DAMP intracel·lular (Oka *et al.*, 2012). En el darrer cas, el treball descriu l'activació de TLR9 al compartiment lisosomal degut a una deficiència en l'enzim que degrada l'ADNmt en aquest compartiment (DNase-II)

En aquest sentit, el control de la qualitat mitocondrial és essencial per evitar la presència de DAMPs mitocondrials i l'activació de respostes pro-inflamatòries cel·lulars. Les mitocòndries danyades són reconegudes, fragmentades, embolcallades i degradades per un procés selectiu anomenat mitofàgia o autofàgia mitocondrial. Més enllà del control de la qualitat, la mitofàgia també és necessària per a la renovació de la població mitocondrial així com per ajustar el nombre de mitocondris als requeriments metabòlics canviants. En les cèl·lules de mamífers, la mitofàgia s'inicia per la formació d'estructures de doble membrana o membrana d'aïllament, on els mitocondris són segrestats, que donarà lloc a la formació d'un mito-autofagosoma. A continuació, els mito-autofagosomes es fusionen amb lisosomes per formar mito-autolisosomes on es degraden els continguts embolcallats. Una altra consideració important és que els mito-autofagosomes es poden fusionar amb cossos multivesiculars també anomenats endosomes tardans, per formar amfisomes. Pel que fa a un punt de vista sistèmic, la secreció de citocines inflamatòries ha demostrat tenir efectes devastadors sobre el creixement.

8.2. Objectius

Els resultats recopilats prèviament van motivar el present treball de tesi doctoral amb l'objectiu de tenir una millor comprensió dels mecanismes que relacionen la deficiència d'OPA1 a múscul esquelètic amb la inflamació sistèmica detectada al ratolí OPA1 KO. Els següents objectius específics s'han dut a terme:

1. Estudiar els efectes sistèmics induïts per la depleció d'OPA1 en múscul esquelètic. Entendre com la depleció d'OPA1, una proteïna de dinàmica mitocondrial, únicament a múscul esquelètic pot donar lloc a un efecte global tant sever.
2. Caracteritzar l'estat inflamatori del múscul i determinar l'origen de la inflamació sistèmica. Analitzar si la inflamació es produïda de manera autònoma i quina és la contribució de la mort cel·lular.
3. Identificar els actors principals responsables de la resposta inflamatòria. Determinar la seqüència d'esdeveniments a nivell molecular que resulten en la inflamació.

8.3. Resultats i discussió

8.3.1. Estudi dels efectes sistèmics de la deficiència d'OPA1 en múscul esquelètic.

Estudis previs realitzats al laboratori van incloure una anàlisi transcriptòmica dels músculs dels ratolins OPA1 KO comparats als ratolins control. L'estudi de l'enriquiment de grups de gens (GSEA) ca revelar un augment ens els gens diana d'ATF4. Entre ells, FGF21 estava molt induït en els músculs deficients d'OPA1. Així mateix, els nivells circulants d'aquesta hormona van detectar-se 4 vegades augmentats. Producció d'alts nivells d'aquesta proteïna estan lligats amb disfunció mitocondrial, amés, també ha estat descrita una correlació entre sobre-expressió de FGF21 i defectes en el creixement (Inagaki *et al.*, 2008). És per això que vam estudiar la seva importància en el fenotip d'OPA1. Per això, es van generar ratolins dobles KO (DKO), en les que Fgf21 estava noquejat globalment i OPA1 era suprimida a múscul esquelètic, amb l'objectiu de rescatar el fenotip relacionat amb els defectes de creixement. L'estudi d'aquest nou model va revelar que Fgf21 no juga un paper rellevant en el menor creixement ja que els ratolins DKO no presenten una normalització ni en el pes de múscul ni en l'expressió de proteïnes relacionades amb el creixement a fetge (Figura 1).

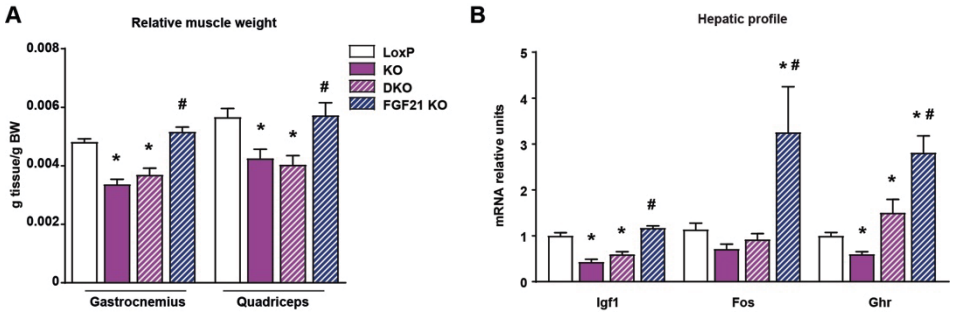

Figura 1. Els defectes de creixement són independents a l'expressió de FGF21. (A) Pes relatiu dels músculs gastrocnemius i quàdriceps. (B) Igf1, Fos and Ghr nivells d'ARNm en fetge dels ratolins loxP, OPA1 KO, DKO i Fgf21 KO (n=10). Les dades estan representades com a mitjana ± Error estàndard * p<0.05 vs. loxP. # p<0.05 vs. DKO.

Basant-nos en les dades que excloïen FGF21 com a responsable del menor creixement, ens vam centrar en un altre paràmetre molt evidentment alterat en els ratolins deficients d'OPA1, la inflamació. S'ha descrit que la inflamació crònica dóna lloc a greus problemes en el desenvolupament i creixement, com

per exemple, en pacient de malalties com la artritis idiopàtica juvenil, malalties renals cròniques o malaltia de Crohn (Wong *et al.*, 2016). L'estudi de models animals demostra que la sobreexpressió de IL6, IL-1β i TNF-α resulten en defectes en el creixement derivat d'una disminució dels nivells d'IGF-1 a plasma (De Benedetti *et al.*, 1997; Zhao *et al.*, 2014). Donat que els animals deficient en OPA1 present nivells elevats de les citocines IL-6 i IL-1β, vam explorar la possibilitat que la inflamació estigués causant les deficiències en el creixement. El plantejament experimental va ser el de tractar els animals amb un anti-inflamatori, salicilat sòdic (Kopp and Ghosh, 1994; M. Yin, Yamamoto and Gaynor, 1998). Després de comprovar que el tractament estava set efectiu (disminució de la inflamació a múscul i en circulació) es van analitzar els diferents paràmetres característics de la deficiència d'OPA1. Es va detectar una lleugera millora en l'increment de pes, també es va recuperar en cert grau l'area de les fibres musculars i es va eliminar la necrosi associada al múscul esquelètic (Figura 2).

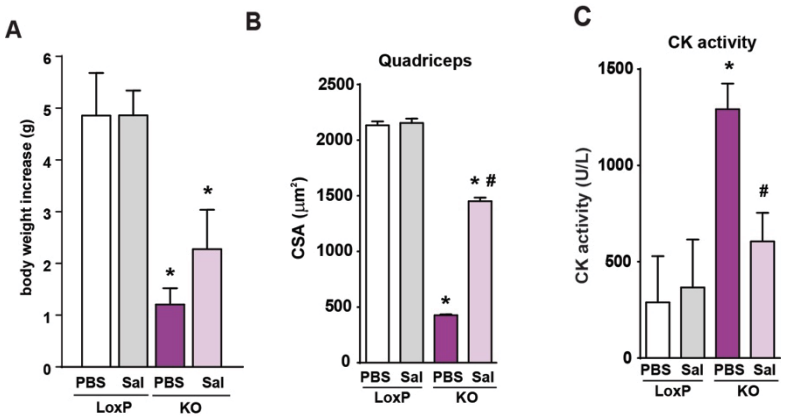

Figura 2. Increment de pes, àrea de fibra i necrosi muscular rescatats amb antiinflamatori. Increment de pes en animals loxP i KO, tractats o no amb salicilat durant 20 dies. (B) Mitjana de l'àrea de la secció transversal de 150 fibres en múscul quàdriceps muscles. (C) Activitat de la creatina quinasa (CK) mesurada en plasmes d'animals dels quatre grups esmentats. Les dades estan representades com a mitjana ± Error estàndard * p<0.05 vs. loxP no tractat. # p<0.05 vs. KO no tractat.

Pel que fa a l'expressió hepàtica de gens relacionats amb el creixement, el salicilat va aconseguir corregir la desregulació dels gens estudiats (Figura 3), així com els nivells d'hormona del creixement (GH)

circulants (Figura 3), suggerint que la inflamació és part essencial del fenotip derivat de la deficiència d'OPA1 pel que fa al creixement de l'animal.

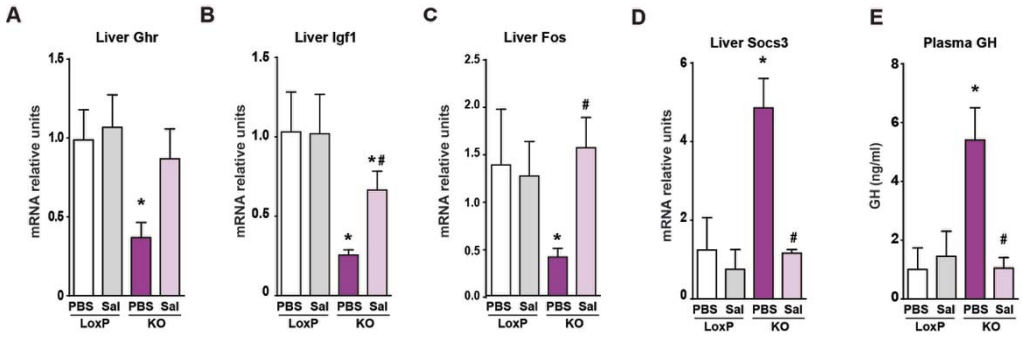

Figura 3. Expressió de gens relacionts amb el creixement i nivells circulants d'hormona del creixement. (A) Ghr, (C) Igf1, (C) Fos, i (D) SOCS3 en animals loxP o OPA1 KO tractats o no amb salicilat. (E) Nivells en plasma de GH. Les dades estan representades com a mitjana ± Error estàndard * p<0.05 vs. loxP no tractat. # p<0.05 vs. KO no tractat.

8.3.2. Caracterització de l'estat inflamatori del múscul i estudi l'origen de la inflamació sistèmica.

Un cop establerta la importància de la inflamació pel fenotip global del model animal de deficiència d'OPA1 en múscul esquelètic, vam decidir determinar si la inflamació era de caràcter muscular i era produïda per la mateixa fibra muscular, o era una repercussió derivada de l'activació del sistema immunitari. Anàlisi de IL-1β, com a marcador d'inflamació, CD68 com a marcador de infiltració de macròfags i activitat de creatina quinasa com a marcador de necrosi muscular (Figura 4).

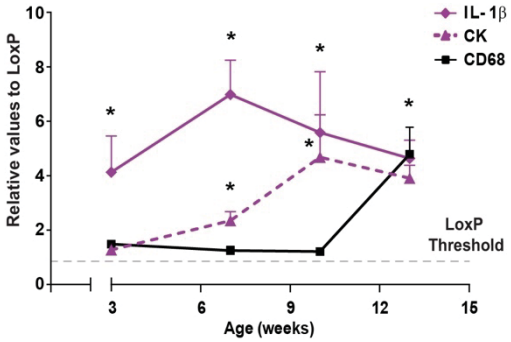

Figura 4. Estudis de la cronologia de la inflamació, la necrosis i la infiltració. Quantificació de l'expressió de IL-1β i de CD68 en gastrocnemius i de l'activitat de creatina quinasa en plasma d'animals loxP i OPA1 KO de 3, 7, 10 i 13 setmanes d'edat. Les tincions es van quantificar amb un plugin del software ImageJ (Trainable Weka Segmentation plugin), 5 imatges per grup. Les dades estan representades com a mitjana ± Error estàndard relatiu al grup loxP * p<0.05 vs. loxP no tractat. # p<0.05 vs. KO no tractat.

Aquests estudis van revelar que la seqüencia d'esdeveniments era, a les 3 setmanes ja hi havia inflamació als músculs deficients d'OPA1, a les 10 setmanes hi havia un augment significatiu de l'activitat de creatina quinasa i només a les 13 setmanes d'edat es va observar una diferencia significativa en els nivells de CD68 (Figura 4).

Això va estar corroborat a nivell de transcrits en un altre model animal on OPA1 és deplecionada un cop el múscul ja s'ha format per la inducció de la recombinasa cre amb dieta amb tamoxifè. La darrera dada que ens fa pensar que la inflamació es produeix al múscul esquelètic intrínsecament és que la depleció d'OPA1 en cèl·lules musculars C2C12 resulta en la inducció d'una resposta inflamatòria tipus NF-κB (Figura 5).

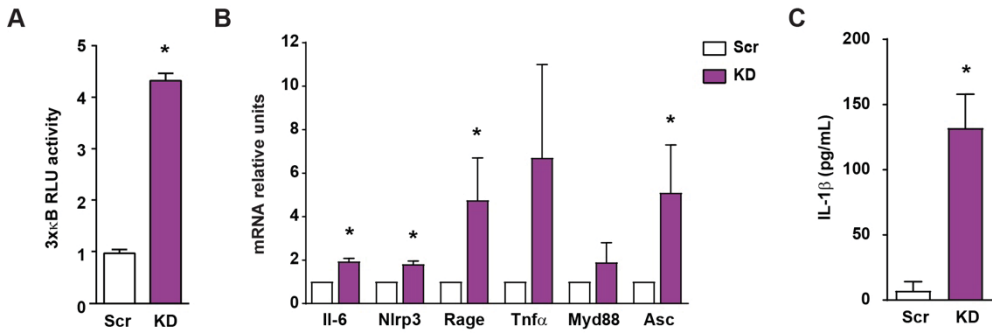

Figura 5. Inflamació en cèl·lules musculars. (A) Activitat transcripcional de promotor d'NF-κB en cèl·lules control (Scr) i OPA1 KD. (B) Expressió de gens diana d'NF-κB. (C) Nivells d'IL-1β al medi extracel·lular. Les dades estan representades com a mitjana ± Error estàndard. * p<0.05 vs. Scr

La inducció dels perfils inflamatoris reportats en múscul esquelètic i en cèl·lules C2C12 s'han descrit en situacions on no hi ha apoptosis i, en el cas del model cel·lular, no hi ha necrosis descrita per l'activitat LDH en medi extracel·lular. Així, les dades recolzen la idea d'una inflamació iniciada de manera autònoma pel múscul esquelètic i independent de mort cel·lular.

8.3.3. Identificació dels actors principals responsables de la resposta inflamatòria.

Per tal de determinar el component específic que desencadena una resposta pro-inflamatòria tan rellevant en un cotext muscular de deficiència d'OPA1, vam caracteritzar l'estat dels mitocondris tant en múscul esquelètic com en cèl·lules.

Pel que fa al múscul esquelètic, la deficiència d'OPA1 causa la desestructuració de la xarxa mitocondrial, i una disfunció mitocondrial greu pel que fa la respiració. En paral·lel, les cèl·lules mostren una xarxa mitocondrial completament fragmentada, una reducció de la respiració (Figura 6). Tot això és compatible amb dues de les funcions que se li han atribuït a OPA1: fusió de la membrana mitocondrial interna i manteniment de la morfologia de crestes, alhora estabilitat de la cadena de transport d'electrons (Figura 6).

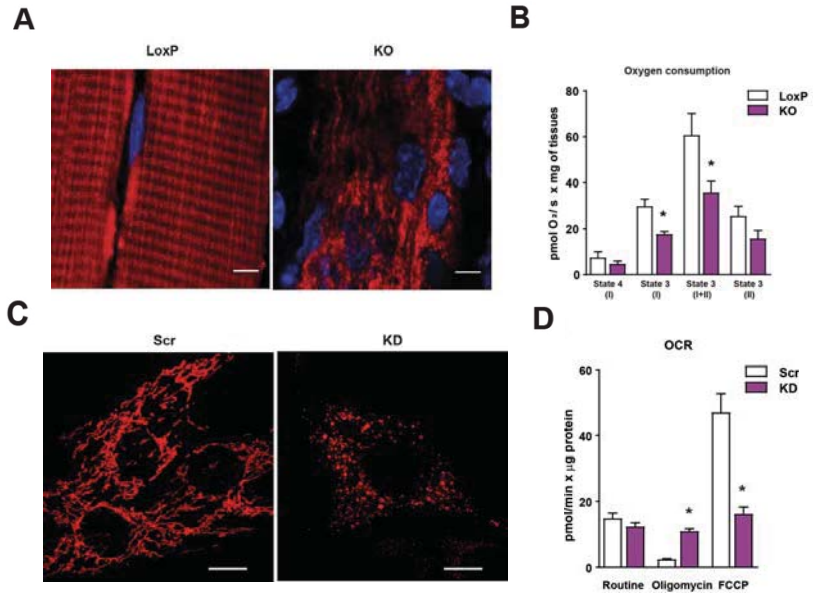

Figura 6. La deficiència d'OPA1 genera disfunció mitocondrial. (A) Imatges representatives de músculs tibialis eletroporats amb el vector MitoDsRed. Barra d'escala, 5 µm. (B) Respiració mitocondrial de miofibres aïllades d'animals loxP o OPA1 KO. (C) Imatges representatives de la morfologia mitocondrial en cèl·lules Scr o OPA1. Barra d'escala, 10µm. (D) Consum d'oxigen mitocondrial en mioblasts Scr i OPA1 KD. (n=5). Les dades estan representades com a mitjana ± Error estàndard. * p<0.05 vs. grups control.

La tercera funció descrita per OPA1 és la seva relació amb l'estabilitat del ADNmt (Amati-Bonneau et al, 2008; Hudson et al, 2008), en correspondència, la depleció d'OPA1 en cèl·lules musculars C2C12 provoca una depleció del ADNmt d'un 50% i indueix el que s'ha descrit com estrès de l'ADNmt (Figura 7) (West *et al.*, 2015).

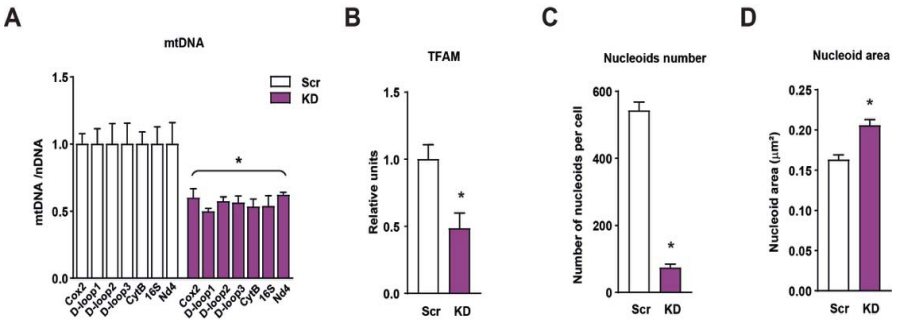

Figura 7. La deficiència d'OPA1 en cèl·lules musculars genera estrès de l'ADNmt. (A) Nivells relatius de ADNmt relatius a AND nuclear (Tert). (B) Nivells proteics de TFAM. (C) Número de nucleoides d'ADNmt per cèl·lula. (D) Àrea de cada nucleoide. Les dades estan representades com a mitjana ± Error estàndard. * p<0.05 vs. Scr.

L'ADNmt és un reconegut DAMP, per la sembla semblança amb l'ADN de bacteri, així vam decidir explorar si aquesta era la senyal que desencadenava tota la resposta. La depleció del ADNmt per tractament crònic amb bromur d'etidi va donar lloc a una normalització dels nivells d'expressió de gens diana d'NF-κB (Figura 8).

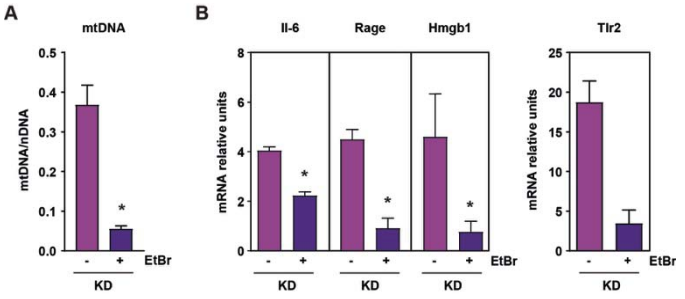

Figura 8. L'eliminació de l'ADNmt rescata l'expressió de gens diana d'NF-κB. (A) Nivells relatius d'ADNmt respecte al ADN nuclear. (B) Expressió de gens diana d'NF-κB en cèl·lules deplecionades d'OPA1 tractades o no amb bromur d'etidi. Les dades estan representades com a mitjana ± Error estàndard. * p<0.05 vs. no tractades.

Donada la implicació de l'ADNmt en la resposta inflamatòria descrita en situacions de deficiència d'OPA1, a continuació vam estudiar les dues vies més descrites per la detecció de l'ADNmt com una senyal d'alerta de desregulació cel·lular. Per una banda, el sensor citosòlic cGAS i per altre TLR9 al compartiment endo-lisosomal.

La possibilitat de que l'ADNmt estigues localitzat en el citosol i fos detectat pel sensor cGAS va ser descartada ja que no hi havia presencia d'ADNmt en fracció citosòlica, tampoc hi havia increment de l'expressió de gens induïts per interferó ni del mateix interferó β, el que composaria una resposta interferó tipus I que és la resposta més rellevant des de l'activació de cGAS. La implicació de cGAS va ser definitivament descartada quan la doble depleció d'OPA1 i cGAS no va suposar un rescat en l'expressió de gens diana d'NF-κB.

Donat que l'ADNmt no es troba al citosol però la deficiència d'OPA1 genera inestabilitat, aleshores vam explorar el mecanisme cel·lular que permet la encapsulació de components cel·lular danyats dins de vesícules. Primer vam determinar si l'ADNmt es trobava en un compartiment que contingués mitocondris i així era. Vam trobar un 100% de dels nucleoides d'ADNmt localitzats en estructures positives per TOM20, un marcador de la membrana mitocondrial externa.

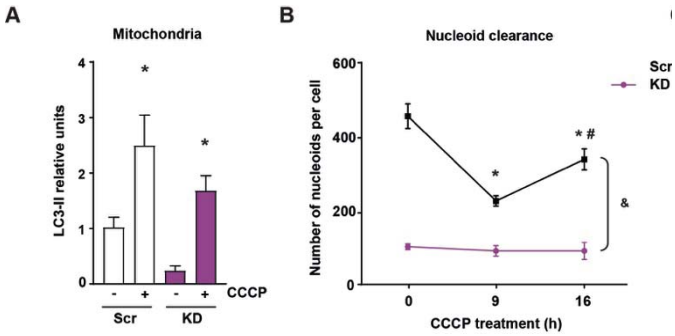

Figura 9. Estudi de la mitofàgia en cèl·lules deficient d'OPA1. (A) Reclutament d'LC3-II a la fracció enriquida en mitocondris després de 30min de tractament amb CCCP. * p<0.05 vs.no tractades. (B) Degradació de nucleoides en temps llargs de tractament amb CCCP en cèl·lules Scr i OPA1 KD. Les dades estan representades com a mitjana ± Error estàndard. * p<0.05 vs. Scr no tractades, # p<0.05 vs. tractament de 9h, & p<0.05 KD vs. Scr.

Així, vam analitzar la funcionalitat de la mitofàgia en aquestes cèl·lules. Vam trobar que la iniciació no estava afectada ja que el reclutament d'LC3-II cap a la fracció enriquida en mitocondris no es veia alterada per la deficiència d'OPA1, ara bé, la capacitat per degradar l'ADNmt sí que es va veure afectada (Figura 9). La situació en múscul esquelètic també suggereix un problema amb la resolució de la mitofàgia. Aquests resultats indiquen que la maquinaria de mitofàgia es capaç de detectar el dany mitocondrial, contenir els mitocondris danyat en mito-autofagosomes, però aquest mito-autofagosomes no finalitzen el procés de degradació.

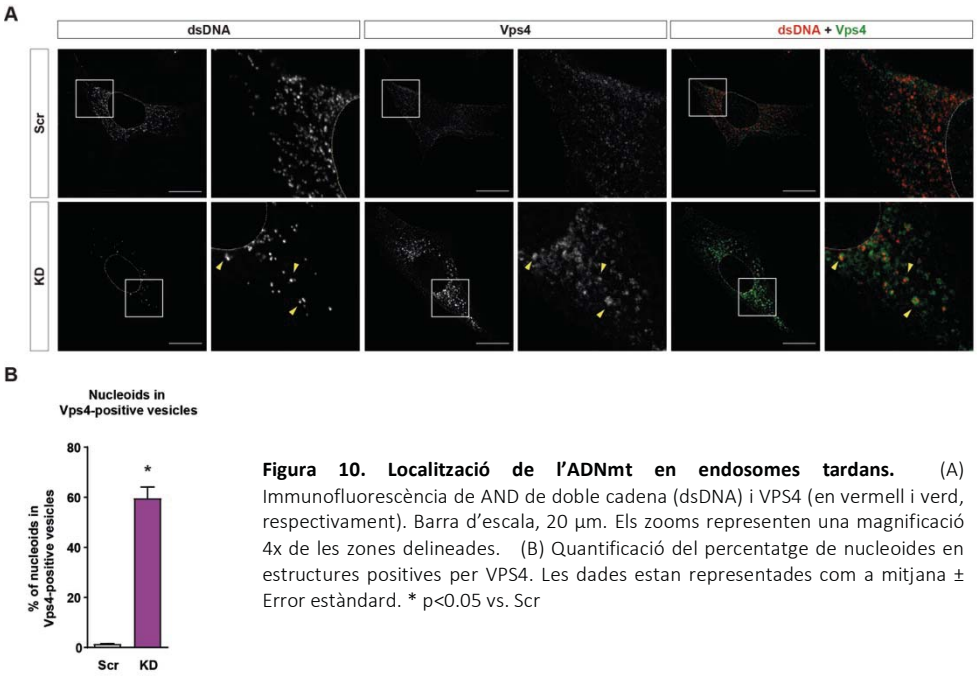

Figura 10. Localització de l'ADNmt en endosomes tardans. (A) Immunofluorescència de AND de doble cadena (dsDNA) i VPS4 (en vermell i verd, respectivament). Barra d'escala, 20 µm. Els zooms representen una magnificació 4x de les zones delineades. (B) Quantificació del percentatge de nucleoides en estructures positives per VPS4. Les dades estan representades com a mitjana ± Error estàndard. * p<0.05 vs. Scr

Després de descriure un problema en la finalització de la mitofàgia vam focalitzar els estudis en detectar el compartiment en que es localitzava el ADNmt no degradat. La deficiència d'OPA1 resulta en la localització del 60% del nucleoides d'ADNmt en estructures positives per VPS4, un marcador de endosoma tardà (Figura 10). Vam poder descartar la presència d'ADNmt en endosomes primerencs o lisosomes.

Per últim, vam estudiar el paper del receptor TLR9 en el reconeixement d'aquest ADNmt no degradat. Aproximadament el 60% dels nucleoides d'ADNmt en una situació de deficiència d'OPA1 es troben en estructures TLR9 positives.

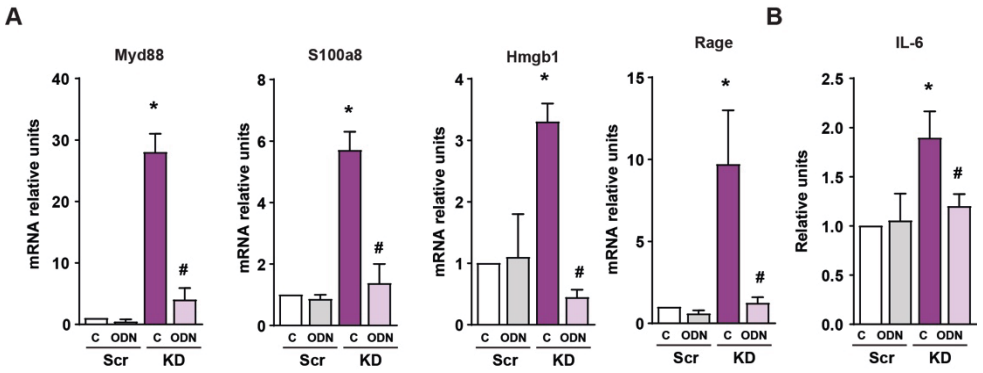

Figura 11. Tractament amb ODN antagonista. (A) Expressió de gens diana NF-κB i (B) nivells d'IL-6 en el medi extracel·lular en cèl·lules Scr i OPA1 KD tractades amb ODN2088 (ODN), antagonista de TLR9 o ODN control (C). Les dades estan representades com a mitjana ± Error estàndard. * p<0.05 vs. Scr control i # p<0.05 ODN vs. control.

Per tal de confirmar la rellevància d'aquest receptor en el procés inflamatori, es van dur a terme experiments de rescat. Les cèl·lules deficients d'OPA1 van normalitzar els nivells d'expressió de gens diana d'NF-κB en ser tractades amb un antagonista de TLR9 (Figura 11).

També van rescatar-se els nivells d'IL6 en el medi extracel·lular de les cèl·lules deficients d'OPA1. A més de la manipulació amb l'antagonista, es van generar cèl·lules deficients tant per OPA1 com per TLR9 (DKD). Aquestes van mostrar, igualment, una normalització dels gens diana d'NF-κB (Figura 12).

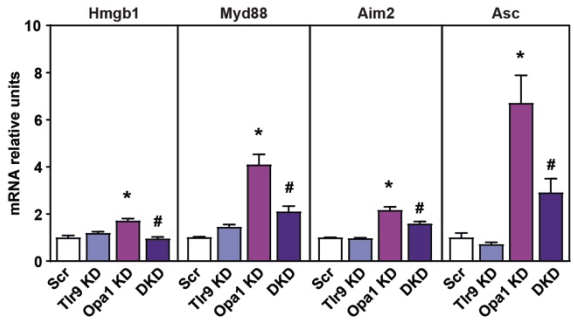

Figura 12. Rescat de l'expressió de gens diana d'NF-κB en eliminar l'expressió de TLR9. Nivells d'expressió de gens diana d'NF-κB en cèl·lules control (Scr), deficients d'OPA1 (OPA1 KD), deficients de TLR9 (TLR9 KD)o deficients d'OPA1 I TLR9 (DKD). Les dades estan representades com a mitjana ± Error estàndard. * p<0.05 vs. Scr control i # p<0.05 vs. OPA1 KD.

Les dades obtingudes indiquen, com es representa a la Figura 13, que la deficiència d'OPA1 genera una deficiència mitocondrial que és detectada per la maquinària mitofàgica que és capaç d'englobar els mitocondris però no de degradar-los correctament. El ADNmt no degradat es troba principalment en endosomes tardans on coincideix amb TLR9. Aquest reconeixement desencadena l'activació d'NF-κB i que, finalment, donarà lloc a la producció de citocines que generaran les alteracions en el creixement observades en el ratolí OPA1 KO.

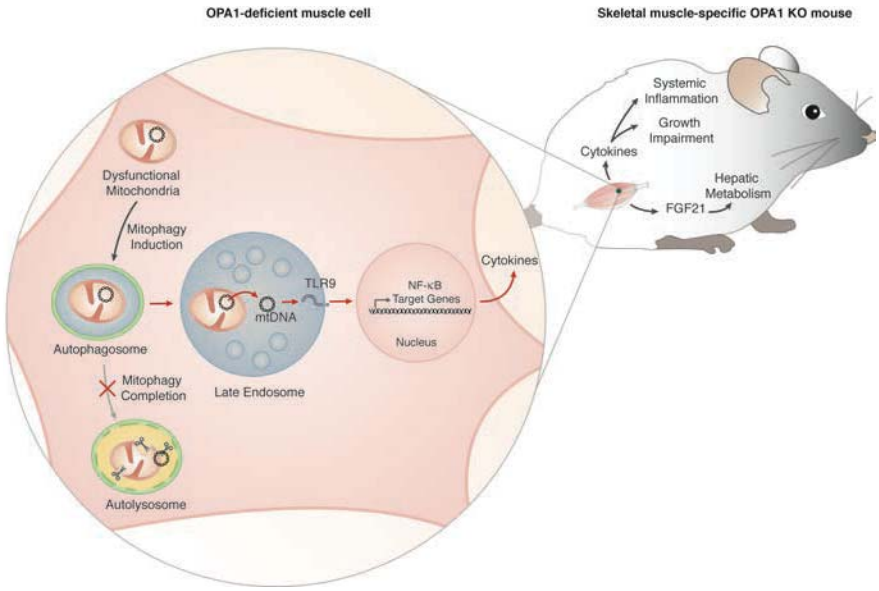

Figura 13. Model esquemàtic dels efectes de la deficiència d'OPA1 en múscul.

8.4. Conclusions

Les dades recopilades en aquesta tesi doctoral ens permeten concloure:

1. La deficiència d'OPA1 en múscul esquelètic causa un greu defecte de creixement en ratolins. Aquests defectes de creixement són independents dels nivells d'FGF21.

2. La deficiència muscular d'OPA1 causa inflamació local i sistèmica. La inflamació sistèmica és responsable dels defectes de creixement observats en els ratolins deficients d'OPA1. Aquesta inflamació és local, autònoma cel·lular i independent de la mort cel·lular.

3. La deficiència d'OPA1 dóna lloc a disfunció mitocondrial. A més, les cèl·lules musculars deficients d'OPA1 es caracteritzen per una reducció de l'ADNmt així com la presència d'estrès d'ADNmt.

4. En cèl·lules deficient d'OPA1, l'eliminació de l'ADNmt cancel·la la inflamació, el que recolza la idea que l'ADNmt és el desencadenant de la resposta inflamatòria. Aquesta resposta és independent de cGAS i es caracteritza per un defecte en la resolució de la mitofàgia en cèl·lules musculars.

5. En un context de deficiència d'OPA1, TLR9 s'activa i és responsable de la resposta inflamatòria detectada en cèl·lules musculars, la qual inclou l'activació de NF-κB i la secreció de citocines.

6. Proposem un model en el que la deficiència d'OPA1 resulta en la formació de compartiments cel·lular semblants amb característiques d'amfisomes on possibilita l'activació de TLR9, que potencialment desencadenaria la inflamació sistèmica.

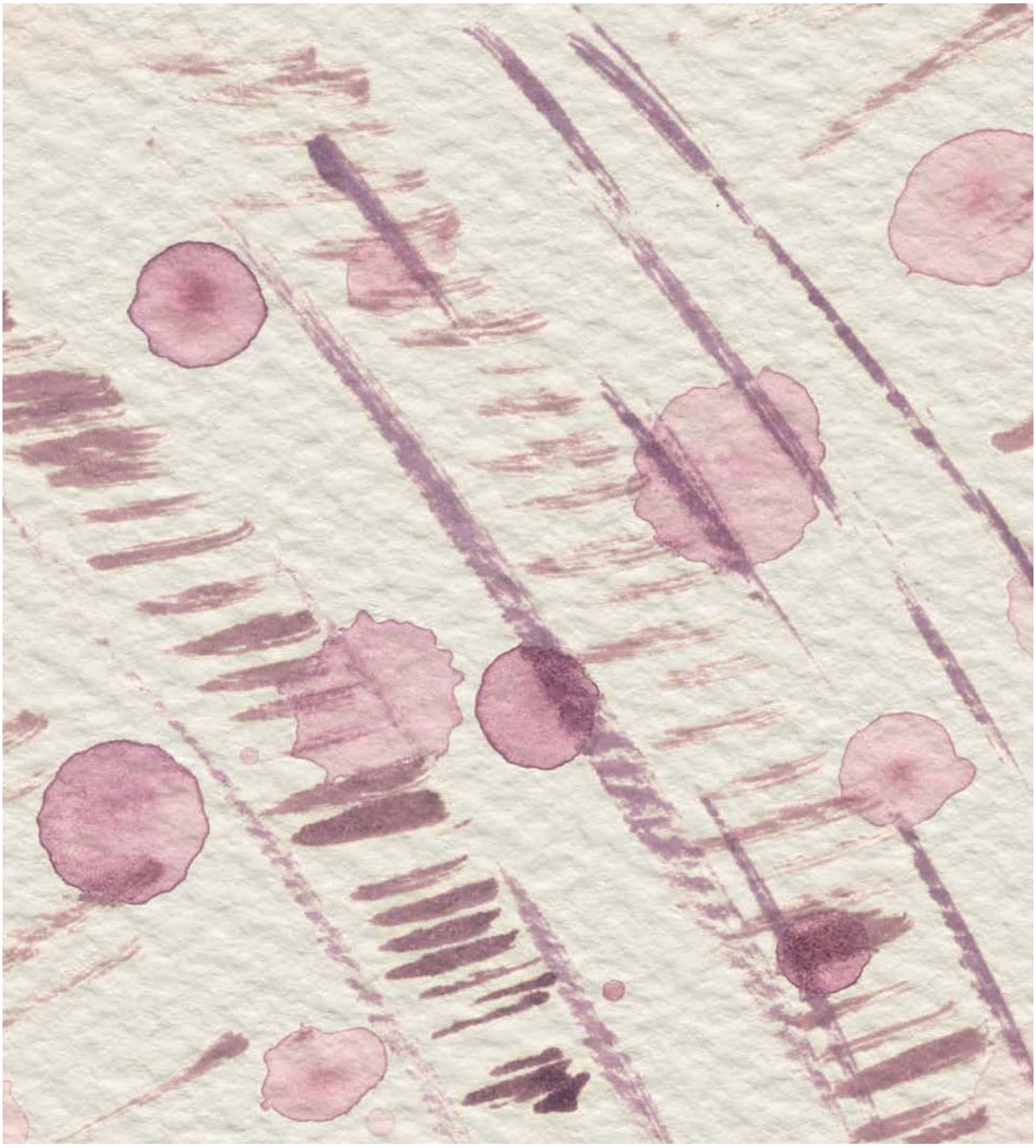

REFERENCES

Akepati, V. R. *et al.* (2008) 'Characterization of OPA1 isoforms isolated from mouse tissues', *Journal of Neurochemistry*, 106(1), pp. 372–383. doi: 10.1111/j.1471-4159.2008.05401.x.

Akiyama, M. *et al.* (2009) 'Increased insulin demand promotes while pioglitazone prevents pancreatic beta cell apoptosis in Wfs1 knockout mice', *Diabetologia*, 52(4), pp. 653–663. doi: 10.1007/s00125-009-1270-6.

Alexander, C. *et al.* (2000) 'OPA1, encoding a dynamin-related GTPase, is mutated in autosomal dominant optic atrophy linked to chromosome 3q28', *Nature Genetics*, 26(2), pp. 211–215. doi: 10.1038/79944.

Amann, R. and Peskar, B. A. (2002) 'Anti-inflammatory effects of aspirin and sodium salicylate', *European Journal of Pharmacology*, 447(1), pp. 1–9. doi: 10.1016/S0014-2999(02)01828-9.

Amati-Bonneau, P. *et al.* (2018) 'OPA1 mutations induce mitochondrial DNA instability and optic atrophy " plus " phenotypes', *Brain*, 131(February), pp. 338–351. doi: 10.1093/brain/awm298.

Anand, R. *et al.* (2014) 'The i-AAA protease YME1L and OMA1 cleave OPA1 to balance mitochondrial fusion and fission', *Journal of Cell Biology*, 204(6), pp. 919–929. doi: 10.1083/jcb.201308006.

Anderson, S. *et al.* (1981) 'Sequence and organization of the human mitochondrial genome', *Nature*, 290(5806), pp. 457–465. doi: 10.1038/290457a0.

Andreeva, L. *et al.* (2017) 'CGAS senses long and HMGB/TFAM-bound U-turn DNA by forming protein-DNA ladders', *Nature*. Nature Publishing Group, 549(7672), pp. 394–398. doi: 10.1038/nature23890.

Arnoult, D. *et al.* (2011) 'Mitochondria in innate immunity', *EMBO Reports*. Nature Publishing Group, 12(9), pp. 901–910. doi: 10.1038/embor.2011.157.

Asakura, Y. *et al.* (2007) 'Serine/threonine kinase PKR: a sentinel kinase that discriminates a signaling pathway mediated by TLR4 from those mediated by TLR3 and TLR9.', *American journal of hematology*. United States, 82(7), pp. 640–642. doi: 10.1002/ajh.20817.

Bader, C. A. *et al.* (2015) 'Atg9 is required for intraluminal vesicles in amphisomes and autolysosomes.', *Biology open*. England, 4(11), pp. 1345–1355. doi: 10.1242/bio.013979.

Badman, M. K. *et al.* (2009) 'Fibroblast growth factor 21-deficient mice demonstrate impaired adaptation to ketosis', *Endocrinology*, 150(11), pp. 4931–4940. doi: 10.1210/en.2009-0532.

Baixauli, F. *et al.* (2015) 'Mitochondrial respiration controls lysosomal function during inflammatory t cell responses', *Cell Metabolism*, 22(3), pp. 485–498. doi: 10.1016/j.cmet.2015.07.020.

Baker, M. J. *et al.* (2014) 'Stress-induced OMA1 activation and autocatalytic turnover regulate OPA1-dependent mitochondrial dynamics', *EMBO Journal*, 33(6), pp. 578–593. doi: 10.1002/embj.201386474.

Ban, T. *et al.* (2017) 'Molecular basis of selective mitochondrial fusion by heterotypic action between OPA1 and cardiolipin', *Nature Cell Biology*, 19(7), pp. 856–863. doi: 10.1038/ncb3560.

Bao, W. *et al.* (2016) 'Toll-like Receptor 9 Can be Activated by Endogenous Mitochondrial DNA to Induce Podocyte Apoptosis', *Scientific Reports*. Nature Publishing Group, 6(September 2015), pp. 1–11. doi: 10.1038/srep22579.

Barbalat, R. *et al.* (2011) 'Nucleic acid recognition by the innate immune system.', *Annual review of immunology*. United States, 29, pp. 185–214. doi: 10.1146/annurev-immunol-031210-101340.

Baricault, L. *et al.* (2007) 'OPA1 cleavage depends on decreased mitochondrial ATP level and bivalent metals', *Experimental Cell Research*, 313(17), pp. 3800–3808. doi: 10.1016/j.yexcr.2007.08.008.

Baris, O. *et al.* (2003) 'Fourteen Novel OPA1 Mutations in Autosomal Dominant Optic Atrophy Including Two De Novo Mutations in Sporadic Optic Atrophy', *Human Mutation*, 623(March), pp. 1–7. doi: 10.1002/humu.9152.

Belenguer, P. and Pellegrini, L. (2013) 'The dynamin GTPase OPA1: More than mitochondria?', *Biochimica et Biophysica Acta - Molecular Cell Research*. Elsevier B.V., 1833(1), pp. 176–183. doi: 10.1016/j.bbamcr.2012.08.004.

De Benedetti, F. *et al.* (1997) 'Interleukin 6 causes growth impairment in transgenic mice through a decrease in insulin-like growth factor-I. A model for stunted growth in children with chronic inflammation.', *The Journal of clinical investigation*. United States, 99(4), pp. 643–650. doi: 10.1172/JCI119207.

De Benedetti, F. (2009) 'The impact of chronic inflammation on the growing skeleton: lessons from interleukin-6 transgenic mice.', *Hormone research*. Switzerland, 72 Suppl 1, pp. 26–29. doi: 10.1159/000229760.

Bereiter-Hahn, J. and Voth, M. (1994) 'Dynamics of mitochondria in living cells: shape changes, dislocations, fusion, and fission of mitochondria.', *Microscopy research and technique*. United States, 27(3), pp. 198–219. doi: 10.1002/jemt.1070270303.

Bergsbaken, T., Fink, S. L. and Cookson, B. T. (2009) 'Pyroptosis: Host cell death and inflammation', *Nature Reviews Microbiology*, 7(2), pp. 99–109. doi: 10.1038/nrmicro2070.

Bleazard, W. *et al.* (1999) 'The dynamin-related GTPase Dnm1 regulates mitochondrial fission in yeast', *Nature cell biology*, 1(5), pp. 298–304. doi: 10.1038/13014.

Boaru, S. G. *et al.* (2015) 'NLRP3 inflammasome expression is driven by NF-κB in cultured hepatocytes', *Biochemical and Biophysical Research Communications*, 458(3), pp. 700–706. doi: 10.1016/j.bbrc.2015.02.029.

Bogenhagen, D. F. (2012) 'Mitochondrial DNA nucleoid structure', *Biochimica et Biophysica Acta - Gene Regulatory Mechanisms*. Elsevier B.V., 1819(9–10), pp. 914–920. doi: 10.1016/j.bbagrm.2011.11.005.

Brown, T. A. *et al.* (2011) 'Superresolution Fluorescence Imaging of Mitochondrial Nucleoids Reveals Their Spatial Range, Limits, and Membrane Interaction', *Molecular and Cellular Biology*, 31(24), pp. 4994–5010. doi: 10.1128/MCB.05694-11.

Broz, P. and Dixit, V. M. (2016) 'Inflammasomes: Mechanism of assembly, regulation and signalling', *Nature Reviews Immunology*, 16(7), pp. 407–420. doi: 10.1038/nri.2016.58.

Cai, D. (2009) 'NFκB-mediated metabolic inflammation in peripheral tissues versus central nervous system', *Cell Cycle*, 8(16), pp. 2542–2548. doi: 10.4161/cc.8.16.9386.

Carelli, V. *et al.* (2015) 'Syndromic Parkinsonism and Dementia Associated with OPA1 Missense

Mutations', *Annals of Neurology*, 78, pp. 21–38. doi: 10.1002/ana.24410.

Catalan-Garcia, M. *et al.* (2016) 'Mitochondrial DNA disturbances and deregulated expression of oxidative phosphorylation and mitochondrial fusion proteins in sporadic inclusion body myositis', *Clinical Science*, 130(19), pp. 1741–1751. doi: 10.1042/CS20160080.

Cereghetti, G. M. *et al.* (2008) 'Dephosphorylation by calcineurin regulates translocation of Drp1 to mitochondria.', *Proceedings of the National Academy of Sciences of the United States of America*. United States, 105(41), pp. 15803–15808. doi: 10.1073/pnas.0808249105.

Chan, D. C. (2006) 'Mitochondria: Dynamic Organelles in Disease, Aging, and Development', *Cell*, 125(7), pp. 1241–1252. doi: 10.1016/j.cell.2006.06.010.

Chan, D. C. (2012) 'Fusion and Fission: Interlinked Processes Critical for Mitochondrial Health', *Annual Review of Genetics*, 46(1), pp. 265–287. doi: 10.1146/annurev-genet-110410-132529.

Chandra, P. *et al.* (2015) 'Mycobacterium tuberculosis Inhibits RAB7 Recruitment to Selectively Modulate Autophagy Flux in Macrophages.', *Scientific reports*. England, 5, p. 16320. doi: 10.1038/srep16320.

Chen, H. *et al.* (2003) 'Mitofusins Mfn1 and Mfn2 coordinately regulate mitochondrial fusion and are essential for embryonic development', *Journal of Cell Biology*, 160(2), pp. 189–200. doi: 10.1083/jcb.200211046.

Chen, H. *et al.* (2010) 'Mitochondrial fusion is required for mtdna stability in skeletal muscle and tolerance of mtDNA mutations', *Cell*. Elsevier Ltd, 141(2), pp. 280–289. doi: 10.1016/j.cell.2010.02.026.

Chen, H., Chomyn, A. and Chan, D. C. (2005) 'Disruption of fusion results in mitochondrial heterogeneity and dysfunction', *Journal of Biological Chemistry*, 280(28), pp. 26185–26192. doi: 10.1074/jbc.M503062200.

Chen, H., McCaffery, J. M. and Chan, D. C. (2007) 'Mitochondrial Fusion Protects against Neurodegeneration in the Cerebellum', *Cell*, 130(3), pp. 548–562. doi: 10.1016/j.cell.2007.06.026.

Chockalingam, A. *et al.* (2009) 'TLR9 traffics through the Golgi complex to localize to endolysosomes and respond to CpG DNA.', *Immunology and cell biology*. England, 87(3), pp. 209–217. doi: 10.1038/icb.2008.101.

Cipolat, S. *et al.* (2004) 'OPA1 requires mitofusin 1 to promote mitochondrial fusion', *Proceedings of the National Academy of Sciences*, 101(45), pp. 15927–15932. doi: 10.1073/pnas.0407043101.

Civiletto, G. *et al.* (2015) 'Opa1 overexpression ameliorates the phenotype of two mitochondrial disease mouse models', *Cell Metabolism*. The Authors, 21(6), pp. 845–854. doi: 10.1016/j.cmet.2015.04.016.

Clark, I. E. *et al.* (2006) 'Drosophila pink1 is required for mitochondrial function and interacts genetically with parkin.', *Nature*. England, pp. 1162–1166. doi: 10.1038/nature04779.

Clayton, D. A. (1982) 'Replication of animal mitochondrial DNA', *Cell*, 28(4), pp. 693–705. doi: 10.1016/0092-8674(82)90049-6.

Cogliati, S. *et al.* (2013) 'Mitochondrial cristae shape determines respiratory chain supercomplexes

assembly and respiratory efficiency', *Cell*. The Authors, 155(1), pp. 160–171. doi: 10.1016/j.cell.2013.08.032.

Cogliati, S., Enriquez, J. A. and Scorrano, L. (2016) 'Mitochondrial Cristae: Where Beauty Meets Functionality', *Trends in Biochemical Sciences*. Elsevier Ltd, 41(3), pp. 261–273. doi: 10.1016/j.tibs.2016.01.001.

Collins, L. V. *et al.* (2004) 'Endogenously oxidized mitochondrial DNA induces in vivo and in vitro inflammatory responses', *Journal of Leukocyte Biology*, 75(June), pp. 995–1000. doi: 10.1189/jlb.0703328.1.

Delettre, C. *et al.* (2000) 'Nuclear gene OPA1, encoding a mitochondrial dynamin-related protein, is mutated in dominant optic atrophy', *Nature Genetics*, 26(2), pp. 207–210. doi: 10.1038/79936.

Delettre, C. *et al.* (2001) 'Mutation spectrum and splicing variants in the OPA1 gene', *Human Genetics*, 109(6), pp. 584–591. doi: 10.1007/s00439-001-0633-y.

Demers-Lamarche, J. *et al.* (2016) 'Loss of mitochondrial function impairs Lysosomes∗', *Journal of Biological Chemistry*, 291(19), pp. 10263–10276. doi: 10.1074/jbc.M115.695825.

Denson, L. a *et al.* (2003) 'Interleukin-6 inhibits hepatic growth hormone signaling via upregulation of Cis and Socs-3.', *American journal of physiology. Gastrointestinal and liver physiology*, 284(4), pp. G646-54. doi: 10.1152/ajpgi.00178.2002.

Detmer, S. A. and Chan, D. C. (2007) 'Complementation between mouse Mfn1 and Mfn2 protects mitochondrial fusion defects caused by CMT2A disease mutations', *Journal of Cell Biology*, 176(4), pp. 405–414. doi: 10.1083/jcb.200611080.

Deval, C. *et al.* (2008) 'Amino-acid limitation induces the GCN2 signaling pathway in myoblasts but not in myotubes', *Biochimie*, 90(11–12), pp. 1716–1721. doi: 10.1016/j.biochi.2008.07.004.

Dick, M. S. *et al.* (2016) 'ASC filament formation serves as a signal amplification mechanism for inflammasomes', *Nature Communications*, 7(May). doi: 10.1038/ncomms11929.

Donnelly, N. *et al.* (2013) 'The eIF2α kinases: Their structures and functions', *Cellular and Molecular Life Sciences*, 70(19), pp. 3493–3511. doi: 10.1007/s00018-012-1252-6.

Dooley, H. C. *et al.* (2014) 'WIPI2 links LC3 conjugation with PI3P, autophagosome formation, and pathogen clearance by recruiting Atg12-5-16L1.', *Molecular cell*. United States, 55(2), pp. 238–252. doi: 10.1016/j.molcel.2014.05.021.

Del Dotto, V. *et al.* (2017) 'OPA1 Isoforms in the Hierarchical Organization of Mitochondrial Functions', *Cell Reports*. ElsevierCompany., 19(12), pp. 2557–2571. doi: 10.1016/j.celrep.2017.05.073.

Duhamel, M. *et al.* (2016) 'The proprotein convertase PC1/3 regulates TLR9 trafficking and the associated signaling pathways', *Scientific Reports*, 6(September 2015), pp. 1–13. doi: 10.1038/srep19360.

Duvezin-Caubet, S. *et al.* (2006) 'Proteolytic processing of OPA1 links mitochondrial dysfunction to alterations in mitochondrial morphology', *Journal of Biological Chemistry*, 281(49), pp. 37972–37979. doi: 10.1074/jbc.M606059200.

Eiberg, H. *et al.* (1994) 'Dominant optic atrophy (OPA1) mapped to chromosome 3q region. I. Linkage analysis.', *Human molecular genetics*. England, 3(6), pp. 977–980.

Elachouri, G. *et al.* (2011) 'OPA1 links human mitochondrial genome maintenance to mtDNA replication and distribution', *Genome Research*, 21(1), pp. 12–20. doi: 10.1101/gr.108696.110.

Engelfried, K. *et al.* (2006) 'Charcot-Marie-Tooth neuropathy type 2A: Novel mutations in the mitofusin 2 gene (MFN2)', *BMC Medical Genetics*, 7(53), pp. 1–7. doi: 10.1186/1471-2350-7-53.

Estall, J. L. *et al.* (2009) 'PGC-1alpha negatively regulates hepatic FGF21 expression by modulating the heme/Rev-Erb(alpha) axis.', *Proceedings of the National Academy of Sciences of the United States of America*. United States, 106(52), pp. 22510–22515. doi: 10.1073/pnas.0912533106.

Ewald, S. E. *et al.* (2008) 'The ectodomain of Toll-like receptor 9 is cleaved to generate a functional receptor', *Nature*, 456(7222), pp. 658–662. doi: 10.1038/nature07405.

Fader, C. M. *et al.* (2009) 'TI-VAMP/VAMP7 and VAMP3/cellubrevin: two v-SNARE proteins involved in specific steps of the autophagy/multivesicular body pathways.', *Biochimica et biophysica acta*. Netherlands, 1793(12), pp. 1901–1916. doi: 10.1016/j.bbamcr.2009.09.011.

Fader, C. M. and Colombo, M. I. (2009) 'Autophagy and multivesicular bodies: Two closely related partners', *Cell Death and Differentiation*, 16(1), pp. 70–78. doi: 10.1038/cdd.2008.168.

Fakruddin, M. *et al.* (2018) 'Defective Mitochondrial tRNA Taurine Modification Activates Global Proteostress and Leads to Mitochondrial Disease', *Cell Reports*. ElsevierCompany., 22(2), pp. 482–496. doi: 10.1016/j.celrep.2017.12.051.

Farré, J. and Subramani, S. (2016) 'Mechanistic insights into selective autophagy pathways: lessons from yeast', *Nature Publishing Group*. Nature Publishing Group, 17(9), pp. 537–552. doi: 10.1038/nrm.2016.74.

Fernández-Mosquera, L. *et al.* (2017) 'Acute and chronic mitochondrial respiratory chain deficiency differentially regulate lysosomal biogenesis', *Scientific Reports*. Nature Publishing Group, 7(February), pp. 1–11. doi: 10.1038/srep45076.

Ferre, M. *et al.* (2005) 'eOPA1: an online database for OPA1 mutations.', *Human mutation*. United States, 25(5), pp. 423–428. doi: 10.1002/humu.20161.

Ferre, M. *et al.* (2015) 'Improved locus-specific database for OPA1 mutations allows inclusion of advanced clinical data.', *Human mutation*. United States, 36(1), pp. 20–25. doi: 10.1002/humu.22703.

Fisher, F. M. *et al.* (2014) 'Fibroblast growth factor 21 limits lipotoxicity by promoting hepatic fatty acid activation in mice on methionine and choline-deficient diets', *Gastroenterology*. United States: Elsevier, Inc, 147(5), p. 1073–1083.e3. doi: 10.1053/j.gastro.2014.07.044.

Frezza, C. *et al.* (2006) 'OPA1 Controls Apoptotic Cristae Remodeling Independently from Mitochondrial Fusion', *Cell*, 126(1), pp. 177–189. doi: 10.1016/j.cell.2006.06.025.

Friedman, J. R. *et al.* (2011) 'ER tubules mark sites of mitochondrial division', *Science*, 334(6054), pp. 358–362. doi: 10.1126/science.1207385.

Fukui, R. *et al.* (2009) 'Unc93B1 biases Toll-like receptor responses to nucleic acid in dendritic cells toward DNA- but against RNA-sensing.', *The Journal of experimental medicine*. United States, 206(6), pp. 1339–1350. doi: 10.1084/jem.20082316.

Galluzzi, L. *et al.* (2017) 'Molecular definitions of autophagy and related processes', *The EMBO Journal*, 36(13), pp. 1811–1836. doi: 10.15252/embj.201796697.

Garcia-Martinez, I. *et al.* (2016) 'Hepatocyte mitochondrial DNA drives nonalcoholic steatohepatitis by activation of TLR9.', *The Journal of clinical investigation*. United States, 126(3), pp. 859–864. doi: 10.1172/JCI83885.

Gentz, S. H. L. *et al.* (2013) 'Implication of eIF2alpha kinase GCN2 in induction of apoptosis and endoplasmic reticulum stress-responsive genes by sodium salicylate.', *The Journal of pharmacy and pharmacology*. England, 65(3), pp. 430–440. doi: 10.1111/jphp.12002.

Goh, K. C., deVeer, M. J. and Williams, B. R. (2000) 'The protein kinase PKR is required for p38 MAPK activation and the innate immune response to bacterial endotoxin', *EMBO Journal*, 19(16), pp. 4292–4297. doi: 10.1093/emboj/19.16.4292.

Gordon, P. B. and Seglen, P. O. (1988) 'Prelysosomal convergence of autophagic and endocytic pathways.', *Biochemical and biophysical research communications*. United States, 151(1), pp. 40–47.

Green, N. M. and Marshak-Rothstein, A. (2011) 'Toll-like receptor driven B cell activation in the induction of systemic autoimmunity.', *Seminars in immunology*. England, 23(2), pp. 106–112. doi: 10.1016/j.smim.2011.01.016.

Griparic, L. *et al.* (2004) 'Loss of the Intermembrane Space Protein Mgm1/OPA1 Induces Swelling and Localized Constrictions along the Lengths of Mitochondria', *Journal of Biological Chemistry*, 279(18), pp. 18792–18798. doi: 10.1074/jbc.M400920200.

Griparic, L., Kanazawa, T. and Van Der Bliek, A. M. (2007) 'Regulation of the mitochondrial dynamin-like protein Opa1 by proteolytic cleavage', *Journal of Cell Biology*, 178(5), pp. 757–764. doi: 10.1083/jcb.200704112.

Guasti, L. *et al.* (2014) 'Elevated FGF21 leads to attenuated postnatal linear growth in preterm infants through gh resistance in chondrocytes', *Journal of Clinical Endocrinology and Metabolism*, 99(11), pp. E2198–E2206. doi: 10.1210/jc.2014-1566.

Guillery, O. *et al.* (2008) 'Metalloprotease-mediated OPA1 processing is modulated by the mitochondrial membrane potential', *Biology of the Cell*, 100(5), pp. 315–325. doi: 10.1042/BC20070110.

Gunter, T. E. *et al.* (1998) 'The Ca2+ transport mechanisms of mitochondria and Ca2+ uptake from physiological-type Ca2+ transients.', *Biochimica et biophysica acta*. Netherlands, 1366(1–2), pp. 5–15.

Guo, Y. *et al.* (2016) 'Fibroblast growth factor 21 potentially inhibits microRNA-33 expression to affect macrophage actions', *Lipids in Health and Disease*. Lipids in Health and Disease, 15(1), pp. 1–4. doi: 10.1186/s12944-016-0381-6.

Gustafsson, C. M., Falkenberg, M. and Larsson, N.-G. (2016) 'Maintenance and Expression of Mammalian Mitochondrial DNA', *Annual Review of Biochemistry*, 85(1), pp. 133–160. doi: 10.1146/annurev-

biochem-060815-014402.

Hamacher-Brady, A. *et al.* (2016) 'Mitophagy programs: Mechanisms and physiological implications of mitochondrial targeting by autophagy', *Cellular and Molecular Life Sciences*. Springer International Publishing, 73(4), pp. 775–795. doi: 10.1007/s00018-015-2087-8.

Hayashi, K., Sasai, M. and Iwasaki, A. (2015) 'Toll-like receptor 9 trafficking and signaling for type i interferons requires PIKfyve activity', *International Immunology*, 27(9), pp. 435–445. doi: 10.1093/intimm/dxv021.

Heo, J. M. *et al.* (2015) 'The PINK1-PARKIN Mitochondrial Ubiquitylation Pathway Drives a Program of OPTN / NDP52 Recruitment and TBK1 Activation to Promote Mitophagy', *Molecular Cell*. Elsevier Inc., 60(1), pp. 1–14. doi: 10.1016/j.molcel.2015.08.016.

Hermann, G. J. and Shaw, J. M. (1998) 'Mitochondrial dynamics in yeast.', *Annual review of cell and developmental biology*. United States, 14, pp. 265–303. doi: 10.1146/annurev.cellbio.14.1.265.

Hockenbery, D. *et al.* (1990) 'Bcl-2 is an inner mitochondrial membrane protein that blocks programmed cell death.', *Nature*. England, 348(6299), pp. 334–336. doi: 10.1038/348334a0.

Honda, K. *et al.* (2005) 'Spatiotemporal regulation of MyD88-IRF-7 signalling for robust type-I interferon induction.', *Nature*. England, 434(7036), pp. 1035–1040. doi: 10.1038/nature03547.

Hong, E. E. *et al.* (2013) 'Regionally Specific and Genome-Wide Analyses Conclusively Demonstrate the Absence of CpG Methylation in Human Mitochondrial DNA', *Molecular and Cellular Biology*, 33(14), pp. 2683–2690. doi: 10.1128/MCB.00220-13.

Hoyt, C. S. (1980) 'Autosomal Dominant Optic Atrophy A Spectrum of Disability', *Ophthalmology*. American Academy of Ophthalmology, Inc, 87(3), pp. 245–251. doi: 10.1016/S0161-6420(80)35247-0.

Hudson, G. *et al.* (2008) 'Mutation of OPA1 causes dominant optic atrophy with external ophthalmoplegia, ataxia, deafness and multiple mitochondrial DNA deletions: A novel disorder of mtDNA maintenance', *Brain*, 131(2), pp. 329–337. doi: 10.1093/brain/awm272.

Ichinohe, T., Pang, I. K. and Iwasaki, A. (2010) 'Influenza virus activates inflammasomes via its intracellular M2 ion channel', *Nature Immunology*. Nature Publishing Group, 11(5), pp. 404–410. doi: 10.1038/ni.1861.

Inagaki, T. *et al.* (2008) 'Inhibition of Growth Hormone Signaling by the Fasting-Induced Hormone FGF21', *Cell Metabolism*, 8(1), pp. 77–83. doi: 10.1016/j.cmet.2008.05.006.

Ingerman, E. *et al.* (2005) 'Dnm1 forms spirals that are structurally tailored to fit mitochondria', *Journal of Cell Biology*, 170(7), pp. 1021–1027. doi: 10.1083/jcb.200506078.

Ishihara, N. (2004) 'Mitofusin 1 and 2 play distinct roles in mitochondrial fusion reactions via GTPase activity', *Journal of Cell Science*, 117(26), pp. 6535–6546. doi: 10.1242/jcs.01565.

Ishihara, N. *et al.* (2006) 'Regulation of mitochondrial morphology through proteolytic cleavage of OPA1', *EMBO Journal*, 25(13), pp. 2966–2977. doi: 10.1038/sj.emboj.7601184.

Ishii, K. J. *et al.* (2006) 'A Toll-like receptor-independent antiviral response induced by double-stranded

B-form DNA.', *Nature immunology*. United States, 7(1), pp. 40–48. doi: 10.1038/ni1282.

Ishikawa, H. and Barber, G. N. (2008) 'STING is an endoplasmic reticulum adaptor that facilitates innate immune signalling.', *Nature*. England, 455(7213), pp. 674–678. doi: 10.1038/nature07317.

Ishikawa, H., Ma, Z. and Barber, G. N. (2009) 'STING regulates intracellular DNA-mediated, type I interferon-dependent innate immunity.', *Nature*. England, 461(7265), pp. 788–792. doi: 10.1038/nature08476.

Jayashankar, V., Mueller, I. A. and Rafelski, S. M. (2016) 'Shaping the multi-scale architecture of mitochondria', *Current Opinion in Cell Biology*. Elsevier Ltd, 38, pp. 45–51. doi: 10.1016/j.ceb.2016.02.006.

Ji, H. *et al.* (2002) 'Critical roles for interleukin 1 and tumor necrosis factor alpha in antibody-induced arthritis.', *The Journal of experimental medicine*. United States, 196(1), pp. 77–85.

Jiang, X. *et al.* (2014) 'Activation of mitochondrial protease OMA1 by Bax and Bak promotes cytochrome c release during apoptosis', *Proceedings of the National Academy of Sciences*, 111(41), pp. 14782–14787. doi: 10.1073/pnas.1417253111.

Jo, E.-K. *et al.* (2016) 'Molecular mechanisms regulating NLRP3 inflammasome activation', *Cellular and Molecular Immunology*, 13(2), pp. 148–159. doi: 10.1038/cmi.2015.95.

Johnston, P. B. *et al.* (1979) 'A clinicopathologic study of autosomal dominant optic atrophy', *American Journal of Ophthalmology*. United States, 88(5), pp. 868–875. doi: 10.1016/0002-9394(79)90565-8.

Julian, M. W. *et al.* (2012) 'Mitochondrial Transcription Factor A Serves as a Danger Signal by Augmenting Plasmacytoid Dendritic Cell Responses to DNA', *The Journal of Immunology*, 189(1), pp. 433–443. doi: 10.4049/jimmunol.1101375.

Kanneganti, T. D. (2015) 'The inflammasome: Firing up innate immunity', *Immunological Reviews*, 265(1), pp. 1–5. doi: 10.1111/imr.12297.

Karanasios, E. *et al.* (2008) 'Dynamic association of the ULK1 complex with omegasomes during autophagy induction', *Journal of Cell Science*, 131(2), pp. 314–317.

Käser, M. *et al.* (2003) 'Oma1, a Novel Membrane-bound Metallopeptidase in Mitochondria with Activities Overlapping with the m-AAA Protease', *Journal of Biological Chemistry*, 278(47), pp. 46414–46423. doi: 10.1074/jbc.M305584200.

Kaufman, B. a *et al.* (2000) 'In organello formaldehyde crosslinking of proteins to mtDNA: identification of bifunctional proteins.', *Proceedings of the National Academy of Sciences of the United States of America*, 97(14), pp. 7772–7. doi: 10.1073/pnas.140063197.

Kawaguchi, M. *et al.* (2011) 'Inflammasome activation of cardiac fibroblasts is essential for myocardial ischemia/reperfusion injury', *Circulation*, 123(6), pp. 594–604. doi: 10.1161/CIRCULATIONAHA.110.982777.

Khaminets, A., Behl, C. and Dikic, I. (2018) 'Ubiquitin-Dependent And Independent Signals In Selective Autophagy', *Trends in Cell Biology*. Elsevier, 26(1), pp. 6–16. doi: 10.1016/j.tcb.2015.08.010.

Kijima, K. *et al.* (2005) 'Mitochondrial GTPase mitofusin 2 mutation in Charcot-Marie-Tooth neuropathy type 2A.', *Human genetics*. Germany, 116(1–2), pp. 23–27. doi: 10.1007/s00439-004-1199-2.

Kim, J. Y. *et al.* (2005) 'Mitochondrial DNA content is decreased in autosomal dominant optic atrophy', *Neurology*, 64, pp. 966–972.

Kim, K. H. *et al.* (2013) 'Autophagy deficiency leads to protection from obesity and insulin resistance by inducing Fgf21 as a mitokine', *Nature Medicine*. Nature Publishing Group, 19(1), pp. 83–92. doi: 10.1038/nm.3014.

Kim, S. H. *et al.* (2015) 'Fibroblast growth factor 21 participates in adaptation to endoplasmic reticulum stress and attenuates obesity-induced hepatic metabolic stress', *Diabetologia*, 58(4), pp. 809–818. doi: 10.1007/s00125-014-3475-6.

Kjer, P., Jensen, O. A. and Klinken, L. (1983) 'Histopathology of eye, optic nerve and brain in a case of dominant optic atrophy.', *Acta ophthalmologica*. Denmark, 61(2), pp. 300–312.

Klionsky, D. J. *et al.* (2016) 'Guidelines for the use and interpretation of assays for monitoring autophagy (3rd edition)', *Autophagy*, 12(1), pp. 1–222. doi: 10.1080/15548627.2015.1100356.

Klionsky, D. J., Eskelinen, E.-L. L. and Deretic, V. (2014) 'Autophagosomes, phagosomes, autolysosomes, phagolysosomes, autophagolysosomes... Wait, I'm confused', *Autophagy*. United States, 10(4), pp. 549–551. doi: 10.4161/auto.28448.

Kopp, E. and Ghosh, S. (1994) 'Inhibition of NF-kappa B by sodium salicylate and aspirin', *Science*, 265(5174), pp. 956–959. doi: 10.1126/science.8052854.

Koshiba, T. *et al.* (2004) 'Structural Basis of Mitochondrial Tethering by Mitofusin Complexes', *Science*, 305(5685), p. 858 LP-862. Available at: http://science.sciencemag.org/content/305/5685/858.abstract.

Koshiba, T. *et al.* (2011) 'Mitochondrial membrane potential is required for MAVS-mediated antiviral signaling', *Science Signaling*, 4(158). doi: 10.1126/scisignal.2001147.

Krysko, D. V. *et al.* (2011) 'Emerging role of damage-associated molecular patterns derived from mitochondria in inflammation', *Trends in Immunology*. Elsevier Ltd, 32(4), pp. 157–164. doi: 10.1016/j.it.2011.01.005.

Kubicky, R. A. *et al.* (2012) 'Role of fibroblast growth factor 21 (FGF21) in undernutrition-related attenuation of growth in mice', *Endocrinology*, 153(5), pp. 2287–2295. doi: 10.1210/en.2011-1909.

Kukat, C. *et al.* (2011) 'Super-resolution microscopy reveals that mammalian mitochondrial nucleoids have a uniform size and frequently contain a single copy of mtDNA', *Proceedings of the National Academy of Sciences*, 108(33), pp. 13534–13539. doi: 10.1073/pnas.1109263108.

Kukat, C. *et al.* (2015) 'Cross-strand binding of TFAM to a single mtDNA molecule forms the mitochondrial nucleoid', *Proceedings of the National Academy of Sciences*, 112(36), pp. 11288–11293. doi: 10.1073/pnas.1512131112.

Kutukculer, N., Caglayan, S. and Aydogdu, F. (1998) 'Study of pro-inflammatory (TNF-alpha, IL-1alpha, IL-6) and T-cell-derived (IL-2, IL-4) cytokines in plasma and synovial fluid of patients with juvenile chronic arthritis: correlations with clinical and laboratory parameters.', *Clinical rheumatology*. Germany, 17(4),

pp. 288–292.

Labrousse, A. M. *et al.* (1999) 'C. elegans dynamin-related protein DRP-1 controls severing of the mitochondrial outer membrane', *Molecular Cell*, 4(5), pp. 815–826. doi: 10.1016/S1097-2765(00)80391-3.

Lamkanfi, M. (2011) 'Emerging inflammasome effector mechanisms', *Nature Reviews Immunology*. Nature Publishing Group, 11(3), pp. 213–220. doi: 10.1038/nri2936.

Lamkanfi, M. and Dixit, V. M. (2014) 'Mechanisms and functions of inflammasomes', *Cell*. Elsevier Inc., 157(5), pp. 1013–1022. doi: 10.1016/j.cell.2014.04.007.

Lamphier, M. *et al.* (2014) 'Novel Small Molecule Inhibitors of TLR7 and TLR9: Mechanism of Action and Efficacy In Vivo', *Molecular Pharmacology*, 85(3), pp. 429–440. doi: 10.1124/mol.113.089821.

Lamphier, M. S. *et al.* (2006) 'TLR9 and the recognition of self and non-self nucleic acids.', *Annals of the New York Academy of Sciences*. United States, 1082, pp. 31–43. doi: 10.1196/annals.1348.005.

Landes, T. *et al.* (2010) 'The BH3-only Bnip3 binds to the dynamin Opa1 to promote mitochondrial fragmentation and apoptosis by distinct mechanisms', *EMBO Reports*, 11(6), pp. 459–465. doi: 10.1038/embor.2010.50.

Larsson, N. G. *et al.* (1998) 'Mitochondrial transcription factor A is necessary for mtDNA maintenance and embryogenesis in mice', *Nature Genetics*, 18(3), pp. 231–236. doi: 10.1038/ng0398-231.

Latz, E. *et al.* (2004) 'TLR9 signals after translocating from the ER to CpG DNA in the lysosome', *Nature Immunology*, 5(2), pp. 190–198. doi: 10.1038/ni1028.

Lawson, V. H., Graham, B. V and Flanigan, K. M. (2005) 'Clinical and electrophysiologic features of CMT2A with mutations in the mitofusin 2 gene', *Neurology*, 65, pp. 197–204.

Lazarou, M. *et al.* (2015) 'The ubiquitin kinase PINK1 recruits autophagy receptors to induce mitophagy', *Nature*, 524(7565), pp. 309–314. doi: 10.1038/nature14893.

Lee, B. L. and Barton, G. M. (2014) 'Trafficking of endosomal Toll-like receptors.', *Trends in Cell Biology*. England: Elsevier Ltd, 24(6), pp. 360–369. doi: 10.1016/j.tcb.2013.12.002.

Legros, F. (2004) 'Organization and dynamics of human mitochondrial DNA', *Journal of Cell Science*, 117(13), pp. 2653–2662. doi: 10.1242/jcs.01134.

Leifer, C. A. *et al.* (2004) 'TLR9 is localized in the endoplasmic reticulum prior to stimulation.', *Journal of immunology (Baltimore, Md. : 1950)*. United States, 173(2), pp. 1179–1183.

Lenaers, G. *et al.* (2012) 'Dominant optic atrophy', *Orphanet Journal of Rare Diseases*, 7(1), pp. 1–12. doi: 10.1186/1750-1172-7-46.

De Leo, M. G. *et al.* (2016) 'Autophagosome-lysosome fusion triggers a lysosomal response mediated by TLR9 and controlled by OCRL', *Nature Cell Biology*, 18(8), pp. 839–850. doi: 10.1038/ncb3386.

Lewis, S. C., Uchiyama, L. F. and Nunnari, J. (2016) 'ER-mitochondria contacts couple mtDNA synthesis with Mitochondrial division in human cells', *Science*, 353(6296). doi: 10.1126/science.aaf5549.

Li, S. *et al.* (2005) 'Requirement for serum response factor for skeletal muscle growth and maturation revealed by tissue-specific gene deletion in mice.', *Proceedings of the National Academy of Sciences of the United States of America*, 102(4), pp. 1082–7. doi: 10.1073/pnas.0409103102.

Li, Y., Berke, I. C. and Modis, Y. (2012) 'DNA binding to proteolytically activated TLR9 is sequence-independent and enhanced by DNA curvature', *EMBO Journal*. Nature Publishing Group, 31(4), pp. 919–931. doi: 10.1038/emboj.2011.441.

Liao, C. *et al.* (2017) 'Dysregulated mitophagy and mitochondrial organization in optic atrophy due to OPA1 mutations.', *Neurology*. United States, 88(2), pp. 131–142. doi: 10.1212/WNL.0000000000003491.

Liesa, M., Palacin, M. and Zorzano, A. (2009) 'Mitochondrial Dynamics in Mammalian Health and Disease', *Physiological Reviews*, 89(3), pp. 799–845. doi: 10.1152/physrev.00030.2008.

Lieskovska, J., Guo, D. and Derman, E. (2003) 'Growth impairment in IL-6-overexpressing transgenic mice is associated with induction of SOCS3 mRNA', *Growth Hormone and IGF Research*, 13(1), pp. 26–35. doi: 10.1016/S1096-6374(02)00135-1.

Lindgren, U. *et al.* (2015) 'Mitochondrial pathology in inclusion body myositis', *Neuromuscular Disorders*. Elsevier B.V., 25(4), pp. 281–288. doi: 10.1016/j.nmd.2014.12.010.

Liu, E. Y. *et al.* (2015) 'Loss of autophagy causes a synthetic lethal deficiency in DNA repair.', *Proceedings of the National Academy of Sciences of the United States of America*. United States, 112(3), pp. 773–778. doi: 10.1073/pnas.1409563112.

Liu, L. *et al.* (2012) 'Mitochondrial outer-membrane protein FUNDC1 mediates hypoxia-induced mitophagy in mammalian cells.', *Nature cell biology*. England, 14(2), pp. 177–185. doi: 10.1038/ncb2422.

Liu, N. *et al.* (2014) 'Requirement of MEF2A, C, and D for skeletal muscle regeneration', *Proceedings of the National Academy of Sciences*, 111(11), pp. 4109–4114. doi: 10.1073/pnas.1401732111.

Liu, Y. *et al.* (2015) 'Hypoxia induced HMGB1 and mitochondrial DNA interactions mediate tumor growth in hepatocellular carcinoma through Toll-like receptor 9', *Journal of Hepatology*, 63(1), pp. 114–121. doi: 10.1016/j.jhep.2015.02.009.

Loson, O. C. *et al.* (2013) 'Fis1, Mff, MiD49, and MiD51 mediate Drp1 recruitment in mitochondrial fission', *Molecular Biology of the Cell*, 24(5), pp. 659–667. doi: 10.1091/mbc.E12-10-0721.

Lu, B. *et al.* (2012) 'Novel role of PKR in inflammasome activation and HMGB1 release', *Nature*, 488(7413), pp. 670–674. doi: 10.1038/nature11290.

Lu, B. *et al.* (2013) 'Phosphorylation of Human TFAM in Mitochondria Impairs DNA Binding and Promotes Degradation by the AAA+Lon Protease', *Molecular Cell*. Elsevier Inc., 49(1), pp. 121–132. doi: 10.1016/j.molcel.2012.10.023.

Malik, A. *et al.* (2016) 'Idiopathic inflammatory myopathies: Clinical approach and management', *Frontiers in Neurology*, 7(MAY). doi: 10.3389/fneur.2016.00064.

Malka, F. *et al.* (2005) 'Separate fusion of outer and inner mitochondrial membranes', *EMBO Reports*,

6(9), pp. 853–859. doi: 10.1038/sj.embor.7400488.

Man, S. M. and Kanneganti, T. D. (2015) 'Regulation of inflammasome activation', *Immunological Reviews*, 265(1), pp. 6–21. doi: 10.1111/imr.12296.

Man, S. M., Karki, R. and Kanneganti, T. D. (2016) 'AIM2 inflammasome in infection, cancer, and autoimmunity: Role in DNA sensing, inflammation, and innate immunity', *European Journal of Immunology*, 46(2), pp. 269–280. doi: 10.1002/eji.201545839.

Mariathasan, S. *et al.* (2006) 'Cryopyrin activates the inflammasome in response to toxins and ATP', *Nature*, 440(7081), pp. 228–232. doi: 10.1038/nature04515.

Matsunaga, K. *et al.* (2010) 'Autophagy requires endoplasmic reticulum targeting of the PI3-kinase complex via Atg14L.', *The Journal of cell biology*. United States, 190(4), pp. 511–521. doi: 10.1083/jcb.200911141.

Matsushima, Y., Goto, Y. and Kaguni, L. S. (2010) 'Mitochondrial Lon protease regulates mitochondrial DNA copy number and transcription by selective degradation of mitochondrial transcription factor A (TFAM)', *October*. doi: 10.1073/pnas.1008924107/-/DCSupplemental.www.pnas.org/cgi/doi/10.1073/pnas.1008924107.

McCarthy, C. G. *et al.* (2015) 'Circulating mitochondrial DNA and Toll-like receptor 9 are associated with vascular dysfunction in spontaneously hypertensive rats', *Cardiovascular Research*, 107(1), pp. 119–130. doi: 10.1093/cvr/cvv137.

Mclelland, G. *et al.* (2014) 'Parkin and PINK 1 function in a vesicular trafficking pathway regulating mitochondrial quality control', *The EMBO Journal*, 33(4), pp. 282–295. doi: 10.1002/embj.201385902.

McLelland, G. L. *et al.* (2016) 'Syntaxin-17 delivers PINK1/parkin-dependent mitochondrial vesicles to the endolysosomal system', *Journal of Cell Biology*, 214(3), pp. 275–291. doi: 10.1083/jcb.201603105.

Merkwirth, C. *et al.* (2008) 'Prohibitins control cell proliferation and apoptosis by regulating OPA1-dependent cristae morphogenesis in mitochondria', *Genes and Development*, 22(4), pp. 476–488. doi: 10.1101/gad.460708.

Mills, E. L., Kelly, B. and O'Neill, L. A. J. (2017) 'Mitochondria are the powerhouses of immunity', *Nature Immunology*, 18(5), pp. 488–498. doi: 10.1038/ni.3704.

Mishra, P. *et al.* (2014) 'Proteolytic cleavage of Opa1 stimulates mitochondrial inner membrane fusion and couples fusion to oxidative phosphorylation', *Cell Metabolism*. Elsevier Inc., 19(4), pp. 630–641. doi: 10.1016/j.cmet.2014.03.011.

Mishra, P. and Chan, D. C. (2014) 'Mitochondrial dynamics and inheritance during cell division, development and disease', *Nature Reviews Molecular Cell Biology*. Nature Publishing Group, 15(10), pp. 634–646. doi: 10.1038/nrm3877.

Moore, A. S. and Holzbaur, E. L. F. (2016) 'Dynamic recruitment and activation of ALS-associated TBK1 with its target optineurin are required for efficient mitophagy', *Proceedings of the National Academy of Sciences*, pp. 1–10. doi: 10.1073/pnas.1523810113.

Mügge, F. L. B. and Silva, A. M. (2017) 'Aspirin metabolite sodium salicylate selectively inhibits

transcriptional activity of ATF6α and downstream target genes', *Scientific Reports*, 7(1), pp. 1–12. doi: 10.1038/s41598-017-09500-x.

Muñoz, J. P. *et al.* (2013) 'Mfn2 modulates the UPR and mitochondrial function via repression of PERK', *EMBO Journal*, 32(17), pp. 2348–2361. doi: 10.1038/emboj.2013.168.

Muñoz, J. P. and Zorzano, A. (2015) 'Analysis of Mitochondrial Morphology and Function Under Conditions of Mitofusin 2 Deficiency', in Weissig, V. and Edeas, M. (eds) *Mitochondrial Medicine: Volume II, Manipulating Mitochondrial Function*. New York, NY: Springer New York, pp. 307–320. doi: 10.1007/978-1-4939-2288-8_21.

Nakahira, K. *et al.* (2011) 'Autophagy proteins regulate innate immune responses by inhibiting the release of mitochondrial DNA mediated by the NALP3 inflammasome', *Nature Immunology*. Nature Publishing Group, 12(3), pp. 222–230. doi: 10.1038/ni.1980.

Nakahira, K., Hisata, S. and Choi, A. M. (2015) 'The roles of Mitochondrial DAMPs in Diseases.', *Antioxidants & redox signaling*, 23(17), pp. 1–78. doi: 10.1089/ars.2015.6407.

Narendra, D. *et al.* (2008) 'Parkin is recruited selectively to impaired mitochondria and promotes their autophagy', *Journal of Cell Biology*, 183(5), pp. 795–803. doi: 10.1083/jcb.200809125.

Neuspiel, M. *et al.* (2008) 'Cargo-selected transport from the mitochondria to peroxisomes is mediated by vesicular carriers.', *Current biology : CB*. England, 18(2), pp. 102–108. doi: 10.1016/j.cub.2007.12.038.

Ngo, H. B. *et al.* (2014) 'Distinct structural features of TFAM drive mitochondrial DNA packaging versus transcriptional activation.', *Nature communications*. England, 5, p. 3077. doi: 10.1038/ncomms4077.

Noguera, E. (2014) *Paper de les proteïnes de fusió mitocondrial Opa1 i Mfn1 durant la diferenciació miogènica*.

Nunnari, J. and Suomalainen, A. (2012) 'Mitochondria: In sickness and in health', *Cell*. Elsevier Inc., 148(6), pp. 1145–1159. doi: 10.1016/j.cell.2012.02.035.

Oka, T. *et al.* (2012) 'Mitochondrial DNA that escapes from autophagy causes inflammation and heart failure.', *Nature*. England, 485(7397), pp. 251–255. doi: 10.1038/nature10992.

Okamoto, K. and Shaw, J. M. (2005) 'Mitochondrial Morphology and Dynamics in Yeast and Multicellular Eukaryotes', *Annual Review of Genetics*, 39(1), pp. 503–536. doi: 10.1146/annurev.genet.38.072902.093019.

Olichon, A. *et al.* (2003) 'Loss of OPA1 perturbates the mitochondrial inner membrane structure and integrity, leading to cytochrome c release and apoptosis', *Journal of Biological Chemistry*, 278(10), pp. 7743–7746. doi: 10.1074/jbc.C200677200.

Olichon, A. *et al.* (2007) 'Effects of OPA1 mutations on mitochondrial morphology and apoptosis: relevance to ADOA pathogenesis.', *Journal of cellular physiology*. United States, 211(2), pp. 423–430. doi: 10.1002/jcp.20950.

Olichon, A. *et al.* (2007) 'OPA1 alternate splicing uncouples an evolutionary conserved function in mitochondrial fusion from a vertebrate restricted function in apoptosis', *Cell Death and Differentiation*,

14(4), pp. 682–692. doi: 10.1038/sj.cdd.4402048.

Otera, H. *et al.* (2010) 'Mff is an essential factor for mitochondrial recruitment of Drp1 during mitochondrial fission in mammalian cells', *Journal of Cell Biology*, 191(6), pp. 1141–1158. doi: 10.1083/jcb.201007152.

Ozaki, Y. *et al.* (2015) 'Rapid increase in fibroblast growth factor 21 in protein malnutrition and its impact on growth and lipid metabolism', *British Journal of Nutrition*, 114(9), pp. 1410–1418. doi: 10.1017/S0007114515002846.

Palikaras, K. and Tavernarakis, N. (2014) 'Mitochondrial homeostasis: The interplay between mitophagy and mitochondrial biogenesis', *Experimental Gerontology*. Elsevier Inc., 56, pp. 182–188. doi: 10.1016/j.exger.2014.01.021.

Park, J. *et al.* (2006) 'Mitochondrial dysfunction in Drosophila PINK1 mutants is complemented by parkin.', *Nature*. England, pp. 1157–1161. doi: 10.1038/nature04788.

Pelka, K. *et al.* (2014) 'Cutting edge: the UNC93B1 tyrosine-based motif regulates trafficking and TLR responses via separate mechanisms.', *Journal of immunology (Baltimore, Md. : 1950)*. United States, 193(7), pp. 3257–3261. doi: 10.4049/jimmunol.1301886.

Pereira, R. O. *et al.* (2017) 'OPA1 deficiency promotes secretion of FGF21 from muscle that prevents obesity and insulin resistance.', *The EMBO journal*. England, 36(14), pp. 2126–2145. doi: 10.15252/embj.201696179.

Pernas, L. and Scorrano, L. (2016) 'Mito-Morphosis: Mitochondrial Fusion, Fission, and Cristae Remodeling as Key Mediators of Cellular Function', *Annual Review of Physiology*, 78(1), pp. 505–531. doi: 10.1146/annurev-physiol-021115-105011.

Pesch, U. E. *et al.* (2001) 'OPA1 mutations in patients with autosomal dominant optic atrophy and evidence for semi-dominant inheritance.', *Human molecular genetics*. England, 10(13), pp. 1359–1368.

Picca, A. *et al.* (2017) 'Circulating mitochondrial DNA at the crossroads of mitochondrial dysfunction and inflammation during aging and muscle wasting disorders', *Rejuvenation Research*, XX(Xx), p. rej.2017.1989. doi: 10.1089/rej.2017.1989.

Piccioli, P. and Rubartelli, A. (2013) 'The secretion of IL-1β and options for release', *Seminars in Immunology*. Elsevier Ltd, 25(6), pp. 425–429. doi: 10.1016/j.smim.2013.10.007.

Politi, Y. *et al.* (2014) 'Paternal Mitochondrial Destruction after Fertilization Is Mediated by a Common Endocytic and Autophagic Pathway in Drosophila', *Developmental Cell*. Elsevier Inc., 29(3), pp. 305–320. doi: 10.1016/j.devcel.2014.04.005.

Polson, H. E. J. *et al.* (2010) 'Mammalian Atg18 (WIPI2) localizes to omegasome-anchored phagophores and positively regulates LC3 lipidation.', *Autophagy*. United States, 6(4), pp. 506–522. doi: 10.4161/auto.6.4.11863.

Potthoff, M. J. *et al.* (2009) 'FGF21 induces PGC-1 and regulates carbohydrate and fatty acid metabolism during the adaptive starvation response', *Proceedings of the National Academy of Sciences*, 106(26), pp. 10853–10858. doi: 10.1073/pnas.0904187106.

Quinsay, M. N. *et al.* (2010) 'Bnip3 mediates permeabilization of mitochondria and release of cytochrome c via a novel mechanism.', *Journal of molecular and cellular cardiology*. England, 48(6), pp. 1146–1156. doi: 10.1016/j.yjmcc.2009.12.004.

Quirós, P. M. *et al.* (2012) 'Loss of mitochondrial protease OMA1 alters processing of the GTPase OPA1 and causes obesity and defective thermogenesis in mice', *EMBO Journal*, 31(9), pp. 2117–2133. doi: 10.1038/emboj.2012.70.

Raimundo, N. *et al.* (2016) 'Mechanisms of communication between mitochondria and lysosomes', *International Journal of Biochemistry and Cell Biology*. Elsevier Ltd, 79, pp. 345–349. doi: 10.1016/j.biocel.2016.08.020.

Rawat, R. *et al.* (2010) 'Inflammasome up-regulation and activation in dysferlin-deficient skeletal muscle', *American Journal of Pathology*. American Society for Investigative Pathology, 176(6), pp. 2891–2900. doi: 10.2353/ajpath.2010.090058.

Al Rawi, S. *et al.* (2011) 'Postfertilization autophagy of sperm organelles prevents paternal mitochondrial DNA transmission.', *Science (New York, N.Y.)*. United States, 334(6059), pp. 1144–1147. doi: 10.1126/science.1211878.

Riggs, A. C. *et al.* (2005) 'Mice conditionally lacking the Wolfram gene in pancreatic islet beta cells exhibit diabetes as a result of enhanced endoplasmic reticulum stress and apoptosis', *Diabetologia*, 48(11), pp. 2313–2321. doi: 10.1007/s00125-005-1947-4.

Rojansky, R., Cha, M.-Y. and Chan, D. C. (2016) 'Elimination of paternal mitochondria in mouse embryos occurs through autophagic degradation dependent on PARKIN and MUL1.', *eLife*. England, 5. doi: 10.7554/eLife.17896.

Sagan, L. (1967) 'On the origin of mitosing cells', *Journal of Theoretical Biology*, 14(3), p. 225–IN6. doi: 10.1016/0022-5193(67)90079-3.

Santiago-Raber, M. L., Baudino, L. and Izui, S. (2009) 'Emerging roles of TLR7 and TLR9 in murine SLE', *Journal of Autoimmunity*. Elsevier Ltd, 33(3–4), pp. 231–238. doi: 10.1016/j.jaut.2009.10.001.

Sato, M. and Sato, K. (2011) 'Degradation of paternal mitochondria by fertilization-triggered autophagy in C. elegans embryos.', *Science (New York, N.Y.)*. United States, 334(6059), pp. 1141–1144. doi: 10.1126/science.1210333.

Scarpulla, R. C., Vega, R. B. and Kelly, D. P. (2012) 'Transcriptional integration of mitochondrial biogenesis', *Trends in Endocrinology and Metabolism*. Elsevier Ltd, 23(9), pp. 459–466. doi: 10.1016/j.tem.2012.06.006.

Sebastian, D. *et al.* (2012) 'Mitofusin 2 (Mfn2) links mitochondrial and endoplasmic reticulum function with insulin signaling and is essential for normal glucose homeostasis', *Proceedings of the National Academy of Sciences*, 109(14), pp. 5523–5528. doi: 10.1073/pnas.1108220109.

Sebastián, D. *et al.* (2016) 'Mfn2 deficiency links age-related sarcopenia and impaired autophagy to activation of an adaptive mitophagy pathway', *The EMBO Journal*, 35(15), pp. 1677–1693. doi: 10.15252/embj.201593084.

Shahzad, K. *et al.* (2015) 'Nlrp3-inflammasome activation in non-myeloid-derived cells aggravates diabetic nephropathy', *Kidney International*, 87(1), pp. 74–84. doi: 10.1038/ki.2014.271.

Shibutani, S. T. and Yoshimori, T. (2014) 'A current perspective of autophagosome biogenesis.', *Cell research*. England, 24(1), pp. 58–68. doi: 10.1038/cr.2013.159.

Shimada, K. *et al.* (2012) 'Oxidized Mitochondrial DNA Activates the NLRP3 Inflammasome during Apoptosis', *Immunity*. Elsevier Inc., 36(3), pp. 401–414. doi: 10.1016/j.immuni.2012.01.009.

Shintani, Y. *et al.* (2013) 'TLR9 mediates cellular protection by modulating energy metabolism in cardiomyocytes and neurons', *Proceedings of the National Academy of Sciences*, 110(13), pp. 5109–5114. doi: 10.1073/pnas.1219243110.

Shock, L. S. *et al.* (2011) 'DNA methyltransferase 1, cytosine methylation, and cytosine hydroxymethylation in mammalian mitochondria', *Proceedings of the National Academy of Sciences*, 108(9), pp. 3630–3635. doi: 10.1073/pnas.1012311108.

Sica, V. *et al.* (2015) 'Organelle-Specific Initiation of Autophagy.', *Molecular cell*. United States, 59(4), pp. 522–539. doi: 10.1016/j.molcel.2015.07.021.

Silva, A. M. A. M. *et al.* (2007) 'Salicylates trigger protein synthesis inhibition in a protein kinase R-like endoplasmic reticulum kinase-dependent manner', *The Journal of biological chemistry*. United States, 282(14), pp. 10164–10171. doi: 10.1074/jbc.M609996200.

Song, Z. *et al.* (2007) 'OPA1 processing controls mitochondrial fusion and is regulated by mRNA splicing, membrane potential, and Yme1L', *Journal of Cell Biology*, 178(5), pp. 749–755. doi: 10.1083/jcb.200704110.

Song, Z. *et al.* (2009) 'Mitofusins and OPA1 Mediate Sequential Steps in Mitochondrial Membrane Fusion Zhiyin', *Molecular biology of the cell*, 20, pp. 3525–3532. doi: 10.1091/mbc.E09.

Soubannier, V. *et al.* (2012) 'A vesicular transport pathway shuttles cargo from mitochondria to lysosomes', *Current Biology*. Elsevier Ltd, 22(2), pp. 135–141. doi: 10.1016/j.cub.2011.11.057.

Stein, A. and Sia, E. A. (2017) 'Mitochondrial DNA repair and damage tolerance.', *Frontiers in bioscience (Landmark edition)*, 22, pp. 920–943. Available at: http://www.ncbi.nlm.nih.gov/pubmed/27814655.

Stetson, D. B. and Medzhitov, R. (2006) 'Recognition of cytosolic DNA activates an IRF3-dependent innate immune response.', *Immunity*. United States, 24(1), pp. 93–103. doi: 10.1016/j.immuni.2005.12.003.

Sun, L. *et al.* (2012) 'Cyclic GMP-AMP Synthase Is a Cytosolic DNA Sensor That Activates the Type I Interferon Pathway', *Science*. United States, 339(December), pp. 1–10. doi: 10.1126/science.1232458.

Sutterwala, F. S., Haasken, S. and Cassel, S. L. (2014) 'Mechanism of NLRP3 inflammasome activation', *Annals of the New York Academy of Sciences*, 1319(1), pp. 82–95. doi: 10.1111/nyas.12458.

Tabeta, K. *et al.* (2006) 'The Unc93b1 mutation 3d disrupts exogenous antigen presentation and signaling via Toll-like receptors 3, 7 and 9.', *Nature immunology*. United States, 7(2), pp. 156–164. doi: 10.1038/ni1297.

Takeuchi, O. and Akira, S. (2010) 'Pattern Recognition Receptors and Inflammation', *Cell*. Elsevier Inc., 140(6), pp. 805–820. doi: 10.1016/j.cell.2010.01.022.

Taylor, P. R. *et al.* (2005) 'Macrophage Receptors and Immune Recognition', *Annual Review of Immunology*, 23(1), pp. 901–944. doi: 10.1146/annurev.immunol.23.021704.115816.

Temiz, P., Weihl, C. C. and Pestronk, A. (2009) 'Inflammatory myopathies with mitochondrial pathology and protein aggregates', *Journal of the Neurological Sciences*. Elsevier B.V., 278(1–2), pp. 25–29. doi: 10.1016/j.jns.2008.11.010.

Tezze, C. *et al.* (2017) 'Age-Associated Loss of OPA1 in Muscle Impacts Muscle Mass, Metabolic Homeostasis, Systemic Inflammation, and Epithelial Senescence', *Cell Metabolism*. Elsevier Inc., 25(6), p. 1374–1389.e6. doi: 10.1016/j.cmet.2017.04.021.

Tieu, Q. *et al.* (2002) 'The WD repeat protein, Mdv1p, functions as a molecular adaptor by interacting with Dnm1p and Fis1p during mitochondrial fission.', *The Journal of cell biology*. United States, 158(3), pp. 445–452. doi: 10.1083/jcb.200205031.

Twig, G. *et al.* (2008) 'Fission and selective fusion govern mitochondrial segregation and elimination by autophagy', *EMBO Journal*, 27(2), pp. 433–446. doi: 10.1038/sj.emboj.7601963.

Van, B. *et al.* (2015) 'Mitsugumin 56 (hedgehog acyltransferase-like) is a sarcoplasmic reticulum-resident protein essential for postnatal muscle maturation', *FEBS Letters*. Federation of European Biochemical Societies, 589(10), pp. 1095–1104. doi: 10.1016/j.febslet.2015.03.028.

Vane, J. R. (1971) 'Inhibition of prostaglandin synthesis as a mechanism of action for aspirin-like drugs', *Nature New Biology*, 231(25), pp. 232–235. doi: 10.1038/newbio231232a0.

Varanita, T. *et al.* (2015) 'The Opa1-dependent mitochondrial cristae remodeling pathway controls atrophic, apoptotic, and ischemic tissue damage', *Cell Metabolism*, 21(6), pp. 834–844. doi: 10.1016/j.cmet.2015.05.007.

Verhoeven, K. *et al.* (2006) 'MFN2 mutation distribution and genotype / phenotype correlation in Charcot – Marie – Tooth type 2', *Brain*, 129, pp. 2093–2102. doi: 10.1093/brain/awl126.

Vidoni, S. *et al.* (2013) 'Why Mitochondria Must Fuse to Maintain Their Genome Integrity', *Antioxidants & Redox Signaling*, 19(4), pp. 379–388. doi: 10.1089/ars.2012.4800.

Vogel, F. *et al.* (2006) 'Dynamic subcompartmentalization of the mitochondrial inner membrane', *Journal of Cell Biology*, 175(2), pp. 237–247. doi: 10.1083/jcb.200605138.

Votruba, M., Moore, A. T. and Bhattacharya, S. S. (1998) 'Clinical features, molecular genetics , and pathophysiology of dominant optic atrophy', *Journal of Medical Genetics*, 35, pp. 793–800. doi: 10.1136/jmg.35.10.793.

Wai, T. and Langer, T. (2016) 'Mitochondrial Dynamics and Metabolic Regulation', *Trends in Endocrinology and Metabolism*. Elsevier Ltd, 27(2), pp. 105–117. doi: 10.1016/j.tem.2015.12.001.

Wang, D. Z. *et al.* (2001) 'The Mef2c gene is a direct transcriptional target of myogenic bHLH and MEF2 proteins during skeletal muscle development.', *Development (Cambridge, England)*, 128, pp. 4623–4633.

Wei, Y. *et al.* (no date) 'Prohibitin 2 Is an Inner Mitochondrial Membrane Mitophagy Receptor Article Prohibitin 2 Is an Inner Mitochondrial Membrane Mitophagy Receptor', *Cell*. Elsevier Inc., pp. 1–15. doi: 10.1016/j.cell.2016.11.042.

Wek, R. C., Jiang, H.-Y. and Anthony, T. G. (2006) 'Coping with stress: eIF2 kinases and translational control The family of eIF2 (eukaryotic initiation factor 2) kinases regulate translation during different stress conditions', pp. 7–11. Available at: http://www.biochemsoctrans.org/content/ppbiost/34/1/7.full.pdf.

Wenceslau, C. F. *et al.* (2013) 'Mitochondrial-derived N-formyl peptides: Novel links between trauma, vascular collapse and sepsis', *Medical Hypotheses*. Elsevier Ltd, 81(4), pp. 532–535. doi: 10.1016/j.mehy.2013.06.026.

West, A. P. *et al.* (2015) 'Mitochondrial DNA stress primes the antiviral innate immune response', *Nature*, 520(7548), pp. 553–557. doi: 10.1038/nature14156.

West, A. P. and Shadel, G. S. (2017) 'Mitochondrial DNA in innate immune responses and inflammatory pathology', *Nature Reviews Immunology*. Nature Publishing Group, 17(6), pp. 363–375. doi: 10.1038/nri.2017.21.

West, A. P., Shadel, G. S. and Ghosh, S. (2011) 'Mitochondria in innate immune responses', *Nature Reviews Immunology*. England: Nature Publishing Group, 11(6), pp. 389–402. doi: 10.1038/nri2975.

Westermann, B. (2010) 'Mitochondrial fusion and fission in cell life and death', *Nature Reviews Molecular Cell Biology*. Nature Publishing Group, 11(12), pp. 872–884. doi: 10.1038/nrm3013.

Wong, S. C. *et al.* (2016) 'Growth and the Growth Hormone-Insulin Like Growth Factor 1 Axis in Children With Chronic Inflammation: Current Evidence, Gaps in Knowledge, and Future Directions.', *Endocrine reviews*. United States, 37(1), pp. 62–110. doi: 10.1210/er.2015-1026.

Wong, Y. C. and Holzbaur, E. L. F. (2014) 'Optineurin is an autophagy receptor for damaged mitochondria in parkin-mediated mitophagy that is disrupted by an ALS-linked mutation', *Proceedings of the National Academy of Sciences of the United States of America*, pp. 1–10. doi: 10.1073/pnas.1405752111.

Wree, A. *et al.* (2014) 'NLRP3 inflammasome activation results in hepatocyte pyroptosis, liver inflammation, and fibrosis in mice', *Hepatology*, 59(3), pp. 898–910. doi: 10.1002/hep.26592.

Wu, J. *et al.* (2013) 'Cyclic GMP-AMP is an endogenous second messenger in innate immune signaling by cytosolic DNA', *Science*, 339(6121), pp. 826–830. doi: 10.1126/science.1229963.

Yamano, K., Matsuda, N. and Tanaka, K. (2016) 'The ubiquitin signal and autophagy : an orchestrated dance leading to mitochondrial degradation', *EMBO Reports*, 17(3), pp. 300–316. doi: 10.15252/embr.201541486.

Yim, H. C. H. and Williams, B. R. G. (2014) 'Protein kinase R and the inflammasome.', *Journal of interferon & cytokine research : the official journal of the International Society for Interferon and Cytokine Research*, 34(6), pp. 447–54. doi: 10.1089/jir.2014.0008.

Yin, M. J., Yamamoto, Y. and Gaynor, R. B. (1998) 'The anti-inflammatory agents aspirin and salicylate inhibit the activity of IκB kinase-β', *Nature*, 396(6706), pp. 77–80. doi: 10.1038/23948.

Yin, M., Yamamoto, Y. and Gaynor, R. B. (1998) 'The anti-inflammatory agents aspirin and salicylate inhibit the activity of I B kinase- ', pp. 77–80.

Yoon, Y. and McNiven, M. A. (2001) 'Mitochondrial division: New partners in membrane pinching', *Current Biology*, 11(2), pp. 67–70. doi: 10.1016/S0960-9822(01)00011-2.

Yoshida, K. *et al.* (2017) 'PKR induces the expression of NLRP3 by regulating the NF-κB pathway in Porphyromonas gingivalis-infected osteoblasts', *Experimental Cell Research*. Elsevier Inc., 354(1), pp. 57–64. doi: 10.1016/j.yexcr.2017.03.028.

Youle, R. J. and Narendra, D. P. (2011) 'Mechanisms of mitophagy', *Nature Publishing Group*. Nature Publishing Group, 12(1), pp. 9–14. doi: 10.1038/nrm3028.

Yu, E. P. K. and Bennett, M. R. (2014) 'Mitochondrial DNA damage and atherosclerosis', *Trends in Endocrinology and Metabolism*. Elsevier Ltd, 25(9), pp. 481–487. doi: 10.1016/j.tem.2014.06.008.

Zanna, C. *et al.* (2008) 'OPA1 mutations associated with dominant optic atrophy impair oxidative phosphorylation and mitochondrial fusion.', *Brain : a journal of neurology*. England, 131(Pt 2), pp. 352–367. doi: 10.1093/brain/awm335.

Zeviani, M. (2008) 'OPA1 mutations and mitochondrial DNA damage: keeping the magic circle in shape.', *Brain : a journal of neurology*. England, 131(Pt 2), pp. 314–317. doi: 10.1093/brain/awm339.

Zhang, J. Z. *et al.* (2014) 'Mitochondrial DNA induces inflammation and increases TLR9/NF-κB expression in lung tissue', *International Journal of Molecular Medicine*, 33(4), pp. 817–824. doi: 10.3892/ijmm.2014.1650.

Zhang, L. *et al.* (2016) 'Intra-peritoneal administration of mitochondrial DNA provokes acute lung injury and systemic inflammation via toll-like receptor 9', *International Journal of Molecular Sciences*, 17(9), pp. 1–16. doi: 10.3390/ijms17091425.

Zhang, Q. *et al.* (2010) 'Circulating mitochondrial DAMPs cause inflammatory responses to injury', *Nature*. Nature Publishing Group, 464(7285), pp. 104–107. doi: 10.1038/nature08780.

Zhang, W. *et al.* (2013) 'Phosphorylation Events in Selective Mitophagy : Possible Biochemical Markers ?', *Current Pathobiology Reports*, 1(4), pp. 273–282. doi: 10.1007/s40139-013-0033-8.

Zhao, Y. *et al.* (2014) 'Distinct mechanisms of induction of hepatic growth hormone resistance by endogenous IL-6, TNF-α, and IL-1β.', *American journal of physiology. Endocrinology and metabolism*, 307(2), pp. E186-98. doi: 10.1152/ajpendo.00652.2013.

Zhong, B. *et al.* (2008) 'The adaptor protein MITA links virus-sensing receptors to IRF3 transcription factor activation.', *Immunity*. United States, 29(4), pp. 538–550. doi: 10.1016/j.immuni.2008.09.003.

Zhou, R. *et al.* (2011) 'A role for mitochondria in NLRP3 inflammasome activation', *Nature*, 469(7329), pp. 221–226. doi: 10.1038/nature09663.

Zhuang, Y. *et al.* (2015) 'Mitochondrial dysfunction confers albumin-induced NLRP3 inflammasome activation and renal tubular injury', *American Journal of Physiology-Renal Physiology*, 308(8), pp. F857–F866. doi: 10.1152/ajprenal.00203.2014.

Zorzano, A. *et al.* (2010) 'Mitochondrial fusion proteins: Dual regulators of morphology and metabolism', *Seminars in Cell and Developmental Biology*. Elsevier Ltd, 21(6), pp. 566–574. doi: 10.1016/j.semcdb.2010.01.002.

Zuchner, S. *et al.* (2004) 'Mutations in the mitochondrial GTPase mitofusin 2 cause Charcot-Marie-Tooth neuropathy type 2A.', *Nature genetics*. United States, 36(5), pp. 449–451. doi: 10.1038/ng1341.

Zuchner, S. *et al.* (2005) 'Emerging pathways for hereditary axonopathies.', *Journal of molecular medicine (Berlin, Germany)*. Germany, 83(12), pp. 935–943. doi: 10.1007/s00109-005-0694-9.

Watercolor illustrations

were painted by J.A. Rodríguez